



University
of Basel

Swiss Nanoscience Institute



EINE INITIATIVE DER UNIVERSITÄT BASEL
UND DES KANTONS AARGAU

Annual Report 2020 Supplement Swiss Nanoscience Institute University of Basel

The Swiss Nanoscience Institute (SNI) is a research initiative of the Canton of Aargau and the University of Basel.

This report summarizes work conducted at the Swiss Nanoscience Institute (SNI) in 2020.

Swiss Nanoscience Institute
Klingelbergstrasse 82
4056 Basel
Switzerland
www.nanoscience.ch

Cover image: Scanning electron microscope image of parts of a spin qubit device which was fabricated by means of electron beam lithography. It is colored in rainbow colors, because the structures arrange themselves at a distance a little smaller than the wavelength of visible light and show different colors depending on the viewing angle. (Jann Hinnerk Ungerer, SNI PhD Student, Department of Physics, University of Basel)

© Swiss Nanoscience Institute, March 2021

Contents

SNI PhD School reports		
P1304	Monitoring β -barrel membrane protein folding	2
P1402	Pushing the limits of lightweight materials	4
P1501	Nanomechanical membranes for multiplexed viscosity and liquid density measurements in real-time	6
P1503	Filming biological factories	8
P1505	Demonstration of voltage-controlled three-electron-beam interference with Boersch phase shifter	10
P1601	Optical effects in water splitting electrodes: modeling and experiments	12
P1602	The physico-chemistry of metal-organic ionic complexes upon sublimation and deposition	14
P1603	Mesoscale dynamics of the yeast nuclear pore complex transport channel	16
P1604	Solid-supported planar membranes: How polymers affect the properties and activity of biomolecules	18
P1606	Smart peptide nanoparticles for efficient and safe gene therapy	20
P1607	Understanding phonon propagation in nanodevices	22
P1701	Monolayer semiconducting MoS ₂ with superconducting contacts	24
P1702	Development of a 3D poly(methyl methacrylate) microfluidic device for biomedical applications	26
P1704	Engineering mechanical properties of protein binders	28
P1705	Towards label-free HTS in enzyme engineering	30
P1706	Fiber-based cavity optomechanics	32
P1707	Giant Stark splitting of an excitation in bilayer MoS ₂	34
P1708	Freeform optical structure	36
P1801	Nano-sized plasma membrane vesicles as an emerging EV platform for therapeutic applications	38
P1802	Enhancing directed evolution with deep learning	40
P1803	Energy dissipation on suspended graphene	42
P1804	Picoscopic mass analysis of mammalian cells	44
P1806	Image the twist!	46
P1807	Towards circuit-quantum electrodynamics with gate-tuneable nanowire devices	48
P1808	Coupling an ultracold ion to a metallic nanowire	50
P1901	Visual proteomics to study neurodegenerative diseases	52
P1902	MIMYO: Mimicking MYOcardial tissue with a 3D nanofiber network	54
P1903	Towards non-invasive temperature mapping	56
P1904	Recording movements of biomolecules in action	58
P1905	Applying nanowire MFM to 2D materials	60
P1906	Screening for nm-sized self-assembled molecular containers	62
P1907	Light-mediated strong coupling of a nanomechanical membrane to atomic spins	64
P1908	Towards molecular VOC sensors – nanowires from chiral Pt(II) Isocyanide complexes	66
Argovia project reports		
A13.08	Disruptive power storage technology applying electrolyte nano dispersion	68
A14.04	A detector for pesticides in drinking water	70
A14.07	Origami heart model based on nano-patterned paper scaffold for directed cardiac tissue engineering	72
A14.13	Novel cancer-targeted nanoparticles	74
A14.15	Nano-in-nano platform system for local drug delivery	76
A14.19	Customized, nanostructured grating compressors for high repetition rate ultrafast laser	78
A15.01	Mechanoresponsive liposomes – formulation and process development	80
A15.08	Post-treatment of wear-resistant implant coatings	82
A15.09	Design of chemically patterned UV-curable coatings with anti-fingerprint properties	84
A15.10	'Less is more' – High throughput nanoparticle detection for quality control of complex food matrices	86
A15.11	Antibacterial titanium nanostructures by helium plasma irradiation	88
Publication list		90

Monitoring β -barrel membrane protein folding

Project P1304: Folding mechanisms of β -barrel outer membrane proteins and their catalysis by natural holdases and foldases

Project Leader: S. Hiller and D. J. Müller

Collaborators: N. Ritzmann (SNI PhD Student), P. Rios Flores, T. Raschle, and J. Thoma

β -barrel membrane proteins are essential functional components of the outer membrane of Gram-negative bacteria, mitochondria and chloroplasts. Membrane proteins have highly interesting folding properties, since they fold in an external environment that comprises hydrophobic and hydrophilic phases. The biogenesis of these outer membrane proteins (Omps) poses a complex biophysical challenge to the pro- and eukaryotic cell, because the Omps are synthesized at locations distant from their target membrane. The overall essential biological function of Omp biogenesis is accomplished by molecular chaperones that pass the unfolded substrates from the ribosome to the destination membrane [1]. In the Gram-negative bacterium *E. coli*, the periplasmic chaperones SurA and Skp transport the substrate to the Bam complex, which folds and inserts them into the outer membrane [2]. The in vitro and the in vivo folding mechanisms of β -barrel Omps from mitochondria or Gram-negative bacteria are so far not understood at atomic resolution. The same polypeptide chains can refold in vitro in the absence of chaperones and other proteins, resulting in the same three-dimensional β -barrel structures. In this project, we employ structural biological and nanotechnological approaches to characterize the folding process of complex Omps at atomic resolution. In the following we report on recent papers, which we published since starting our project and thereafter provide an overview of the following challenges in this project.

Monitoring Backbone Hydrogen Bond Formation

The three-dimensional structure of a β -barrel membrane protein is defined by backbone hydrogen bonds between adjacent strands. The biogenesis pathways of β -barrel membrane proteins are essential, but the underlying mechanism is still unclear. To obtain insight into this process, we characterized folding of the 8-stranded OmpX from *E. coli* as a model system and found that the residue-specific kinetics of interstrand hydrogen-bond formation are uniform in the entire β -barrel and synchronized to formation of the tertiary structure [3]. OmpX folding thus propagates via a long-lived conformational ensemble state in which all backbone amide protons engage in hydrogen bonds only transiently. Stable formation of the entire OmpX hydrogen bond network occurs downhill of the rate-limiting transition state and thus appears cooperative on the overall folding time scale.

Chaperone Assisted Insertion and Folding

The correct insertion and folding of membrane proteins is essential to function in living cells. Whereas in living cells molecular chaperones increase the folding yields of soluble proteins by suppressing misfolding and aggregation, it is not understood how they modulate the insertion and folding of integral membrane proteins into membranes. To study this process, we used single-molecule force spectroscopy (SMFS)

and NMR spectroscopy to characterize how periplasmic holdase chaperones SurA and Skp shape the folding trajectory of the large β -barrel Omp FhuA from *E. coli* [4]. After having unfolded and extracted a single FhuA from the lipid membrane by SMFS, we thus monitored how the unfolded polypeptide inserts and folds back into the membrane. The presence of either of the two periplasmic chaperones SurA or Skp prevented misfolding of FhuA by stabilizing a dynamic, unfolded state. Thereby SurA allowed the unfolded substrate to stepwise insert and fold the unfolded FhuA polypeptide towards its native structure.

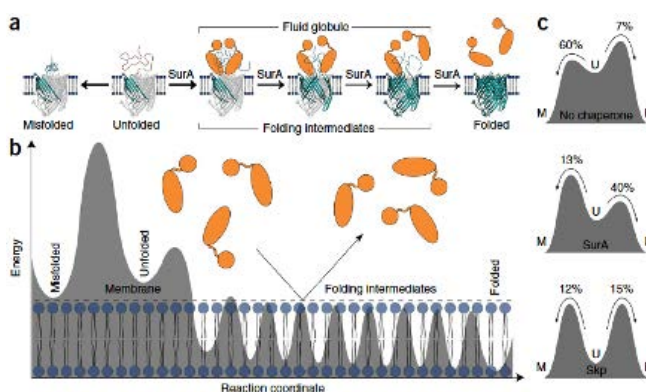


Fig. 1 Folding pathways and free-energy landscape of FhuA receptors. a) Insertion and folding pathways of FhuA in the absence of chaperones and in the presence of SurA (orange). Without chaperones, the majority of unfolded FhuA receptors misfold. SurA stabilizes the unfolded state of FhuA and promotes step-wise insertion and folding of β -hairpins in the lipid membrane. This stepwise insertion of secondary structures proceeds until the receptor completed folding. b) Hypothetical folding free-energy landscape of FhuA in the presence of SurA. SurA (orange) is spatially excluded from the lipid membrane (blue). Each β -hairpin inserted into the lipid membrane is stabilized by a free-energy well. c) Modulation of the folding free-energy landscape by chaperones. The free-energy barriers separating the unfolded (U) from the misfolded (M) and folded (F) states, are determined from the observed folding probabilities. Image taken from ref [4].

Directed Insertion of Membrane Proteins

To study whether we could apply the knowledge gained in this proposal and guide the insertion of membrane proteins, we engineered light-driven proton pumps having either a red (RFP) or green (GFP) fluorescent protein fused to its N- or C-terminus [5]. The hydrophilic fluorescent proteins allowed the directed insertion of proton pumps into liposomes and to select the liposomes depending on fluorescence. The thus manufactured nanoreactors were used to generate proton gradients by light, which is a prerequisite to power a broad

variety biomolecular processes. In the future, this side project will enable to supply nanoscopic factories with energy and to translocate polypeptides or other molecules across membranes.

Maltoporin Unfolding Pathways

The next challenge in this project was to study whether Omps generally unfold and fold similarly to FhuA. We hence first unfolded maltoporin LamB from *E. coli* by SMFS [6]. It was observed that also maltoporin stepwise unfolds β -hairpins until the β -barrel has been completely unfolded and extracted from the membrane. Thereby the folding probability of a β -hairpin was found to be correlated to its mechanical stability. The study was fundamental to characterize at later stage the insertion and folding of other Omps by BAM.

BamA Unfolding Pathways

The next challenge in this project was to characterize the unfolding pathways of BamA. These unfolding pathways can then later be used as fingerprint to study the folding of BamA. To approach as native as possible conditions for the unfolding and later for the folding process we developed the utilization of outer membrane vesicles (OMVs) released from *E. coli* to study Omps in the native membrane environment. Enriched in the native membrane of the OMV we characterize the assembly, folding, and structure of OmpG, FhuA, Tsx, and BamA. Comparing Omps in OMVs to those reconstituted into artificial lipid membranes, we observe different unfolding pathways for some Omps. The observation highlights the importance of the native membrane environment to maintain the native structure and function relationship of Omps.

Next we studied the unfolding pathways of BamA in OMV in detail [8]. It was observed that the core component of BamA adopts several conformations, which are thought to facilitate the insertion and folding of β -barrel proteins into the bacterial outer membrane. Which factors alter the stability of these conformations remains to be quantified. We thus applied SMFS to characterize the mechanical properties of BamA from *E. coli*. In contrast to the N-terminal periplasmic polypeptide-transport-associated (POTRA) domains, it was found that the C-terminal transmembrane β -barrel domain of BamA is mechanically much more stable. Exposed to mechanical stress this β -barrel stepwise unfolds β -hairpins until unfolding has been completed. Thereby, the mechanical stabilities of β -barrel and β -hairpins are modulated by the POTRA domains, the membrane composition and the extracellular lid closing the β -barrel. We anticipate that these differences in stability, which are caused by factors contributing to BAM function, promote conformations of the BamA β -barrel required to insert and fold outer membrane proteins.

Latest progress and Challenges Ahead

To understand how BAM inserts and folds Omps we have recorded several millions of folding and insertion experiments by SMFS. The extensive data is currently analyzed and additional controls are being made. Furthermore, recent discoveries highlight the importance of BAM as a promising antibiotic target [9], which underlines the relevance of understanding BAM-mediated Omp folding. By SMFS we have thus also characterized how the newly discovered natural antibiotic darobactin affects the mechanical properties of BAM. By further conducting dynamic SMFS experiments we quantified how the thermodynamic, kinetic and mechanical properties of the BAM structure are affected by the antibiotic. The extensive experiments have been concluded and are currently analyzed. We hope that the final structural and

functional insights gained in this project will be helpful in the understanding of the insertion and folding mechanism of BamA and how these activities can be inhibited by novel antibiotics.

References

- [1] T. J. Knowles, A. Scott-Tucker, M. Overduin, I. R. Henderson, Membrane protein architects: the role of the BAM complex in outer membrane protein assembly, *Nat Rev Microbiol* **7**, 206 (2009)
- [2] J. G. Sklar, T. Wu, D. Kahne, T.J. Silhavy, Defining the roles of the periplasmic chaperones SurA, Skp, and DegP in *Escherichia coli*, *Genes Dev* **21**, 2473 (2007)
- [3] T. Raschle, P. Rios Flores, C. Opitz, D.J. Müller, S. Hiller, Monitoring backbone hydrogen bond formation in β -barrel membrane protein folding, *Angew Chem Int Ed* **55**, 5952 (2016)
- [4] J. Thoma, B.M. Burmann, S. Hiller, D.J. Müller, Impact of holdase chaperones Skp and SurA on the folding of β -barrel outer membrane proteins, *Nat Struct Mol Biol* **22**, 795 (2015)
- [5] N. Ritzmann, J. Thoma, S. Hirschi, D. Kalbermatter, D. Fotiadis, D. J. Müller, Fusion domains guide the oriented insertion of light-driven proton pumps into liposomes, *Biophys J* **113**, 1181 (2017)
- [6] J. Thoma, N. Ritzmann, D. Wolf, E. Mulvihill, S. Hiller, D. J. Müller, Maltoporin LamB unfolds beta-hairpins along mechanical stress-dependent unfolding pathways, *Structure* **25**, 1139 (2017)
- [7] J. Thoma, S. Manioglou, D. Kalbermatter, P. D. Bosshart, D. Fotiadis, D.J. Müller, Protein-enriched outer membrane vesicles as a native platform for outer membrane protein studies, *Communications Biology* **1**, 23 (2018)
- [8] J. Thoma, Y. Sun, N. Ritzmann, D.J. Müller, POTRA-domains, extracellular lid and membrane composition modulate the conformational stability of the beta-barrel assembly factor BamA, *Structure* **26**, 987 (2018)
- [9] Y. Imai, K. J. Meyer, A. Iinishi, Q. Favre-Godal, R. Green et al., A new antibiotic selectively kills Gram-negative pathogens, *Nature* **576**, 459 (2019)

Pushing the limits of lightweight materials

Project P1402: Lightweight structures based on hierarchical composites

Project Leader: C. Dransfeld and C. Schönenberger

Collaborators: W. Szmyt (SNI PhD Student) and C. Padeste

Context

When high mechanical performance at low weight is required, carbon fibre (CF)-reinforced polymer composites outperform all known engineering materials. However, the mechanical benefits of this composite type are mostly pronounced only in the direction of the fibre. Upon shear or compression loads, the material properties are limited by the fibre-matrix interface. In this project, we aim to enhance the interface by carbon nanotubes (CNTs) on the surface of the CF obtaining hierarchical composites. We aimed at a dense and aligned CNT growth on the CF for maximum off-axis mechanical improvements. Such a morphology is achievable by means of catalytic chemical vapour deposition (CVD) [1]. However, it has been shown, that CVD leads to severe deterioration of the CF mechanical properties by etching of the CF surface with the metallic catalyst nanoparticles used in the process [2]. In our past works, we have demonstrated that application of a 12 nm Al_2O_3 film on CF allows protecting the fibre by blocking the migration of the catalyst [3,4]. Moreover, we have developed a method of coating of the CF with the Al_2O_3 , which ensures a strong adhesion of the film to the CF [5]. Synthesizing homogeneous, dense and aligned CNTs on CFs has however remained a challenge, which we addressed in our recent work. Moreover, when CNTs are to be grown homogeneously on CF tows or fabrics, one needs to ensure that the chemical vapours get delivered to the CNT growth locations at sufficient rates, therefore gas transport kinetics in such fibre arrays needs to be well-understood. We identified that the theory in this aspect is lacking in the literature and developed the analytical model of gas transport in fibrous structures.

Methods and results

The morphology of CNT arrays synthesised by chemical vapour deposition (CVD) is strictly determined by the dispersion of the catalyst nanoparticles (typically iron) on the substrate surface. We present our new strategy of coating of Al_2O_3 -coated substrates, such as CF, with iron catalyst for a homogeneous, dense and aligned CNT growth. We coated the substrates with iron catalyst precursor by dipping in solutions of iron nitrate in isopropanol. We demonstrated by dynamic light scattering experiments that the ageing of iron nitrate solution is a critical factor in the process, due to gradual precipitation of solid nanoparticles in the solution. We identified that the nanoparticles of desirable sizes (~10 nm) precipitate in the solutions within 25-30 min ageing time. To analyse the quality of nanoparticle coatings, we carried out the CVD process on the iron catalyst-coated substrates without delivery of carbon precursor for CNT growth, which led to the formation of iron nanoparticles on the substrate surfaces. The nanoparticle coatings were analysed by scanning electron microscopy (SEM)(Fig. 1). We observed agglomeration issues and sample-scale inhomogeneities, which

inevitably lead to undesirable CNT growth morphology. Therefore, prior to dip-coating in the iron nitrate solutions, we applied an amine surface functionalisation by (3-aminopropyl)trimethoxysilane solution in ethanol (aminosilane treatment) for promotion of more homogeneous precipitation of the iron catalyst precursor. The results confirmed that the treatment is beneficial to the nanoparticle dispersion, which could be substantiated by evaluating the area disorder of the Delaunay triangulation, for recipes with and without aminosilane. The CNT growth experiments have confirmed, that the enhanced quality of the nanoparticle coating results in an improved CNT morphology (Fig. 2). The developed processing route from Al_2O_3 -coating to CNT-growth is shown in figure 3.

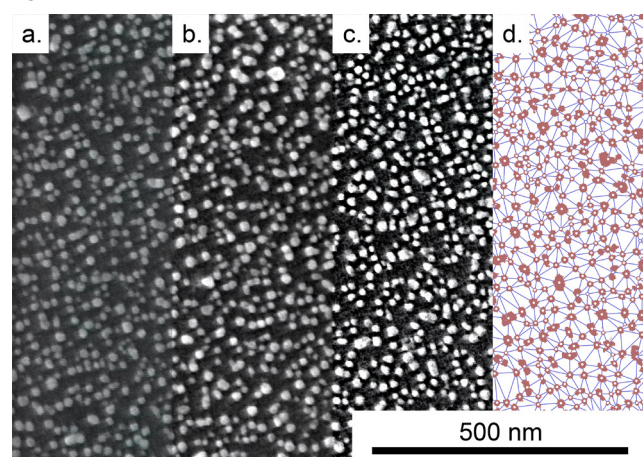


Fig. 1 Catalyst nanoparticle coating – SEM image analysis. Subsequent analysis steps are shown, from local contrast enhancement to nanoparticle segmentation and Delaunay triangulation for dispersion quality assessment.

Further on, we developed the new theoretical framework of gas transport in fibrous media. In order to fundamentally describe the gas transport kinetic parameters within fibre arrays, we considered the gas transport to be governed by a random walk of gas molecules, following the Einstein-Smoluchowski diffusion model. For this purpose, we evaluated the length of the flight path of a gas molecule from one collision to another, whether the collision occurs with another gas molecule or with the solid wall. This route let us to analytically describe the gas transport kinetics dependent on the average distances between fibres (equivalently, fibre length per volume) and average fibre diameter [6]. The model developed is applicable at a wide range of pressures: from low pressures, where molecule-wall collisions dominate, to higher pressures, where the molecules mostly collide with each other. We compared the analytical model against stochastic Monte-Carlo simulation and observed an excellent

agreement (Fig. 4), which constitutes a strong validation of the model.

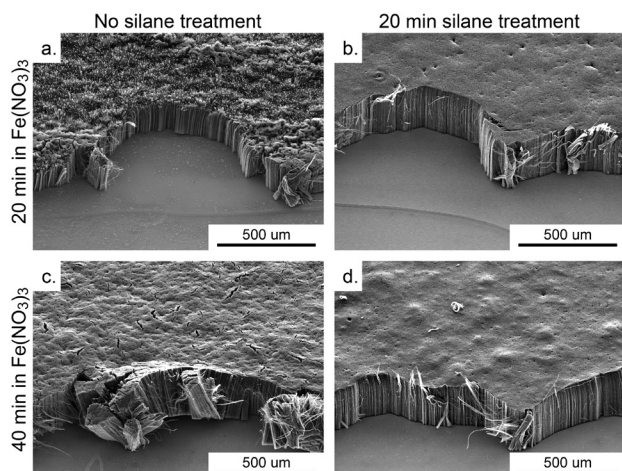


Fig. 2 CNT growth results on silicon showing the beneficial effect of aminosilane treatment and the influence of immersion time in the iron nitrate solution.

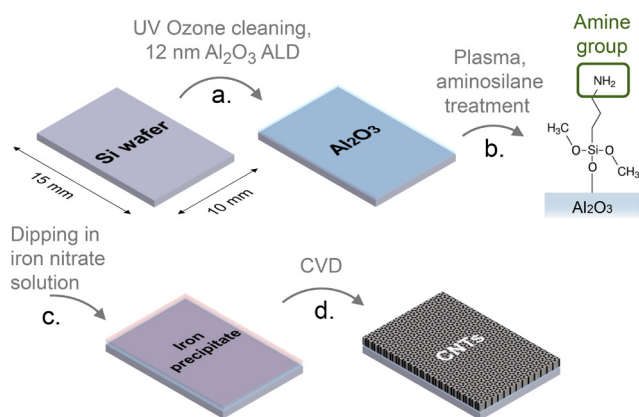


Fig. 3 Steps of the novel sample preparation approach with aminosilane illustrated for the case of the silicon substrate. The carbon fibres undergo the same treatment. a) Al₂O₃-coating, b) amine surface functionalisation, c) precipitation of the catalyst precursor film onto the substrate surface, d) CNT growth by CVD.

Summary and conclusion

We report a new method of homogeneous coating of complex Al₂O₃-coated substrates, such as CF fabrics or tows, with iron catalyst nanoparticles, which enables CNT growth on these substrates at high density, alignment and homogeneity. We elucidate the significance of the ageing effect of the catalyst precursor solution and confirm the beneficial effect of the aminosilane treatment on the catalyst coating homogeneity and dispersion quality. The recipe developed results in remarkable CNT growth morphology, as desired for hierarchical composites. Moreover, the novel theoretical framework of gas transport in fibrous structures paves the way for further understanding of the CNT growth on CF tows or fabrics with further impact on other kinds of gas-phase processing challenges of fibrous structures.

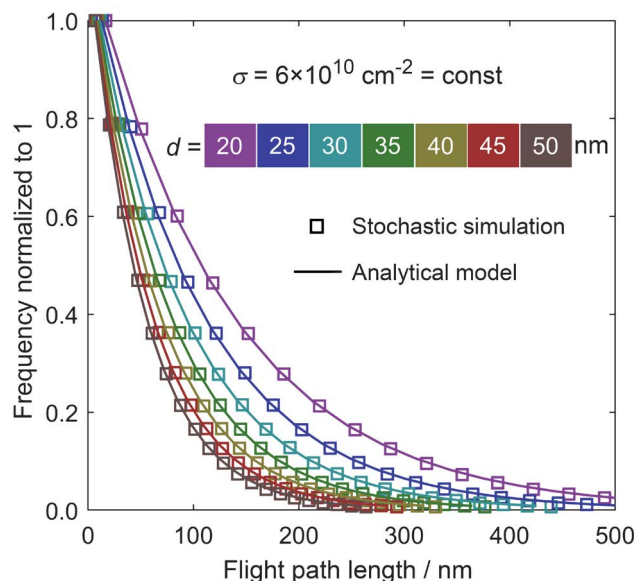


Fig. 4 Flight path length of the gas molecule within an array of nanoscale fibres evaluated at a range of fibre diameters d at the given fibre axes length per volume σ : comparison of the analytical model and the stochastic simulation shows an excellent agreement. The values of d and σ are typical for a dense CNT array, however the model is applicable for microscale fibres as well.

References

- [1] H. Qian, E. S. Greenhalgh, M. S. P. Shaffer, A. Bismarck, Carbon nanotube-based hierarchical composites: a review, *J. Mater. Chem.* **20**, 4751 (2010)
- [2] H. Qian, A. Bismarck, E. S. Greenhalgh, M. S. P. Shaffer, Carbon nanotube grafted carbon fibres: A study of wetting and fibre fragmentation, *Compos. Part Appl. Sci. Manuf.* **41**, 1107–1114 (2010)
- [3] S. Vogel, C. Dransfeld, B. Friedler, J. Gobrecht, Protective effect of thin alumina layer on carbon fibre to preserve tensile strength during CNT growth by CVD. in Proceedings of ECCM16 - 16th European Conference on Composite Materials (2014)
- [4] W. Szmyt et al., Protective effect of ultrathin alumina film against diffusion of iron into carbon fiber during growth of carbon nanotubes for hierarchical composites investigated by ptychographic X-ray computed tomography, *Carbon* **115**, 347–362 (2017)
- [5] W. Szmyt, M. Calame, C. Padeste, C. Dransfeld, Nano-engineering of fibre surface for carbon fibre-carbon nanotube hierarchical composites. in Proceedings of ICCM22 - 22nd International Conference on Composite Materials (2019)
- [6] W. Szmyt, C. Guerra-Nuñez, C. Dransfeld, I. Utke, Solving the inverse Knudsen problem: Gas diffusion in random fibrous media, *J. Membr. Sci.*, arXiv:2006.04883 (2020)

Nanomechanical membranes for multiplexed viscosity and liquid density measurements in real-time

Project P1501: Nanomechanical mass and viscosity measurement-platform for cell imaging

Project Leader: T. Braun and E. Meyer

Collaborators: P. Oliva (SNI PhD Student), Marc Sulliger (Master Student), B. Bircher, C. Padeste, N. Opara, C.-A. Schönenberger, F. Huber, and H. P. Lang

Introduction

To date, most methods used to determine the viscosity and mass density of liquids have two drawbacks: Long measurement time (in the range of minutes) and high sample consumption (in the range of milliliters). Unfortunately, this limitation makes viscometry inappropriate to characterize biological processes, despite the immense potential as a label- and functionalization-free method. Nanomechanical transducers promise to overcome these limitations.

We developed a micro-viscometer allowing liquid characterization using nano-mechanical membranes. The instrument is geared to measure small aqueous droplets' viscosity and liquid density values (Fig. 1).

brane (2) form a well, which can be filled with the test liquid. The stoichiometric membrane windows are made of Si₃N₄-films (thickness 200 nm) with a high tensile stress (1GPa). (3) Temperature-controlled copper plate; (4) Fused silica capillary for sample deposition on the silicon-nitride membrane; (5) Sample droplet; (6) Temperature sensor used to regulate the temperature of the membrane holder; (1) Silicon frame with (2) silicon-nitride membrane. Inset: Silicon-nitride membrane with sample priming; (B) Temperature and humidity controlled chamber mounted on a XY-stage; (7) Humidity chamber made of plexiglass; (8a) Inlet and (8b) outlet of humid air; (9) Temperature sensor monitoring the temperature of the humidity chamber; (10) Humidity sensor monitoring the relative humidity inside the chamber; (11) XY-stage. Adapted from Oliva et al., 2019 [1].

Small sample droplets are placed on the nanomechanical membrane (Fig. 1A). Measurements are performed in a climate chamber under precisely controlled humidity and temperature. A photo-thermal system is used to actuate the gold-coated nanomechanical membrane. A laser detection system records the membrane's response (Fig. 2), and a three-point calibration system [2, 3] allows the real-time determination of the liquid's viscosity and mass-density from 1 μ L droplets.

Characterization of filament formation

Figure 2 depicts the real-time measurement of the polymerization of globular G-actin to filamentous F-Actin. During the data acquisition, a decreasing amplitude and a slight frequency shift were observed [1]. These two behaviors are related to F-actin formation, where the increasing viscosity leads to higher damping, which implicates decreasing quality factors. At the same time, filament growth results in a denser liquid. Corresponding to the three steps of actin polymerization, i.e., nucleation, elongation, and a steady-state phase, three states are revealed by the curves presented in figure 2. In the absence of polymerization inducing buffer, fluctuating eigenfrequencies and quality factors were visible, but no significant decrease or increase of the quality factor and eigenfrequency were observed over time. Furthermore, subsequent electron microscopy of the sample only revealed filaments for the positive control (Fig. 2b). Comparable results were obtained during the fibrillation of amyloid proteins (data not shown).

Transducer improvements

Our analysis of the membrane response showed that a significant part of the nanomechanical membrane's vibrational energy dissipates into the chip base. Thereby, resonator modes couple to the surrounding substrate's modes, which leads to a significant energy loss of the resonator. In practice, this is a dominating damping factor. To increase the vibrational amplitudes, we envisage blocking the phonon-tunneling into the nanomechanical membrane's clamping base by a "membrane in the middle" approach – preliminary amended transducers were produced and are depicted in figure 3.

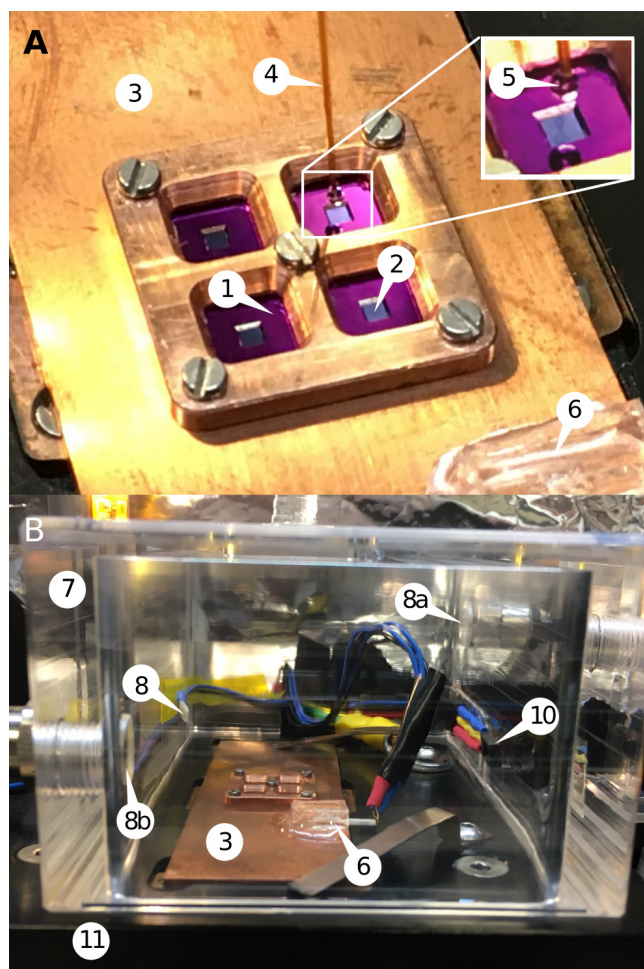


Fig. 1 Nanomechanical membrane transducer, liquid handling system, and environment control. (A) Array of membrane transducers and sample priming: Silicon-frame (1) and the silicon-nitride mem-

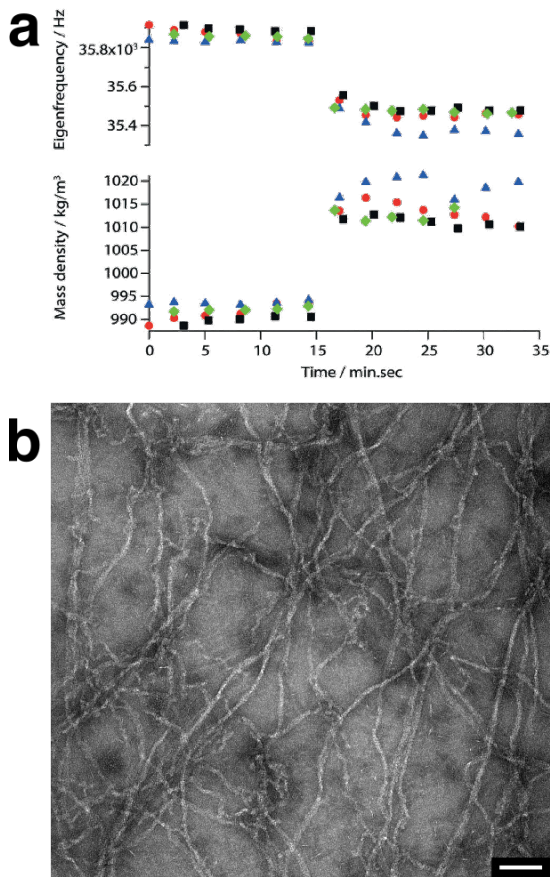


Fig. 2 Real-time characterization of F-actin formation: (a) & (b) Measured eigenfrequencies, quality factors and the corresponding mass densities and viscosities of polymerizing actin. The values were calculated by applying the reduced order model. Each color and each mark represents one measurement performed with the same silicon-nitride membrane. The red, black, blue and green marks represent the first, second, third, and fourth run respectively. (c) After the real-time measurement of the viscosity the sample was removed from the membrane and negative stain electron microscopy was performed. The images conformed the fibrillation of the G-actin to F-actin. Scale bar: 500 nm.

Increased performance of the transducer will lead to improved, more precise measurements with less noise.

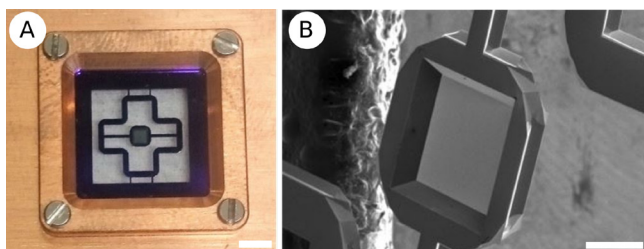


Fig. 3 Microfabricated phonon-tunneling suppressed sensor-chips (preliminary results). A) Membrane sensor mounted on a temperature controlled copper chip-holder. Scale bar: 2 mm. B) Tilted scanning electron microscopy (SEM) image visualizing various microfabrication issues. Figure adapted from the Master thesis Marc Sulliger, C-CINA, Biozentrum University Basel.

Summary and outlook

The sensor system and data analysis software can now characterize amyloid proteins' fibrillation in a functionalization and label-free manner. Furthermore, the existing instruments provide a base for a new nanomechanical imaging platform.

References

- [1] P. Oliva, B. A. Bircher, C.-A. Schoenenberger, T. Braun, Array based real-time measurement of fluid viscosities and mass-densities to monitor biological filament formation, *Lab. Chip*, **19**, 1305 (2019)
- [2] B. A. Bircher, R. Krenger, T. Braun, *Automated high-throughput viscosity and density sensor using nanomechanical resonators*, *Sens. Actuators, B*, **223**, 784 (2016)
- [3] M. Heinisch, T. Voglhuber-Brunnmaier, E. K. Reichel, I. Dufour, B. Jakoby, *Reduced order models for resonant viscosity and mass density sensors*, *Sensors and Actuators A: Physical*, **220**, 76 (2014)

Filming biological factories

Project P1503: Watching giant multienzymes at work using high-speed AFM

Project Leader: T. Maier and R. H. Y. Lim

Collaborators: S. Singh (SNI PhD Student), Y. Sakiyama, and F. Benning

Multienzymes are biological assembly lines

The metabolism of all cellular life requires protein catalysts, the enzymes, to catalyze chemical reactions for efficient progression in a crowded aqueous environment. All enzymes recognize one or more specific substrates in a single catalytic center and catalyze product formation by stabilizing the transition state to reduce the required activation energy. So-called multienzymes integrate two or more independent enzymatic units or domains, each responsible for catalyzing one reaction step along a metabolic pathway. Multienzymes have evolved in pro- and eukaryotes for different pathways. Their key advantages include the increased local concentration of intermediates, the prevention of side reactions by rapid turnover and the coordinated regulation of reaction steps. Consistently they are often used for pathways with reactive intermediates, and highly complex or insoluble products. A critical requirement of multienzyme action is to enable efficient transfer of intermediates between spatially separated active sites. In some examples, this is achieved by simple diffusion, while advanced options including the passage through internal tunnels between active sites and the covalent tethering of intermediates to mobile carrier protein domains have evolved for the most complex multienzymes. Many relevant multienzymes show a very dynamic behavior with large-scale domain motions [1], but the link between dynamics and overall catalytic function and substrate transfer is poorly understood.

To better understand the functional architecture of multienzymes and to reveal multienzyme blueprints for synthetic biology, we are (i) developing methods to analyze large-scale domain motions of multienzymes and (ii) aim to employ these methods to study selected multienzymes of human metabolism and microbial secondary metabolite formation. Our approach is to develop two complimentary methods for studying multienzyme dynamics in solution complementing static structure determination by X-ray crystallography and cryo electron microscopy single particle analysis. The first method is High Speed Atomic Force Microscopy (HS-AFM), which allows direct albeit low spatio-temporal resolution visualization of protein dynamics. The second approach builds on efficient multi-site fluorescence labeling for single molecule Förster resonance energy transfer (smFRET), which provides highest available spatio-temporal resolution for dynamic studies.

The model systems we are studying are human fatty acid synthase (FAS), one of the most complex multienzymes [2], and related microbial polyketide synthases (PKS). FAS is responsible for all steps of the synthesis of palmitate by iterative elongation of carbohydrate-derived precursors. It employs six types of enzymatic domains, which together catalyze over 40 biochemical reaction steps, and a mobile integral acyl car-

rier protein (ACP) domain, which shuttles covalently-bound intermediates to the enzymatic sites. FAS upregulation is linked to cancer [3] and several metabolic disorders, making FAS an interesting target for therapeutic intervention. Polyketide synthases (PKS) use the same biosynthetic logic as FAS but produce considerably more complex natural products of outstanding biological activity, including antibiotics, immuno-suppressants and statins. In addition to an iterative mode of precursor elongation as in FAS, PKS can form large assembly lines of multiple modules, each carrying out only one round of precursor elongation and modification. The intermediates are vectorially shuttled from module to module in these nanomachines. Variations in domain composition of modules result in altered substrate selectivity and distinct extents of precursor modification by different PKS enzymes resulting in a massive diversity of polyketide products in nature. Their unique properties render PKS one of the most relevant systems for customized synthesis of drug candidates using biocombinatorial approaches. Poor understanding of substrate transfer in PKS is a major bottleneck in exploiting this potential. We are addressing this problem in our lab already by high-resolution analysis of trapped transient states of substrate transfer in PKS [4].

Earlier, we have focused on establishing HS-AFM for multienzymes, using FAS to demonstrate the identification of conformational states along a movie timeline for individual FAS molecules [5]. In 2020, this projects main effort was on completing a toolkit for non-natural amino acid labeling by genetic code expansion to enable multi-site labeling fluorescent labeling of multienzymes.

Genetic code expansion for fluorescent labelling

Fluorescent labeling combined with smFRET analysis provides high spatial ($\pm 3 \text{ \AA}$) and temporal resolutions ($\pm 1 \text{ ms}$) in following distances between individual label pairs. It provides “ruler-type” data highly complementary to the overall surface representation at lower spatial and temporal resolution obtained from HS-AFM, and fully captures the time- and resolution-scales of multienzyme conformational dynamics.

smFRET analysis of multienzymes requires specific dual-site fluorophore labeling. Chemical modification based on sulfhydryl or primary-amine-reactive dyes is the most common and efficient labeling technique for small proteins with a limited number of reactive sites without functional relevance. However, multienzymes are giant polypeptides with hundreds of functional groups and they critically require cysteine and lysine residues for their enzymatic functions. As a consequence an alternative strategy is required to efficiently tackle multienzyme dual-site fluorescent labeling.

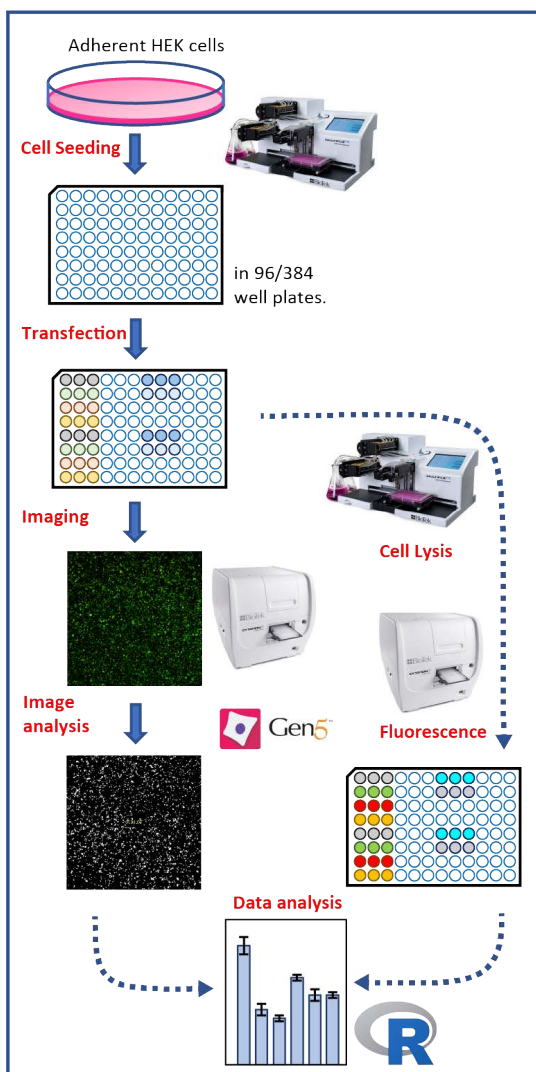


Fig. 1 Pipeline for screening genetic code expansion systems for non-natural amino-acid labeling in adherent human cells.

Genetic code expansion (GCE) is a method to biosynthetically introduce either non-natural amino acids, for example fluorescent amino acids or biorthogonal chemically-reactive groups, which can later be used as unique labeling sites via biorthogonal reactions, at specific positions in proteins. GCE involves supplementing a protein expression host with a non-native protein-production machinery composed of a tRNA and cognate tRNA synthase that introduces unnatural amino acids in polypeptides in response to specific genetic codons, often those naturally used as stop codons. We focus on mammalian protein expression systems because those are the most suitable for (i) introducing the necessary post translational modifications of multienzymes and (ii) producing the large polypeptides of multienzymes.

For human protein expression systems, several GCE systems have already been developed, but they have been shown to work mostly for small and relatively simple proteins, while extensive screening is often required even for obtaining low yields in single-site labeling of more complex proteins using a single GCE system. Critical screening parameters include the choice of GCE systems as well as the targeted positions in the protein sequence.

We have now developed an efficient vector toolkit and pipeline (Fig. 1) for GCE-based labeling of proteins in human cell lines by transient transfection.

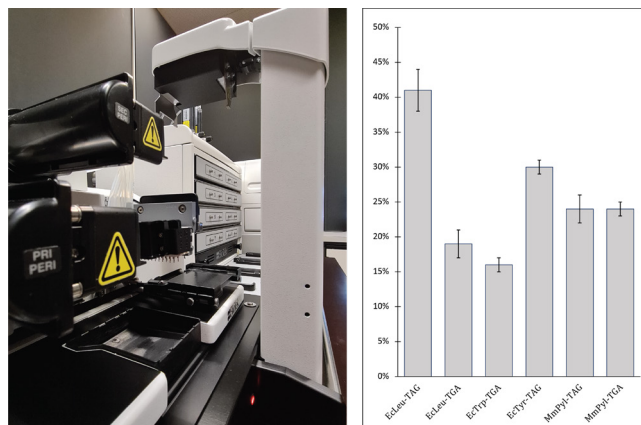


Fig. 2 High-throughput screening of genetic code expansion for non-natural amino acid labeling. Right: Robotic setup for liquid handling, incubation, plate reading and fluorescent imaging. Left: Overall efficiency of stop-codon suppression for different GCE systems tested in the robotic setup, the choice of tRNA/tRNA synthetase and stop codon is provided as x axis label.

It consists of set of gene vectors for transiently transfecting different GCE systems and fluorescent reporters into HEK293 cells. A tandem RFP (Red Fluorescent Protein)-GFP (Green Fluorescent Protein)-based fluorescent reporter allows rapid quantitative comparison of the inherent yields of different GCE systems. We have established protocols for mammalian cell expression in suspension for large scale and in adherent form for high-throughput screening. A fully automated robotic setup for liquid handling, incubation, fluorescence imaging and fluorescent reading has been established and enables efficient identification of productive GCE systems and conditions (Fig. 2).

We are now moving towards applying the established technology to FAS and PKS systems to demonstrate the opportunities opened up by this toolkit and to obtain unique insights into multienzyme dynamics.

References

- [1] A. Hagmann, M. Hunkeler, E. Stutfeld, T. Maier, *Hybrid Structure of a Dynamic Single-Chain Carboxylase from Deinococcus radiodurans*. *Structure*, **24(8)**, 1227-1236 (2016)
- [2] T. Maier, M. Leibundgut, N. Ban, *The crystal structure of a mammalian fatty acid synthase*, *Science*, **321(5894)**, 1315-1322 (2008)
- [3] J. V. Swinnen, K. Brusselmans, G. Verhoeven, *Increased lipogenesis in cancer cells: new players, novel targets*. *Curr Opin Clin Nutr Metab Care*, **9(4)**, 358-365 (2006)
- [4] D. A. Herbst, C. R. Huitt-Roehl, R. P. Jakob, J. M. Kravetz, P. A. Storm, J. R. Alley et al. *The structural organization of substrate loading in iterative polyketide synthases*, *Nat Chem Biol* **14(5)**, 474-479 (2018)
- [5] F. M. C. Benning, Y. Sakiyama, A. Mazur, H. S. T. Bukhari, R. Y. H. Lim, T. Maier, *High-Speed Atomic Force Microscopy Visualization of the Dynamics of the Multienzyme Fatty Acid Synthase*, *ACS Nano*, **11(11)**, 10852-10859 (2017)

Demonstration of voltage-controlled three-electron-beam interference with Boersch phase shifter

Project P1505: A programmable e-beam shaper for diffractive imaging of biological structures at Å resolution
Project Leader: S. Tsujino and J. P. Abrahams
Collaborator: P. Thakkar (SNI PhD Student)

Introduction

Electron beam manipulation is a fast-growing research field. Reports have been made in recent years of devices to selectively manipulate the phase of high-energy electron beam [1–4]. In this work, we report fabrication of a three-layer Boersch phase shifter device which is fabricated with state-of-the-art electron beam lithography and etching methods. Further, we also demonstrate the functioning of the device in a standard 200 keV transmission electron microscope in far-field diffraction regime. The relative phase shift of the transmitted electron beam has been observed as interference of three-beam in the presence of voltage bias of less than 2 V to individual elements.

Two-beam Interference

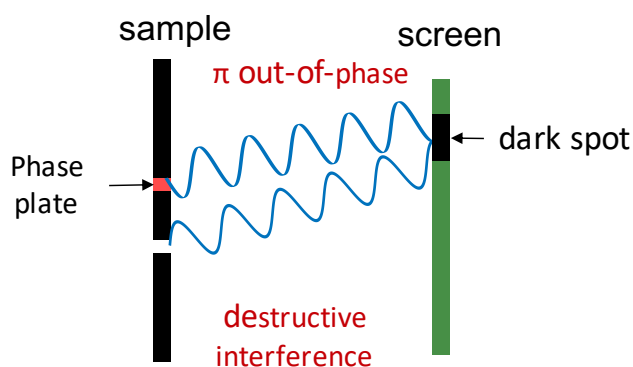


Fig. 1 Graphical explanation of two-beam interference. The interference pattern can be manipulated selectively by placing a “phase plate” in front of one of the apertures.

Let’s assume a simple setup for two-beam interference with two apertures. The sample is placed in front of a light source as shown in figure 1 (at left side of the sample; not shown in the figure). The light passing through these two apertures will diffract and an interference pattern is seen on the screen placed at a distance quite larger than the wavelength of the light source. The interference pattern will consist either peaks or troughs depending on the optical path difference between both the beams. If both the beams are in-phase, they will interfere constructively and form a bright spot on the screen, whereas if they are out-of-phase, we’ll see destructive interference. Now, if we put a phase plate in front of one of the apertures which can alter the phase of the beam traveling through it, we can essentially manipulate the interference pattern. With our device, we plan to achieve this with slightly increase complexity where three individual apertures act as individual phase shifting element. This allows for a more sophisticated manipulation

of three-beam electron interference pattern which has the potential to be scaled for an array of elements using similar lithography methods.

Fabrication of three-layer Boersch phase shifting elements

We fabricated a device with three individually controllable phase shifting elements using e-beam lithography and reactive ion etching methods. Silicon nitride membrane (~200 nm) is used as substrate which is suspended on a silicon frame (~250 μm). The bottom surface of the substrate is evaporated with chromium (~50 nm) layer. Three apertures are then patterned using an e-beam resist and etched through the silicon nitride and chromium layer to facilitate uninterrupted beam transmission through the apertures. The apertures are $0.90 \pm 0.05 \mu\text{m}$ big and separated by $1.8 \pm 0.05 \mu\text{m}$ from center-to-center. Gold ring-shaped electrodes are then fabricated around the etched apertures. A transmission electron microscope image of the fabricated three-layer Boersch device is shown in figure 2. For more detailed fabrication process of the device, please refer to the article [5].

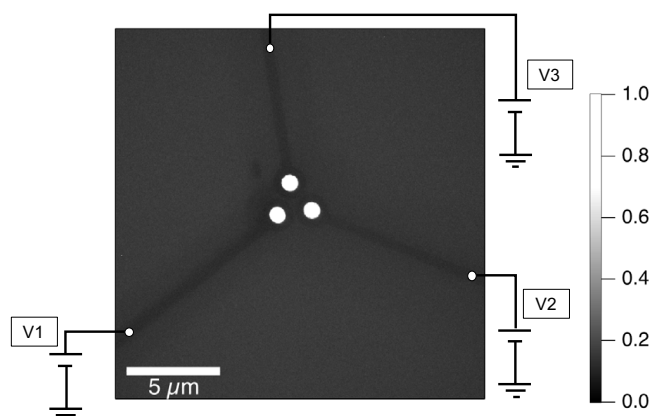


Fig. 2 A low-magnification transmission electron microscope image of the three-layer Boersch phase shifter device. The image shows uninterrupted 100% electron transmission through the etched apertures seen in white. The ring electrodes and the contact strips are seen in dark gray. A graphical representation of three-beam interference experiment is also shown where voltages V1, V2 and V3 are applied individually to the phase shifter elements.

Voltage-controlled three-beam interference

We performed a far-field diffraction experiment in a 200 keV transmission electron microscope with our device. The setup of the experiment is represented in figure 2 where three voltage sources are connected to three phase shifter elements. The bottom surface of the sample is biased at ~2 V

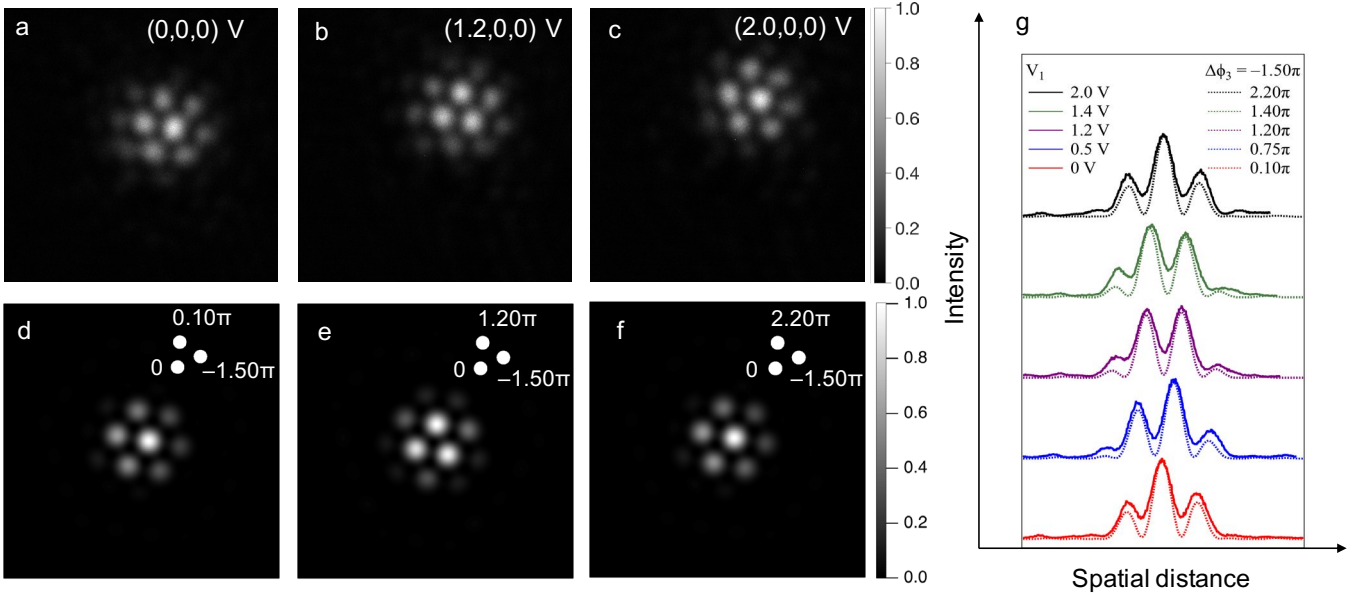


Fig. 3 In-situ phase control of high-energy electrons in a transmission electron microscope. a)-c) show three-beam interference of the device for $V_1 = 0$ V, 1.2 V and 2 V from left to right. The corresponding 2D Fourier simulation is shown in the images below d)-f). We observed an intrinsic phase offset (-1.50π) for a phase shifter element which might be present possibly due to surface charging around the aperture that could be later on compensated by applying few volts to the respective phase shifter element. g) Intensity cross section of diffraction from phase shifter element 1 for $V_1 = 0$ V, 0.5 V, 1.2 V, 1.4 V and 2 V.

as part of the protection system of the holder used to avoid mechanical contact of the holder with the pole pieces of the microscope. We used a holder from DENSolutions (SH30) with four electrical connections inserted at the sample plane of the microscope.

We observed hexagonal interference pattern of three apertures at a virtual screen distance of ~ 1400 m in unbiased condition. The interference pattern with six bright spots (Fig. 3) changed gradually under relative voltage biasing of the phase shifter element. It is capable of achieving relative phase shift of π rad per 1 V applied voltage. We observed a similar linear relationship between applied voltage and the phase shift for all three apertures with small voltage offset for one aperture. This could be ascribed to charging around the aperture and can easily be compensated by applying few volts to that phase shifter element. The 2D Fourier optic simulation predicts a phase offset of -1.50π rad which closely matches with the experimental value of -1.30π rad.

In addition, the fabricated device is also capable of generating vortex beam by applying voltages corresponding to $-2\pi/3$ and $2\pi/3$ to two phase shifter elements, the results of which are not shown here. A detailed investigation of the device performance is presented in the article published in Journal of Applied Physics [5].

Summary and outlook

In conclusion, we demonstrate the functioning of a three-layer device consisting of three individually controllable phase shifter elements. We manipulate relative phase of electrons by applying relative voltage bias to the elements. The three-layer device is capable of manipulating the phase from 0 to 2π with voltage bias of maximum 2 V. Although, few drawbacks of the device that arises from unshielded metal contact strips are not discussed here. These are compensated by small voltage bias to the phase shifter elements. However, the complexity increases for an array of elements with three-layer structure which can be eliminated by fur-

ther introducing a metal layer on top of the ring electrodes making it a five-layer structure. The future generation of device fabrication method will allow for rapid fabrication of an array of elements with increased flexibility in the performance of the device and will aid in the ongoing research in the field of electron beam shaping.

Reference

- [1] J. Verbeeck, A. Béch e, K. M uller-Casparry, G. Guzzinati, M. A. Luong, M. Den Hertog, *Demonstration of a 2x2 programmable phase plate for electrons*, *Ultramicroscopy*, **190**, 58–65 (2018)
- [2] R. Shiloh, Y. Lereah, Y. Lilach, A. Arie, *Sculpturing the electron wave function using nanoscale phase masks*, *Ultramicroscopy*, **144**, 26–31 (2014)
- [3] R. Shiloh, P.-H. Lu, R. Remez, A. H. Tavabi, G. Pozzi, R. E. Dunin-Borkowski, A. Arie, *Nanostructuring of electron beams*, *Phys. Scr.*, **94(3)**, 34004 (2019)
- [4] A. H. Tavabi, H. Larocque, P.-H. Lu, M. Duchamp, V. Grillo, E. Karimi, R. E. Dunin-Borkowski, G. Pozzi, *Generation of electron vortices using nonexact electric fields*, *Phys. Rev. Res.*, **2(1)**, 13185 (2020)
- [5] P. Thakkar, V. A. Guzenko, P.-H. Lu, R. E. Dunin-Borkowski, J. P. Abrahams, S. Tsujino, *Fabrication of low aspect ratio three-element Boersch phase shifters for voltage-controlled three electron beam interference*, *J. Appl. Phys.*, **128(13)**, 134502, (2020)

Optical effects in water splitting electrodes: modelling and experiments

Project P1601: Optical plasmonic nanostructures for enhanced photochemistry

Project Leader: E. C. Constable and S. Fricke

Collaborators: L. Driencourt (SNI PhD Student), B. Gallinet, and C. E. Housecroft

Introduction

Hydrogen is a promising energy carrier in the production of sustainable energy. However, methane reforming processes that emit CO₂ are currently used for industrial scale production. Water electrolysis is an alternative that would enable sustainable hydrogen production, but requires a renewable, non-CO₂-emitting source of electricity (e.g. photovoltaic, wind, hydroelectric). In photoelectrochemical (PEC) water splitting, electricity is directly produced from sunlight inside the electrolyzing electrode, which can be made of a metal oxide semiconductor having a high resistance against corrosion and a low cost. Despite intensive efforts, efficient performance is currently limited and enhancement strategies are critically required. The external quantum efficiency (EQE) of a PEC water splitting system can be expressed as:

$$EQE = \eta_{abs} \cdot \eta_{sep} \cdot \eta_{trans}$$

Where η_{abs} is the light absorption efficiency, η_{sep} is the efficiency of electron/hole pairs separation and transport (in a photoanode, holes are transferred to the aqueous electrolyte and electrons to the back-contact), and η_{trans} is the charge transfer efficiency.

Modelling optical enhancement

We demonstrated a method to study optical enhancement strategies in photoelectrodes, such as plasmonic effects, light scattering, thin-film effects and nanostructuring (Fig. 1a). The model combines near-field electromagnetic simulations with a charge transport model that describes the minority carriers (electrons in a p-type semiconductor, holes in an n-type semiconductor). The model was validated on published experimental data reporting optical enhancement strategies. In host-guest geometries (Fig. 1b), the metal oxide semiconductor is deposited on a nanostructured scaffold. Additional light absorption can take place because of the increased surface area, whereas η_{sep} is similar to a flat configuration. The simulated EQE and photocurrent (Fig. 1c) were in quantitative agreement with the measured data from Qiu et al. [1], showing that the optical enhancement due to the nanostructured morphology can be precisely modelled.

Optical enhancement with silver nanoparticles

Photoanodes with molybdenum-doped bismuth vanadate (Mo:BiVO₄) as a metal oxide semiconductor were fabricated with a sol-gel method. The fabrication process involves spin-coating of an acetic acid/acetylacetone solution containing Bi, V and Mo salts, followed by annealing. A 40 nm Mo:BiVO₄ layer was fabricated with such a process.

Silver nanoparticles of size 50 nm protected with a 20 nm SiO₂ shell (Ag@SiO₂) were subsequently deposited on the surface by inkjet printing. A homogeneous coverage with ~20% filling factor was achieved (Fig 2a.). The optical enhancement

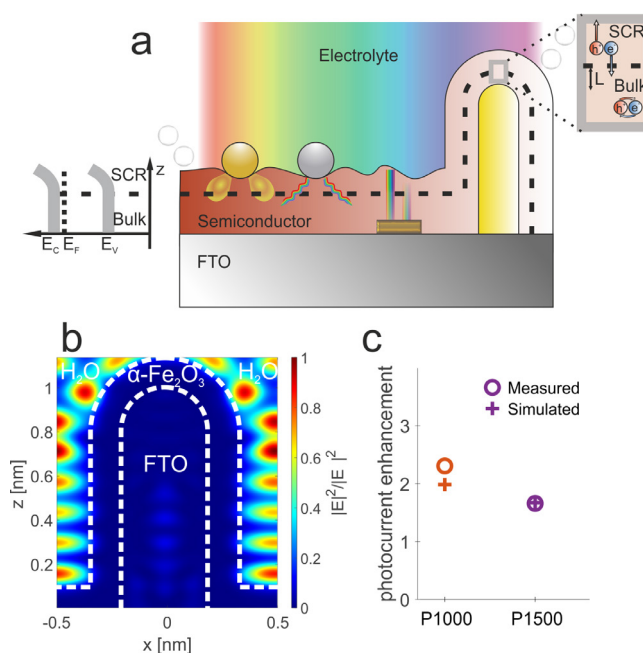


Fig. 1 a) Sketch of an n-type semiconductor electrode illuminated from the electrolyte side, and different optical effects that can improve the water splitting efficiency. b) Simulated electric field intensity in a hematite layer deposited on a nanostructured FTO scaffold. c) Simulated photocurrent enhancement with respect to the planar structure, compared with measured data from Ref. 1.

provided by the nanoparticles was then studied experimentally and theoretically in back illumination configuration (light incident from the substrate side). For that, the photoelectrochemical measurements were performed by adding a sacrificial hole scavenger (0.5 M H₂O₂) to the aqueous electrolyte, such that 100% charge transfer efficiency can be assumed and the effect of the nanoparticles can be only optical. Simulations with periodic boundary conditions were performed by using a realistic value for the Mo:BiVO₄ layer thickness (Fig. 2b). An increased EQE for the sample with Ag@SiO₂ was observed experimentally and theoretically, with a good spectral and quantitative agreement (Fig. 2c). The broader experimental enhancement can be explained by the agglomerates of nanoparticles that are visible in figure 2b and by the non-perfectly monodisperse size distribution. Moreover, the simulated and measured photocurrent enhancement are in excellent agreement (Fig. 2d).

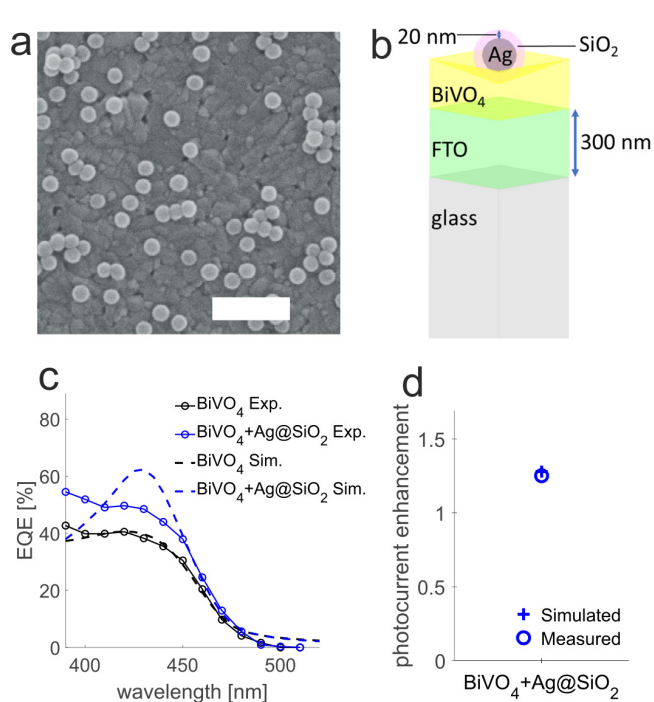


Fig. 2 a) SEM image of Ag@SiO₂ nanoparticles printed on Mo:BiVO₄ (scalebar: 500 nm). b) Scheme of the simulated unit cell. c) Measured and simulated EQE in back-illumination configuration. d) Measured and simulated photocurrent enhancement ratio between the sample with Ag@SiO₂ nanoparticles with respect to the bare sample.

To study the mechanism behind this optical enhancement and to be able to distinguish resonant scattering from the plasmonic properties of silver with respect to non-resonant scattering, a simulation was performed with gold instead of silver. The SiO₂ shell thickness and the filling factor were maintained the same as for silver. The EQE spectra (Fig. 3a) and the electric field intensity maps (Fig. 3b-c) show that an optical enhancement is observed only with silver. This indicates that the observed enhancement of photoelectrochemical performances is driven by the plasmon resonance of silver.

Conclusion

We have presented a method for studying optical enhancement in water splitting photoelectrodes. It was shown that a quantitative agreement within experimental errors was obtained for both a periodically nanostructured sample and sample containing randomly distributed plasmonic nanoparticles. Moreover, the reason behind the observed enhancement with Ag@SiO₂ could be identified non-ambiguously. The method can be used further to design photoelectrodes with optimal optical performances.

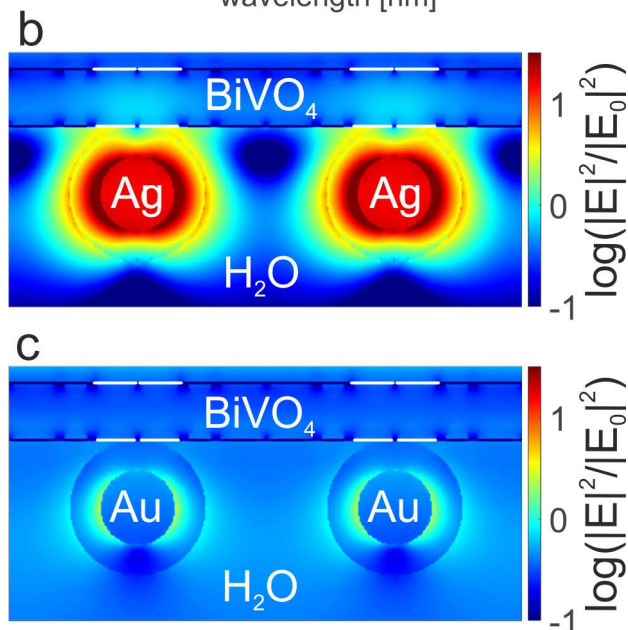
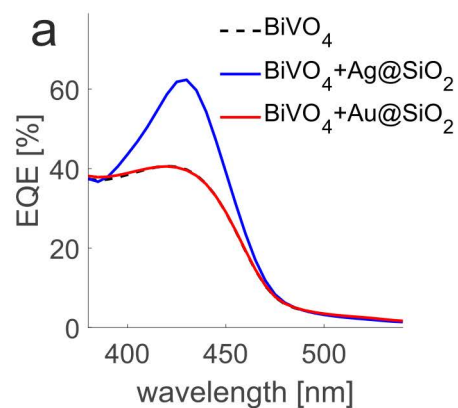


Fig. 3 a) EQE for a structure with either gold or silver nanoparticles. b)-c) Electric field intensity maps at 427nm with b) Ag@SiO₂ nanoparticles and c) Au@SiO₂ nanoparticles. The light is normally incident from the top and polarized in the plane of the cross section.

References

- [1] Y. Qiu, S-F. Leung, Q. Zhang, B. Hua, Q. Lin, Z. Wei, K-H. Tsui, Y. Zhang, S. Yang, Z. Fan, *Efficient photoelectrochemical water splitting with ultrathin films of hematite on three-dimensional nanophotonic structures*. *Nano Lett.* **14**, 2123–2129 (2014)

The physico-chemistry of metal-organic ionic complexes upon sublimation and deposition

Project P1602: Self-assembly and magnetic order of 2D spin lattices on surfaces

Project Leader: T. A. Jung and J. Dreiser

Collaborators: M. Heydari (SNI PhD Student), R. Sk, D. Luthi, V. Jacobsen, A. Ahsan, A. Doll, N. Daffé, O. Popova, and G. Morgan

Introduction

In view of the manifold opportunities of novel quantum technology applications and spintronic devices, the precise assembly of spin bearing structures into pre-defined architectures still provides a grand challenge. By using H-bond engineering between fluorine and hydrogen substituents on phthalocyanines we have assembled 2D spin-checkerboards and investigated their unique properties [1]. Also, we have investigated the stronger interaction and exchange coupling mediated by coordination bonds [2] to create specific on-surface molecular architectures and explore the exchange interaction therein. In our present effort, we focus on supramolecular assembly techniques for this purpose, as they allow to specifically direct the assembly process by the chemical structure of the components. We use organic salts comprised of a complex, non-planar spin bearing cation with trigonal prismatic coordination geometry (in this case, Mn/OEt ligand) and a tetrahedral-shaped anion in the form of tetraphenylborate (Fig. 1) [3]. We have observed that physical vapour deposition is possible for these compounds which provides a very clean and reliable approach to fabricate ultra-thin films and on-surface supramolecular structures. Due to the Coulomb interaction between the negatively charged anions and the positively charged cations, one or more ion pairs are transferred to the substrate at a time.

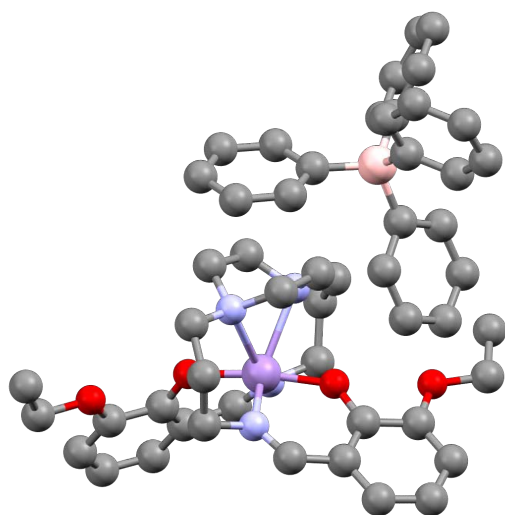


Fig. 1 Three dimensional ball-and-stick crystal structure of the metal-organic ionic salt $[MnL7]BPh_4$. The cation is a non-planar spin bearing coordination system with rare trigonal prismatic geometry and tetraphenylborate is the anion. Color code: red: O; blue: N; grey: C; rose: B; violet: Mn

Results

$[MnL7]BPh_4$ (Fig. 1) has been sublimed onto Au(111) and Cu(111) metallic surfaces at room temperature under ultrahigh vacuum conditions ($p = 2 \times 10^{-10}$ mbar). Low temperature scanning tunneling microscopy (LT-STM) at $T = 4$ K has been used to investigate the initial and progressing stages of surface deposition of this ionic compound. In the first rounds of experiments (not shown) we noted that the number density distribution of different observed features on both substrates depends critically on the deposition rate (temperature) of the crucible. For this purpose, experiments have been performed at predefined ‘high’ ($\sim 7 \times 10^{-4}$ Å/sec) and ‘low’ ($\sim 3 \times 10^{-5}$ Å/sec) deposition rates to systematically investigate this phenomenon. In the ‘high’ rate deposition and STM study reported in figure 2 (a-e) anion and cation derived nucleates can be observed. The observed 1:1 cation:anion ratio suggests that both ions are charge neutralized on contact with the substrate and segregate into different condensates. The cation-derived object exhibits structural features associated with the metal-containing complex and is recognized by a bright lobe and two phenyl-like substituents of lower apparent height in the STM images. (Fig. 2d). Note that the observed separation and condensation of the anion and cation derived components provide proof for the neutralization in this on-surface dissociation process.

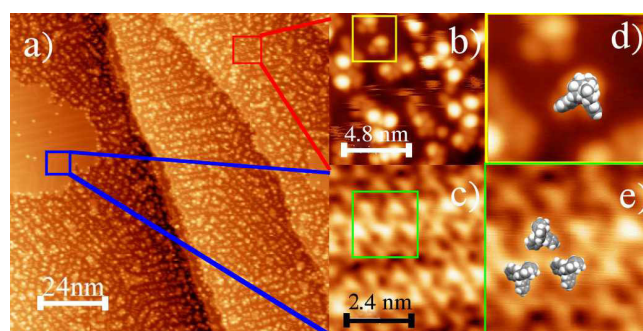


Fig. 2 Dissociation and segregated assembly of anion and cation derived modules: STM micrographs of $[MnL7]BPh_4$ deposited onto Au(111) at a ‘high’ rate of $\sim 7 \times 10^{-4}$ Å/sec a) Two characteristically different patterns can be identified, a close-packed island and a larger area covered by smaller aggregates following the linear domains of the Au(111)22x3 surface reconstruction. b), d) Monomer, dimer, and oligomers units of cation derived modules can be identified based on the overlay of the molecular structures in a zoom sequence. c), e) identification of the anionic derived component in the close packed assembly.

A first sample with very low coverage (0.05 Hz \sim few percent of surface area) has been prepared at ‘low’ deposition rate to investigate the structure of the isolated fragments

and building blocks of different possible assemblies on the surface by STM (Fig. 3a). Isolated, stably adsorbed molecules sitting at the 'elbow' sites of the herringbone reconstruction are identified as (partially) decomposed anion derived modules. To identify the mobile modules we have subsequently increased the coverage in subsequent deposition steps (Fig. 3 a-c).

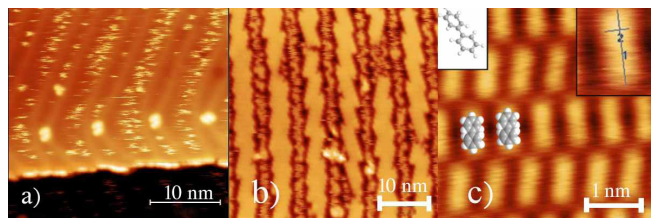


Fig. 3 Predominant observation of anion derived objects after deposition of $[MnL7]BPh_4$ at 'low' rate ($\sim 3 \times 10^{-5} \text{ \AA/sec}$) a) At lower coverage on Au(111) a considerable fraction of mobile adsorption precursors are recognized. $V_t = 1.5 \text{ V}$, $I_t = 20 \text{ pA}$. b) after increasing the molecular coverage in extended deposition cycles at 'low' rate linear close packed domains with $\sim 4 \text{ nm}$ width and separated by mobility zones become visible. c) Remarkably, the structure identified here is a short linear unit, -- characteristically different from both the tetrahedral tetraphenylborate and the cation which are observed at high rate (Fig. 2). c) The dumbbell shape leads to a tentative assignment of the new module to a biphenyl ($V_t = 200 \text{ mV}$, $I_t = 60 \text{ pA}$).

In figure 3b) and c) at increased coverage induced by 'low rate' deposition, we observe compact layers in a stripe morphology exhibiting no residual mobility at 5K. The imaged molecular module can be clearly distinguished from the anion and cation derived features shown in figure 2 and is tentatively associated with a biphenyl. This identification is further supported by the fact that after annealing of the sample at 100°C for 1 hour, these bars are completely desorbed from the surface while only a few other modules remain bound to the surface. The neutral bi-phenyl may form by dissociation of the anion inside the crucible at lower temperatures, before sublimation of the ion-pairs starts. Interestingly, the rate of decomposition is higher than the sublimation at 'low' rates/crucible temperatures and the opposite is true at 'high' rates/ crucible temperatures. This indicates that the activation energy is lower and the kinetics is more complex for the decomposition process than for the sublimation of ion pairs which would be expected to follow a simple Arrhenius relation.

To identify the different chemical species deposited at 'high' and at 'low' rate we have performed surface chemical analysis (Fig. 4). This data confirms that after low rate deposition predominantly the oxygen-free anion derived modules are identified. This indicates that at temperatures lower than the sublimation temperature for the intact organic salt, a chemical conversion occurs in the crucible which releases a small and charge neutral decomposition product.

Note that after 'high' rate deposition and segregation of the ions on the Cu(111) substrate (data not shown) we also observed tetraphenylborate deposited in a partially fractionated mode, tentatively assigned as a $(BPh_2)^+$ fragment. The assignment was made on the basis that some phenyl-like features are close to a bright point that could be associated to a boron atom, hence the suggestion of BPh_2^+ .

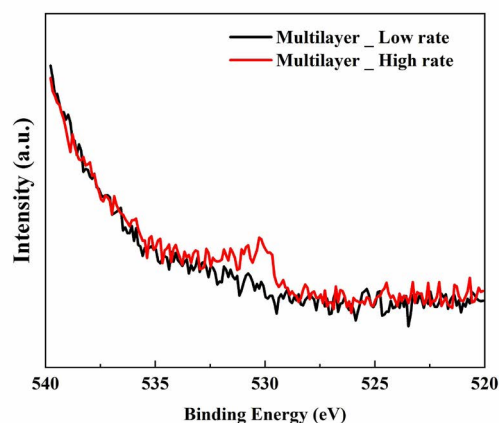


Fig. 4 XPS spectra recorded at the O 1s core levels on a multilayer of what leaves the crucible with $[MnL7]BPh_4$ after deposition onto Au(111) held at $T=300 \text{ K}$. The O 1s peak for the sample prepared at high rate (red curve) indicates the presence of cation derived species in contrast to the low rate sample (black curve).

In conclusion, we report an unprecedented on-surface dissociation process. This actually comprises an unexpectedly complex case, as the possibility to create single Mn spin containing ad-layers by sublimation of the molecular salt is combined with the dissociation of the tetraphenylborate anion at lower than sublimation temperatures. On the other hand the ion pairs dissociate and re-aggregate after charge neutralization on the metal substrates and form a wealth of different self-organized features to be explored for their spin-interaction among other physico chemical characteristics. This latter process needs further investigation as it is expected to be critically dependent on the surface chemistry of the substrate, the crucible temperature and the sample temperature as the deposition occurs.

References

- [1] J. Girovsky et al. *Long-range ferrimagnetic order in a two-dimensional supramolecular Kondo lattice*, Nature Comm. **8**, 15388 (2017)
- [2] C. Wackerlin, D. Siewert, T. A. Jung, N. Ballav, *On-surface coordination chemistry: direct imaging of the conformational freedom of an axial ligand at room temperature*, Phys. Chem. Chem. Phys. **15**, 16510–16514 (2013)
- [3] E. Cremades, J. Echeverra, S. Alvarez, *The Trigonal Prism in Coordination Chemistry*, Chem. Eur. J. **16**, 10380–10396 (2010)

Mesoscale dynamics of the yeast nuclear pore complex transport channel

Project P1603: A mechano-optical microscope for studying force transduction in living cells

Project Leader: R. H. Y. Lim and E. Meyer

Collaborator: T. Kozai (SNI PhD Student)

Introduction

The nuclear pore complex (NPC) is the main gateway for biomolecular exchange between the cytoplasm and nucleus in eukaryotic cells. The NPC transport channel possesses numerous intrinsically disordered proteins termed phenylalanine-glycine repeat nucleoporins or FG Nups. The FG Nups are tethered to the inner wall of the transport channel and collectively function as a permeability barrier that mediates the selective transport of biomolecules into and out of the nucleus. Despite being central to NPC function, visualizing the intrinsically disordered FG Nups in *Saccharomyces cerevisiae* (Baker's yeast) NPCs remains a formidable problem. This lags significantly behind our understanding of yeast NPC scaffold structure that is being revealed in ever increasing detail [1]. Given that NCT proceeds rapidly through NPCs in milliseconds further complicates matters as FG Nup behavior should ideally be studied at such transport-relevant timescales. Recently, we resolved the dynamic behavior of FG Nups inside non-transporting NPCs at ~ 200 ms timescales by high-speed atomic force microscopy (HS-AFM) [2]. Still, the permeability barrier remains difficult to rationalize under transporting conditions [3].

Characterization of isolated yeast NPCs

NPCs isolated from the nucleus of are used in this study. The overall structure of the isolated yeast NPC has been determined at sub-nanometer precision [1]. However, the dynamic behavior of FG Nups inside the isolated yeast NPC has yet to be resolved. In collaboration with Prof. Michael Rout (Rockefeller University), we have now visualized FG Nup dynamics inside isolated yeast NPCs for the first time. Each NPC is composed of sub-complexes that assemble into a ring-like structure composed of eight spokes as shown in the accompanying cross-sectional profiles. Representative HS-AFM images reveal isolated NPCs without and with a feature known as the "central plug" that occludes the pore [4] (Fig. 1a-b). Subsequent height analyses (Fig. 1c) do not show any significant difference between NPCs with and without the central plug (Fig. 1d). Moreover, the pore depths and thicknesses of the NPCs with and without central plugs were characterized (Fig. 1e and f).

Visualizing the dynamic behaviors of FG Nups within the NPC transport channel

We next focused on resolving FG Nup behavior within isolated yeast NPCs. In NPCs lacking the central plug, the FG Nups are seen to dynamically and stochastically extend into and retract from the pore interior (Fig. 2a). This behavior is similar to the diffusive motion of FG Nups resolved within NPCs obtained from *Xenopus laevis* oocyte nuclei [2]. In central channels with plugs, fluctuating FG Nups can also be resolved in the space between the central plug and the NPC walls (Fig. 2c). Hence, it appears that FG Nups interact with

the central plug dynamically and intermittently. In addition, the average thicknesses of the central plug, entanglement and single FG Nup filament were characterized (Fig. 2d).

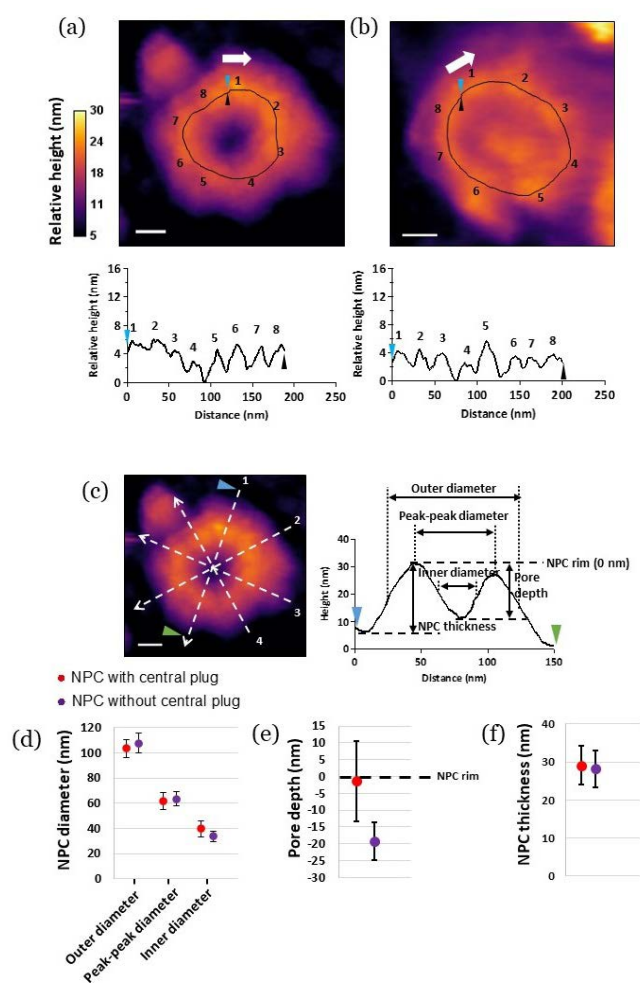


Fig. 1 Isolated yeast NPCs without a) and with b) central plugs. Corresponding cross-sectional profiles show 8 spokes (numbered) that surround the NPC scaffold. The direction in which the cross-sectional profiles are obtained is shown with the arrows. c) NPC diameter is calculated as an average over 4 measurements at different rotations (dashed-lines and numbered). The outer and inner diameters were measured from the full-width at half-maximum (FWHM) of the spokes. NPC thickness and pore depth were measured at different rotations (measured from each of the NPC rims). NPC rim is 0 nm as a basis for the pore depth. Corresponding cross-sectional profile is obtained from the dashed white line (#1) in the AFM image. (d-f) Various measurements of the NPC. Scale bars: 20 nm.

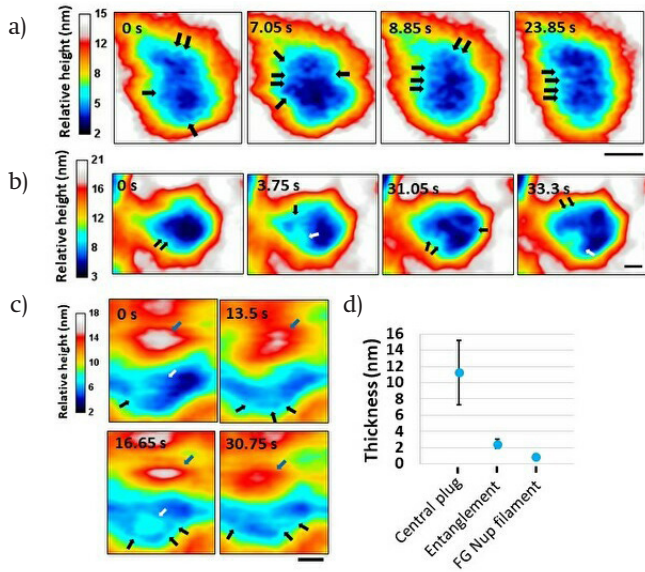


Fig. 2 a) b) Barrier dynamics of FG Nups within NPCs lacking central plugs. c) Dynamic behavior of FG Nups within a central pore featuring a central plug. Black, white and blue arrows indicate single FG Nup filament, entanglement and central plug, respectively. Frame rates, 150 ms/frame. Scale bars: 10 nm. d) Thicknesses of central plug, FG Nup entanglements and a single FG Nup.

Visualizing transport-relevant effects in isolated yeast NPCs

Central plugs might be composed of cargos and nuclear transport receptors such as karyopherins (or Kaps). However, little is known about how the central plug is formed or if it serves any function. Kap95, an import receptor in yeast, recognizes specific cargos either directly or via an adapter Kap60. Kap60 therefore mediates the binding of cargos to the FG Nups via Kap95. Binding of Kap95 to the FG Nups is an energetically favored process. On the other hand, unbinding requires Gsp1-GTP. Here, we treated NPCs with Gsp1-GTP followed by Kap60-95 to test if their binding facilitated the formation of central plugs. Figure 3a shows that the percentage of NPCs with central plugs is reduced after Gsp1-GTP treatment, and increases following Kap60-95 treatment. This indicates that Gsp1-GTP displaced central plugs and Kap60-95 pre-complexes reformed central plugs. Subsequently, we investigated how Gsp1-GTP would affect the central plug (Fig. 3b). After Gsp1-GTP addition, the central plug disappeared, and entanglements and FG Nup filaments appeared.

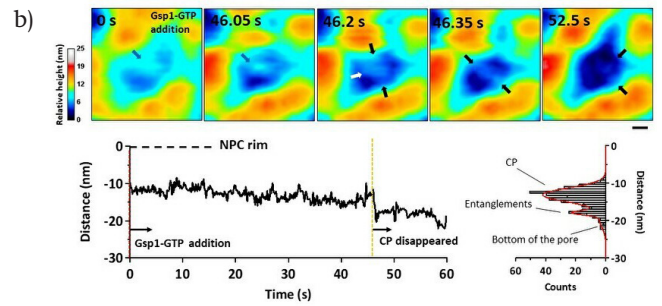


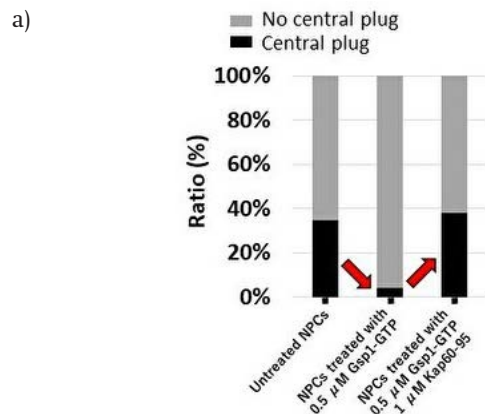
Fig. 3 a) Gsp1-GTP treatment leads to a reduction of central plugs in isolated yeast NPCs. Addition of Kap60-Kap95 increases the incidence of NPCs with central plugs. b) HS-AFM visualizes the dissolution of a central plug following Gsp1-GTP addition. The blue, white and black arrows indicate the central plug, entanglements and FG-Nup filaments, respectively. Kymograph analysis shows the time dependence and vertical distances between maximum height of the spoke and the bottom of the pore, entanglements or the central plug in the pore. Corresponding histogram is shown on the right. Frame rate, 150 ms/frame. Scale bar: 10 nm.

Summary

We have used HS-AFM to investigate FG Nup dynamics within isolated yeast NPCs. This will serve to elucidate how the FG Nups behave under transporting conditions as well as clarifying the role and potential function of the central plug.

References

- [1] S. J. Kim et al., *Integrative structure and functional anatomy of a nuclear pore complex*, Nature **555**, 475–482 (2018)
- [2] Y. Sakiyama, A. Mazur, L. E. Kapinos, R. Y. H. Lim, *Spatiotemporal dynamics of the nuclear pore complex transport barrier resolved by high-speed atomic force microscopy*, Nature Nano. **11**, 719–724 (2016)
- [3] K. Huang, M. Tagliazucchi, S. H. Park, Y. Rabin, I. Szleifer, *Nanocompartmentalization of the nuclear pore lumen*, Biophys. J. **118**, 219–231 (2020)
- [4] D. Stoffler, K. N. Goldie, B. Feja, U. Aebi, *Calcium-mediated structural changes of native nuclear pore complexes monitored by time-lapse atomic force microscopy*, J. Mol. Biol. **287**, 741–752 (1999)



Solid-supported planar membranes: how polymers affect the properties and activity of biomolecules

Project P1604: Selective reconstitution of biomolecules in polymer-lipid membranes

Project Leader: W. Meier and U. Pieleš

Collaborator: S. Di Leone (SNI PhD Student)

Introduction

A controllable insertion of proteins to synthetic membranes is very attractive for many applications including biosensors, bioengineered scaffolds or drug screening. The functional insertion of biomolecules (i.e. proteins) into a synthetic environment is a challenging task, because of often denaturation. Poly(dimethylsiloxane)-block-poly(2-methyl-2-oxazoline) (PDMS-b-PMOXA) amphiphilic block copolymers are excellent candidates for the preparation of functional membranes on solid support, due to their biocompatibility and mechanical resistance [1]. Quartz crystal microbalance with dissipation (QCM-D) was utilized to monitor the real-time kinetics of membrane formation depending on concentration and polymer composition and then to estimate the membrane quality via BSA adsorption. We used atomic force microscopy (AFM) to characterize the morphology and mechanical properties of the polymer and hybrid membranes. Finally, fluorimetry measurements were performed to evaluate the activity of the enzymes after the combination with the artificial membrane. Our findings on planar supported membranes based on polymers and hybrids are crucial for designing and developing a new class of smart active surfaces.

Result and discussion

Supported hybrid membranes

Here we used PDMS-b-PMOXA with addition of phospholipids as matrix to create a platform [2], which served as a support for the insertion of the model protein cytochrome c. The combination of polymers and lipids creates hybrid membranes with enhanced flexibility and facilitates the interaction with pro-

teins. We produced with the established Langmuir-Blodgett (LB) method a membrane composed of PDMS-b-PMOXA and DPPC (1,2-dipalmitoyl-sn-glycero-3-phosphocholine) and then we successfully combined the protein through two different strategies, insertion and conjugation (Fig. 1) [3]. By applying different approaches, it was possible to drive the protein to a specific membrane domain (polymer or lipid).

AFM studies were crucial to observe the domain separation in the morphology of hybrid membranes (Fig. 2). Furthermore, we explored the interaction of cytochrome c with two strategies: insertion and conjugation.

Solvent-assisted polymer membrane formation

A second pathway for the preparation of functional membranes based on PDMS-b-PMOXA copolymers involved the development of a new straightforward methodology, called solvent-assisted method [4]. This method consists of switching the polymer solvent from organic to aqueous buffer, which induces a self-assembly into membrane. By comparing membranes obtained with polymers of different PDMS chain length, it was possible to observe a rough structure composed of protrusions with an island shape, which consists of incomplete-fused vesicles onto the silica support during the solvent-exchange process [5]. The length of the hydrophobic block plays a key role in this regard, affecting the dimension of those islands: higher PDMS block length lead to bigger polymer islands. Differently, the solvent-exchange method was not successful for the membrane preparation, when it was applied to the triblock copolymers, such as PMOXA6PDMS36PMOXA6. The drying process probably influenced the organization of the polymer assembly, with a

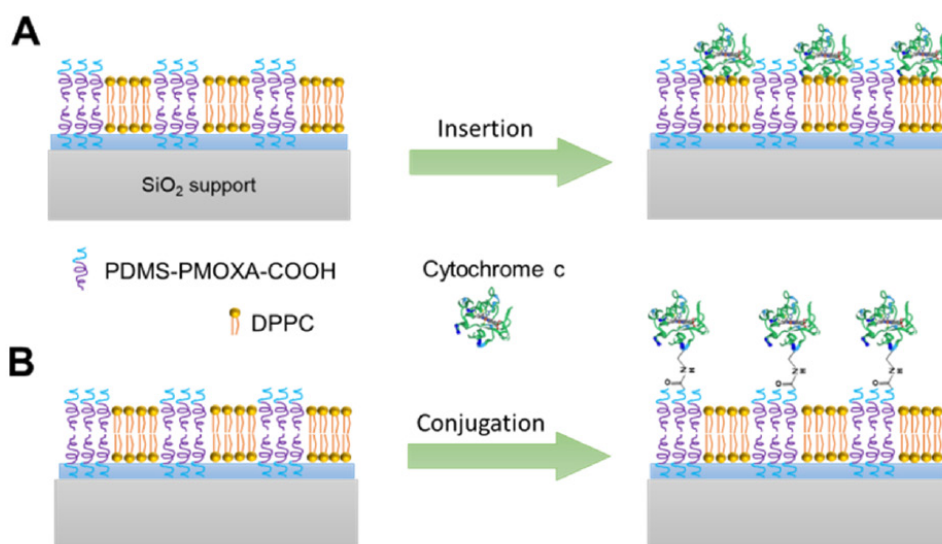


Fig. 1 Schematic representation of protein combination with different membrane domains: insertion (A) and covalent conjugation (B).

consecutive polymer detachment from the support. Furthermore, we achieved the functional insertion of a synthetic Ruthenium metallo-enzyme [6] into the membrane obtained with diblock copolymers, based on the biotin-avidin specific interaction. Specifically, we used a biotin-functionalized copolymer for preparing the biomimetic surface. The polymer self-assembly with solvent-assisted method allowed the ending biotin functional group to be accessible for the binding with avidin, which was monitored and quantified in real-time (Fig. 3). The experiment was performed for all the membranes at different biotin-PDMS35PMOXA12/PDM-S61PMOXA9 composition. Increasing the percentage of biotinylated polymer in the mixture, resulted in a higher quantity of avidin attachment.

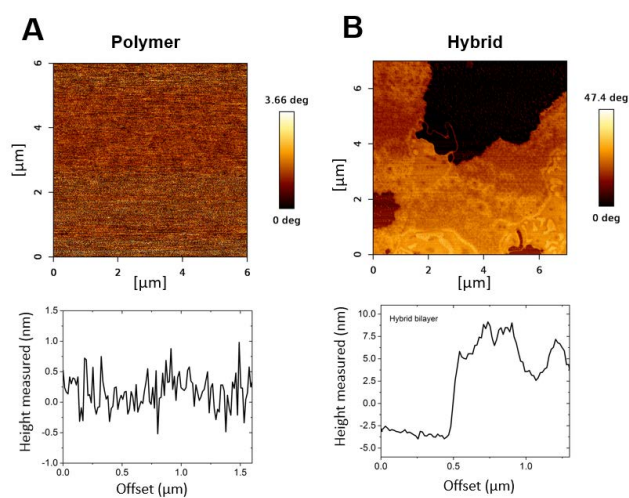


Fig. 2 AFM characterization of solid-supported bilayers. Phase profile (up) and cross section (down) of polymer (A) and hybrid (B) membranes.

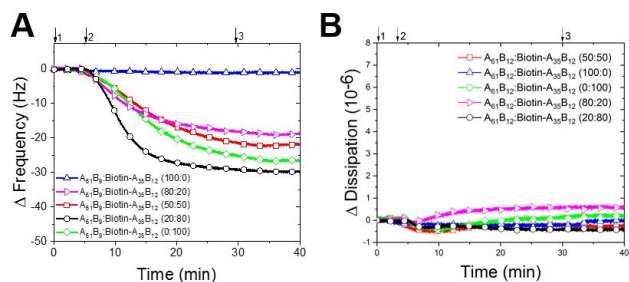


Fig. 3 QCM-D frequency (A) and dissipation (B) plots of avidin attachment onto membrane formed by biotin-A35B12 and A61B9 polymers at different weight ratio.

The fluorimetry was used to compare the activity of the metallo-enzyme (Ruthenium cofactor) when free in solution or bound to the polymer membrane over 72 hours. Here we report the concentration of a substrate converted by the enzyme into a fluorescent species. We demonstrated in this way that, the enzyme was still accessible after the membrane combination and able to perform its catalytic action.

Conclusions

We presented the LB approach as a basis to drive/study the decoration of hybrid membrane composed of polymers and lipids with cytochrome c. In the next step the solid-supported polymer membranes were prepared by developing a novel preparation method. Such solvent-assisted method enable us to prepare polymer membranes with high reproducibility and minor defects. The enzyme-membrane combination was tested for the different type of membranes: polymer and hybrid. Interestingly, the enzyme (cytochrome c) remained accessible upon the attachment/insertion to the membranes and preserved its activity. This approach opens up the possibility of several different enzyme-membrane combination. Thus, the further anchoring of biomolecules, such as DNA strands, represents a promising approach for the development of solid-supported membranes with novel properties.

References

- [1] D. Wu, S. Rigo, S. Di Leone, A. Belluati, E. C. Constable, C. E. Housecroft, C. G. Palivan, *Brushing the surface: cascade reactions between immobilized nanoreactors*, *Nanoscale* **12**, 1551-1562 (2020)
- [2] A. Krywko-Cendrowska, S. Di Leone, M. Bina, S. Yorulmaz-Avsar, C. G. Palivan, W. Meier, *Recent Advances in Hybrid Biomimetic Polymer-Based Films: from Assembly to Applications*, *Polymers* **12**(5), 1003 (2020)
- [3] S. Di Leone, Stefano, S. Yorulmaz Avsar, A. Belluati, R. Wehr, C. G Palivan, W. Meier, *Polymer-Lipid Hybrid Membranes as a Model Platform to Drive Membrane-Cytochrome c Interaction and Peroxidase-like Activity*, *J. Phys. Chem. B* **124**, 22, 4454-4465 (2020)
- [4] S. R. Tabaei, J.-H. Choi, Z. Haw, Z. Goh, P. Vladimirov, N.-J. Cho, *Solvent-Assisted Lipid Bilayer Formation on Silicon Dioxide and Gold*, *Langmuir* **30**, 34, 10363-10373 (2014)
- [5] K. Jaskewicz, M. Makowski, M. Kappl, K. Landfester, Katharina, A. Kroeger, *Mechanical Properties of Poly(dimethylsiloxane)-block-poly(2-methyloxazoline) Polymersomes Probed by Atomic Force Microscopy*, *Langmuir* **28**, 34, 12629-12636 (2012)
- [6] T. Heinisch, F. Schwizer, B. Garabedian, E. Csibra, M. Jeschek, J. Vallapurackal, V. B. Pineiro, P. Marlière, S. Panke, T. R. Ward, *E. coli surface display of streptavidin for directed evolution of an allylic deallylase*, *Chem. Sci.* **9**, 5383-5388 (2018)

Smart peptide nanoparticles for efficient and safe gene therapy

Project P1606: Smart peptide nanoparticles for efficient and safe gene therapy

Project Leader: C. G. Palivan and J. Benenson

Collaborator: S. Tarvirdipour (SNI PhD Student)

Introduction

Nonviral delivery systems are increasingly gaining importance in gene therapy due to their tunable physicochemical characteristics and low immunogenicity [1]. Of particular interest are peptide-based carriers, especially a class of membrane active peptides with intrinsic targeting or membrane translocating properties that support an improvement of the delivery systems [2]. Nevertheless, engineering non-viral carriers that deliver compounds with therapeutic effects, for example therapeutic oligonucleotides, directly into the nucleus, remains a challenge [3]. Accordingly, we aim at merging the advantages of peptide-based carriers with the propensity for nuclear localization by developing a peptide-based non-viral system that promotes the translocation of an antisense oligonucleotide (AON) into the nucleus via a nuclear localization sequence (NLS).

The design of our amphiphilic NLS-peptide involves modifications of the previously published peptide, (HR)3gT [4]. Two lysine-arginine repeating units, which represent a minimal, classical NLS, were added to the hydrophilic domain. Subsequently, the hydrophobic domain was extended to preserve a hydrophilic to hydrophobic weight ratio similar to that of (HR)3gT. The resulting NLS-peptide self-assembles into multi-compartment micelles (MCMs) in the presence of 22 nucleotide single-stranded DNA (22nt ssDNA)(Fig. 1).

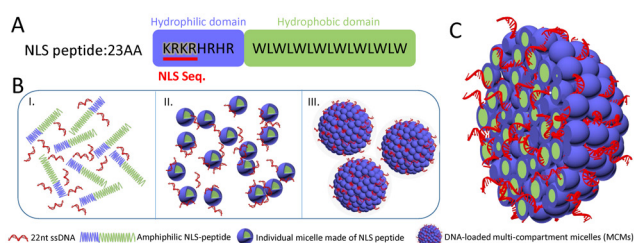


Fig. 1 (A) Amino acid sequence of the amphiphilic NLS-peptide. (B) Sequential self-assembly process of NLS-peptide in the presence of short, single-strand DNA (ssDNA). (C) A sectioned, self-assembled multi-compartment micelle entrapping ssDNA.

Subsequently, 22nt-ssDNA loaded NLS-MCMs were characterized by a combination of physicochemical methods.

Material and methods

NLS-peptide comprising 23 amino acids was synthesized on a rink amide resin, purified, and analyzed by time-of-flight mass spectrometer (MALDI-TOF-MS) in the positive mode. The self-assembly of 22nt-ssDNA loaded NLS-MCMs was achieved via the solvent exchange method [4].

The size of DNA-free and DNA-loaded NLS-MCMs was measured by dynamic light scattering (DLS), complemented by nanoparticle tracking analysis (NTA), and their surface charge measured by Zeta Sizer Nano ZSP. The supramolecular architecture was assessed by transmission electron microscopy (TEM) and cryogenic EM (cryo-EM). To analyze the entrapment of 22nt-ssDNA into NLS-MCMs, fluorescence correlation spectroscopy (FCS) was used. Cytotoxicity analysis was performed using CellTiter 96 Aqueous One Solution Cell Proliferation Assay (MTS). The cellular uptake of nanoparticles by HeLa-GFP-H2B cells was examined by confocal laser scanning microscopy (CLSM).

Results

TEM and cryo-EM analysis of self-assembled 22nt-ssDNA loaded NLS-MCMs revealed that the newly designed peptide is able to form spherical, multi-compartment micellar structures (Fig. 2A, B). The hydrodynamic diameter of 22nt-ssDNA loaded NLS-MCMs was below 100nm as indicated by DLS and NTA (Fig. 2C, D).

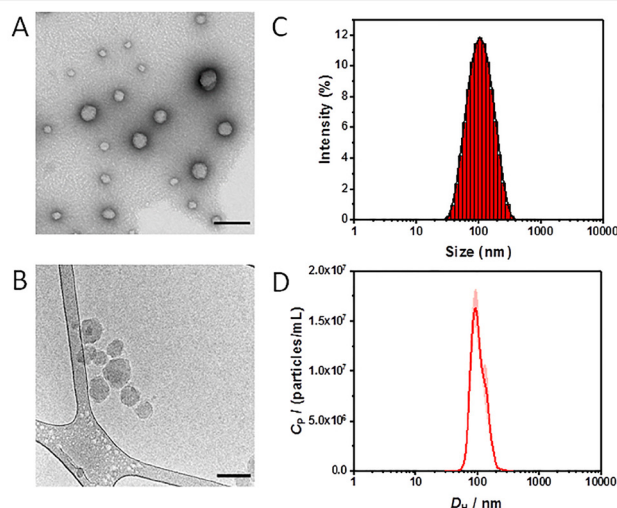


Fig. 2 Size and architecture of 22nt-ssDNA loaded NLS-MCMs. (A) TEM, (B) Cryo-EM, (C) DLS, and (D) NTA. Scale bars, 100 nm.

Moreover, DLS measurements revealed a PDI of 0.18 for 22nt-ssDNA loaded NLS-MCMs which indicates a monodisperse system. The entrapment of DNA in NLS-MCMs was assessed by FCS (Fig. 3). The number of DNA molecules per MCM was calculated by dividing the count per molecule (CPM) of 22nt-ssDNA loaded NLS-MCMs by the corresponding Atto550-DNA in solution, which revealed an entrapment of 9.3 ± 4.4 DNA strands per NLS-MCM.

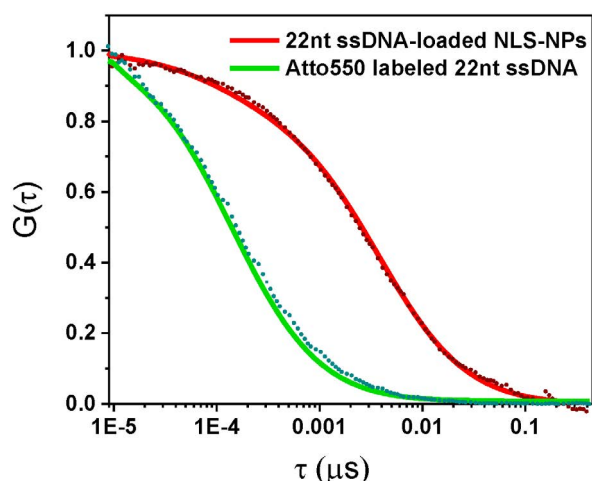


Fig. 3 Normalized FCS autocorrelation curves of self assembled Atto550-labeled 22nt-ssDNA loaded NLS-MCMs (red) and Atto550-labeled 22nt-ssDNA (green).

Zeta potential measurements showed that the surface charge of the NLS-MCMs decreased from 45 ± 7 mV to 20 ± 5 mV when negatively charged DNA was entrapped (Fig. 4). These results corroborate that the DNA payload is bound between the individual micelles of the multi-compartment rather than being merely attached to their surface.

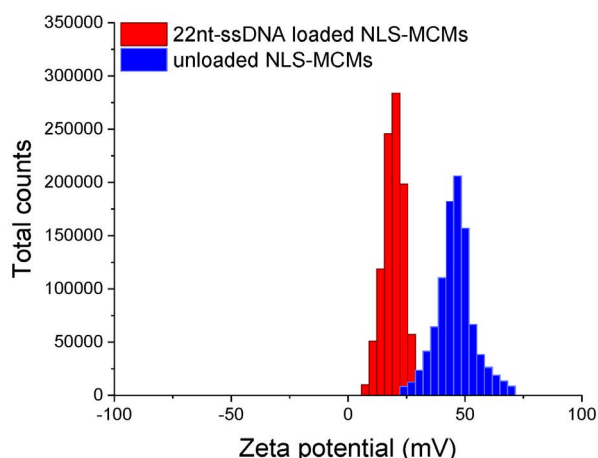


Fig. 4 Zeta potential of NLS-MCMs with (red) or without 22nt-ssDNA (blue).

Cell proliferation assays with different concentrations of NLS-MCMs indicated that NLS-MCMs had no toxic effects on HeLa cells after 24 h of incubation independent of whether or not ssDNA was entrapped (Fig. 5). In contrast, lipofectamin transfection demonstrated a 40% lower cell viability compared to NLS-MCMs at the highest DNA concentration.

Cellular uptake of NLS-MCMs loaded with fluorescently labelled DNA in H2B-GFP expressing HeLa cells was examined by CLSM (Fig. 6). Uptake efficiency of 22mer ssDNA was higher for NLS- than for (HR)3gT MCMs. Conceivably, the increased cellular uptake is related to the cell penetrating properties of lysine-arginine repeats that are exposed on the surface of the NLS-MCMs in addition to a higher positive surface charge and lower size compared to (HR)3gT MCMs.

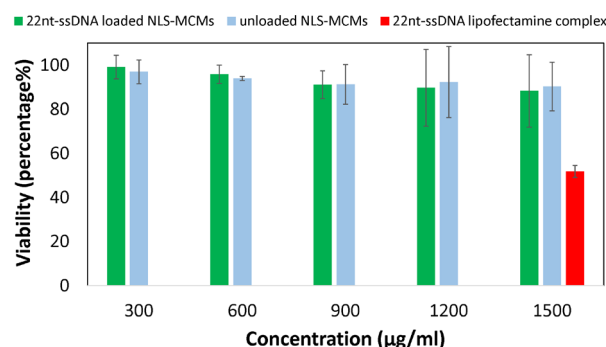


Fig. 5 Effect of unloaded and 22nt-ssDNA loaded NLS-MCMs on cell proliferation compared to 22nt-ssDNA lipofectamine complex.

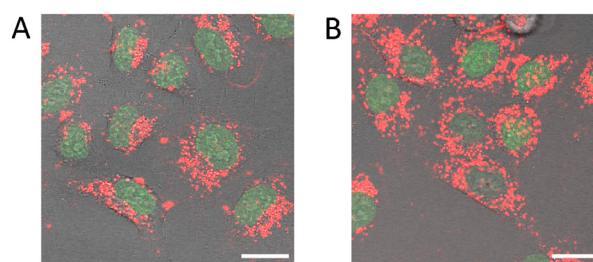


Fig. 6 CLSM merged images of H2B-GFP expressing HeLa cells treated with DNA-loaded (HR)3gT (A), and NLS MCMs (B) for 24 hours. Scale bars, 20 μ m.

Conclusion and outlook

The extension of the hydrophilic domain of the (HR)3gT peptide by an NLS led to an MCM delivery system capable of targeting a DNA payload to the nucleus. DNA was entrapped throughout the MCMs during self-assembly via electrostatic interactions between DNA and peptide. The two additional KR repeats in the peptide enhanced the effectiveness of the MCMs to overcome biological barriers, resulting in a higher cellular uptake efficiency. Owing to the biocompatibility of the peptide, the cell toxicity remained low for NLS-MCMs. Our findings show that NLS-MCMs have the features required for a safe and efficient peptide-based gene delivery nanosystem. Our future efforts are directed towards entrapment of therapeutic AONs to ultimately develop an efficient, peptide particle mediated gene therapy.

References

- [1] Z. Kang, Q. Meng, K. Liu, *Peptide-based gene delivery vectors*, *J. Mater. Chem. B* **7**, 1824-1841(2019)
- [2] S. Tarvirdipour, X. Huang, V. Mihali, C-A. Schoenenberger, C. G. Palivan, *Peptide-Based Nanoassemblies in Gene Therapy and Diagnosis: Paving the Way for Clinical application*, *Molecules* **25**, 3482 (2020)
- [3] C. Zelmer, L. P. Zweifel, L. E. Kapinos, I. Craciun, Z. P. Güven, C. G. Palivan, R. Y. Lim, *Organelle-specific targeting of polymersomes into the cell nucleus*, *PNAS* **117**, 2770-2778 (2020)
- [4] S. Tarvirdipour, C-A. Schoenenberger, Y. Benenson, C. G. Palivan, *A self-assembling amphiphilic peptide nanoparticle for the efficient entrapment of DNA cargoes up to 100 nucleotides in length*, *Soft Matter* **16**, 1678-1691 (2020)

Understanding phonon propagation in nano devices

Project P1607: Understanding and engineering of phonon propagation in nanodevices by employing energy resolved phonon emission and adsorption spectroscopy

Project Leader: I. Zardo and C. Schönenberger

Collaborators: L. Gubser (SNI PhD Student), M. Nilsson, A. Baumgartner, F. Thomas, C. Jünger, G. Fülöp, L. Sorba, and V. Zannier

Introduction

During the last few decades research has improved our knowledge and control over electrons and photons, enabling impressive advances for electronic and optoelectronic applications. The same degree of control is still lacking for phonons. The ability to manipulate phonons and phonon transport on a quantum level would lead to full control over heat flow in nanodevices. This could be used in the form of phonon transistors [1] and to realize logic gates [2].

The goal of the project is twofold. First, efficient phonon emitters and detectors have to be developed. Second, the developed devices can then be used to investigate and engineer phonon dispersions. To realise the former, inelastic tunneling through the states of a double quantum dot shall be used as phonon emitter and detector.

Double quantum dot phonon emitter/detector

The group of Jason Petta has demonstrated a maser driven by single-electron tunneling through a double quantum dot (DQD) in a semiconducting nanowire (NW) [3]. Such a device is based on inelastic tunneling through the energy states of the two QDs, when the system is driven by an applied bias voltage.

A schematic of the investigated DQD structure is presented in figure 1. Under an applied bias, an electron undergoes three subsequent tunnel transitions: i) from source to eigenstate ϵ_1 of QD1; ii) from ϵ_1 to ϵ_2 in QD2; iii) from ϵ_2 to drain.

Inelastic tunnelling takes place if the energy levels are detuned ($\epsilon_1 \neq \epsilon_2$). The electron will then tunnel through the DQD emitting/absorbing a particle (a photon or a phonon) able to account for the energy difference. When $\epsilon_1 > \epsilon_2$, tunnelling can only take place if such a particle is emitted. Hence, the device acts as a photon or phonon emitter. Analogously, when $\epsilon_2 > \epsilon_1$, tunnelling can only take place if a particle is simultaneously absorbed. The device now acts as a detector.

In the work of Liu et al. [3], the DQD system was coupled to a microwave cavity, as their interest was focused on phonon emission and absorption. In absence of such a cavity, the emission/absorption of phonons is expected to be dominate. This makes the DQD system an excellent choice to emit and detect monochromatic phonons.

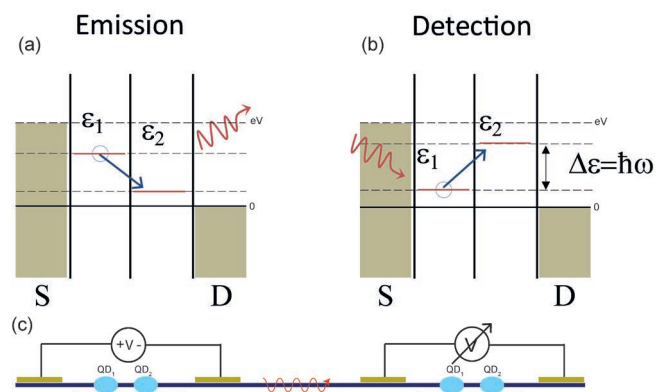


Fig. 1 Illustration of a) a phonon emitter and b) detector using a double quantum dot (DQD). Driven by an applied bias, inelastic tunneling is used to either emit or detect phonons. c) Schematic of an envisaged device. Inside the semiconducting nanowire two double quantum dots (light blue) are defined by local bottom gates (red). Phonons are then generated by an applied bias through source (S)-drain (D) contacts in the left DQD system and detected by measuring the voltage in the right DQD.

Device and electron transport characterization

The DQD is defined by an InAs/InP heterostructure. This approach allows for very small QDs with a large level spacing > 1 meV [4].

To test the function of the DQD acting as a detector alone, the device design was adapted to include a Joule heater in addition to the side gates, which are used to change the chemical potential of the QDs and the source and drain contacts, through which the DC current and the differential conductance are measured (Fig. 2).

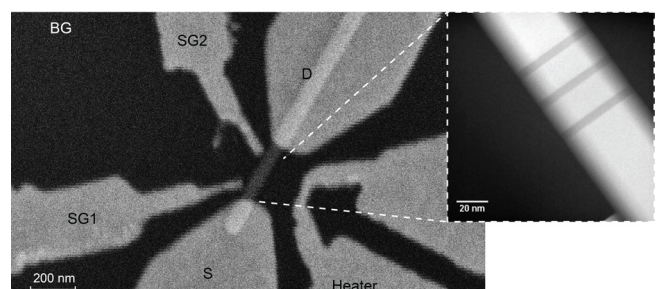


Fig. 2 Scanning electron microscope image of a device consisting of an InAs nanowire with three in situ grown InP tunnel barriers of length 5.2, 6.8, 5.4 nm, separated by 19 nm of InAs forming the QDs. The NW is contacted by two Ni/Au contacts (S/D) using sulphur passivation. Two side gates (SG) were fabricated close to the

NW. The doped Si/SiO₂ acts as a global back gate. Additionally, a Ti/Au strip with a constriction close to the DQD section of the NW acts as a local Joule heater. Inset: Transmission electron microscope image of an InAs NW with symmetrical InP barriers. The InP segments act as tunnel barriers due to their larger bandgap.

Electrical transport measurements were performed in a He4 cryostat ($T_{\text{bath}} = 1.7$ K) as well as in a dilution refrigerator ($T_{\text{bath}} = 55$ mK). From the measurement of the differential conductance as a function of the gate voltages V_{SG1} and V_{SG2} (Fig. 3) at 55 mK, several characteristic values of the DQD could be extracted, namely the charging energies of both QDs, $E_{\text{C1}} = 5.8$ meV, $E_{\text{C2}} = 5.6$ meV, as well as the inter dot charging energy, $E_{\text{CM}} = 2.5$ meV. The DQD further shows well defined excited state lines at ~ 1.2 meV with respect to the ground state. Similar values were obtained performing the same analysis on the measurements at 1.7 K.

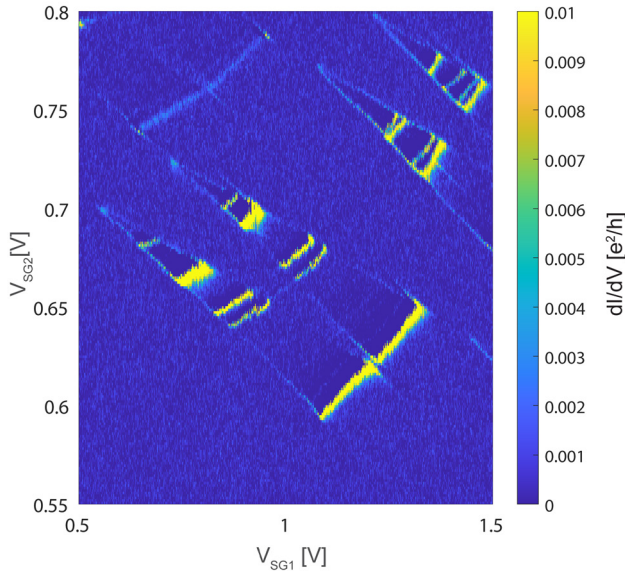


Fig. 3 Differential conductance measurement as a function of the voltage applied to SG1 and SG2 at $V_{\text{SD}}: -3$ mV DC bias and a constant back gate voltage of 6V. These measurements were recorded at a bath temperature of 55 mK.

Heat dependent electron transport

To see the effect of temperature on electron transport, no electrical bias will be applied, as the electrical drive would quickly overshadow the temperature drive. We expect to see two distinct transport mechanism, which can be differentiated by their position on the charge stability diagram. Both exhibit a current polarity reversal upon passing the DQD triple point along their respective axis. The thermal gradient between source and drain sides (caused by non-perfect heater placement) causes thermoelectric transport, which is most pronounced when the QD states are in resonance, since it is an elastic process. Additionally we expect an inelastic tunnelling process, caused by phonon/photon absorption to appear along the detuning axis. The latter process further requires the energy of the absorbed particle to be larger than the electron temperature in the NW leads, putting significant constraints on the engineering of the heater and nanowire [5].

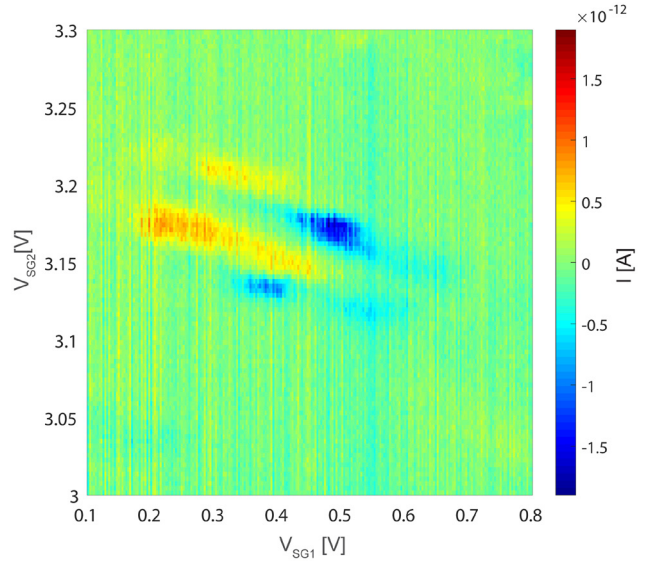


Fig. 4 DC current measurements as a function of the voltage applied to SG1 and SG2 at effectively zero DC bias and a constant back gate voltage of 4 V at a temperature of 1.7 K with 6 V applied to the Joule heater.

We have observed both effects by measuring the DC current through the DQD at different heating currents (Fig. 4). At zero heating the current through the DQD is supposed to be zero. Due to imperfect filtering of the measurement lines there seems to be some photon coupling in, resulting in a minor signature of photon absorption. By increasing the heating current a clear increase in current through the DQD can be observed. Signatures of both thermoelectric, as well as inelastic transport, are visible.

Outlook

We could clearly show the onset of different electron transport processes with increasing heating current. Unfortunately, a hot metal strip does not only heat the substrate (phonons) but also emit radiation (photons). To continue towards the goal of a phonon detector we have to evaluate the significance of the radiation contribution to the measured signal.

References

- [1] B. Li, L. Wang, G. Casati, *Negative differential thermal resistance and thermal transistor*, Appl. Phys. Lett. **88**, 143501 (2006)
- [2] L. Wang and B. Li, *Thermal Logic Gates: Computation with Phonons*, Phys. Rev. Lett. **99**, 177208 (2007)
- [3] Y.-Y. Liu, J. Stehlik, C. Eichler, M. J. Gullans, J. M. Taylor, J. R. Petta, *Semiconductor double quantum dot micromaser*, Science **347(6219)**, 285-287 (2015)
- [4] S. Roddaro, A. Pescaglini, d. Ercolani, L. Sorba, F. Beltram, *Manipulation of Electron Orbitals in Hard-Wall InAs/InP Nanowire Quantum Dots*, Nano Lett. 2011, **11(4)**, pp 1695-1699
- [5] S. Dorsch, A. Svilans, M. Josefsson, B. Goldozian, M. Kumar, C. Thelander, A. Wacker, A. Burke, *Heat driven transport in serial double quantum dot devices*, arxiv:2003.11357

Mono layer semiconducting MoS₂ with superconducting contacts

Project P1701: Van der Waals 2D semiconductor nanostructures with superconducting contacts

Project Leader: A. Baumgartner and C. Schönenberger

Collaborators: M. Ramezani (SNI PhD student), I. C. Sampaio, K. Watanabe, and T. Taniguchi

Introduction

Two-dimensional semiconductors with superconducting contacts are expected to form the basis for a large variety of new phenomena to study, based on the interplay of induced superconductivity, already demonstrated in graphene [1, 2], and the large spin-orbit and electron-electron interactions, for example in molybdenum di-sulfide (MoS₂) [3]. In addition, one might gain more control over phenomena like Cooper pair splitting, coherent transport in quantum dots [4], or Majorana bound states. In this project, we already established high quality normal metal electrical contacts to atomically thin layers of van der Waals (vdW) materials, such as MoS₂ in standard geometries. Then we reported first signatures of low quality superconducting bottom contacts and demonstrated high quality normal metal contacts using vertical interconnect access (VIA) Au contacts. In this reporting period, we now combine the two approaches and demonstrate superconducting MoRe VIA contacts to MoS₂, with convincing evidence of a superconducting energy gap and a weak to intermediate coupling strengths between the superconductor and the semiconductor, which we characterised at cryogenic temperatures and in large magnetic fields.

Materials and Methods

Figure 1a shows an optical microscopy image of an investigated device. The fabrication technique can be summarized by the following steps: 1) Housing of vertical access: the contact area is defined by electron beam lithography (EBL) on the designated top hBN (t-hBN, ≈40nm thickness) on a Si/SiO₂ wafer, and etched through using reactive ion etching with a 20:5:5 sccm SF₆:O₂:Ar mixture at 25 mTorr pressure and 50 W power. 2) VIA metal deposition: in a second EBL step, a slightly larger area (VIA housing at the centre) is defined to improve the adhesion of the metal to the hBN. The interface is cleaned using a mild O₂ plasma. The type-II superconductor MoRe with a reported bulk critical temperature of T_c≈6-10K and a critical magnetic field of H_c≈8-13 T [5] is then deposited by sputter deposition with a thickness roughly 10% larger than that of the t-hBN. 3) Stacking of required layers: the t-hBN layer with the VIAs is transferred to an inert gas (N₂) glove box (partial pressures of H₂O and O₂ <0.1 ppm), and used to consecutively pick up a single layer MoS₂ flake, a bottom hBN flake (b-hBN, ≈25nm thickness), and a multilayer graphene (MLG) flake serving as backgate. 4) this stack is then deposited onto a cleaned Si/SiO₂ wafer and Ti/Au (10/50nm) leads are fabricated by standard EBL techniques connecting the VIAs to the bond pads. The sample is annealed for 30 minutes at 350° in a vacuum chamber with forming gas flow.

An optical microscopy image of one of the devices is shown in figure 1a. Presently, this process only yields ~50% useful contacts for MoRe (~100% for Au), so we investigate only the indicated contacts at cryogenic temperatures.

We have characterized this device in a dilution refrigerator (T_{base} ≈60 mK), and in a variable temperature insert (T_{base} ≈1.7 K), both equipped with a magnet with fields perpendicular to the sample plane.

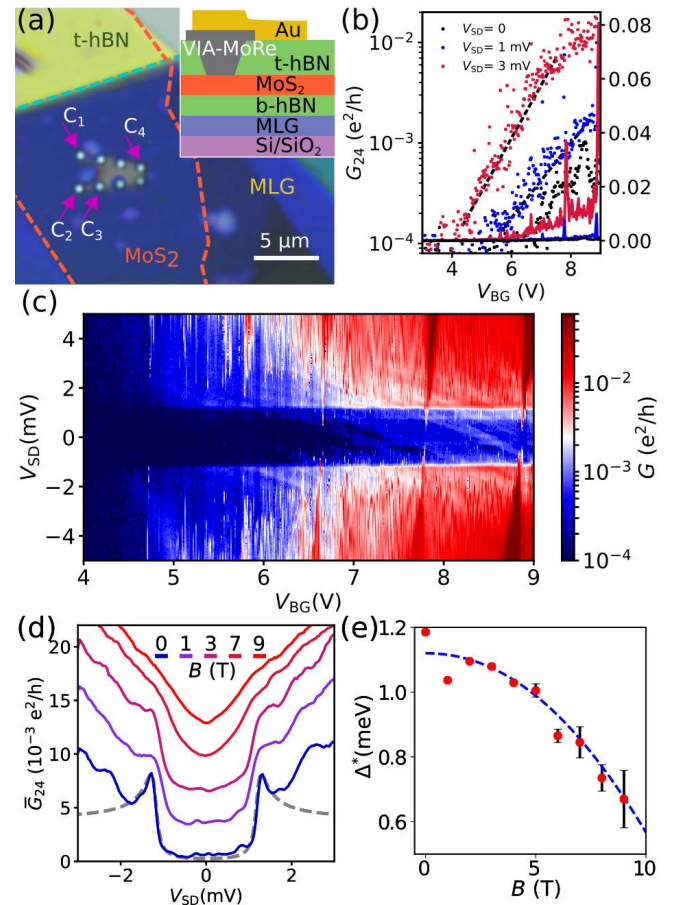


Fig. 1 a) Optical microscopy image of a VIA contacted MoS₂ device. Inset: schematic layer structure. b) G_{24} vs V_{BG} at the indicated bias voltages. c) G_{24} vs V_{BG} and V_{SD} at $B=0$. d) G_{24} vs V_{SD} averaged over the gate voltage interval $V_{BG}=7.3-7.4$ V. e) Extracted induced gap at various magnetic field (red dots) and a theoretical fit (blue dashed line).

Results and discussions

Figure 1b shows the differential conductance G_{24} measured between contacts 2 and 4 as a function of the backgate voltage V_{BG} for different bias voltages V_{SD} . The observed exponential increase in the conductance suggests that there are still Schottky barriers formed at the contacts. However, the

colorscale plot in figure 1c clearly demonstrates a superconducting energy gap in the transport characteristics, independent of the gate voltage. For increasing magnetic fields this energy gap is suppressed, which excludes other mesoscopic effect forming gaps in transport, such as Coulomb blockade (CB). IV (current/voltage) characteristics at $V_{BG} = 9$ V and for various indicated magnetic fields are shown in figure 1d. As a measure of the energy gap, we plot in figure 1e the inflection points found for the curves in figure 1d. For $B=0$, we find $\Delta_0 \approx 1.1$ meV, in good agreement with the bulk properties of MoRe [3]. The extracted energy gap shrinks with increasing magnetic field, with an extrapolated (upper) critical field of ~ 15 T, at which the gap disappears. In addition, the cross section at $B=0$ can be well described by the model by Blonder, Tinkham and Klapwijk (BTK) [6], including a broadening parameter proposed by Dynes [7], shown as gray dashed line in figure 1d. These findings are consistent with a normal metal / superconductor (S/N) junction in the weak tunneling limit and with sharp Schottky barriers forming at the contact interfaces.

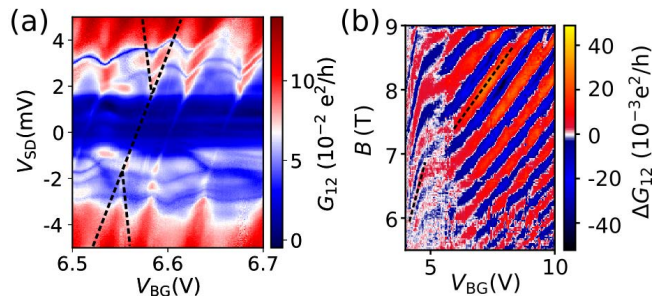


Fig. 2 a) G_{12} vs V_{BG} and V_{SD} at $B=0$. b) G_{12} vs V_{BG} and B at $T=1.7$ K showing SdH oscillations.

However, many of the interesting aimed for phenomena require a stronger coupling to the semiconductor. Preliminary data pointing towards such stronger couplings are shown in figure 2a: for contact pair C_1 - C_2 we find CB diamonds shifted in energy and in gate voltage as indicated by the dashed lines. These structures are in good agreement with a superconductor directly coupled to a quantum dot (QD) [4], here formed unintentionally by potential variations near contact C_1 . These shifted CB diamonds are “connected” by a faint resonance previously identified as resonant Andreev tunneling [4], a phenomenon that only occurs for reasonably strong coupling of the superconducting reservoir to the QD.

As a final step, we demonstrate that the intrinsic properties of the two-dimensional MoS_2 are intact in the bulk of the crystal. For this, we performed magnetoconductance measurements at high bias voltages (above the superconducting energy gap), where the contact characteristics are similar to a normal metal. Figure 2b shows clear Shubnikov de Haas (SdH) oscillations, suggesting a high quality of the MoS_2 . The onset of the oscillations in magnetic field at the lowest plotted value $Bq \approx 5$ T is typically interpreted as the charge carriers closing a cyclotron orbit before being scattered. Based on the Drude model for the sample resistivity, $\rho = m^*/(ne^2\tau_p)$, and considering that the momentum scattering time τ_p is usually larger than τ_q , we find an upper limit for the carrier mobility $\mu = 1/(nep) \approx 2500$ $\text{cm}^2/(\text{Vs})$ at $V_{BG} = 10$ V. At low enough electron densities ($V_{BG} < 5$ V), we find a transition in the SdH characteristics consistent with only the two lowest conduction bands being occupied [3], which can only be observed with low enough disorder potential fluctuations.

In conclusion, we have demonstrated the first superconducting contacts to MoS_2 , which are, however, still hampered by Schottky barriers. In the next phase we will test different superconducting materials and further improve the device fabrication with the aim to demonstrate the superconducting proximity effect, and in parallel, we will work on gate-defined nanostructures based on the techniques developed here.

References

- [1] D. I. Indolese, R. Delagrangé, P. Makk, J. R. Wallbank, K. Watanabe, T. Taniguchi, C. Schönenberger, *Signatures of van Hove singularities probed by the supercurrent in a graphene-hBN superlattice*. Phys. Rev. Lett. **121**, 137701 (2018)
- [2] I. V. Borzenets et al. *Ballistic graphene Josephson junctions from the short to the long junction regimes*. Phys. Rev. Lett. **117**, 237002 (2016)
- [3] R. Pisoni et al. *Interactions and magnetotransport through spin-valley coupled Landau levels in monolayer MoS_2* . Phys. Rev. Lett. **121**, 247701 (2018)
- [4] J. Gramich, A. Baumgartner, C. Schönenberger, *Resonant and Inelastic Andreev Tunneling Observed on a Carbon Nanotube Quantum Dot*. Phys. Rev. Lett. **115**, 216801 (2015)
- [5] M. Witcomb, D. Dew-Hughes, *The σ -phase in molybdenum-rhenium; microstructure and superconducting hysteresis*. J. Less-Common Met. **31**, 197 (1973)
- [6] G. E. Blonder, M. Tinkham, T. M. Klapwijk, *Transition from metallic to tunneling regimes in superconducting microconstrictions: Excess current, charge imbalance, and supercurrent conversion*. Phys. Rev. B **25**, 4515 (1982)
- [7] R. Dynes, V. Narayanamurti, J. P. Garno, *Direct Measurement of Quasiparticle-Lifetime Broadening in a Strong-Coupled Superconductor*. Phys. Rev. Lett. **41**, 1509 (1978)

Development of a 3D poly(methyl methacrylate) microfluidic device for biomedical applications

Project P1702: Single organelle size sorting by a nanofluidic device

Project Leader: Y. Ekinici and R. Lim

Collaborators: T. Mortelmans (SNI PhD Student), X. Li, and T. Braun

Research context

During the second half of the 20th century, the developments in micro- and nanofabrication paved the way for further downscaling of integrated circuits [1]. These advances in microfabrication not only had a significant impact on the semiconductor landscape, but also sparked the interest of researchers in a wide variety of scientific disciplines, such as micromechanical systems (MEMS) and microfluidics. For example, scientists at Stanford University fabricated a microscale gas chromatography system, which allowed for the investigation of very low sample volumes with a high degree of sample control and without any notable performance loss [2]. This revolutionized molecular analysis techniques and gave birth to the field of microfluidics and “miniaturized Total Analysis Systems” (μ TAS) [3].

Currently, advanced micro- and nanofabrication techniques have become more widely available and the field has reached scientific adolescence [4]. However, most microfluidic devices are designed in 2D while the height of the channel remains constant [5]. By changing the height within the channel, a new degree of freedom is obtained, and more complex sample manipulations can be performed. The presented work uses grayscale e-beam lithography (g-EBL) nanopatterning techniques to fabricate a three-dimensional (3D) capillary poly(methyl methacrylate) (PMMA) microfluidic device, capable of trapping particles at well-defined positions depending on their size. In doing so, the particle size can optically be determined with precision in the nanoscale. This allows for the device to be applied in various disciplines of biomedical sciences where size-determination of cells or sub-cellular structures are of relevance, such as in Parkinson’s disease [6, 7].

In this annual report, a key nanofabrication parameter is outlined and a theoretical approach towards a passive PMMA microfluidic device using capillary pumps is discussed, and insights into critical design parameters are provided.

Results and discussion

The fabrication of such a 3D PMMA microfluidic device is highly challenging and requires state-of-the-art nanofabrication methods. To this extent, we systematically studied the use of g-EBL to reliably pattern structures with a nanoscale height change, but on a millimeter length scale [8]. It was found that the time between electron beam exposure and subsequent development (t_{ED}) plays a crucial role in controlling the resist topography. More specifically, when the resist was developed at a short t_{ED} , the achieved depth for a given electron dose was significantly higher when compared to a development at large t_{ED} -values. This dependency could be described by the following exponential fit function:

$$d(t_{ED}) = (d_0 - d_{ss})e^{-\frac{t_{ED}-t_0}{\tau}} + d_{ss}$$

Eq. 1 Exponential fit function describing the dependency of development depth on t_{ED}

where $d(t_{ED})$ is the removed resist thickness for a development at a given time after electron exposure. d_0 and d_{ss} , respectively represent the initial film thickness before development and the steady-state thickness after development, both of which can be determined experimentally. In addition, it was found that a post-exposure bake (PEB) reduced the development depth and was correlated with the PEB-time (Fig. 1). However, this procedure induces stress in the resist film, which is unwanted for controlled and reproducible grayscale patterning (Fig. 1 Inset).

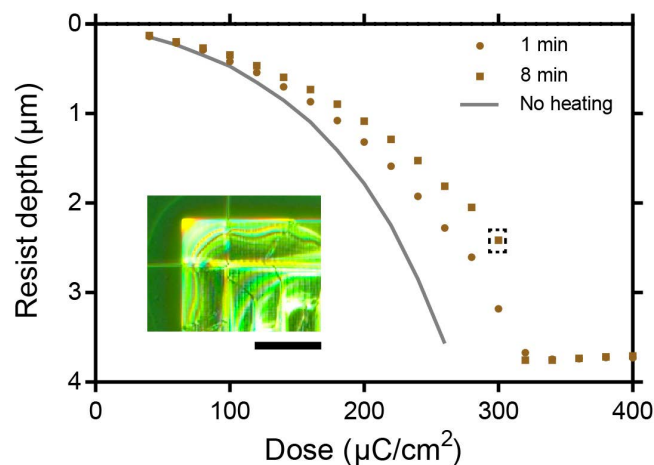


Fig. 1 Influence of a PEB at 80°C on the contrast curve of PMMA 950 K. The inset of the figure shows a light-microscopy image of a region exposed at 300 $\mu\text{C}/\text{cm}^2$ and subjected to an 8 min PEB. The scale bar is 100 μm .

To enable the designed device to be easy in operation and versatile in application, the fluid must passively enter the microfluidic channel without the use of external loading elements, such as syringe pumps or peripheral control elements. The filling front in such devices will therefore be mostly determined by the channel geometry and its surface properties, such as wettability and roughness [9, 10].

The microfluidics module from Comsol Multiphysics was used to acquire a more in-depth understanding of the filling front in a simplified 2D PMMA-based microfluidic device (Fig. 2)[11]. It was observed that the velocity field decreases sharply in the channel section and is rather stable once the capillary pump is reached, evidencing a high degree of control over the fluid flow. By adjusting the geometry of the

structures inside the capillary pump region, it is possible to precisely control the velocity field magnitude. The latter is of utmost importance as biological samples have non-negligible elasticity components, which will influence their trapping position.

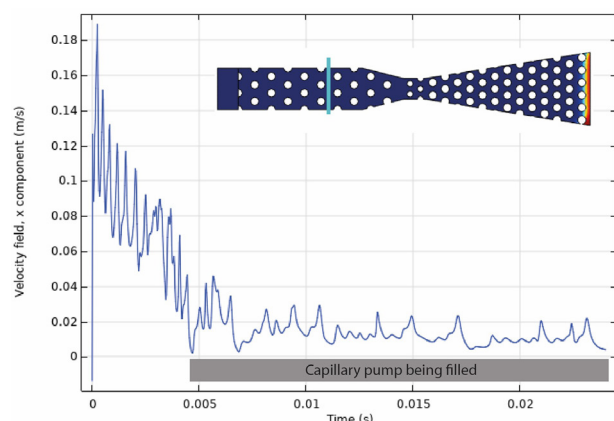


Fig. 2 COMSOL modeling to determine the velocity profile of water in a capillary 2D PMMA microfluidic device. Top right inset: The blue line marks the location in the 2D model where the velocity field is monitored, with the filled line marking the channel region and the dotted line representing the capillary pump.

In addition to controlling the velocity of the flow field, it is imperative that the device is characterized by homogeneous liquid filling. To this extent, retention valves have been known to prevent premature liquid drainage [10]. The use of such valves in a simplified 2D PMMA microfluidic device was also theoretically investigated through a series of COMSOL simulations (Fig. 3). It was shown that when no retention valve is present in the device design, an air bubble can occur before the capillary pump region (red color), which will significantly hamper the further fluid flow. However, once a retention valve is introduced, the air bubble disappears. This effect is even more pronounced when followed by a flow resistor.

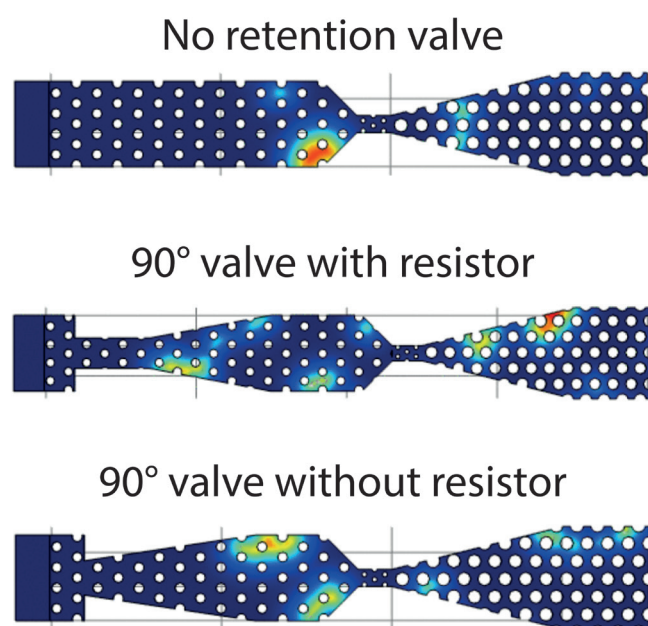


Fig. 3 Influence of a retention valve and flow resistor on the filling factor of simplified 2D PMMA microfluidic devices.

To summarize, a high degree of freedom over the device topography is obtained through an extensive study of the resist material. Moreover, a theoretical simulation has provided key insights into critical device design parameters, such as a capillary pump, inflow resistors and retention valves. In our ongoing work we are investigating the practical differences of these various flow elements on the trapping of polystyrene nanoparticles.

References

- [1] M. Hitzbleck, E. Delamarche, *Reagents in microfluidics: an 'in' and 'out' challenge*, Chem. Soc. Rev. **42**, 8494–8516 (2013)
- [2] S. C. Terry, J. H. Herman, J. B. Angell, *A Gas Chromatographic Air Analyzer Fabricated on a Silicon Wafer*. IEEE Trans. Electron Devices **26**, 1880–1886 (1979)
- [3] N. Convery, N. Gadegaard, *30 Years of Microfluidics*, Micro Nano Eng. **2**, 76–91 (2019)
- [4] G. M. Whitesides, *The origins and the future of microfluidics*, Nature **442**, 368–373 (2006)
- [5] A. M. Streets, Y. Huang, *Chip in a lab : Microfluidics for next generation life science*, Biomicrofluidics **7**, 1–23 (2013)
- [6] A. Bose, M. F. Beal, *Mitochondrial dysfunction in Parkinson's disease*, J. Neurochem. **139**, 216–231 (2016)
- [7] S. H. Shahmoradian et al., *Lewy pathology in Parkinson's disease consists of a crowded organellar membranous medley*, bioRxiv 137976 (2017)
- [8] T. Mortelmans, D. Kazazis, V. A. Guzenko, C. Padeste, T. Braun, X. Li, Y. Ekinci, *Grayscale e-beam lithography: Effects of a delayed development for well-controlled 3D patterning*, Microelectron. Eng. **225**, 111272 (2020)
- [9] R. Safavieh, D. Juncker, *Capillaries: Pre-programmed, self-powered microfluidic circuits built from capillary elements*, Lab Chip **13**, 4180–4189 (2013)
- [10] A. Olanrewaju, M. Beaugrand, M. Yafia, D. Juncker, *Capillary microfluidics in microchannels: From microfluidic networks to capillary circuits*, Lab Chip **18**, 2323–2347 (2018)
- [11] L. Gervais, E. Delamarche, *Toward one-step point-of-care immunodiagnostics using capillary-driven microfluidics and PDMS substrates*, Lab Chip **9**, 3330–3337 (2009)

Engineering mechanical properties of protein binders

Project P1704: Evolving protease enzymes with new sequence specificity using peptide-hydrogel cell encapsulation

Project Leader: M. Nash and S. Reddy

Collaborator: J. López Morales (SNI PhD Student)

Biological evolution employs iterated mutation and natural selection to provide solutions for challenges that organisms face in the natural world. However, the traits that result from natural selection only occasionally overlap with features of biomolecules that are sought by humans for engineering applications and/or therapeutic purposes. Rational design of proteins coupled to artificial directed evolution can tweak the course of natural evolution to obtain the desired properties in a protein.

In this project, we selected a cell receptor called programmed death ligand 1 (PDL1 or CD274) based on its clinical relevance, as the bait to the engineered binder. This receptor is overexpressed in cells from different types of cancer and helps them to evade the immune system from eliminating spreading cancer cells [1]. The extracellular domain of PDL1 (PDL1-ECD) was cloned, expressed, and purified from inclusion bodies from *E. coli*. The purified antigen containing a Spytag-peptide was incubated with an Spycatcher-GFP fusion polypeptide for bioconjugation. The assembled protein was then observed and validated by SDS PAGE analysis (Fig. 1a).

The second step of the construction of an AntiPDL1 binder is to obtain a positive control that specifically interacts with the antigen. Two engineered scaffolds were therefore selected: a derivative of a fibronectin Kringle domain called adnectin [2] and an engineered affibody. Both binders' genes were cloned and transformed into a yeast system for cell surface display due to the high efficiency of yeast homologous recombination exploited for *in vivo* library cloning, its widespread use for directed evolution, and its easy manipulation during force analysis and measurements. The display system consists of genetically encoded gene plasmids thermo-chemically introduced into yeast cells. The plasmid contains a signal peptide and an AGA2P domain that translocate from the cell membrane to the cell wall and form a complex with the anchored AGA1P via disulfide bridges, exposing therefore the C-terminal part of AGA2 and the mutant construct to the medium [3]. The displayed scaffolds contain different additional peptide sequences that can be labeled with fluorescent antibodies for imaging and flow cytometric analysis. Optimal expression conditions of constructs of interest were assessed by immunolabeling and cytometry, where 24 h of expression at 20°C were the best conditions for the display on yeast cells.

To validate both the antigen and positive controls, antigen binding was assessed by fluorescence activated cell sorting (FACS). It is a technology with which mixtures of cells can be analyzed, counted, and separated with a flow cytometer instrument. The analysis can be carried out on suspended cells with a size ranging between 0.2 and 100 micrometers, which are first stained with different fluorescent markers

such as fluorescent proteins, fluorescently labeled antibodies and/or many other stains. In the flow cytometer, these particles/cells pass a laser at up to 130 km/h. The scattered light reveals the size and internal structure of the cell, while the fluorescence indicates which stain the cell contains. Cells displaying the desired characteristics are identified and counted. Finally, the fluid stream is divided into many miniscule droplets. Droplets which contain a desired cell are electrically charged and diverted by an electric field into different collecting tubes. The various separated cells can subsequently be investigated using microscopy, biochemical and functional experiments. Therefore, yeast cells are stained (red) if they correctly display full length proteins and become doubly labeled if the interaction with the antigen (green) is positive.

Fluorescently labeled displaying cells were incubated with 500 nM of PDL1-GFP (green) at saturating antigen concentration. A negative control was designed to display the empty framework of the system but without the potential binder of interest and showed no unspecific binding to neither the fluorescent Spycatcher-GFP nor to the PDL1-GFP antigen of interest. On the other hand, both the adnectin and the affibody showed a positive binding response to the prepared antigen and no unspecific binding to Spycatcher-GFP (Fig. 1b), confirming and validating the establishment of the desired antigen and the right positive control binders.

The next stage involves the selection of the scaffold to be engineered. To improve the mechanical properties of the scaffold, a surface that offers several hydrogen bonding side chains is necessary. To observe that, a homology model of the complex between the positive binder adnectin and PDL1 was built using the ClusPro server (Fig. 1c) that performs three computational steps as follows: (i) rigid-body docking by sampling billions of conformations; (ii) root-mean-square deviation (RMSD)-based clustering of the 1,000 lowest-energy structures generated, to find the largest clusters that will represent the most likely models of the complex; and (iii) refinement of selected structures using energy minimization[4]. Analysis and further understanding of the simulated docked interacting surfaces correlate with the reported binding loops. Key positions and secondary structures were identified and will be then engineered in a bacterial single domain as an *de novo* protein design strategy.

We envision that the outcome of this project will offer a molecule with biomedical impact in diseases that currently lack treatments or diagnosis tools; and an efficient platform for directed evolution of proteins within the rising field of mechanobiology.

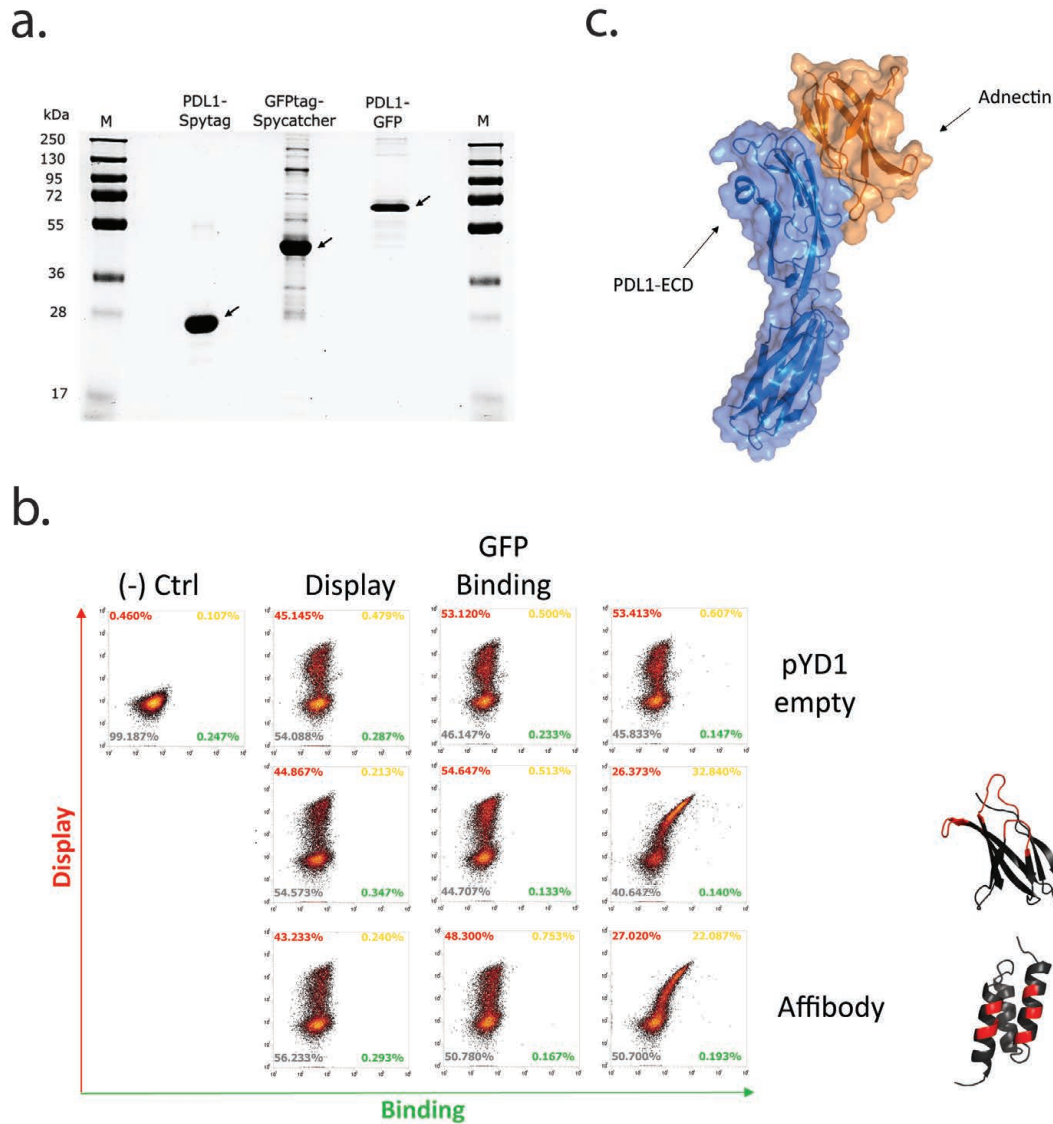


Fig. 1 Strategy for engineering mechanical properties of scaffold domains. *a)* SDS PAGE analysis of the fluorescent PDL1-GFP antigen. Bio-conjugation was performed using microbial superglue Spy system to prepare fluorescent PDL1. PDL1-Spytag (27 kDa); GFP-Spycatcher (43 kDa); conjugated PDL1-GFP (70 kDa). *b)* FACS plots of anti PDL1 binders adnectin and affibody displayed on yeast cell surfaces (red) and specific binding to PDL1-GFP (green). A shift to the yellow quadrant validates the positive binding with double staining. $n=15\ 000$. *c)* Homology docking model of adnectin specifically binding to PDL1. Interacting residues and patches will be further studied for engineering a scaffold that binds PDL1, based on the 3D structure of the complex.

References

- [1] J. M. Chemnitz, R. V. Parry, K. E. Nichols, C. H. June, J. L. Riley, *SHP-1 and SHP-2 associate with immunoreceptor tyrosine-based switch motif of programmed death 1 upon primary human T cell stimulation, but only receptor ligation prevents T cell activation.* *J. Immunol.*, **173**, 945–54(2004)
- [2] D. J. Donnelly et al. *Synthesis and Biologic Evaluation of a Novel ^{18}F -Labeled Adnectin as a PET Radioligand for Imaging PD-L1 Expression.* *J. Nucl. Med.* **59**, 529–535 (2018)
- [3] E. T. Boder, K. D. Wittrup, *Yeast surface display for screening combinatorial polypeptide libraries.* *Nat. Biotechnol.* **15**, 553–557 (1997)
- [4] D. Kozakov, D. Hall, B. Xia, K. A. Porter, D. Padhorny, C. Yueh, D. Beglov, S. Vajda, *The ClusPro web server for protein–protein docking.* *Nature Protocols* **12**, 255–278 (2017)

Towards label-free HTS in enzyme engineering

Project P1705: Genetic selection of nanocatalysts

Project Leader: S. Panke, P. S. Dittrich, and T. R. Ward

Collaborator: E. Rousounelou (SNI PhD Student)

Introduction

Directed evolution represents a powerful tool for developing biocatalysts for synthetic organic chemistry and homogeneous catalysis, including new-to-nature transformations [1, 2]. A successful directed evolution experiment depends on two factors: genetic diversity and high throughput screening/selection methods. Thanks to the substantial advances in our ability to generate genetic diversity and large variant libraries, the main limitation of each directed evolution experiment is the efficiency of screening methods for the identification of desired variants [3]. Conventional screening methods rely mostly on optical (fluorescent) readouts, which often have a defined and limited reaction scope, since an optical readout is usually not easily related to the outcome of a biotechnologically relevant chemical reaction [4]. While methods employing mass spectrometry (MS) are label-free (and therefore quite general) and can directly analyze products of useful chemical reactions, they are currently slow and destructive. As a consequence, they require elaborate workflows to separately store the genetic information than can be retrieved in case of success.

To overcome these fundamental problems, we are developing a novel high-throughput screening (HTS) methods that [i] addresses the speed issue by coupling droplet-based microfluidics with MALDI MS and [ii] compensates the destructiveness of MS analysis by co-analyzing the product or side-products of the reaction with unique peptide barcodes that maintain the genotype-phenotype linkage. In figure 1 an overview of the method is illustrated. Firstly, a library of unique DNA and peptide barcode combinations is generated, which is identified via next generation sequencing. The enzyme variant library is then cloned into the barcoded vectors so that every variant is associated with a unique combination of a DNA and a peptide barcode. The barcoded enzyme library is transformed into *E. coli* competent cells, followed by single cell spotting onto a picolitre array and cell lysis (Fig. 1.1). After enzyme/peptide barcode expression, each sample is incubated with candidate substrate(s) and co-factor(s) (Fig. 1.1) and the reaction is analyzed by MALDI-TOF MS. The mass spectrum of each sample delivers information about the product amount or distribution, but also its unique identity via the peptide barcode (Fig. 1.2). The latter is uniquely linked to the variant, but also to a DNA barcode

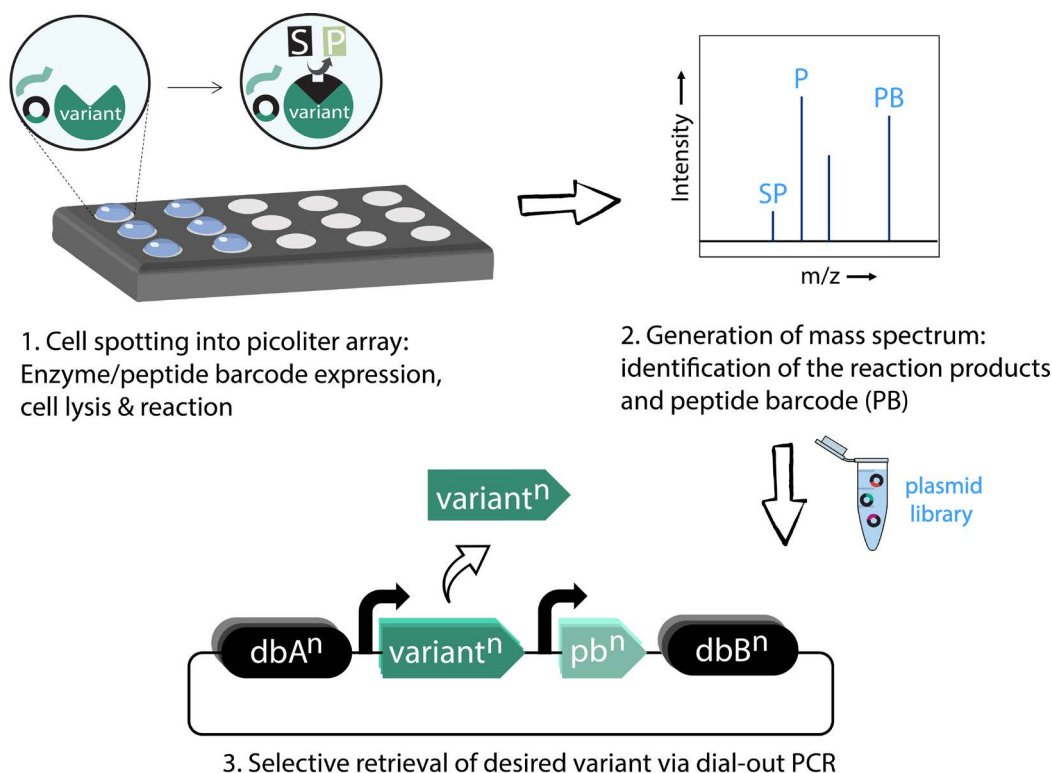


Fig. 1 Simplified overview of the proposed HTS method. For further information, refer to text.

and thus, after designing DNA primers specific to the DNA barcode, the desired variant can be retrieved by PCR, from a large pool of variants, and the genotype can be determined by sequencing (Fig. 1.3).

Designing and testing the peptide barcode library

The peptide barcodes are encoded on the same plasmid that encodes the enzyme variant and their role is to uniquely identify the variant they are associated with during MS analysis. Therefore, the peptide barcode library is composed of genetically encoded peptide sequences designed for optimal detection via MALDI-MS. Each barcode is 10 – 16 amino acids long, produces a unique signal and contains at least one proline residue to facilitate peptide sequencing via collision – induced fragmentation (CID). To increase ionization efficiency, each peptide barcode is devoid of methionines and cysteines which cause oxidation and cross-linking and contains only one basic amino-acid at the C-terminus, since basic residues at central positions tend to reduce the ionization efficiency of a peptide [5].

After the generation of the peptide barcode library using a python script, the peptides were screened in silico for their detectability, based exclusively on their amino acid sequences. From this final set of peptide barcodes, 50 peptides were randomly selected, synthesized and analyzed in MALDI-TOF. All of the 50 peptides showed high ionization efficiency and were detectable even at low concentrations (0.006 μ M). The peptides are now being tested for their ability to express efficiently in *E. coli* cells. Their expression will be monitored in vivo using a translational cassette (TCC). The TCC is encoding a mRNA sequence that forms a secondary structure in the absence of translation and contains a response gene signal (red fluorescent protein, rfp). Only when the upstream peptide barcode gene is fully translated, the secondary structure is resolved, allowing the translation of rfp and therefore, fluorescence to be observed. Moreover, the fluorescent signal is proportional to the expression level of the upstream peptide barcode that is analyzed each time.

Designing the DNA barcode library and selectively retrieving a desired variant

While the peptide barcode uniquely identifies the enzyme variant that was analyzed, the sample that was assayed is destroyed in the process due to its ionization and with it the genetic information of the improved enzyme variant (located on a plasmid). To retrieve this information, we need to map the peptide barcode information back to the specific plasmid from which it originated, and which is still available from a duplicate of the plasmid library (see Fig. 1.3). To achieve this, the plasmids are barcoded (“tagged”) with a set of random 30mer oligonucleotides, so that the peptide barcodes are unambiguously linked to a unique set of DNA barcodes and subsequently to a unique enzyme variant.

In an initial proof-of-principle experiment, we confirmed our ability to retrieve a specific gene when mixed with a pool of similar genes. More specifically, the gene for yellow fluorescent protein (yfp) flanked with specific DNA barcode set was mixed in different ratios (up to 1:106) with the DNA barcoded pool of the green fluorescent protein (gfp) and was each time successfully and selectively retrieved. The two genes differ only in 5 point mutations, so we can safely assume that our power to selectively retrieve the yfp gene is not influenced by the gene sequence. Subsequently, a large DNA barcoded yfp pool (library diversity 108) was generated, in which every yfp gene was linked to a unique ID sequence. After sending for Sanger sequencing 100 colonies from the pool and designing optimal retrieval primers unique for the 100 DNA barcoded

plasmids, we performed 100 dial-out PCRs on the initial pool with the goal to selectively retrieve each time one of these 100 sequences. The retrieved PCRs produced a strong band for 97% of the attempts with a few off-target products and 95% were error-free as confirmed by Sanger sequencing. The next step is to link the generated DNA barcode library with the peptide barcode library and analyse the generated plasmid pool via next generation sequencing (NGS).

References

- [1] U. T. Bornscheuer, G. W. Huisman, R. J. Kazlauskas, S. Lutz, J. C. Moore, K. Robins, *Engineering the third wave of biocatalysis*. *Nature* **485**, 185–194 (2012)
- [2] M. Jeschek, S. Panke, T. R. Ward, *Artificial Metallo-enzymes on the Verge of New-to-Nature Metabolism*. *Trends Biotechnol.* **36**, 60–72 (2018)
- [3] C. Zeymer, D. Hilvert, *Directed Evolution of Protein Catalysts*. *Annu. Rev. Biochem.* **87**, 131-157 (2018)
- [4] M. Wójcik, A. Telzerow, W. J. Quax, Y. L. Boersma, *High-throughput screening in protein engineering: Recent advances and future perspectives*. *Int. J. Mol. Sci.* **16**, 24918–24945 (2015)
- [5] P. Liigand, K. Kaupmees, A. Kruve, *Influence of the amino acid composition on the ionization efficiencies of small peptides*. *J. Mass Spectrom.* **6**, 481-487 (2019)

Fiber-based cavity optomechanics

Project P1706: Ultrasensitive force microscopy and cavity optomechanics using nanowire cantilevers

Project Leader: M. Poggio and F. Braakman

Collaborator: D. Jäger (SNI PhD Student)

Introduction

Nanoscale mechanical resonators such as thin membranes or nanowire crystals have the potential to uniquely enrich the capabilities of force microscopy. Currently, force microscopy techniques rely heavily on micron-sized cantilevers as force transducing elements, such as silicon beams or quartz tuning forks. In recent years, a new direction has emerged that replaces these conventional cantilevers with bottom-up grown nanoscale structures, such as carbon nanotubes or nanowires. Their small size and nearly defect-free crystal structures leads to potentially record force sensitivities, low mechanical losses and high operation frequencies. Several experiments have recently demonstrated the potential and versatility of this approach. In our own lab, we have demonstrated a new type of force microscopy using nanowires, in which we have shown sensitivity not only to the magnitude of forces, but also their direction [1].

Furthermore, nanomechanical resonators enable fundamental studies into the hybridization of different physical quantities, such as light and mechanical motion. Such hybrid systems form a promising platform to implement measurements operating at the limits imposed by quantum uncertainty and quantum non-demolition measurements. They may also allow investigation of quantum decoherence mechanisms, entanglement, and ultimately the transition from quantum to classical physics. We focus on two types of particularly interesting hybrid structures: nanowire heterostructures and 2D membranes with defects. Both systems can combine excellent mechanical properties with bright optically active qubits in the form of embedded quantum dots or crystal defects. These qubits themselves already form interesting objects of study, as they are potentially very sensitive meters of localized electric and strain fields [2]. Moreover, when coupled to a mechanical degree of freedom, qubits can through their nonlinear character generate very large enhancement of the radiation pressure interaction between light and matter, as well as boost optical cooling of the mechanical resonator [3].

Our aim is to enable operation of such hybrid systems in regimes dominated by quantum effects, by improving optical excitation and detection of the mechanical resonator and embedded quantum emitters. To reach this goal, we will:

1: Integrate such hybrid systems into high-finesse optical cavities. Read-out of both the mechanical motion and of the photons emitted by embedded quantum emitters can be much improved by placing the system inside an optical cavity. Moreover, such a cavity allows to strongly couple the motion as well as quantum emitters to the cavity light field. In particular, this provides a straightforward path to the realization of a tri-partite hybrid system [3]. Such a tri-partite

system allows to significantly enhance optical cooling and will allow the observation and utilization of quantum states of motion.

2: Implement resonant excitation of quantum emitters in a force microscopy setup. This will significantly reduce the optical linewidth of the dots and should allow for mechanical displacement sensitivity reaching the Heisenberg uncertainty limit.

Optical Setup

In previous years, we have constructed a table top optical setup that serves as the basic platform for our experiments.

The setup allows to insert two beams of light with tunable frequency difference into an optical cavity. The cavity can be measured through reflection or transmission and stabilized using a Pound-Drever-Hall scheme. This will enable basic optomechanical experiments, such as optical cooling of a mechanical oscillator, as well as basic cavity QED experiments, allowing the measurement of a tri-partite hybrid system.

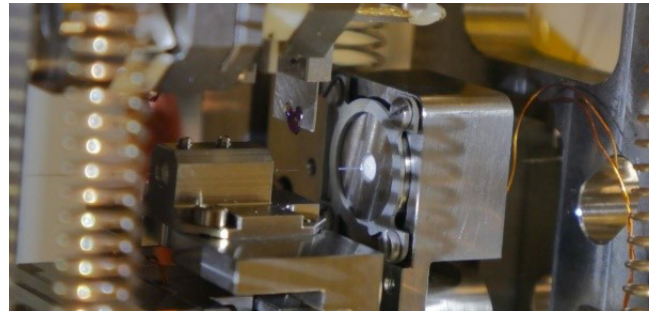


Fig. 1 A photograph of our fiber Fabry-Perot cavity mounted in a probe allowing operation at low temperature and vacuum.

This year we have adapted this setup to work in a cryostat at 4 K (Fig. 1). We have constructed a probe that allows us to control the alignment and length of our cavity in situ using piezoelectric actuators, while also improving its stability.

Using this new probe, we were able to cool down the cavity and retain its optical properties that we previously measured with our table top setup. In addition, we have implemented white light spectroscopy of our cavity to characterize its mode spectrum in a single shot.

Finally, we have added a confocal scanning microscope to this probe that allows us to characterize quantum emitters via spectroscopy and the properties of mechanical resonators using reflection measurements with a high-speed detector.

To excite the mechanical resonator a piezoelectric actuator can be used. In addition, we are working on a more local optical excitation using a second laser that is modulated with an acousto-optical modulator.

Membranes

As a first step towards creating a tri-partite hybrid system, we focus on membranes of hexagonal boron nitride (hBN), which has been shown to contain crystal defects that can serve as quantum emitters. These emitters are ultra-bright, highly stable and can be observed at room temperature [4]. In addition, hBN membranes are mechanical oscillators with favorable frequencies (MHz regime), low mass, and high quality factors.

We have successfully used high temperature annealing recipes to create quantum emitters, resulting in defects located at edges of the hBN flakes. Using this method, we were able to observe several of these emitters in spectroscopy measurements (Fig. 2).

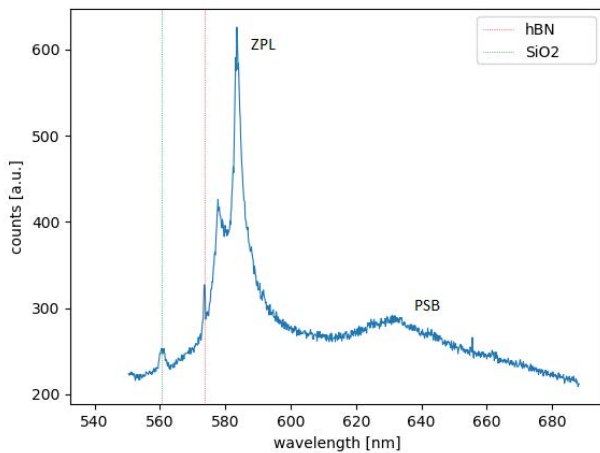


Fig. 2 Spectrum of an emitter found in an exfoliated and subsequently annealed hBN flake. The strong zero-phonon line emission is clearly visible next to a weak phonon sideband.

To use these flakes as mechanical resonators that can be placed inside our cavity, we have developed a wet transfer technique that allows us to place them on top of silicon nitride hole grids ('Holey membranes' manufactured by Norcada), resulting in hBN drum resonators (Fig. 3).

The emitters have to be placed in a location where the dynamic strain of the oscillator is high, and where they can be positioned well within the cavity field without introducing clipping losses. To this end we have tested methods to deterministically create these emitters. We have continued to investigate patterned holes created by a focused ion beam. It has been reported that emitters form with high fidelity at these patterned locations [5]. We are also investigating the possibility of other techniques to implant emitters away from boundaries, such as electron irradiation and plasma etching of the hBN flakes. Especially plasma etching has shown promising early results in creating a very high density of emitters with some of them located towards the middle of the flake. With masking this could also be used to pattern the resonator or to only create emitters in certain locations. Plasma treatment can also help to reduce fluorescent background emission caused by impurities.

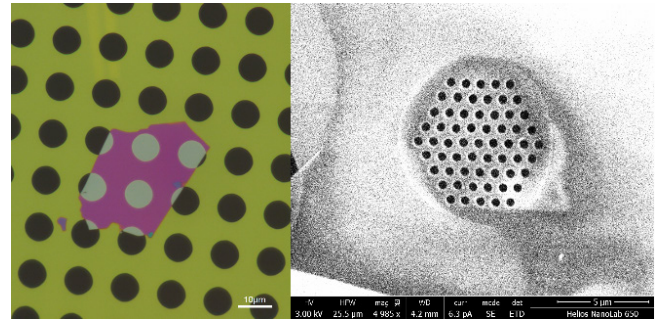


Fig. 3 Optical microscope image of hBN drum resonator (left). SEM image of a patterned hBN flake spanning across a hole in a silicon nitride membrane, creating a drum resonator (right).

More recently we started investigating the optical and mechanical properties of these emitters and hBN resonators with our low temperature confocal setup and we are in the process of combining these hBN devices with our optical cavity.

Outlook

Building on these results, our next steps will be to:

- insert an hBN membrane into a fiber based optical cavity and measure the optomechanical coupling strength.
- measure strain-mediated coupling between hBN flake motion and an embedded emitter at low temperature using our confocal setup.
- engineer mechanical properties of hBN drum resonators using custom made Norcada silicon nitride membranes.
- develop a fabrication procedure to deterministically position quantum emitters in our hBN resonators.

References

- [1] N. Rossi, F. R. Braakman, D. Cadeddu, D. Vasyukov, G. Tütüncüoğlu, A. Fontcuberta i Morral, M. Poggio, *Vectorial scanning force microscopy using a nanowire sensor*, Nat. Nanotechnol. **12**, 150 (2017)
- [2] M. Montinaro, G. Wüst, M. Munsch, Y. Fontana, E. Russo-Averchi, M. Heiss, A. Fontcuberta i Morral, R. J. Warburton, M. Poggio, *Quantum dot opto-mechanics in a fully self-assembled nanowire*, Nano Lett. **14**, 4454 (2014)
- [3] J. Restrepo, C. Ciuti, I. Favero, *Single-Polariton Optomechanics*, Phys. Rev. Lett. **112**, 013601 (2014)
- [4] T. Tran, K. Bray, M. Fordet al., *Quantum emission from hexagonal boron nitride*, Nat. Nanotechnol. **11**, 37–41 (2016)
- [5] J. Ziegler, R. Klaiß, A. Blaikie, D. Miller, V. R. Horowitz, B. J. Alemán, *Deterministic Quantum Emitter Formation in Hexagonal Boron Nitride via Controlled Edge Creation*, Nano Lett. **19** (3), 2121-2127 (2019)

Giant Stark splitting of an exciton in bilayer MoS₂

Project P1707: Nano-photonics with van der Waals heterostructures
 Project Leader: R. J. Warburton and I. Zardo
 Collaborators: L. Sponfeldner (SNI PhD Student) and N. Leisgang

Transition metal dichalcogenides (TMDs) constitute a versatile platform for atomically thin optoelectronic devices and spin-valley memory applications. In monolayers, optical absorption is strong, but the transition energy is essentially not tunable as the neutral exciton has no out-of-plane electric dipole [1]. In contrast, interlayer exciton transition energies in heterobilayers are widely tunable in applied electric fields, but their coupling to light is considerably reduced. In homobilayer MoS₂, the situation is potentially different: Recent studies have shown a strong absorption feature up to room temperature, interpreted as an interlayer exciton [2].

Our experiments focused on momentum-direct excitonic transitions at the K point. Excitons in bilayer TMDs can be sorted into two categories: Intralayer and interlayer excitons. Intralayer A- and B-excitons consist of an electron and a hole located in the same MoS₂ layer. The interlayer A-exciton IE₁ (IE₂) consists of an electron state localised in layer L₁ (L₂) and a hole hybridised across both [2] (Fig. 1a). We show a tuning over 120 meV of interlayer excitons (IE) in bilayer MoS₂ due to their large in-built electric dipole. Additionally, we probe the interaction between intra- and interlayer excitons [3].

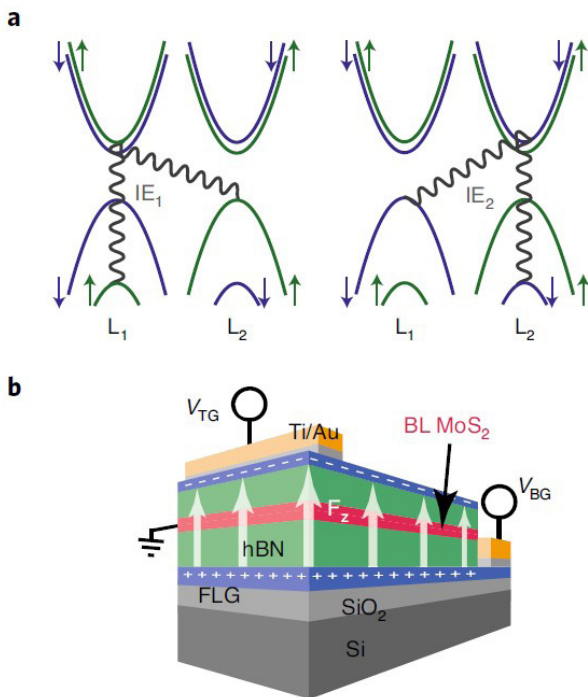


Fig. 1 a) Band structure and schematics of intralayer excitons in bilayer MoS₂ at the K point. b) Schematic of the studied van der Waals heterostructure consisting of contacted homobilayer MoS₂ encapsulated in hBN.

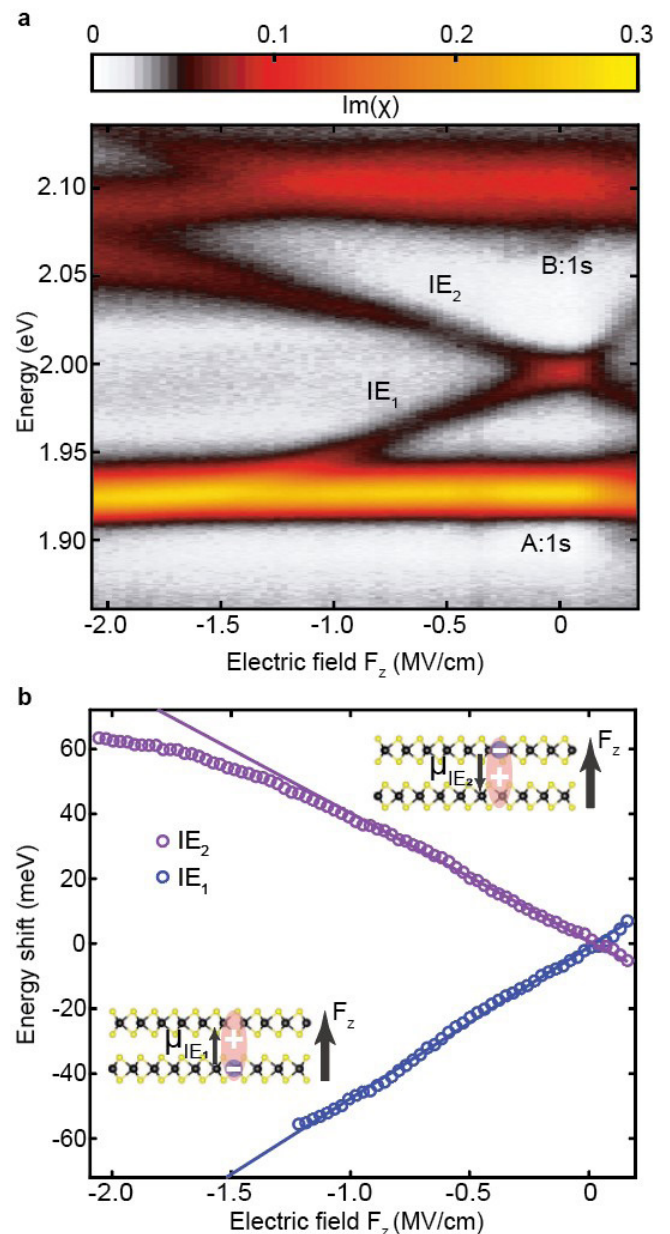


Fig. 2 a) Absorption of bilayer MoS₂ as a function of the applied electric field F_z. Im(χ) is the imaginary part of the optical susceptibility, a measure of the absorption strength. b) Interlayer exciton energies extracted from the spectra shown in a). The solid lines are linear fits to the data. The insets show the spatial extension of the interlayer excitons. The dipole moment μ is determined by the slope of the linear fit.

We study the semiconducting transition-metal dichalcogenide (TMD) homobilayer MoS_2 . The structure of our sample is shown in figure 1b. An electrically grounded homobilayer of MoS_2 is encapsulated in hBN. The electric field F_z across the device is controlled by applying voltages to the top and bottom electrodes.

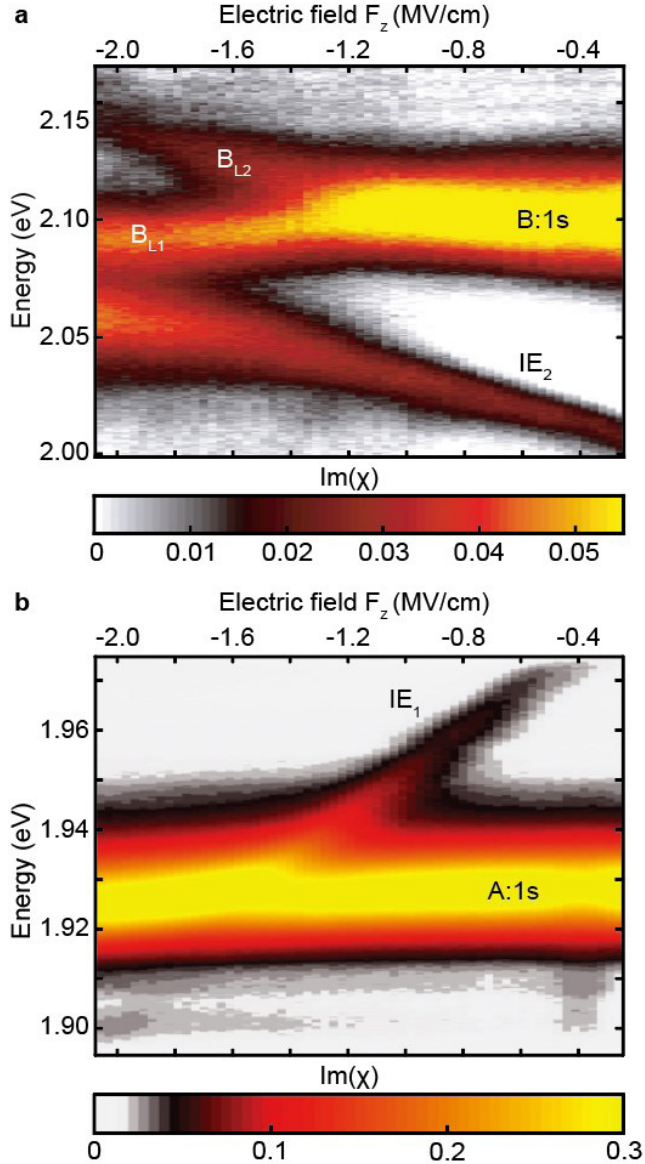


Fig. 3 Absorption of homobilayer MoS_2 as a function of applied electric field F_z . a) centred around the B-exciton and, b) centred around the A-exciton highlighting the different nature of exciton-exciton interaction.

The excitonic transitions are probed optically with absorption spectroscopy. Figure 2a shows the absorption of bilayer MoS_2 as a function of the applied electric field F_z . Three resonances can be identified at zero electric field: The intralayer A- and B-excitons at 1.93 eV and 2.10 eV, respectively, and the interlayer A-exciton IE. Applying an electric field leads to a splitting of the IE into two clear resonances. The degeneracy between IE_1 and IE_2 is lifted due to their opposing dipole moments μ , see insets of figure 2b. The extracted transition energies of the interlayer excitons are shown in figure 2b. For small-to-moderate fields the energetic shifts are linear, indicating a first-order Stark shift due to a static dipole moment of each IE. The solid purple and blue lines in figure 2b

are linear fits to the IE energies. We extract a dipole moment of $\mu\text{IE}_1 = 0.47 e \text{ nm}$ and $\mu\text{IE}_2 = -0.39 e \text{ nm}$ with e being the electron charge. This experiment confirms the microscopic picture in figure 1a and proposed originally in Ref. [2]: The electron is confined to either layer, the hole delocalized across both.

As F_z is increased further, the interlayer excitons are energetically brought close to resonance with the intralayer exciton states. While the interaction of IE_1 with the intralayer A-exciton is comparably weak (compare Fig. 3b), we observe a clear avoided crossing of the blue-shifted interlayer exciton with the intralayer B-exciton (compare Fig. 3a), indicating a strong mixing between the two different states. The intensity evolution of each resonance behaves quite differently for the IE_2 -B and IE_1 -A crossing. Most strikingly, the IE_1 resonance is strong on the high energy side of the A-exciton and barely visible on the low energy side.

The excitonic interaction is well-described by a model of two coupled optical dipoles with different oscillator strength driven by a light field. Applying the model to the excitonic absorption reveals the nature of the excitonic coupling, attractive or repulsive. While the interlayer excitons interact attractively with the A-excitons, they interact repulsively with the B-excitons. Our model also predicts constructive interference in one eigenmode ("bright"), destructive interference in the other eigenmode ("dark"), near the energetic crossing of the bare states. We argue that this is a general feature of coupled excitons.

In summary, the interlayer exciton in homobilayer MoS_2 possesses both a high oscillator strength and a large in-built electric dipole moment. For optoelectronics, these highly tunable excitonic transitions hold great promise for non-linear optics with polaritons on account of strong exciton-exciton interactions. Additionally, homobilayer MoS_2 is a remarkable system where one observes inter- and intralayer exciton interactions of opposite nature.

References

- [1] J. G. Roch, N. Leisgang, G. Froehlicher, P. Makk, K. Watanabe, T. Taniguchi, C. Schönerberger, R. J. Warburton, *Quantum-Confined Stark Effect in a MoS_2 Monolayer van der Waals Heterostructure*. *Nano Lett.* **18**, 1070-1074 (2018)
- [2] I. C. Gerber et al. *Interlayer excitons in bilayer MoS_2 with strong oscillator strength up to room temperature*. *Phys. Rev. B* **99**, 035443 (2019)
- [3] N. Leisgang, S. Shree, I. Paradisanos, L. Sponfeldner, L. et al. *Giant Stark splitting of an exciton in bilayer MoS_2* . *Nat. Nanotechnol.* **15**, 901-907 (2020)

Freeform optical structure

Project P1708: Non-visual effects of LED lighting on humans

Project Leader: E. Meyer and R. Ferrini

Collaborator: T. Aderneuer (Associate SNI PhD Student)

The potential for freeform optical microstructures (FFOMS) has been demonstrated in application such as automotive lighting, aerospace, augmented reality, and precision engineering.

As a result of their asymmetric shapes, FFOMS can overcome several severe limitations of the more standard spherical and aspherical (symmetrical) microlenses [1]. For example, in imaging optical systems FFOMS can handle optical aberrations more effectively and produce larger fields of view and can produce asymmetric light distributions in non-imaging systems. Oftentimes these performance improvements come together with a system simplification in the form of a reduction in the number of required optical components.

Recent advances in precision manufacturing have enabled the realization of complex microstructuring at industrially relevant volumes triggering industrial interest in and boosting demand for FFOMS [2]. Prominent precision microstructuring technologies are for example, ultra-fast laser ablation, grayscale laser photolithography, two-photon polymerization and ultra-precision (fast tool servo) diamond micromachining.

As a flip side, the more intricate surface profiles of FFOMS poses challenging demands on surface representation and sample characterization [3]. The lack of efficient and reliable inspection processes will hinder further progress in manufacturing, discourage optical designers from using them and ultimately make the future of the FFOMS technology uncertain.

Reverse engineering of freeform optics

Manufacturing deviations, with respect to the nominal designs, often translate in performance degradation. The ability to quantify it is fundamental to identify which deviations need to be corrected and which ones have only a negligible (or at least acceptable) impact.

On the other hand, contrary to the more standard symmetric microlenses, characterized by relatively few and well-understood parameters (sag, radius of curvature, conic constant, etc.), the description of freeform surfaces typically requires a much larger parameter space or even non-parametric representations.

Therefore, surface profilometry on its own is of limited help. On the other hand, because of the (typically) small area of prototypes, the experimental testing of the FFOMS optical performance is prone to large experimental errors and often, simply unfeasible.

We have demonstrated a method to accurately predict the optical functionality from experimentally measured surface topology.

Firstly, the measured profile, given in the form of point clouds, is fitted to a NURBS surface. This representation has the following advantages:

- It can represent complex surfaces using a manageably low amount of data
- it is widely implemented in CAD and optical simulation software tools
- it enables (contrary to e.g., analytical expressions) the representation of local deformations (i.e., manufacturing deviations).

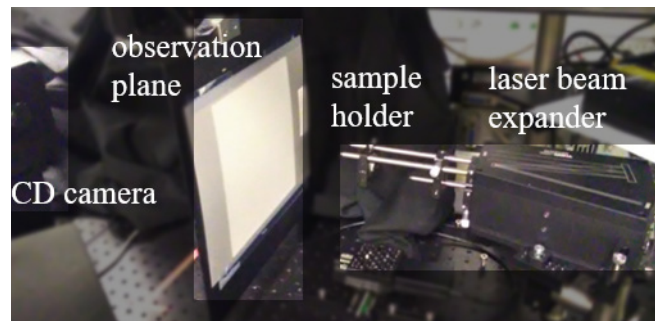


Fig. 1 Optical setup used to measure the illuminance distribution produced by precisely illuminated FFOMS. The setup comprises a laser light source, a beam expander, a sample holder, an observation plane (Lambertian diffuser), and a CCD luminance camera.

In a second step, the NURBS surface is used to build a 3D ray-traceable CAD model whose performance can therefore be predicted through optical simulations.

This approach to convert measured surface topology into a 3D CAD model, widely applied in the field of mechanical engineering (reverse engineering), is however, much less exploited for optical applications.

Comparison between predicted and measured optical performance

To validate the predictions provided by the described method (Fig. 2), we have compared them to the performance experimentally measured in the optical bench (Fig. 3).

The experimental setup contains of a laser light source, a beam expander, a sample holder, an observation plain, and a CCD camera. The beam is restricted to a size of 2 mm diameter that hits the freeform sample, the redirected light distribution on the target plan is measured by the CCD camera.

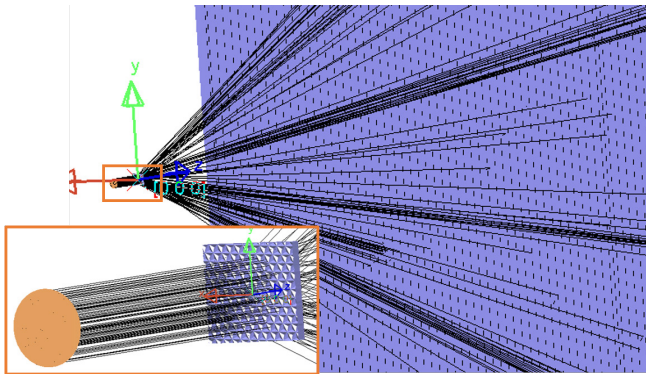


Fig. 2 Raytracing of the 3D CAD-model under same conditions used in the experimental characterization. The simulations were performed using LightTools. The rays are shown in black. The inset shows the collimated light source.

These experimental conditions are strictly reproduced in the optical simulation software. This way, the simulated light distributions can be compared with those recorded by the CCD camera.

We selected FFOMS used in a commercially available deglaring thin-film solution. The light distributions (predicted and measured) are shown in figure 3.

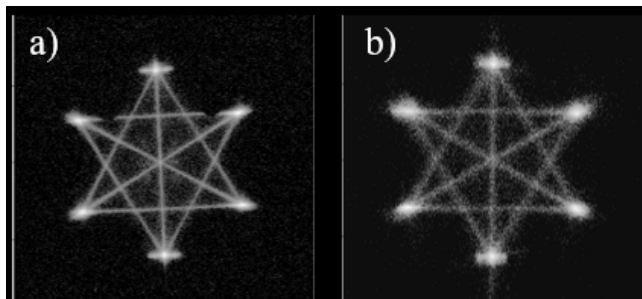


Fig. 3 Illuminance distributions provided by the deglaring FFOMS. The relative illumination is displayed in logarithmic scale to visualize dim features. a) Measured; b) Predicted.

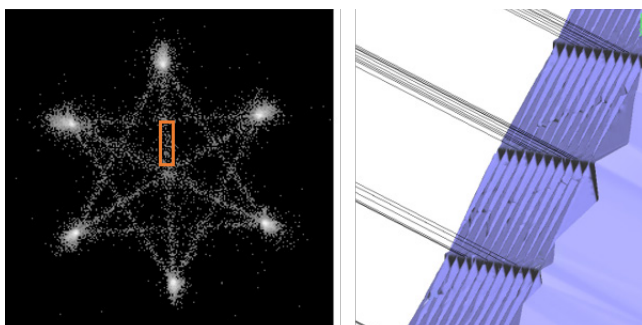


Fig. 4 The selected area (orange rectangle) on the observation plane is linked by back-tracing to the responsible geometry of the freeform surface. It shows that the edges of the surface redirect the light to the selected part on the observation plane.

As mentioned earlier, the ultimate objective is to identify, and subsequently correct, the problematic deviations; in our

example, those responsible of the light between the (hexagonally distributed) hotspots (red square in Fig. 4).

Simulations (Analysis in a region) indicate that the edges or the micropyramids are responsible for the light redirection to the selected area. This is a valuable information to improve manufacturing if the observed broadening needs to be minimized.

Conclusion

We have presented and validated an effective method that exploits the recent advances in surface topology to rapidly identify problematic manufacturing deviations then speeding-up the manufacturing of FFOMS.

The described method can accurately simulate and successfully predict the optical performance of manufactured freeform microstructures without confronting the limitations of experimental optical setups.

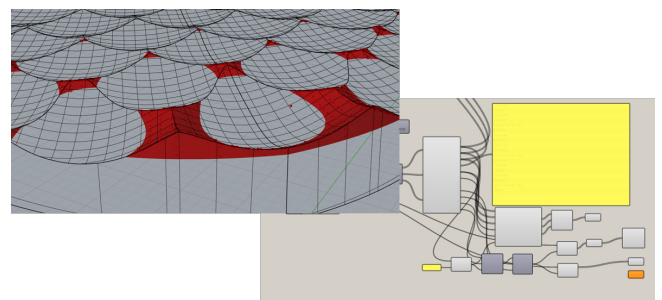


Fig. 5 Left: Optical design with user specified height analysis. Right: Script to read out geometrical properties.

Outlook

A further challenge for FFOMS technology is to analyze designs upon their manufacturability. The fabrication process of FFOMS is complex and typically includes multiple steps such as design, mastering, tooling, up-scaling, and replication; all with certain (different) limits.

We aim to implement design for manufacturing tools that enable optical designers to implement these limitations at the design phase in order to avoid costly and time-consuming trial and error steps. A first trial is shown in figure 5 which shows a script programmed to automatically extract the height distribution of a freeform microlens array.

References

- [1] F. Z. Fang, X. D. Zhang, A. Weckenmann, G. X. Zhang, C. Evans, *Manufacturing and measurement of freeform optics*. CIRP Annals **62**, 823–846 (2013)
- [2] T. Gissibl, S. Thiele, A. Herkommer, H. Giessen, *Sub-micrometre accurate free-form optics by three-dimensional printing on single-mode fibres*. Nat. Communicat. **7**, 11763 (2016)
- [3] X. Jane Jiang, P. Scott, *Advanced Metrology: Freeform surfaces*, (Academic Press, Oxford, 2020)

Nano-sized plasma membrane vesicles as an emerging EV platform for therapeutic applications

Project P1801: Bioinspired nanoscale drug delivery systems for efficient targeting and safe in vivo application

Project Leader: J. Huwyler and C. Palivan

Collaborator: C. Alter (SNI PhD Student)

Introduction

Extracellular vesicles (EV) are extremely important for the new era of bio-pharmaceutical engineering due to their potential for therapeutic applications. EVs, which are secreted by cells, are hollow sphere lipid vesicles equipped with proteins, encapsulate nucleic acids (i.e. mRNA and DNA), and are classified into two classes: exosomes and apoptotic bodies (ApoBDs) [1]. In the human body, ApoBDs are rapidly cleared by professional and non-professional phagocytes via a process called “efferocytosis” to remain tissue homeostasis [2]. Therapeutic nucleic acids, proteins or small molecular weight drugs were loaded exogenously into EVs and successfully delivered to cells in vitro and in vivo, but only few EV technologies have progressed into clinical trials. Indubitably, one of the major drawbacks for clinical translation is the EV production. Typical EV secretion rates range between 60 – 170 exosomes/cell/hour, depending on the cell line [3].

A valuable alternative to the standard EV production protocol, which can be applied to nearly all cell lines, is based on the generation of chemically induced ApoBDs (vesicles). The vesicles are harvested and processed by size homogenization into nano-sized plasma membrane vesicles (nPMVs). Bioactive molecules in EVs can be recognized by other cells, similar to liposomes.

Material and methods

Chemical vesiculation agents were used to induce apoptosis and membrane blebbing in Huh7 cells. The blebbing process started few minutes after incubation (37°C and 5% CO₂) and the produced ApoBDs/GPMVs (blebs) were harvested from donor cells after 6 hours (Fig. 1 A).

To produce nanosized particles we stained GPMVs with a lipophilic dye (DiI) and homogenized (Fig. 1 B). In addition, we observed biomolecule decoration of nPMVs in Cryo-TEM (Fig. 1 C).

Results and discussion

DiI labeled nPMVs derived from Huh7 were incubated on Huh7 cells for 15 minutes, 1, 4, and 24 hours. The uptake of these fluorescently labeled nanoparticles was measured by fluorescence activated cell sorting (FACS) and confocal laser scanning microscopy (CLSM). We observed a time-dependent uptake (RFU). The uptake was fast in the first 4 hours, then started to saturate and reached the highest value after 24 hours. In a next experiment, we incubated DiI labeled Huh7 derived nPMVs, DOPC:PS, and DOPC liposomes on Huh7, HepG2, and THP-1 M0 macrophages for 4 hours. In the non-professional phagocyte cell line Huh7 and tissue cell line HepG2 we observed an extremely low uptake of DOPC liposomes.

Conclusion

We were able to produce high yields of cell derived nPMVs from Huh7 cells with our vesiculation technique, processing, and purification steps. Furthermore, we observed a fast and efficient uptake of homogenized nanovesicles in all tested cell lines. These results offer new perspectives for the design of novel EV based therapeutic systems.

References

- [1] G. van Niel, G. D’Angelo, G. Raposo, *Shedding light on the cell biology of extracellular vesicles*, Nat. Rev. Mol. Cell Biol. **19**, 213–228 (2018)
- [2] M. R. Elliott, K. S. Ravichandran, *The Dynamics of Apoptotic Cell Clearance*. Dev. Cell **38**, 147–160 (2016)
- [3] Y. -J. Chiu, W. Cai, Y.-R. V. Shih, I. Lian, Y.-H. Lo, *A Single-Cell Assay for Time Lapse Studies of Exosome Secretion and Cell Behaviors*. Small **12**, 3658–3666 (2016)

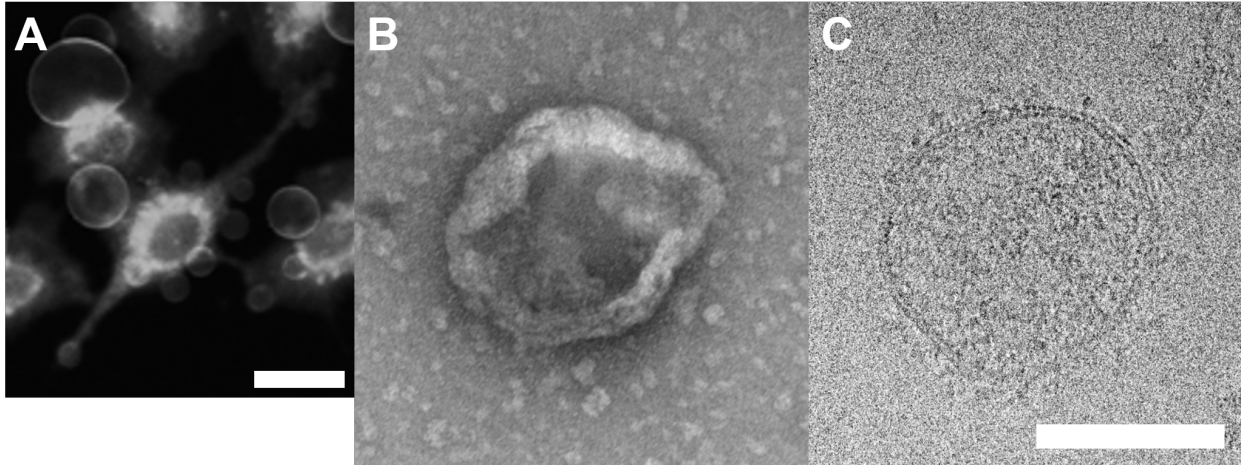


Fig. 1 A: Chemically induced vesicle formation on Huh7 cells. Scale bar = 10 μ m. B: TEM image of a nPMV. C: Cryo-TEM image revealed decoration of nPMVs with proteins. Scale bar = 100 nm.

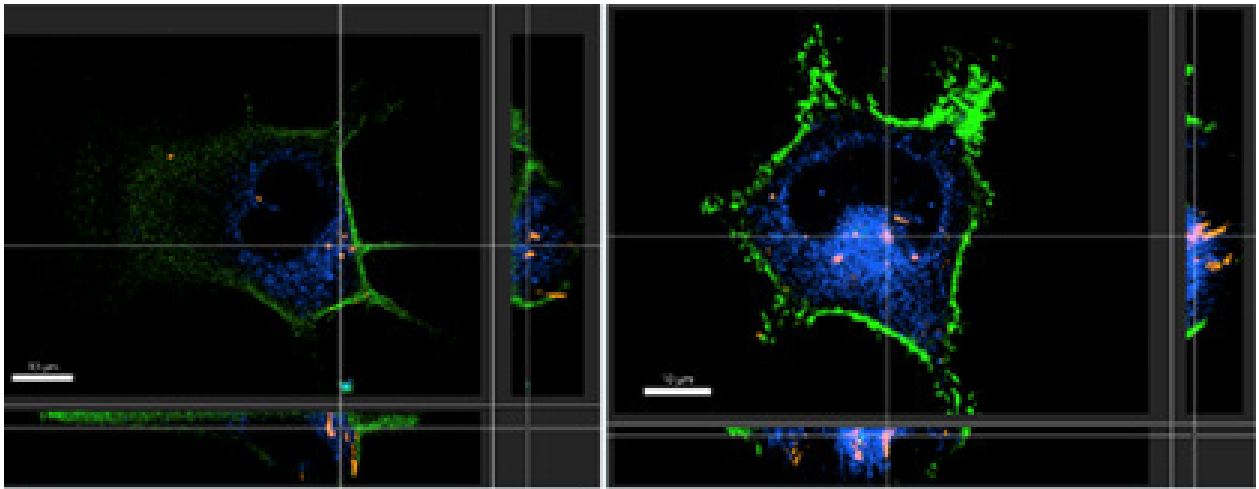


Fig. 2 Uptake of two different types observed in CLSM of nano-cell derived vesicles in the Huh7 cell line. Scale bar = 10 μ m.

Enhancing directed evolution with deep learning

Project P1802: From Schrödinger's equation to biology: Unsupervised quantum machine learning for directed evolution of anti-adhesive peptides

Project Leader: M. Nash and A. von Lilienfeld

Collaborator: V. Doffini (SNI PhD Student)

Introduction

The Covid-19 pandemic showed us that our deeply interconnected world is extremely vulnerable to highly contagious pathogens. In this context, viruses are not the only threat we might face in future epidemic scenarios. Specifically, bacteria that show antibiotic resistance characteristics are an enormous hazard to humanity, and this topic has garnered increased interest from across the biomedical research community in recent years. It is crucial to explore new strategies to fight against antibiotic resistant pathogens and develop new pharmacological treatments.

In our project, we focus on a specific class of microbes which use specialized surface proteins called adhesins to bind human tissue and spread the infection inside the host. The detailed structure and mechanism behind many such bacterial binding adhesin domains are known, while for others no structural information is available. Such adhesins typically bind short peptide sequences located on abundant blood or cell-surface proteins of the intended host (Fig. 1). The goal of our project is to identify novel peptide candidates which bind strongly to the bacterial adhesin of the pathogen agent, inhibiting it from attaching to the host's cells.

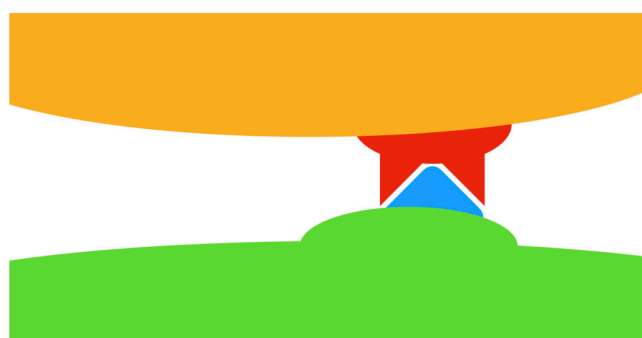


Fig. 1 Schematic representation of the binding between the pathogen (in orange) and the human cell (green). The binding protein of the microorganism is highlighted in red, while the attach site of the human cell is shown in blue.

By using state of the art technologies like deep mutational scanning and next generation sequencing, it is already possible to generate data for millions of different peptide variants in a relative short amount of time. Despite the fact that this might sound like a lot of data, they cover just a minimal fraction of the enormous space of possible amino acid combinations, even for small chains. For example, even for a peptide of a couple dozen amino acids, the number of total possible combinations are many orders of magnitude greater than the stars in the whole universe. Practically, this problem usually leads to a repetitive approach, called directed evolu-

tion, where mutations are screened and ranked based on a fitness function. In our case, the fitness function would be a measure of the binding strength between the adhesin protein and the peptide. After this first screening, the best mutations are selected, fixed and millions of new variants are produced changing the amino acids on the other positions. Afterwards, the new variants are screened and ranked again and the procedure is repeated for many iterations until an optimum is reached. Unfortunately, such protocol is not exempt from criticism; firstly, by exploring just single point mutations it is likely to get stuck on a local optimum instead of finding the global one; and secondly, since the presented protocol needs to be repeated multiple times, the burden of experiments needed is still high and it impacts negatively the time, resources and costs involved.

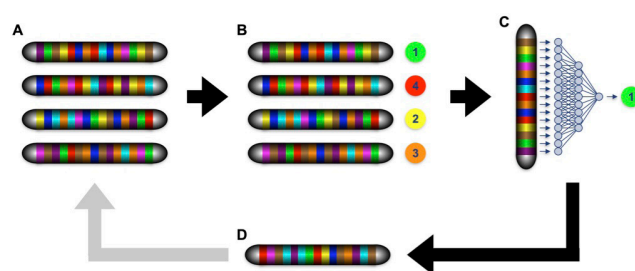


Fig. 2 Schematic representation of deep learning enhanced directed evolution. Starting from the upper left, a library containing many mutants is synthesized (A). Then, the different variants are sequenced and sorted based on a chosen fitness output (B). After that, a neural network is trained to connect the specific sequences to the fitness variable (C). Finally, the model is used to perform in-silico screening of new variants. The best candidates are synthesized in the lab (D) and, eventually, added to the library for a new iteration.

In order to increase the efficiency as well as the accuracy of directed evolution, we propose a deep learning assisted approach (Fig. 2). Such a methodology is still based on screening and ranking peptides, but in this case a deep neural network is fitted to connect the specific amino acid residues to the corresponding fitness function value. If successful, the deep neural network can be used to screen in-silico many more variants than are available experimentally, giving the possibility to efficiently find the maximum of the fitness function without the need of many iterations as in the "classical" directed evolution approach. Moreover, since we are not anymore constrained by fixing the single best mutations found in the previous screening, the fitness maximum we reach using this modified methodology should theoretically be the global one.

Material and methods

In the first part of the project, we focused on the synthesis and fluorescent labeling of one of the binding proteins of a pathogenic organism as well as the production of an E. Coli library. This library contains millions of bacteria, where each of the individual cells displays on its surface a randomized peptide of defined length. By tuning the time, temperature and inducer concentration following a three-dimensional central composite design, we were able to find satisfactory conditions for the peptide display on the E. Coli cell surface. This library was then screened using the bacterial adhesin labelled with a fluorescent dye molecule (Fig. 3). Peptides that strongly bind the adhesin will keep the fluorescent label after washing. The fluorescent intensity is detected by flow cytometry analysis and the cells are sorted, isolated and enriched for positive binders.

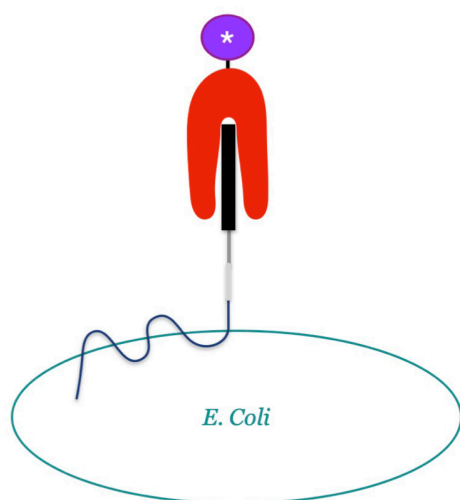


Fig. 3 Schematic representation of the binding between the protein of the pathogenic organism (in red) and one of the randomized peptides (in black) displayed on the cell surface of an E. Coli. The fluorescent label is shown in violet.

Results and discussion

Here we present one of the preliminary screens of our peptide library. Flow cytometry analysis clearly shows the vast majority of randomized peptides do not bind the labelled protein as indicated by most cells appearing in the left part of the plot in figure 4. Nevertheless, by looking on the upper right quadrant of the same figure, one could see that there are candidate peptides that show binding activity. The linear correlation between binding and expression level is also a positive sign. Indeed, if the expression level of a surface displayed peptide variant that binds to the label protein increases, one should expect it to bind more of the adhesin.

Outlook

In the second part of this project the different peptides will be ranked and sequenced. The good candidates could be amplified in another screening to finally prove the binding with the labelled protein. Afterwards, the deep learning model will be trained on top of these data. Such step will be the most critical and challenging; firstly, there are many degrees of freedom, from the encoding strategies to the structure of the model; and secondly, the peculiar distribution, called Tweedie distribution, along the fitness function, where most of the data are zeros, is extremely difficult to describe by any machine learning model. Indeed, what could happen is that the neural network will always return zero independently on the input sequence given. As a matter of fact, such model will still be

able to correctly predict the fitness of most of the sequences but it would be completely useless. To overcome this behavior, new strategies will be necessary.

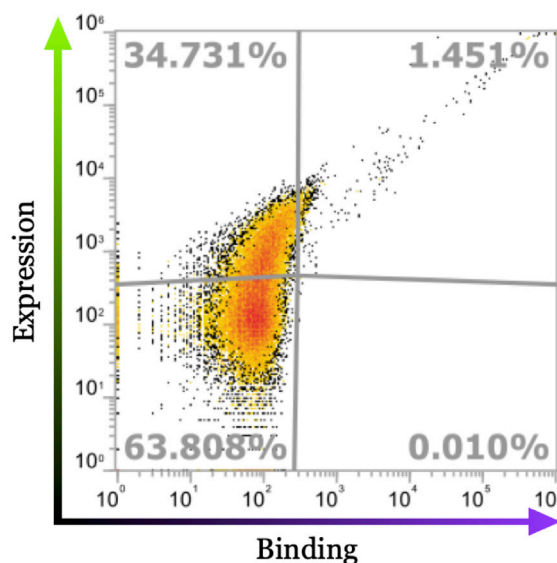


Fig. 4 Screening plot of the binding between the peptide library and the labelled protein of the pathogenic organism. Each point corresponds to one distinct peptide. On the abscissa is shown the binding strength while on the ordinate is the expression level or, in other words, how many peptides are displayed on the cell surface of the E. Coli.

References

- [1] R. Vanella, D. Tien Ta, M. A. Nash, *Enzyme-mediated hydrogel encapsulation of single cells for high-throughput screening and directed evolution of oxidoreductases*, *Biotechnology and Bioengineering*, **116(8)**, 1878–1886 (2019)
- [2] K. Yang, Z. Wu, F. Arnold, *Machine-learning-guided directed evolution for protein engineering*, *Nature Methods* **16(8)**, 687–694 (2019)
- [3] Z. Wu, S. B. J. Kan, R. D. Lewis, B. J. Wittmann, F. H. Arnold, *Machine learning-assisted directed protein evolution with combinatorial libraries*, *Proceedings of the National Academy of Sciences*, **116(18)**, 8852–8858 (2019)

Energy dissipation on suspended graphene

Project P1803: Nanoscale mechanical energy dissipation in quantum systems and 2D-materials
 Project Leader: E. Meyer and M. Poggio
 Collaborator: A. Ollier (SNI PhD Student)

Introduction

Surface deformations on graphene shows quantum dot-like (QD) behavior. Here, the sample is a circular free-standing graphene (FSG) sheet where the surface deformations have a 1D-ribbon-like (1DRG) shape. The measured dissipation exhibits single electron charging due to tip gating of the graphene nano-ribbons-like structures. When a tip is oscillating over a QD, this leads to charging and discharging events between the QD and the metallic substrate below. These effects are detectable using SPM methods. In the atomic force microscopy (AFM) this is seen as jumps in the frequency shift parabola followed by peaks in the dissipation curve [1]. Each peak corresponds to Coulomb rings (CR) in real space [2]. Here, we applied the pendulum AFM (p-AFM) to measure the dissipation. In this configuration, the very soft cantilever is positioned perpendicularly to the sample surface to avoid the snapping of the tip into contact. The p-AFM is few orders of magnitude more sensitive than normal AFM. The measurements were made under ultra-high vacuum and at a temperature of 5 K.

Single electron charging dissipation peaks

Figure 1 shows typical frequency shift and dissipation spectra recorded all over FSG. The black curve corresponds to the frequency shift and the red curve is the corresponding fit. The spectrum is characterized by the parabolic shape due to the capacitive force between the tip and the sample. In addition to the parabolic background, some jumps are visible at various bias voltages (arrows) [1]. These jumps are attributed to changes in the electrostatic force due to single electron charging i.e tunneling between the 1DRG-QD and the metallic substrate that serves as electron reservoir. This phenomenon is called Coulomb blockade (CB). The jumps in the frequency shift spectra are accompanied by peaks in the dissipation spectra, (blue curve).

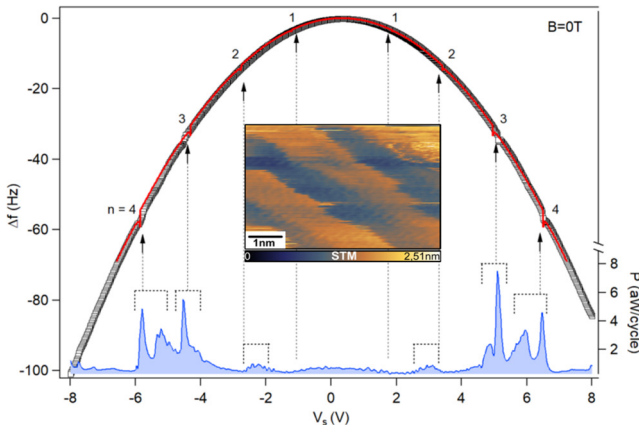


Fig. 1 Frequency shift and dissipation of the AFM cantilever as a function of the sample bias voltage. The arrows point to the jumps

of the frequency shift caused by single electron charging in the 1DRG-QD that appear as peaks on the dissipation curve. The inset is the STM image of the wrinkle on the free-standing graphene sheet.

Quantum capacitance

To better understand the physics behind these observations, a capacitance model was used to describe the system (Fig. 2a). The tip is represented by C_{tip} and the sample by $C_{sub}=C_Q+C_{par}$, where C_{par} is a parasitic capacitance that leads to the parabolic shape of the frequency shift and C_Q is the quantum capacitance. C_{tip} and C_{par} are geometric capacitances whereas C_Q is more complex. It was calculated according to the formula [3]:

$$C_Q = \frac{4e^2}{\pi\hbar v_f} \sum_n \frac{\eta}{\sqrt{\eta^2 - x_n^2}} \Theta(\eta - x_n) \quad (1)$$

where $\eta=E_t/kT$, $x_n=E_n/kT$, $E_n=(n\pi\hbar v_f)W$ and $\Theta(\dots)$ is the Heaviside unit step function. The effect of simulated C_Q for $W=2.25$ nm wrinkle is shown in figure 2b. The force can then be calculated according to the formula [1]:

$$F = \frac{1}{(C_{tip}+C_{sub})^2} \frac{\partial C_{tip}}{\partial z} \left(\frac{q^2}{2} - C_{sub}q(V - V_{CPD}) + \frac{1}{2} C_{sub}^2 (V - V_{CPD})^2 \right) \quad (2)$$

where $q=ne$ and V_{CPD} are the charge and the contact potential difference voltage, respectively. The frequency shift can finally be calculated and fit to the experimental data:

$$\Delta f(d) = \frac{f_0^2}{kA} \int_0^{1/f_0} F[d + A \cos(2\pi f_0 t)] \cos(2\pi f_0 t) dt + \Delta f_{par} \quad (3)$$

The experimental and simulated data are shown in black and red color respectively in figure 1 and figure 2b.

Magnetic field dependance

At 0 T the model can perfectly reproduce the experimental data (Fig. 2b). When a magnetic field B is applied, the dissipation peaks shift to lower voltages until they disappear at large magnetic field ($\sim 1,2$ T). To simulate the magnetic field effect a Peierls phase was added as suggested by J. Güttinger et al. [4]. Figure 3a shows the dissipation maps versus B . The vanishing of the peaks is clearly visible around $\pm 1,2$ T. The bright features marked by arrows correspond to the high dissipation peaks. They follow a linear behavior with respect to V_s following:

$$V_s = \frac{\hbar v_f}{2e\alpha} \left(\frac{2n\pi}{W} - BL \cos(\theta) \right) \quad (4)$$

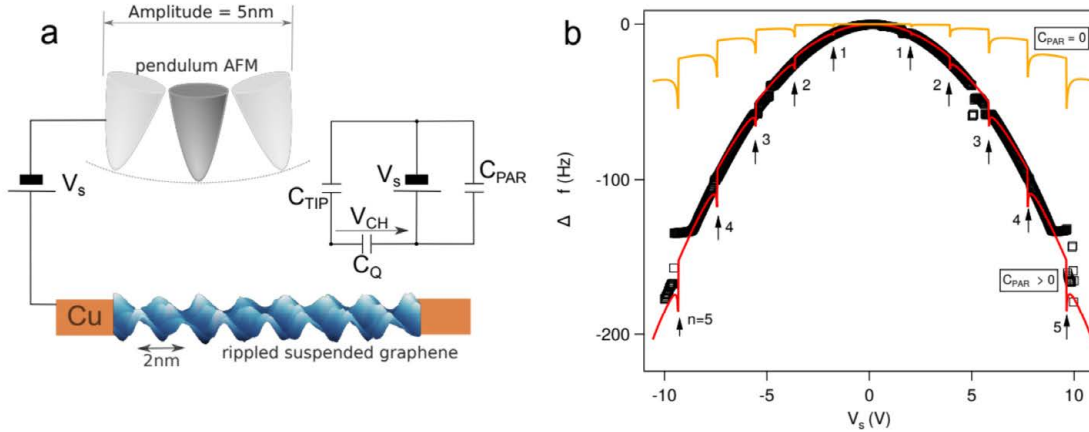


Fig. 2 Equivalent capacitance circuit and voltage dependent frequency shift spectra at $d=80$ nm distance over the surface. The schematic of the tip/sample geometry and the equivalent circuit is shown in (a). On (b) frequency shift parabola show the jumps caused by the electron charging in the 1DRG-QD. The black points are the experimental data, while the red line is the simulated Δf fit. The yellow curve is $C_{sub}=C_Q$ without the parasitic contribution.

According to the Bohr-Sommerfeld magnetic phase accumulation model, the de Broglie's wave of electrons moving inside the potential well is reflected from the wrinkle walls interface with an additional magnetically induced shift in the phase, the so called Peierls phase. For $B=0$ T we assume that the wavefunction leakage is negligible, namely an infinitely rigid quantum well. Figure 3b shows dissipation peaks for different B field and the Peierls phase is given for each spectrum. Its value enables to calculate CQ for each B field and reproduce the Δf curves. In the real space, dissipation peaks manifest as CR as presented on figure 3c. The sample bias is equal to $U=-7,84$ V. For $B=0$ T all the CR features are clearly visible. For $B=1$ T the features become less pronounced until they disappear completely for $B=2$ T.

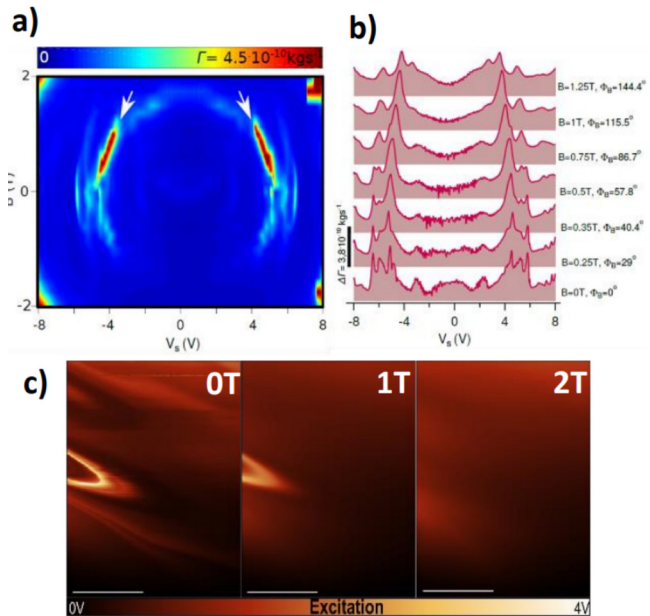


Fig. 3 Energy dissipation as a function of magnetic field changing in the range from -2 T to 2 T measured on the 1DRG-QD. The dissipation map versus B is presented in (a), where the arrows point out the high dissipation features with a linear behaviour. The Peierls phases used to simulate the magnetic field are given in (b) for every B field. (c) shows the CR at 0 T, 1 T and 2 T respectively. The scale bar is $1 \mu\text{m}$.

Conclusion

In conclusion, the measurements show that wrinkles in the free-standing graphene exhibit QDs like behavior. The detailed analysis showed that force and dissipation are sensitive to quantum capacitance of quasi-one-dimensional graphene. A quantum capacitance model enables us to describe and reproduce theoretically the measurements. Moreover, under magnetic field the measurements can be well fitted by adding a Peierls phase to the electronic wave-function.

References

- [1] R. Stomp, Y. Miyahara, S. Schaer, Q. Sun, H. Guo, P. Grutter, S. Studeniki, P. Poole, A. Sachrajda, *Detection of single-electron charging in an individual InAs Quantum dot by noncontact atomic force microscopy*, PRL **94**, 056802 (2005)
- [2] L. Cockins, Y. Miyahara, S. D. Bennett, A. A. Clerk, S. Studenikin, P. Poole, A. Sachrajda, P. Grutter, *Energy levels of few-electron quantum dots imaged and characterized by atomic force microscopy*, PNAS, **107**(21), 9496-9501 (2010)
- [3] T. Fang, A. Konar, H. Xing, D. Jena, *Carrier statistics and quantum capacitance of graphene sheets and ribbons*, App. Phys. Letters **91**, 092109 (2007)
- [4] J. Güttinger, C. Stampfer, F. Libisch, T. Frey, J. Burgdörfer, T. Ihn, K. Ensslin, *Electron-hole crossover in graphene quantum dots*, PRL **103**, 046810 (2009)

Picoscopic mass analysis of mammalian cells

Project P1804: Picoscopic Mass Analysis of Mammalian Cells

Project Leader: D. J. Müller, Ch. Gerber, and W. Meier

Collaborators: I. Incaviglia (SNI PhD Student), S. Herzog, and G. Fläschner

The accurate quantification of some basic physical observables in cell biology and physiology is currently limited by a lack of tools. One such observable is the cell mass. We have recently invented an AFM-based picobalance to directly measure the inertial mass of single mammalian cells¹. While optically observing the cell morphology and state the balance allows to measure the mass of adherent cells at ms time resolution over the time course of several days and at pg mass sensitivity. Now, fundamental standing questions in biology can be addressed by applying the picobalance. One such question is, how cells regulate growth (e.g. cell mass) throughout the cell cycle and whether this regulation is cell type specific. In other words, do epithelial cells, fibroblasts, parental and daughter cells or neurons regulate mass the same way throughout the cell cycle? And how different is the mass regulation between healthy and cancer cells, particularly since we already know that many cancer cells undergo unregulated growth? This project thus aims to further develop and apply the picobalance to address basic questions of how adherent cells regulate growth at a time and mass resolution hitherto unreachable by any other method. By combining nanoscience, biophysics and cell biology the project will establish the picoscopic cell balance technology for the characterization of cell physiological and homeostatic processes such as needed to address basic cellular problems in cell biology, physiology and medicine.

Working principle of the inertial picobalance

The inertial picobalance was recently introduced as a biophysical tool that can be used to non-invasively measure adherent cells at high mass and time resolution [1]. This cell balance constitutes of a silicon microcantilever which is mounted on an inverted optical microscope and operates under cell culture conditions (Fig. 1a). The microcantilever is actively actuated by a low-power intensity-modulated blue laser (405 nm, $\leq 50 \mu\text{W}$), which is focused at the base of the cantilever in order to generate very small oscillation amplitudes in the range of approximately 1–15 Å (Fig. 1b). When a cell is attached at the free end of the microcantilever, changes of the effective mass shifts the natural resonance frequency of the cantilever. These shifts in resonance frequency are tracked through a phase-locked loop (PLL) as feedback system and they are related to the change in mass of the attached cells.

Enhancing the inertial picobalance by extracting viscoelastic properties

To advance our biophysical understanding of the cell state, it is necessary to measure in addition to the mass, the cell mechanical parameters, such as cell stiffness and viscosity. Recently, it has been shown that the stiffness of the cell is an important parameter that for example affects the cellular differentiation, cancer metastasis, and cell spreading [2].

Thus, we refined the goal of this project to further develop the picobalance in order to simultaneously extract cell mass, cell stiffness and cell viscosity.

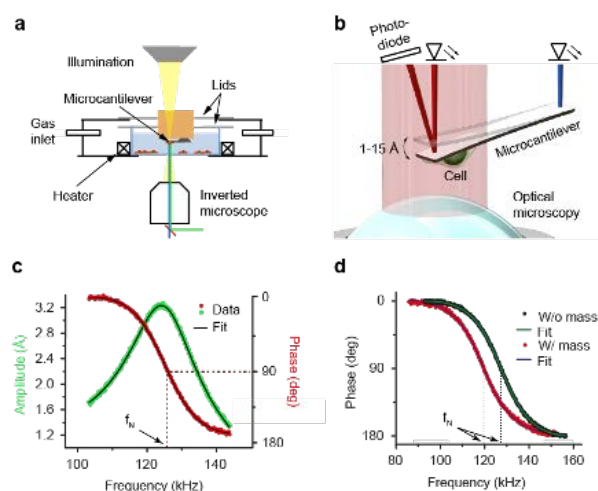


Fig. 1 Working principle of the picobalance. a) A mammalian cell is attached to a microcantilever and is placed in an environmental chamber, which regulates temperature, gas atmosphere and humidity to ensure cell culture conditions. b) To measure the mass of the cell, the cantilever is actuated by an intensity modulated blue laser at its natural resonance frequency (f_N). The movement of the cantilever is monitored by a second infrared laser. The cell can be microscopically observed at all times of the experiment. c) A typical cantilever amplitude (green) and phase (red) response of a micro-cantilever measured in cell culture medium is shown. The fit (thin black lines) re-presents a driven and damped harmonic oscillator model. d) Phase curves of a cantilever with (red) and without (black) a reference weight is shown. The shift of the resonance frequency is used to calculate the cell mass. Thin lines are fits.

Extracting additional parameters: continuous sweep mode

The microcantilever of our picobalance setup can be modelled as a two degrees-of-freedom system, which is characterized by the following relationship relating the Quality factor Q of the microcantilever to the cell stiffness k and viscosity D

$$Q = \frac{\sqrt{Mk}}{D}$$

M is the mass of the resonating microcantilever with the Q factor describing the damping of the resonator [3]. The Q factor, which is defined as the ratio of the energy applied to activate the resonator to the energy lost during one cycle of oscillation, can be extracted from the frequency spectrum curve of the microcantilever.

To gain deeper insight on the interplay between Q factor and stiffness changes, we performed finite element analysis (FEA) simulations where the mass and stiffness of a cell attached to the free-end of the microcantilever are varied systematically, while the resulting Q factors (Fig. 2a) and resonance frequency (Fig. 2b) of the microcantilever are being tracked. In both graphs it can be noticed that, for any given mass, varying the stiffness of the cell results in a change of the Q factor and Resonance frequency of the whole system.

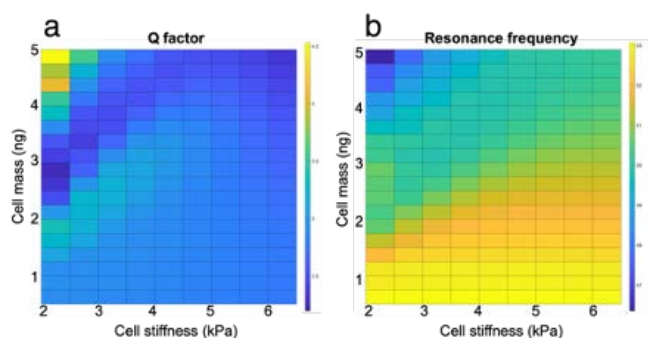


Fig. 2 FEA analysis of a resonating microcantilever having a cell attached to its free end. a) Q factor of the microcantilever versus varying cell mass and cell stiffness of a cell attached to the free end of the cantilever. b) Resonance frequency of the microcantilever versus varying cell mass and cell stiffness.

Fibroblasts measurements

In order to extract the Q factor from our mass measurements, we changed the recording of the microcantilever frequency from using a PLL mode to a continuous sweep mode. In fact, the PLL mode can only tracks resonance frequency shifts at a very high time resolution, whereas in the continuous sweep mode the entire frequency spectrum of the microcantilever is swept across a 20 kHz frequency range every 52 seconds, which is more suitable for our application. Then, a curve fitting of the amplitude response of the microcantilever is performed to obtain the resonance frequency and Q factor values. Using the continuous sweep mode, we screened different fibroblasts lines on a fibronectin substrate. In particular, we tested wild-type fibroblasts (Fig. 2), and the αV -pKO and $\alpha V\beta 1$ -pKO integrin pan-knockout fibroblasts, which have been previously described [4].

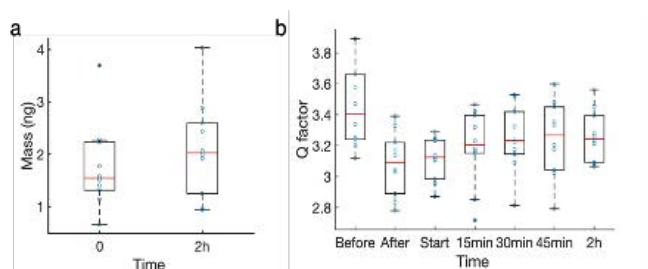


Fig. 3 Picobalance measurements of single fibroblasts adhering to the free end of the microcantilever. a) The mass of a single wild-type fibroblasts is recorded immediately after pick-up by the microcantilevers and after two hours. b) The Q factor of the microcantilever is recorded before the cell is picked up, after pick up, and for the consecutive two hours.

The preliminary measurements show an increase in mass for the fibroblasts of roughly ≈ 0.5 ng over a 2 h time range. More interestingly, the mass changes coincidence by a re-

duction of the Q factor during the first 15 minutes of the picobalance measurements. Currently we perform control measurements to clarify whether this Q factor reduction is due to a cell mass change, which at the moment we think is rather unlikely. If this is not the case we would have a first evidence that we can modify the picobalance to monitor the mass and the mechanical properties of single cells.

Challenges Ahead

The next steps of the project involve 1) relating the Q factor measurements to the mechanical properties through mathematical modelling, 2) performing control experiments in order to disentangle Q factor changes from cell mass changes, 3) performing control experiments to improve the mathematical model relating Q factor changes to cell mechanical properties, 4) addressing biological questions such as the role of different integrins on the regulation of stiffness and viscosity of cells.

References

- [1] D. Martínez-Martín, G. Fläschner, B. Gaub, S. Martin, R. Newton, C. Beerli, et al. *Inertial picobalance reveals fast mass fluctuations in mammalian cells*, *Nature*, **550**, 500–505 (2017)
- [2] K. Park, L. J. Millet, N. Kim, H. Li, X. Jin, G. Popescu, et al. . *Measurement of adherent cell mass and growth (supplementary)*. *Proceedings of the National Academy of Sciences*, **107**, 20691–20696 (2010)
- [3] I. Hickman, *Analog Electronics: Analog Circuitry Explained*, Newnes. p. 42. (2013)
- [4] P. M. Spoerri, N. Strohmeyer, Z. Sun, R. Fässler, D. J. Müller, *Protease-activated receptor signalling initiates $\alpha 5\beta 1$ -integrin-mediated adhesion in non-haematopoietic cells*, *Nature Materials*, **19**, 218-226 (2020)

Image the twist!

Project P1806: Image the twist!

Project Leader: V. Scagnoli and P. Maletinsky

Collaborators: S. Treves (SNI PhD Student), J. White, D. Grundler, K. Wagner, and V. Ukleev

Introduction and motivation

A skyrmion is a topological nanomagnetic configuration comprised of magnetic moments which point radially away from a centre point, similar to that of the spines a hedgehog. Experimentally skyrmions were observed over a decade ago using neutron diffraction [1] and since have been imaged in 2D using various other techniques in a handful of materials [2, 3, 4, 5, 6]. Skyrmion-hosting materials are interesting as they could one day be used to make race track magnetic memory devices [7]. These are non-volatile, solid-state memory which would improve computing storage and processing speed over the state-of-the-art. In order for such devices to become a reality, however, the physics of skyrmions must be fully understood, including their interactions with each other, their formation and annihilation events.

In this project, we will be using a nanoscale, 3D magnetic tomographic imaging technique established recently by our group [8] to study the skyrmion systems using x-rays. This will allow for a fundamental investigation of static and dynamic formation of skyrmion lattices in three-dimensions. Further studies of the dynamics will be conducted using a Nitrogen-Vacancy (NV) setup, which comprises of a single, electronic spin magnetometer, embedded in a diamond scanning probe.

In the first year of this project, we have successfully simulated the skyrmion hosting material $\text{Co}_9\text{Zn}_3\text{Mn}_2$ and its stray fields in three-dimensions; we have also started to characterise samples, in order to determine the best temperature and magnetic field range where the tomography experiment could be performed.

Key experimental results

During the first year of this project, the focus has been on simulations and the characterisation of available crystals. At the time of writing this report, the stray fields for $\text{Co}_9\text{Zn}_3\text{Mn}_2$ have been modelled in three-dimensions and the phase diagrams for $\text{Co}_8\text{Zn}_8\text{Mn}_4$ and $\text{Co}_8\text{Zn}_{10}\text{Mn}_2$ and Cu_2OSeO_3 have been measured.

The simulations revealed that a $\text{Co}_9\text{Zn}_3\text{Mn}_2$ crystal will have a skyrmion lattice which will form when there is a small magnetic field applied to the sample in a random magnetic configuration. These simulations are performed at 0 K, but give a good idea of how the system behaves at room temperature on a mesoscopic scale. From these simulations, images of the skyrmion lattice in 2D and 3D have been produced in addition to 3D images of the stray fields. Further study of the stray field data has allowed the production of graphs, which display how the stray field behaves as one moves away from the skyrmion. This information can then be input into an NV simulation software, which allows the best conditions to conduct NV spectroscopy experiments to be found.



Fig. 1 A close up of the stray field produced by the skyrmion phase in $\text{Co}_9\text{Zn}_3\text{Mn}_2$. These simulations allow for the determination of the stray field's strength at various positions along the surface. This information can then be used in NV simulations to predict the pattern expected from such a measurement.

In parallel, a $\text{Co}_8\text{Zn}_{10}\text{Mn}_2$ single crystal has been characterized using a superconducting quantum interference device (SQUID) magnetometer. We have been able to map the strength of the magnetic sample response as a function of temperature and magnetic field. Here it was found that a transition in magnetic susceptibility occurred at 355 K and so this measurement was followed up with multiple hysteresis loop measurements. This data is then interpolated to make a phase diagram, as seen in figure 2. From this diagram, we can visually see the region of temperature and magnetic field where the skyrmions will form (as marked by the red oval). Comparing these results to those found in [4], the skyrmion pocket in this material forms at very similar values of temperature and magnetic field to that in the literature. This information is important to establish which sample composition would be most suitable for our experiments.

Outlook

The simulations that have been produced in the current stage of the project will help to lay the groundwork for future experiments on the $\text{Co}_9\text{Zn}_3\text{Mn}_2$ crystals. Such experiments include NV magnetometry and X-ray laminography at the Pollux beamline of the Swiss Light Source at the PSI. The magnetometry work conducted on the Cu_2OSeO_3 crystal will help to understand the system better when it comes to X-ray diffraction experiments at beamlines such as the Diamond light source. All of these future measurements will allow the study of skyrmion hosting systems in three-dimensions in static and dynamical settings.

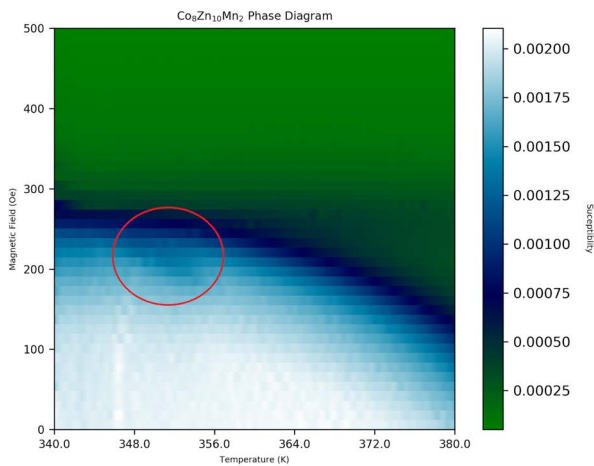


Fig. 2 Phase diagram of $\text{Co}_8\text{Zn}_{10}\text{Mn}_2$. The skyrmion phase pocket can be seen marked by the red oval starting at 348 K. The identification of the skyrmion pocket can be confirmed by comparing this data to that in [4].

References

- [1] S. Mühlbauer, B. Binz, F. Jonietz, C. Pfleiderer, A. Rosch, A. Neubauer, R. Georgii, P. Boni, *Skyrmion Lattice in a Chiral Magnet*, *Science* **323**, 915 (2009)
- [2] W. Münzer, A. Neubauer, T. Adams, S. Mühlbauer, C. Franz, F. Jonietz, R. Georgii, P. Böni, B. Pedersen, M. Schmidt, A. Rosch, C. Pfleiderer, *Skyrmion lattice in the doped semiconductor $\text{Fe}_{1-x}\text{Co}_x\text{Si}$* , *Phys. Rev. B* **81**, 041203 (2010)
- [3] T. Adams, A. Chacon, M. Wagner, A. Bauer, G. Brandl, B. Pedersen, H. Berger, P. Lemmens, C. Pfleiderer, *Long-wavelength helimagnetic order and skyrmion lattice phase in Cu_2OSeO_3* , *PRL* **108**, 237204 (2012)
- [4] Y. Tokunaga, X. Z. Yu, J. S. White, H. M. Rønnow, D. Morikawa, Y. Taguchi, Y. Tokura, *A new class of chiral materials hosting magnetic skyrmions beyond room temperature*, *Nat. Commun.* **6**, 7638 (2015)
- [5] I. Gross, W. Akhtar, A. Hrabec, J. Sampaio, L. J. Martínez, S. Chouaieb, B. J. Shields, P. Maletinsky, A. Thiaville, S. Rohart, V. Jacques, *Skyrmion morphology in ultrathin magnetic films*, *Phys. Rev. Mater.* **2**, 024406 (2018)
- [6] W. Akhtar, A. Hrabec, S. Chouaieb, A. Haykal, I. Gross, M. Belmeguenai, M. S. Gabor, B. Shields, P. Maletinsky, A. Thiaville, S. Rohart, V. Jacques, *Current-induced nucleation and dynamics of skyrmions in a Co-based Heusler alloy*, *Phys. Rev. Appl.* **11**, 034066 (2019)
- [7] S. Parkin, M. Hayashi, L. Thomas, *Magnetic Domain-Wall Racetrack Memory*, *Science* **320**, 190 (2008)
- [8] C. Donnelly, M. Guizar-Sicairos, V. Scagnoli, S. Gliga, M. Holler, J. Raabe, L. J. Heyderman, *Three-dimensional magnetization structures revealed with X-ray vector nanotomography*, *Nature* **547**, 328 (2017)
- [9] L. Rondin, J. P. Tetienne, T. Hingant, J. F. Roch, P. Maletinsky, V. Jacques, *Magnetometry with nitrogen-vacancy defects in diamond*, *Rep. Prog. Phys.* **77**, 056503 (2014)

Towards circuit-quantum electrodynamics with gate-tuneable nanowire devices

Project P1807: Andreev Spin Qubit (ASQ) in Ge/Si Nanowires

Project Leader: C. Schönenberger, F. Braakman, I. Zardo, and D. Zumbühl

Collaborators: J. H. Ungerer (SNI PhD Student), J. Ridderbos, R. Haller, and L. Y. Cheung

Coupling of a superconducting resonator to a spin qubit

In the field of circuit quantum electrodynamics, a superconducting resonator coherently interacts with a quantum system such as a Cooper pair box qubit [1]. For a long time, it has been a goal to demonstrate coherent interactions between a superconducting resonator and a single spin which turns out to be a difficult task due to the small magnetic moment of the spin. Finally, the coupling between a superconducting resonator and a semiconductor spin qubit has been realized by hybridizing a spin in semiconductor quantum dots with its charge degree of freedom and capacitively coupling the two quantum systems [2,3]. These ground-breaking experiments demonstrate that it might be feasible to exploit a superconducting resonator for long-distance coupling of spin qubit quantum processors and thereby contribute to the scaling-up of quantum computers. However, due to insufficient coherence times, an exchange-like interaction mediated by a resonator is still an unsolved problem [4]. Furthermore, the used material platforms rely on spin-orbit interaction induced by micro magnets which inhibits further scaling. For these reasons, we aim on coupling a spin qubit in a nanowire (NW) such as a Ge/Si NW or an Al/InAs NW [5] to a high-impedance resonator. These semiconductor NWs possess exciting properties such as a large, intrinsic spin-orbit interaction or a gate-tunable Landé factor [6] which will mediate the coupling to the high-impedance resonator.

Realizing a nanowire architecture for resonator coupling

In the last SNI annual report, we have reported having achieved the fabrication of high-quality, high-impedance, resonators based on the superconducting material NbTiN. Due to their large electric-field vacuum fluctuations and their resilience to external magnetic-fields, these resonators are perfectly suited for capacitive coupling to a spin qubit in a NW with strong spin-orbit interaction. Figure 1 shows the real and imaginary part of a resonance dip of a notch-type half-wave resonator. From the fit, which is shown in the same figure, large internal (Q_i) and external (Q_e) quality factors are deduced (see caption of Fig. 1)

In the reporting year 2020, we have focused on realizing a framework for the NW which will host a spin qubit. We have implemented Ge/Si NWs and Al/InAs NWs in a circuit QED architecture. Moreover, care has been taken in the engineering of a noise-free environment at microwave frequencies by adding customized superconducting low-pass filters to all SC lines. Due to the limited space, below we will focus on the work on Al/InAs quantum NWs.

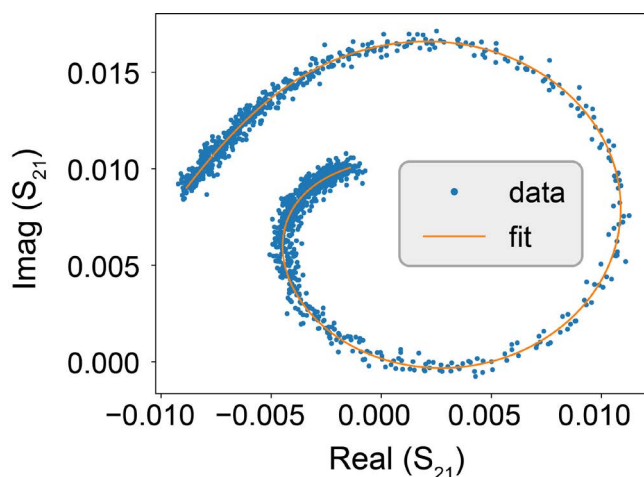


Fig. 1 Real and imaginary part of the transmission through a feed-line coupled to a high-impedance notch-type half-wave resonator. The orange curve corresponds to a fit with $Q_i=950'000 \pm 240'000$ and $Q_e=39'000 \pm 1'000$.

Characterization of Al/InAs shadow junctions

Previous experiments aiming on investigating Andreev bound states in Al/InAs NWs by means of RF-technologies [7] rely on InAs NWs with epitaxially grown aluminum (Al) shells. In these wires, a Josephson junction is formed by means of wet etching the AL shell. However, the wet-etching process is hard to control and little reproducible.

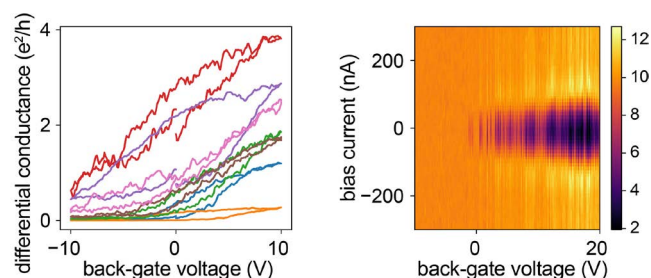


Fig. 2 Left: Zero-bias 2-probe conductance through 7 different InAs/Al shadow-epitaxy NWs at room temperature as a function of back-gate voltage. Right: differential resistance of the NW corresponding to the red curve in the left figure as a function of back-gate voltage and bias current, probed at a temperature of 20 mK. The low resistance state (black) at positive gate voltages point to a region with a finite supercurrent of ~ 50 nA.

Therefore, we have investigated alternatives to the wet etching process. Our collaborators in Copenhagen, Jesper Nygard and coworkers, have recently realized Al/InAs NW Joseph-

son junctions by means of shadow epitaxy [8]. We have investigated several of these junctions in a DC setup. Figure 2 shows the result of those measurements. The left figure shows the zero-bias 2-probe conductance as a function of backgate voltage, measured with a lock-in amplifier at room temperature for 7 different shadow junction wires. The investigated NWs are InAs NWs with a diameter of around 100 nm where two or three of the six facets are coated by Al with a thickness of approximately 10 nm. The Al shell is interrupted by shadow junctions with a length of approximately 100 nm. All 7 wires exhibited the characteristics of a field-effect transistor showing a strong dependence on the backgate voltage at room temperature. The fact that all 7 wires showed the expected behavior is a sign for a remarkable reproducibility of the shadow junctions compared to wet-etched junctions. After measuring the NW response at room temperature, the NW corresponding to the red curve in figure 2 (left) has been cooled down to 20 mK in a dilution refrigerator. The differential resistance as a function of the backgate voltage and bias current is shown on the right side of figure 2. One can clearly observe a gate-voltage dependent resistance dip around zero bias current for positive gate voltages. This suggests that a gate-tunable Josephson junction with supercurrents up to ≈ 100 nA has been realized.

Integration of shadow junction wires into circuit QED architecture

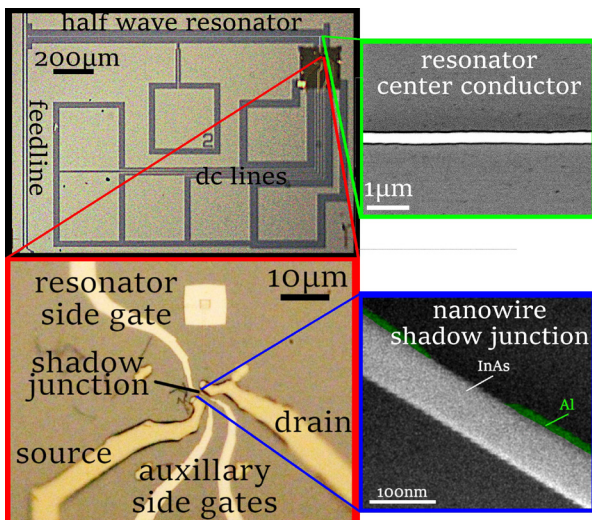


Fig. 3 Images of the different parts of a NW-based circuit quantum electrodynamics device. Black: Optical image, overview of device, NbTiN appears light greenish, Si appears gray to dark gray. Green: Scanning electron micrograph of the resonator center conductor. NbTiN appears white. Red: Zoom onto NW device area. NbTiN contacts appear dark yellow, Ti/Pd gates appear light yellow. The gate leaving the image to the top is galvanically connected to the resonator center conductor. Blue: Scanning electron micrograph of an InAs NW with Josephson junction grown by means of shadow epitaxy. Pictures in green and blue boxes are taken on similar devices.

After confirming that the Al/InAs shadow junction NWs exhibit promising Josephson junctions with a high yield, we have integrated one of these junctions into our circuit QED architecture. Figure 3 shows images of the finished device. The image in the black box shows an optical micrograph of the device featuring a high impedance, superconducting, coplanar waveguide, half-wave resonator etched into a 7 nm thin film of NbTiN. An SEM picture of the resonator center conductor is shown in the green box. On one side, the resonator is coupled to a feeding which is used for resonator readout. The other end of the resonator is galvanically con-

tacted to a side gate that gates an Al/InAs shadow junction (see red box). An SEM micrograph of a similar junction is shown in the blue box. The device which is shown in figure 3 has recently been finalized and loaded into a dilution refrigerator. We are currently performing experiments on the device.

References

- [1] A. Wallraff, D. I. Schuster, A. Blais, L. Funzio, R.- S. Huang, J. Majer, S. Kumar, S. M. Girvin, J. Schoelkopf, *Strong coupling of a single photon to a superconducting qubit using circuit quantum electrodynamics*, Nature **431**, 162 (2004)
- [2] X. Mi, M. Benito, S. Putz, D. M. Zajac, J. M. Taylor, G. Burkhard, J. R. Petta, *A coherent spin-photon interface in silicon*, Nature **555**, 599 (2018)
- [3] N. Samkharadze, G. Zheng, N. Kalhor, D. Brousse, A. Sammak, U. C. Mendes, A. Blais, G. Scappucci, L. M. K. Vandersypen, *Strong spin-photon coupling in silicon*, Science **359**, 1123 (2018)
- [4] F. Borjans, X. G. Croot, M. J. Gullans, J. R. Petta, *Resonant microwave-mediated interactions between distant electron spins*, Nature **577**, 195 (2020)
- [5] M. Hays, V. Fatemi, K. Serniak, D. Boumanm, S. Diamond, G. de Lange, P. Krogstrup, J. Nygård, A. Geresdi, M. H. Devoret, *Continuous monitoring of a trapped superconducting spin*, Nature Physics **16**, 1103 (2020)
- [6] M. Brauns, Joost Ridderbos, A. Li, E. P. A. M. Bakkers, F. Zwanenburg, *Electric-field dependent g-factor anisotropy in Ge-Si core-shell nanowire quantum dots*, Physical Review B **93**, 121408 (2016)
- [7] D. J. van Woerkom et al., *Microwave spectroscopy of spinful Andreev bound states in ballistic semiconductor Josephson junctions*, Nature Physics **13**, 876 (2017)
- [8] D. J. Carrad, M. Bjergfelt, T. Kanne, M. Aagesen, F. Krizek, E. M. Fiordaliso, E. Johnson, J. Nygård, T. S. Jespersen, *Shadow Epitaxy for In Situ Growth of Generic Semiconductor/ Superconductor Hybrids*, Advanced Materials **32**, 23 (2020)

Coupling an ultracold ion to a metallic nanowire

Project P1808: Quantum dynamics of an ultracold ion coupled to a nanomechanical oscillator
Project Leader: S. Willitsch and M. Poggio
Collaborator: M. Weegen (SNI PhD Student)

Introduction

The goal of this project is the implementation of a new solid state-atomic hybrid system in which the advantages of both constituents can be combined. The atomic part of the present system is realized by an ultracold calcium ion in an ion trap. The confinement of ions in linear radio frequency traps has previously enabled the precise control and manipulation of single particles on the quantum level [1]. As the counterpart to the ion in this hybrid system, a single nanowire is used. Nanowires are nanomechanical oscillators which can be interfaced with diverse quantum devices [2, 3]. They can act as sensitive mechanical probes and, in the present case, offer flexible means for the fine-tuning of the trapping potential of the ion.

As ions are charged particles, an interaction between the two systems can be realized by applying a voltage to the nanowire. By tuning the relative position of the nanowire with respect to the ion and employing a controllable drive of its mechanical motion, the ion-nanowire interaction can be flexibly controlled and a coherent manipulation of the ion motion can be achieved.

Here, we report our progress towards the implementation of a quantum interface between an ultracold 40Ca^+ ion and a metallic Ag_2Ga nanowire in a gold-coated alumina wafer segmented-layer ion trap (Fig. 1). We report improvements of the experimental setup, highlight progress in the theoretical modelling of the system and discuss the current state of the experiment.

Experimental setup

The centerpiece of the experiment is a segmented-layer ion chip trap as shown in figure 1. The device is assembled from gold-coated alumina wafers to which DC and RF potentials are applied to confine the ion. The DC electrodes are each divided into seven segments which can be individually addressed for a better control of the trapping potential.

Below the center of the trap, the Ag_2Ga nanowire is mounted on a metallic holder. Its position can be adjusted by nanopositioners stacked up underneath (Fig. 2). This assembly enables changing the position of the nanowire on the fly with nanometer precision. The coupling of the ion to the nanowire is achieved by applying a voltage to the wire and placing it close to the ion. A piezo actuator attached to the holder is used to drive the nanowire motion at a selected frequency and amplitude.

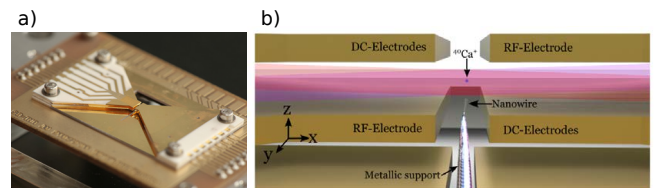


Fig. 1 a) Photograph of the ion trap used in the experiment. b) Side-view schematic of the central region of the trap. The DC and RF voltages applied to the electrodes provide confinement for a single calcium ion. The nanowire is located below the trap center and can be moved close to the ion using nanopositioners to achieve a strong coupling between both systems.

Over the course of the last year, a range of optimizations have been implemented to the trap assembly, such as an improved electrical control of the trap. Furthermore, the connections to the RF electrodes have been stabilized and their resistances have been decreased. These measures enabled the application of higher RF voltage amplitudes for a tighter confinement of the ion which is necessary for reaching the quantum regime of the ion motion. Furthermore, the optical setup for several laser beams required for laser cooling of the ion has been reconfigured to allow a more precise beam shaping and a better laser-cooling performance for the ion.



Fig. 2 Side view photograph of the ion trap corresponding to the schematic in figure 1. The nanowire holder can be seen between the electrodes in the trap center.

An important aspect of the experiment is the identification and characterization of the nanowire resonance peaks. Using a lock-in amplifier, the motion of the nanowire driven by a piezoelectric actuator was measured using a laser beam and a quadrant-photodiode detector. The nanowire is positioned within the focus of the laser beam so that its shadow introduces measurable changes in the photodiode signal. Figure 3 shows a spectrum of motional resonances of the nanowire

as a function of the drive frequency. The mechanical motion of the nanowire can be used to excite and coherently manipulate the ion motion when both oscillators are brought into resonance.

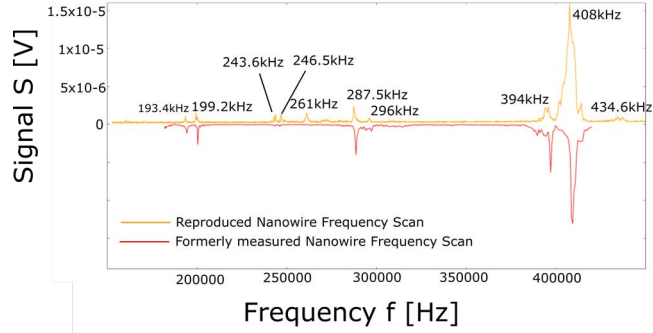


Fig. 3 Frequency spectrum for the nanowire drive. The two measurements were taken several months apart to confirm the reproducibility of the setup.

Theoretical modeling of the hybrid system

In our previous report, we presented a theoretical characterization of the hybrid system using quantum dynamics simulations of the ion interacting with the driven nanowire. We demonstrated the possibility for the creation of very large coherent motional states of the ion via the ion-nanowire interaction (Fig. 4) as well as the creation of genuine quantum states [4].

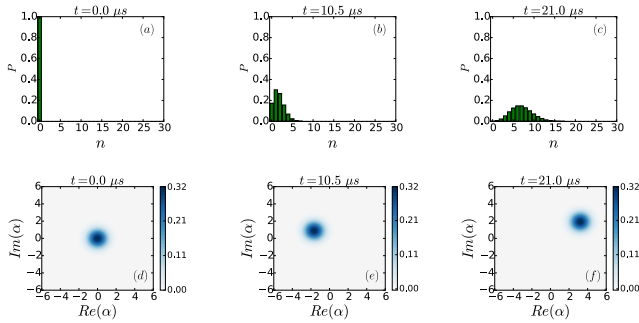


Fig. 4 Creation of large coherent states of the ion motion in the trap under the resonant drive of the nanowire [4] (the nanowire drive frequency f_{nw} is equal to the ion's axial trapping frequency f_{ion}). In this simulation, the ion was initially prepared in its motional ground state.

These studies revealed the importance of trapping-potential anharmonicities for the precise engineering of quantum states of the ion motion. Based on these initial results, we were further exploring possibilities to systematically shape electrode potentials for a rational design of specific anharmonic terms in the trapping potential to generate specific motional quantum dynamics. For this purpose, an evolutionary optimization algorithm has been implemented. This algorithm is used to compute the necessary voltages applied to the DC electrodes of the trap in order to create specific higher-order anharmonic potential terms close to the trap center. Figure 5 shows as an example a harmonic potential with a 6th-order anharmonic term (dashed line) as well as the corresponding numerical potential (full line) from the optimization algorithm generated from a superposition of optimized electrode voltages.

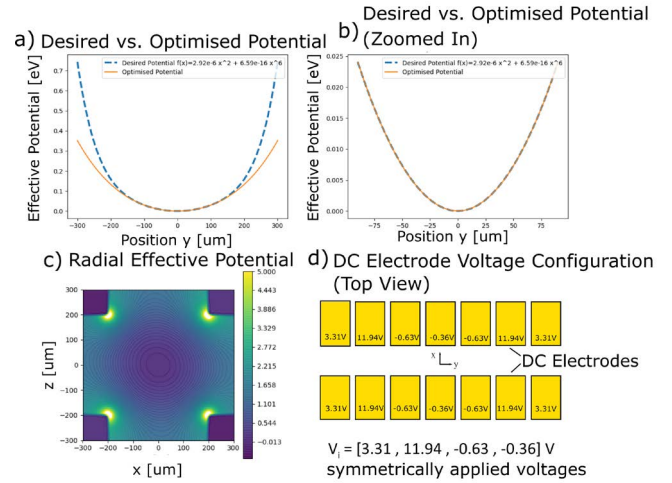


Fig. 5 Trapping potential for a 6th order anharmonicity. a) Complete axial potential over the whole trapping region. Dashed line: target potential; full line: numerically optimized potential from a superposition of individual trap-electrode potentials. b) Magnification of the region near the trap center in which the optimization has been performed. c) Effective radial potential in the complete trapping region. d) Sketch of the DC electrode segments indicating the voltages necessary to obtain the optimized potential.

Outlook

The experimental setup is ready for ion-trapping as the first important milestone for testing the theoretical findings experimentally. After the successful confinement of calcium ions in the trap, cooling of the ions to the motional ground state will be implemented as a prerequisite for manipulating the ion motion in the quantum regime using the nanowire.

References

- [1] S. Willitsch, *Coulomb-crystallised molecular ions in traps: methods, applications, prospects*, Int. Rev. Phys. Chem. **31**(2), 175 (2012)
- [2] M. Montinaro, G. Wüst, M. Munsch, E. Fontana, E. Russo-Averchi, M. Heiss, A. Fontcuberta I Morral, R. J. Warburton and M. Poggio, *Quantum dot optomechanics in a fully self-assembled nanowire*, Nano Lett. **14**(8), 4454 (2014)
- [3] J. M. Pirkkalainen, S. Cho, F. Massel, J. Tuorila, T. Heikkilä, P. Hakonen and M. A. Sillanpää, *Hybrid circuit cavity quantum electrodynamics with a micromechanical resonator*, Nat. Commun. **6**, 6981 (2015)
- [4] P. N. Fountas, M. Poggio, S. Willitsch, *Classical and quantum dynamics of a trapped ion coupled to a charged nanowire*, New J. Phys. **21**(1), 013030 (2019)

Visual proteomics to study neurodegenerative diseases

Project P1901: Microfluidics to Study Huntington's Disease by Visual Proteomics

Project Leader: T. Braun, E. Pecho-Vrieseling, and H. Stahlberg

Collaborator: A. Fränkl (SNI PhD Student)

Introduction

Stereotypic spatiotemporal spreading of pathological lesions through the nervous system is a hallmark of many neurodegenerative diseases. The prion-like spreading model provides an elegant explanation for this observation, postulating that misfolded proteins (amyloids) can disease healthy cells by imprinting their misfold onto endogenous proteins. However, the precise spreading mechanism and information carrier is still unknown.

Huntington's disease is an archetypal example of the prion-like spreading phenomena: dominantly inherited mutations lead to the misfolding and aggregation of the huntingtin protein, and the lethal disease's onset in a patient's age of around 35 years. Huntington's disease is manifested by uncontrolled movements, depression, and a loss of cognition.

Electron microscopy (EM) is an underrated analytical tool geared to analyze minimal amounts of samples. Optimally, EM is combined with microfluidic, lossless sample preparation methods. In recent years, we developed a modular microfluidic system for single-cell analysis by targeted and untargeted "visual proteomics." We apply and further develop these methods to study the prion-like spreading mechanism involved in neurodegeneration, specifically Huntington's disease.

Single-cell visual proteomics

Our in-house developed, modular system allows the preparation of nL sized sample volumes in a virtually lossless manner for electron microscopy. Importantly, this preparation system can be combined with a single-cell picker, enabling the lysis and take-up of the cellular contents in a fraction of a second. The system is designed for adherent eukaryotic cell systems, such as neurons (Fig. 1A). Finally, a magnetic trap allows the immobilization of super-paramagnetic nanoparticles. The latter can be coupled to cognitive molecules, such as antibodies, to fish target protein complexes from the cell lysate. Figure 1B shows a typical experiment: Neuron-like cells were seeded with amyloid nanoparticles. After an incubation time of a few hours, the extracellular seeds were washed away, and only intracellular seeds remained in the cell-culture as verified by confocal fluorescence microscopy. After further cell-growth, individual cells were lysed and prepared for electron microscopy. Indeed we were able to find the (processed) seeds previously taken up by the neuron. These seeds also can be extracted by our trap, as shown in figure 1C.

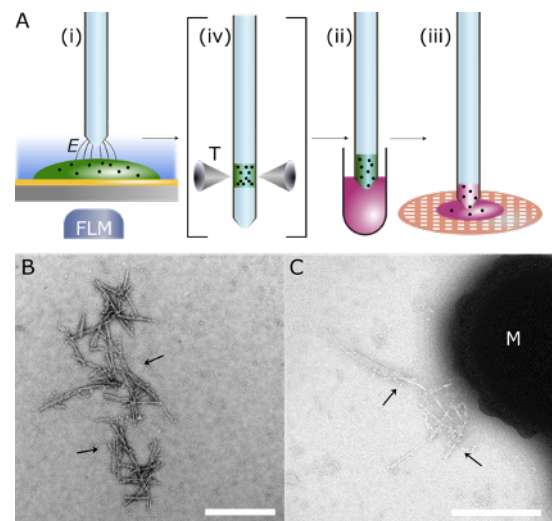


Fig. 1 Single-cell preparation for visual proteomics to analyze incorporated seeds of neuronal cells. A) Single-cell lysis of a selected adherent eukaryotic cell by electroporation and simultaneous aspiration of the cell-content (i) in a volume of ≈ 3 nL, conditioning to remove endogenous salts and introduce heavy metal salts for staining (ii), and dispensing of stained single-cell lysate onto an EM-grid (iii). Note that the cell selection and the lysis process are monitored by fluorescence light microscopy (FLM). Optionally, the electromagnetic trap (T) can be used to immobilize and extract target proteins from the single-cell lysate (iv). B) Typical preparation of a neuron-like cell after seeding with α -syn-fibril fragments. The cells were grown on a poly-lysine functionalized indium thin oxide (ITO) coated glass-slide and differentiated to dopaminergic neurons. Fluorescently labeled α -syn-seeds were added for several hours and extensively washed away afterward. The uptake of the seeds was confirmed by confocal light microscopy. In the cryoWriter system, an individual cell containing visible seeds in the integrated fluorescence microscope was selected, lysed, and prepared, as shown in panel A (i)-(iii). The seeds can be found again, with the same dimensions as the in vitro generated seeds; however, they seem to be processed by the cell, as it is visible by the attached proteins. The arrows indicate the seeds. C) Similar experiment, but the synthetic seeds were biotinylated before the experiment. Streptavidin-coated super-paramagnetic beads (M) were used in a preliminary test to extract the single-cell lysate seeds. Scale bars: 500 nm.

Figure 1A shows that the amyloid seeds were processed in the cell. This is visible by the fuzzy coating of the fibril-fragments. Unfortunately, we do not know the proteins involved and their function. An identification of the attached proteins would be of interest. Since we can immobilize the seeds in the magnetic trap, we can use a secondary antibody, coupled to electron-dense colloidal gold, for identification. This "interaction labeling" is described in figure 2.

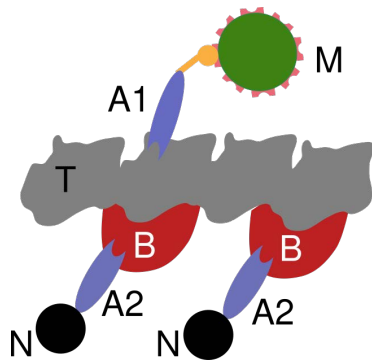


Fig. 2 Interaction labeling of extracted proteins [1, 2] The primary target protein (T) is trapped with a first fragmented antibody (Fab, A1) coupled to a super-paramagnetic bead. Still immobilized, potential binding partners (B) can be labeled using a secondary Fab (A2) coupled to electron-dense nanogold markers (N) easily detected in the EM. In the end, the trap is disabled, and EM samples are written. All steps are performed in the cryoWriter setup.

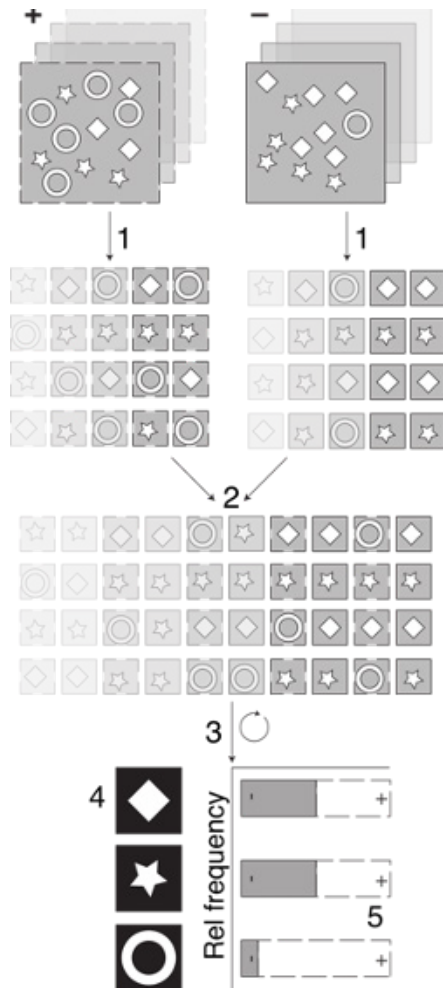


Fig. 3 Principles of “differential visual proteomics” algorithm. Pulse-chase like experiments are performed as positive (+) and negative control (-). Single-cell lysates are prepared for imaging in the EM from both experiments resulting in two stacks of projections of cell lysate constituents (dotted frame for positive control). Three different proteins are shown in white. For analysis, all particles are picked (1), resulting in two galleries of protein projections. Subsequently, the particle galleries are pooled (2). For every particle, the origin (positive or negative control) is known. The combined particle gallery is now subjected to a maximum-likelihood based alignment and classification algorithm (3). The classification and

averaging results in class-averages of higher signal-to-noise ratio compared to the original projections of single molecules (4). Since we know the origin of every particle contributing to a given class, we can screen for classes with significant differences between the positive and negative control (5). These classes are likely responsible for the biological reaction upon the pulse-chase disturbance.

The interaction labeling allows the identification of suspected proteins in an ultrastructure. However, visual proteomics also allows the detection of structural changes in an untargeted and unsupervised manner. We developed a method called “differential visual proteomics” [3] geared to study proteome-wide structural changes of proteins and protein-complexes between a disturbed and an undisturbed cell or between two cell populations. The cells are lysed, and the lysate is prepared in a lossless manner for single-particle EM. The samples are subsequently imaged in the EM. Individual particles are computationally extracted from the images and pooled together while keeping track of which particle originated from which specimen. The obtained particles are then aligned and classified. A final quantitative analysis of the particle classes found identifies the particle structures between positive and negative control samples. The algorithm and a graphical user interface were developed, enabling the analysis and the visualization of the results. The algorithm was tested with simulated and experimental data.

References

- [1] D. Giss, S. Kemmerling, V. Dandey, S. Stahlberg, T. Braun, *Exploring the inter-actome: microfluidic isolation of proteins and interacting partners for quantitative analysis by electron microscopy*, *Anal. Chem.* **86**, 4680–4687 (2014)
- [2] C. Schmidli, S. Albiez, L. Rima, R. Righetto, I. Mohamed, P. Oliva, L. Kovacic, H. Stahlberg, T. Braun, *Microfluidic protein isolation and sample preparation for high-resolution cryo-EM*, *Proc. Natl. Acad. Sci. U.S.A.*, **116**(30), 15007 (2019)
- [3] A. Syntychaki, L. Rima, C. Schmidli, T. Stohler, A. Bieri, R. Sütterlin, H. Stahlberg, T. Braun, *Differential visual proteomics’: Enabling the proteome-wide comparison of protein structures of single-cells*, *J. Proteome Res.*, **18**(9), 3521–3531 (2019)

MIMYO: MImicking MYOcardial tissue with a 3D nanofiber network

Project P1902: Directional 3D nanofiber network to mimic in-vivo myocardial syncytium towards guiding contraction patterns in in-vitro heart models

Project Leader: M. Gullo, M. Poggio, and A. Marsano

Collaborator: F. Züger (SNI PhD Student)

Introduction

Cardiovascular diseases are one of the most common causes of hospitalization or death. The rapidly increasing case number may render it the leading global threat in the industrialized world of the 21st century. Loss of cardiac tissue, following a myocardial infarction, causes an impairment of heart functionality. An additional low intrinsic regenerative capability of the cardiomyocytes (CMs) to replace affected tissue urges the need for novel therapies and methods such as biofabrication to counter this challenge [1–3].

Current methods in the development of patient-specific in-vitro cardiac tissue models are not yet able to closely mimic the contraction dynamics and thus reach functionality comparable to in-vivo myocardial tissue [4]. The correct mimicking of the dynamic myocardial properties necessitates the support of a specialized electrically conductive network, the so-called syncytium, consisting of specialized cell fibers (Purkinje fibers), capable to propagate timely the electrical signal [5]. Myocardial tissue cultures did so far not succeed in expressing a syncytium network in-vitro due to the difficulty to achieve a complete maturation.

The goal of this recently started PhD project is to mimic this very syncytium by implementing electrically conductive nanofibers (NF) into a 3D-engineered myocardial tissue. This should ultimately promote cardiomyocyte maturation by enabling better electrical coupling among neighboring cells. Findings of this project are expected to lay a solid basis towards implantable biohybrid cardiac patches for regenerative medical applications.

Literature search & review

For a solid overview over the field and searching for a possible starting point, an in-depth literature search was carried out during the first semester. Choosing the right nanocomposite for proper electrical conductivity within our bio-fabricated construct and choosing the right fabrication method for these NF as well as its composition was achieved by intense reading and examining the state-of-the-art research.

Out of these gained insights into the biofabrication, first ideas for possible experiments were discussed and prepared. To consolidate the literature search we prepared manuscript reviewing the 3D-biofabrication field in the context of nanocomposites and their use in physiological mimicking electroconductive hydrogels for 3D-printing. The first version is currently under internal review by the PhD

candidate's supervisors and is planned to be submitted for publication early spring.

Hands-on training

The PhD candidate received a training on the inhouse 3D-bioprinting platforms comprising several printing technologies and using a variety of hydrogels as well as polymeric materials. Furthermore, the candidate received a training in the isolation of neonatal cardiomyocyte (CM) and cardiac fibroblasts (CF) from 2-day-old rats enabling him the access to a stable cell source for cell-based experiments. A good understanding and careful cell culturing is necessary for the CM isolation and maintenance during in vitro culture, since CMs are very sensitive.

Results

Current bio-fabricated constructs used to replace damaged tissue, are often produced using a single method, e.g. 3D-extrusion printing. Generally, they lack the possibility to generate and stack different length scales scaffold features and therefore, missing important cues of the native extracellular matrix (ECM)[6], necessary to promote CM attachment and invasion as well as directional cardiac pacing. Therefore, combining electrospinning (ES) and 3D-bioprinting in a one step process would enable the stacking of 3D printed (micrometer range) and ES scaffolds (nanometer range), all within an aseptic environment on a compact 3D-bioprinting configuration (Fig. 1).

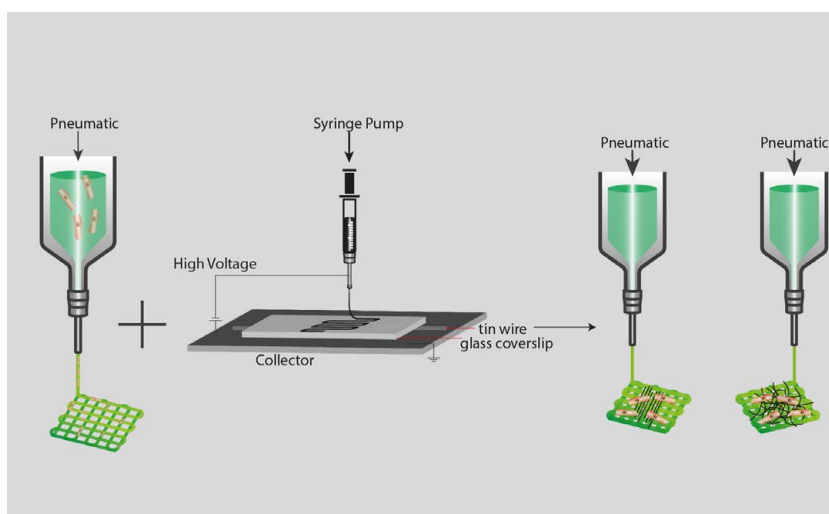


Fig. 1 Schematic representation of the combined electrospinning and 3D-bioprinting setup. Nanofibers can be spun in an aseptic environment directly onto or sandwiched between a 3D printed construct leading to a dual scale engineered tissue either with aligned or random NF.

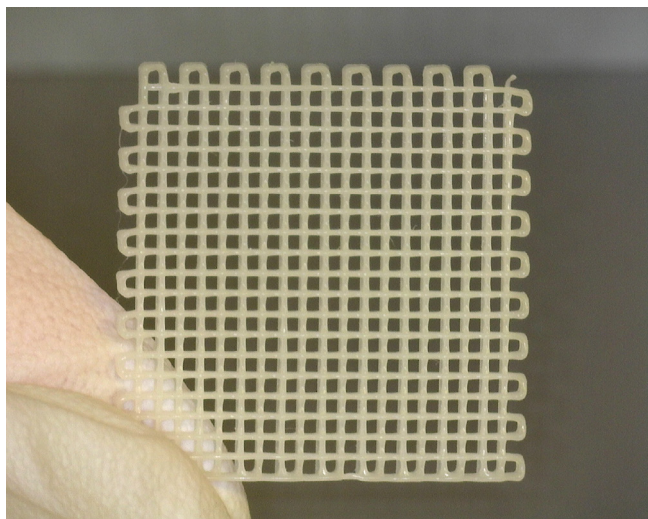


Fig. 2 3D-printed constructs, showing the versatility and precise engineering of three-dimensional design (size 1 x 1 cm²).

Polycaprolactone (PCL) was selected as a first promising candidate for the fabrication of a biodegradable and cytocompatibility scaffold supporting the fragile NF network prior to the cell invasion. The printing parameters were optimized in order to precisely replicate the intended design and achieve high fabrication yields (>90%). Figure 2 shows a printed PCL scaffold (5 layers of 150 μm thickness each) and demonstrates its ease of handling.

NF out of a polyethylene oxide (PEO) solution were continuously and reproducibly spun after optimizing the spinning parameters, such as high voltage (10 kV), feeding rate (0.025 μL/sec), polymer concentration (5% w/v) and working distance (45 mm). The directionality of said NFs was obtained by influencing the electromagnetic field distribution of the collector plate. Therefore, electroconductive tin wires were aligned between the sample holder substrate and the collector plate (Fig. 1). This enables the spinning of aligned nanofibers on the area above the wires and random fiber spinning on the rest of the glass slide (Fig. 3 A-D). Directionality diagram of spun scaffolds using a 2D-Fast Fourier Transformation (2D-FFT) showed high alignment of fibers in the target area and random fiber orientation in the rest of the surface (Fig. 3 E-F).

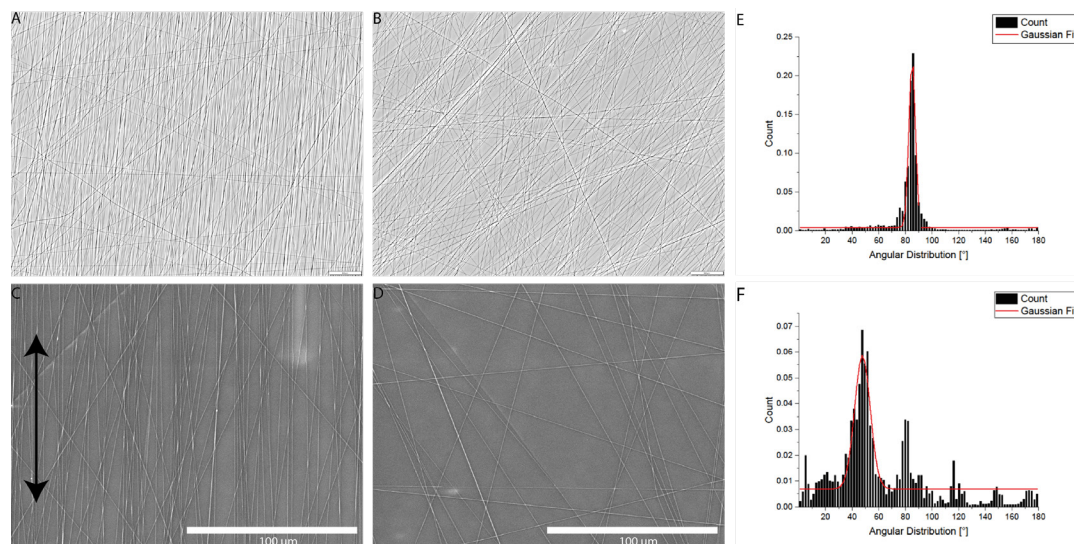


Fig. 3 Electrospraying of 5% PEO solution into nanofibers; A) Light microscope (LM) image of aligned electro spun nanofibers collected on a glass coverslip (scalebar= 100 μm); B) LM image of random electro spun nanofibers collected on a glass coverslip (scalebar= 100 μm); C) SEM image of aligned electro spun nanofibers, black arrow depicts alignment direction; D) SEM image of random electro spun nanofibers; angular distribution of aligned E) and random F) electro spun fibers characterized with 2D-FFT.

Future steps will include the spinning of conductive fibers and the combination of these fibers with 3D-bioprinted constructs. These constructs can then be used for cell experiments, studying the cell maturation of CM in an in-vitro electroconductive environment. Additionally, the used ES setup for dual scale biofabrication is being updated. Higher working distance and interchanged high voltage and grounding of the system should result in more reproducible fiber spinning and better fiber alignment.

References

- [1] M. K. Baig, N. Mahon, W. J. McKenna, A. L. Caforio, R. O. Bonow, G. S. Francis, M. Gheorghiuade, *The pathophysiology of advanced heart failure*, American Heart Journal **135**, S216–S230 (1998)
- [2] S. Mukherjee, J. Reddy Venugopal, R. Ravichandran, S. Ramakrishna, M. Raghunath, *Multimodal biomaterial strategies for regeneration of infarcted myocardium*, Journal of Materials Chemistry **20**, 8819–8831 (2010)
- [3] W.-H. Zimmermann, T. Eschenhagen, *Cardiac Tissue Engineering for Replacement Therapy*, Heart Fail Rev **8**, 259–269 (2003)
- [4] A. Mathur, Z. Ma, P. Loskill, S. Jeeawoody, K. E. Healy, *In vitro cardiac tissue models: Current status and future prospects*, Advanced Drug Delivery Reviews **96**, 203–213 (2016)
- [5] R. E. Ideker, W. Kong, S. Pogwizd, *Purkinje Fibers and Arrhythmias*, Pacing Clin Electrophysiol **32**, 283–285 (2009)
- [6] E. D. Hay, *Cell Biology of Extracellular Matrix: Second Edition*. (Springer Science & Business Media, 2013)

Towards non-invasive temperature mapping

Project P1903: Neutron nanomediators for non-invasive temperature mapping of fuel cells

Project Leader: M. Kenzelmann and P. Boillat

Collaborator: A. Ruffo (SNI PhD Student)

Introduction

Knowing the precise temperature distribution across the inner structure of fuel cells during operation will allow a detailed knowledge of the conditions to which the materials are exposed, which is of high importance for the performance and durability of the fuel cell. To avoid the highly invasive insertion of micro-thermocouples, we proposed the use of magnetic nanoparticles as contactless sensors. The magnetic characteristic can be measured in a fully non-invasive fashion by neutron depolarization imaging, using the loss of magnetization as the temperature approaches the Curie temperature to identify temperature changes. We report here the first results of nanoparticle synthesis and characterization, as well as a first assessment of their suitability for temperature measurement with neutron depolarization imaging.

Ni nanoparticle synthesis and characterization

We focused on Ni nanoparticles as a starting point, as bulk Ni has a reasonably low Curie temperature ($\sim 350^\circ\text{C}$) and there are many different synthesis methods known for producing these nanoparticles.

Two synthesis routes were chosen for this work, denominated here as polyol synthesis [1] and aqueous synthesis [2]. In the polyol synthesis (Fig. 1), the precursor was dissolved in ethylene glycol, and a reducing agent (NaBH_4) was added to the mixture at a slightly elevated temperature (between 25°C and 100°C). This results in the reduction of the precursor to metallic Ni, with the glycol solvent also acting as a capping agent to control the nanoparticles size. In the aqueous synthesis, water was used as a solvent and a separate capping agent, cetyltrimethyl ammonium bromide (CTAB), was added. The aqueous synthesis further required a reduction of the obtained NiOH nanoparticles to Ni by annealing at 400°C in a reducing atmosphere ($5\% \text{H}_2$ in Ar).

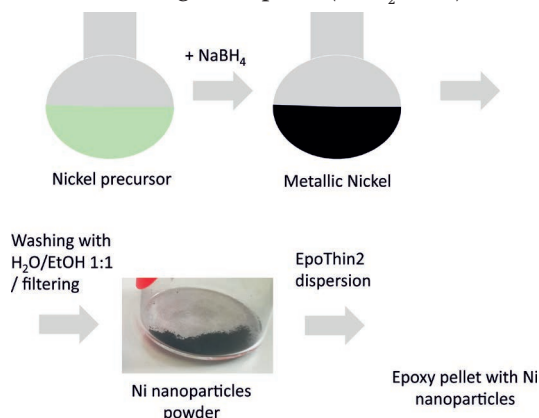


Fig. 1 Summary of the sample synthesis and preparation steps.

The synthesized particles (as well as two types of commercial nanoparticles) were embedded into epoxy pellets for the neutron imaging measurements described in the next section.

The result of the synthesis was assessed using X-ray diffraction (XRD). As seen in figure 2, the presence of a metallic Ni lattice was confirmed for all samples. Furthermore, a significant broadening of the peaks in the XRD pattern for the samples made using the polyol synthesis route was observed, which was indicating small crystallite sizes.

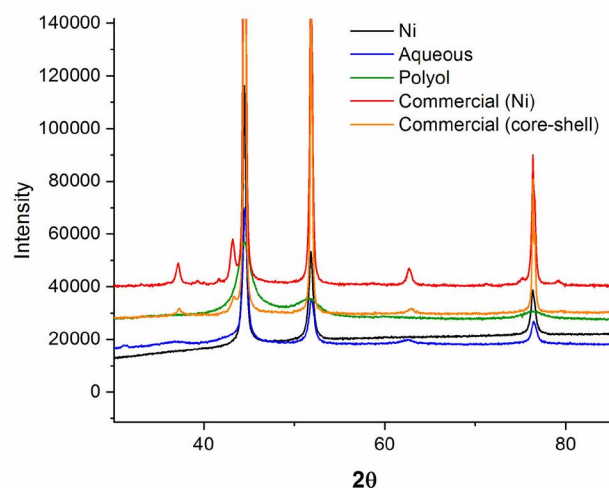


Fig. 2 XRD patterns of the synthesized and commercial Ni nanoparticles, along with a reference Ni pattern.

The latter aspect was assessed quantitatively using Rietveld refinement of the XRD patterns. As summarized in table 1, the crystallite size is significantly smaller for the sample made by polyol synthesis. This is in principle a desired feature, as smaller nanoparticles are expected to feature a lower Curie temperature [3].

Table 1. List of samples and their crystallite sizes according to XRD Rietveld refinement.

Name	Precursor	Synthesis Temp. [$^\circ\text{C}$]	Size [nm]*
Commercial (Ni)	N/A	N/A	177
Commercial (core shell)	N/A	N/A	153
Aqueous	$\text{NiCl}_2 \cdot 6\text{H}_2\text{O}$	$25^\circ\text{C} + 400^\circ\text{C}$	132
Polyol	$\text{Ni}(\text{acet}) \cdot 4\text{H}_2\text{O}$	100°C	22

*Crystallite size from XRD analysis

Neutron imaging measurements

A first neutron imaging campaign was conducted, with the goal of assessing the suitability of the Ni nanoparticles for the proposed application. The main information sought in this measurements was the degree of neutron beam depolarization obtained as a function of the nanoparticle concentration, as well as the temperature dependency of the depolarization.

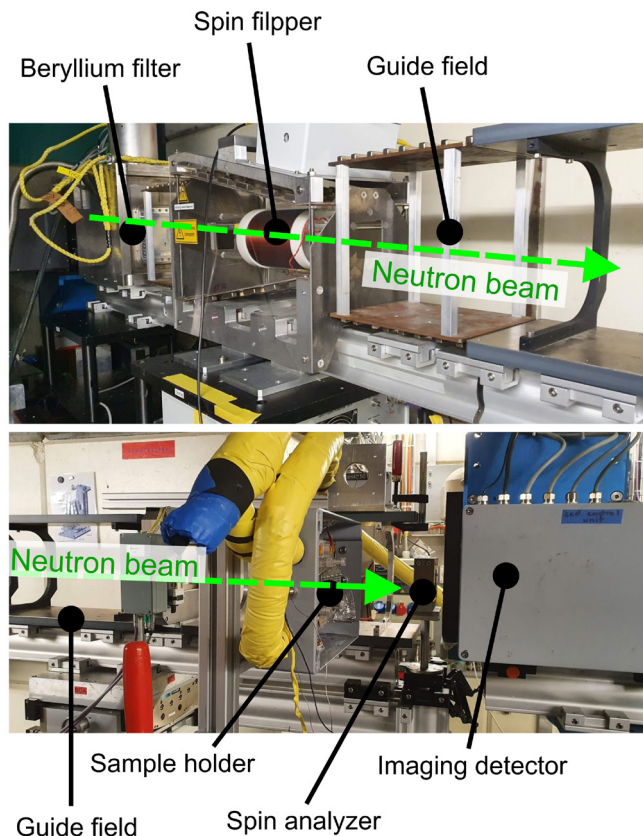


Fig. 3 Neutron depolarization imaging setup at the BOA instrument of SINQ, PSI.

The used imaging setup (Fig. 3) included a Beryllium filter to select only the neutrons with the longest wavelengths and thus enhance the contrast, a spin flipper to be able to choose between a spin-up or spin-down polarized beam, a guide field to maintain the beam polarization, a spin analyzer and an imaging detector. The sample was placed before the spin analyzer, with a distance of approximately 100 mm in order to minimize the impact of the analyzer stray field.

Several samples were measured in the form of epoxy pellets, but also directly as powders (some samples with pure powder and some using PTFE powder as a filler to reduce the concentration). A first coarse analysis did show that the contrast provided by the dilute powders and by the pellets was rather low, and a detailed assessment requires an updated image processing sequence in order to correct for scattered neutrons. With the pure powders, the depolarization was sufficiently strong to be analyzed with the coarse processing (Fig. 4). This analysis could only be conducted with the commercial Ni powders due to the limited quantity of synthesized powders. Nevertheless, they are very insightful for the future choice of nanoparticles.

The first important result is the fact that a strong depolarization is only obtained with very high powder concentrations. In order to integrate the nanoparticles into fuel cell materi-

als, we will need to obtain a measurable depolarization with lower concentrations. This indicates that the focus needs to be placed on particles with stronger magnetic moments. The other important result is that despite temperatures being significantly lower than the Curie temperature – the rather large commercial nanoparticles are expected to result only in a limited reduction of this temperature – a clear impact of the temperature on the depolarization could be identified (Fig. 4).

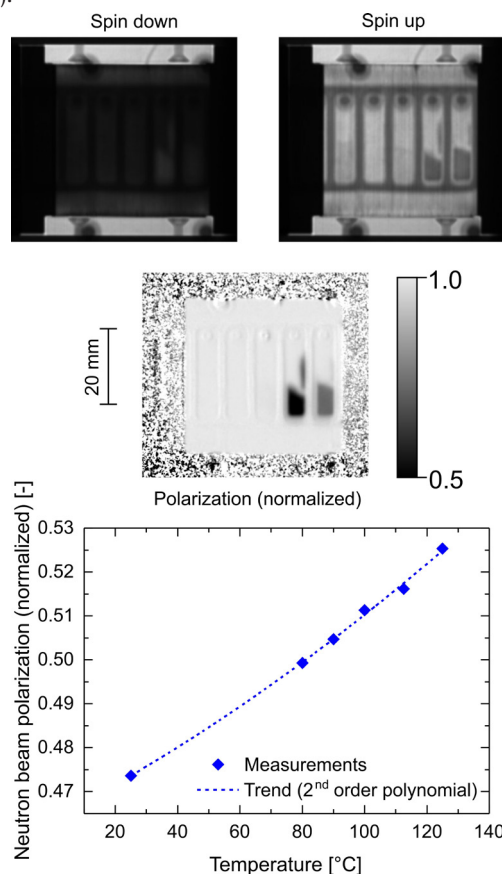


Fig. 4 Neutron depolarization imaging results. The temperature dependency chart corresponds to the pure Ni commercial powder.

These results will inform the further search for the ideal magnetic nanoparticles for this application, and they indicate that the focus needs to be placed on strong magnetic moments, even if this means that the Curie temperature is further away from the temperatures of interest.

References

- [1] F. Fievet, J. P. Lagier, B. Blin, B. Beaudoin, M. Figlarz, *Homogeneous and heterogeneous nucleations in the polyol process for the preparation of micron and sub-micron size metal particles*. Solid State Ion. **32-3**, 198-205 (1989)
- [2] A. Pătru, P. Antitomaso, R. Sellin, N. Jerez, P. L. Taberna, F. Favier, *Size and strain dependent activity of Ni nano and micro particles for hydrogen evolution reaction*. Int. J. Hydrogen Energy, **38**, 11695 (2013)
- [3] J. Chatterjee, M. Bettge, Y. Haik, C. J. Chen, *Synthesis and characterization of polymer encapsulated Cu–Ni magnetic nanoparticles for hyperthermia applications*. J. Magn. Magn. Mater., **293**, 303-309 (2005)

Recording movements of biomolecules in action

Project P1904: Revealing protein binding dynamics using time-resolved diffraction experiments at SwissFEL

Project Leader: C. Padeste and T. Ward

Collaborators: M. Carrillo (SNI PhD Student), I. Martiel, J. Beale, and A. Karpik

The creation of molecular movies of biomolecules “in action” based on time-resolved diffraction experiments has come within reach thanks to the availability of X-ray Free-Electron Lasers (XFELs), such as SwissFEL, the new large-scale facility at PSI. This project targets the development of XFEL-based methods for dynamic studies of protein-binding events, using the binding of photo-cleavable biotin derivatives to streptavidin as a versatile model system.

Background

The flexibility and adaptability of the structure of proteins is a key property with a strong influence on their functionality. The mobility of protein chains allows opening and closing of channels, as well as the adaptation of binding pockets to regulate binding processes [1]. As these movements are very difficult to access with experimental methods, recent research relies mostly on computational methods and model calculations.

X-ray crystallography is one of the most versatile methods for protein-structure determination. It reaches a resolution down to the Angstrom-range for many proteins, provided that they form good-quality crystals of reasonable size. However, standard crystallographic methods are unsuitable to reveal information on dynamic changes within proteins, on the one hand because of the long sampling time and limited time resolution, and on the other hand because the crystal itself imposes a (diffusion-) barrier against interacting molecules. Furthermore, to reduce radiation damage during data collection, high-resolution measurements are usually carried out at cryogenic conditions, where protein dynamics and movements become negligible.

XFELs delivering ultra-bright and femtosecond short X-ray pulses provide attractive means to circumvent these limitations [2]. They allow high-resolution structure-determination at room temperature using crystals of relatively small sizes and are suitable for time-resolved measurements using pump-probe techniques. The special feature of the ultra-high pulse intensity, i.e. damaging or destroying the exposed crystal by the probing laser pulse, has led to the development of serial femtosecond crystallography (SFX), whereby each measurement is carried out on a fresh microcrystal. To deliver the protein crystals at high frequency to the probing X-ray beam, liquid jet and viscous media injection technologies, as well as the so-called fixed-target technology have been developed [3]. In the latter approach, the crystalline sample is deposited on a thin film support, which is mounted on a scanning stage and scanned through the beam in order to sequentially probe the individual microcrystals with the highly focused X-rays. The serial approach also opened the path to dynamic studies, in particular for proteins that react on light stimulation resulting in a conformational change. Important ex-

amples include proteins of the rhodopsin family, where triggering conformational changes by lasers followed by probing with X-rays at different time-points has been demonstrated [4].

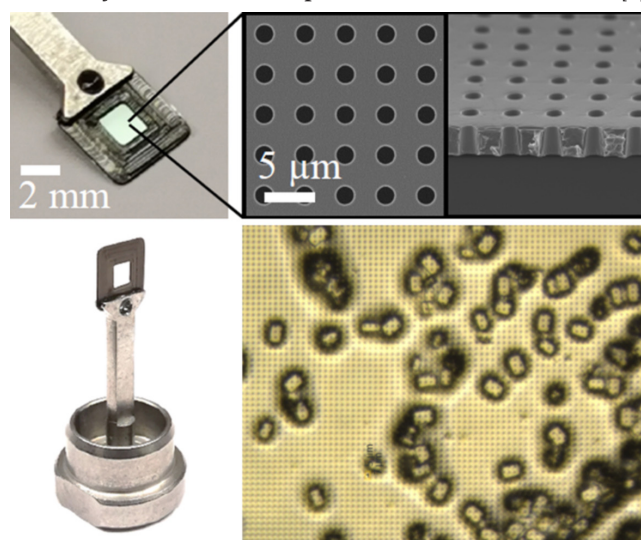


Fig. 1 Solid supports for serial protein crystallography at cryogenic conditions developed at PSI. The perforated membrane allows efficient blotting of the mother liquor of the deposited protein crystal suspension in order to minimize x-ray scattering background. Bottom right: example of a preparation of lysozyme microcrystals prior to shock-freezing of the sample.

The main objective of this project is the tracing of molecular movements during protein binding events using time-resolved diffraction experiments at SwissMX, the SwissFEL end-station dedicated to fixed-target SFX measurements. To achieve this ambitious goal, we will combine the developments of sample preparation and measurement techniques with a streptavidin-based model system.

Solid support development

Development of polymer-based solid supports holding the protein microcrystals for fixed-target experiments has started at PSI a few years ago. In this approach, we were taking advantage of specific properties of polymers such as elasticity, low density and low x-ray scattering, as well as their suitability for mass fabrication using replication technologies. In particular, supports for measurements at cryogenic conditions were fabricated using nanoimprint lithography and 3D printing techniques [5]. These supports consist of a perforated COC membrane of only 3 μm in thickness, which is suspended in a polymer frame (Fig. 1). Such supports proved to be well suited for serial crystallography measurements under cryogenic conditions at both, synchrotrons and XFELs.

The development of polymer supports for room temperature measurements, as needed in this project, is based on prototype devices fabricated at PSI (Fig. 2). Here, we used hot embossing to imprint arrays of cavities in a 50- μm thick polymer film. Openings at the bottom of the cavities allow blotting of the solution containing micro-crystals. This produces a draft that should eventually drag individual crystals to the center of the cavities. Enclosure between two polymer membranes protects the crystals from drying out before the measurement.

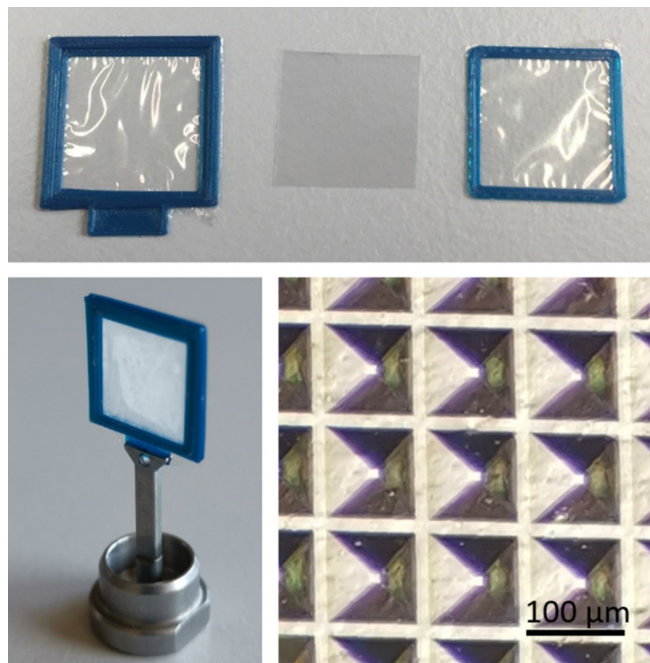


Fig. 2 Prototypes of supports for serial-crystallography measurements at room temperature. A polymeric membrane with cavities holding the protein crystals is sandwiched between two polymer films suspended in 3D printed frames. The cavities of about 100 μm in size are formed in a double replication process starting from a microfabricated silicon master.

For the current project, the holders need to be optimized in the dimensions and arrangements of the cavities to yield optimum crystal distribution. Furthermore, the incoupling of an optical laser beam triggering the photoreaction has to be foreseen and optimized in a way to guarantee activation of crystals exclusively in the probed cavity.

The streptavidin model system

Streptavidin is a highly symmetric tetrameric β -barrel protein with a wide range of biotechnological applications. The most prominent feature is its very high affinity for biotin, which is among the highest known for non-covalent small molecule-protein interactions. By enzymatic or chemical means, biotin can be covalently linked to very diverse targets including protein surfaces, fluorogenic probes, drug molecules or catalytically competent metal complexes, resulting in a wealth of accessible properties and functionalities. More recently, evolved variants of streptavidin have been shown to bind peptides with high affinity (up to nanomolar dissociation constant). Strep-tag II, as used in this project as an alternative binder to biotin, consists of eight amino-acids (Trp-Ser-His-Pro-Gln-Phe-Glu-Lys) [6]. Photocaged derivatives of both, biotin and Strep-tag II, will be employed in this study. Exposure of streptavidin co-crystallized with these caged compounds with 250-350 nm photons induces uncaging and binding to streptavidin at a defined time point.

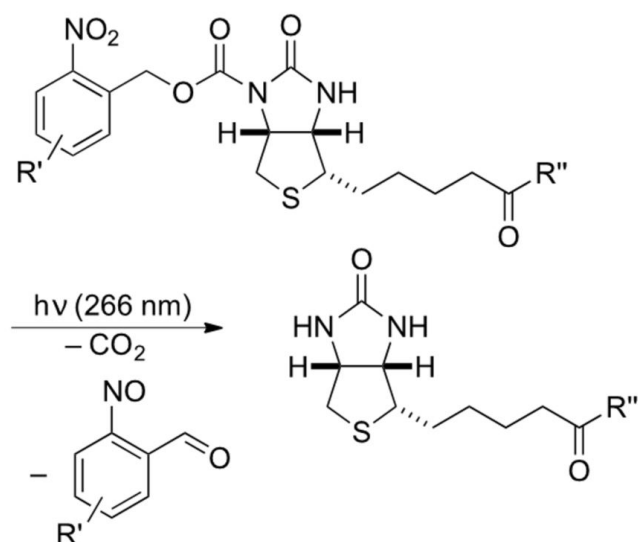


Fig. 3 One of the proposed systems to investigate protein-binding dynamics: The photo-caged biotin does not bind to streptavidin. Exposure with 266 nm photons induces uncaging and binding of this derivative co-crystallized with streptavidin.

References

- [1] A. Stank, D. B. Kokh, J. C. Fuller, R. C. Wade, *Protein Binding Pocket Dynamics*, *Acc. Chem. Res.* **49**, 809 (2016)
- [2] S. Boutet et. al., *High-resolution protein structure determination by serial femtosecond crystallography*, *Science* **337**, 362 (2012)
- [3] M.S. Hunter et al., *Fixed-target protein serial microcristallography with an x-ray free electron laser*, *Sci. Rep.* **4**, 6026 (2014)
- [4] P. Nogly et al., *Retinal isomerization in bacteriorhodopsin captured by a femtosecond x-ray laser*, *Science* **361**, 127 (2018)
- [5] A. Karpik, I. Martiel, P. M. Kristiansen, C. Padeste, *Fabrication of ultrathin suspended polymer membranes as supports for serial protein crystallography*, *Micro and Nano Engineering*, **7**, 100053 (2020)
- [6] T. Schmidt, A. Skerra, *The Strep-tag system for one-step purification and high-affinity detection or capturing of proteins*, *Nat. Protoc.* **2**, 1528 (2007)

Applying nanowire MFM to 2D materials

Project P1905: Magnetic force microscopy with nanowire transducers

Project Leader: M. Poggio and E. Meyer

Collaborator: L. Schneider (SNI PhD Student)

Introduction

Recent years have seen rapid progress in nanometer-scale magnetic imaging technology, with scanning probe microscopy driving remarkable improvements in both sensitivity and resolution. Among the most successful tools are magnetic force microscopy (MFM), spin-polarized scanning tunneling microscopy, as well as scanning magnetometers based on nitrogen-vacancy centers in diamond, Hall-bars, and superconducting quantum interference devices. Here, we aim to apply recently developed nanowire (NW) force sensors as MFM probes. Using NWs functionalized with magnetic tips, we strive to map magnetic fields and dissipation with enhanced sensitivity and resolution compared to the state of the art. With these new capabilities, we intend to study mesoscopic current flow and magnetization in 2D materials.

A key component in any force microscopy is the force sensor, which consists of a mechanical transducer, used to convert force into displacement, and an optical or electrical displacement detector. In MFM, “top-down” Si cantilevers with sharp tips coated by a magnetic material have been the standard transducer for years. Under ideal conditions, state-of-the-art MFM can reach spatial resolutions down to 10 nm, although more typically around 100 nm. These cantilevers are well-suited for the measurement of the large forces and force gradients produced by strongly magnetized samples. The advent of NWs and carbon nanotubes grown by “bottom-up” techniques now gives researchers access to much smaller force transducers than ever before. This reduction in size implies both a better force sensitivity and potentially a finer spatial resolution. Sensitivity to small forces provides the ability to detect weak magnetic fields and therefore to image subtle magnetic patterns; tiny concentrated magnetic tips have the potential to achieve nanometer-scale spatial resolution, while also reducing the invasiveness of the tip on the sample under investigation. Such improvements are crucial for imaging nanometer-scale magnetization textures, as well as for mapping mesoscopic transport in 2D systems, and imaging small ensembles of spins.

Recent research efforts – including in our lab – have demonstrated the use of single NWs as sensitive scanning force sensors [1]. When clamped on one end and arranged in the pendulum geometry, i.e. with their long axes perpendicular to the sample surface to prevent snapping into contact, they probe both the size and direction of weak tip-sample interactions. NWs have been demonstrated to maintain excellent force sensitivities around $1 \text{ aN}/\text{Hz}^{1/2}$ near sample surfaces ($<100 \text{ nm}$), due to extremely low noncontact friction. As a result, NW sensors have been used as transducers in force-detected nanometer-scale magnetic resonance imaging and in the measurement of tiny optical and electrical forces.

Recently, in a proof-of-principle microscopy experiment in the Poggio lab, we showed that a magnet-tipped NW can be sensitive to magnetic field gradients of just a few $\text{mT}/(\text{m Hz}^{1/2})$, equivalent to the gradient produced by a few tens of Bohr magnetons or a few nA of flowing current at a distance of a few hundred nanometers [2]. Such sensitivity compares favorably to that of other magnetic microscopies, including scanning Hall microscopy, scanning SQUID microscopy, and scanning nitrogen-vacancy magnetometry.

The low mechanical losses characteristic of NWs also make them excellent probes of tip-sample dissipation, a contrast that can be used to observe superconducting [3] and bulk structural phase transitions [4], as well as the local density of states. As shown by Grütter et al. [5], dissipation contrast in MFM maps the energy transfer between the tip and the sample and provides excellent contrast for nanometer-scale magnetic structure. Furthermore, energy dissipation plays a central role in the breakdown of topological protection and will provide important contrast for spatial studies of strongly correlated states in 2D vdW materials.

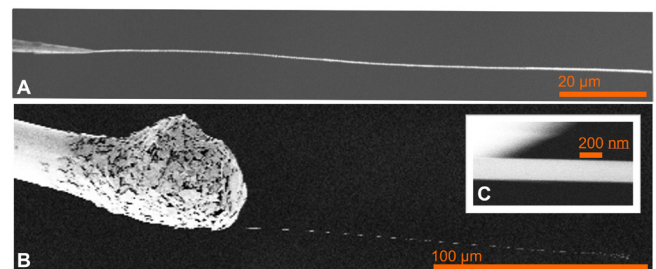


Fig. 1 Ultra-soft SiC NW. A: SiC NW glued onto etched tungsten tip with UV glue. B: 180 μm long and 200 nm thick NW glued onto tungsten wire with silver paste. C: Close-up of NW shown in B.

Goals

Despite these promising features, until now, only one proof-of-principle NW MFM experiment has been carried out on the well-known magnetic field profile of a current-carrying wire [2]. We intend to move past this demonstration stage by:

1. optimizing the magnet-tipped NW transducers to achieve the highest possible sensitivity and resolution;
2. using the new scanning probes to image magnetic skyrmions and current flow in 2D vdW systems.

Results

In the first year of work we can report progress on two fronts.

First, we have learned to pick up and attach individual ultra-soft SiC NWs to larger etched tungsten tips for mounting (Fig. 1). In the past, this type of NW has been used as an ultra-sensitive scanning force sensor, due to its excellent mechanical properties and its extreme aspect ratio [6]. Such wires can be longer than 200 μm and less than 200 nm in diameter. We next plan to functionalize these NWs with magnetic tips by evaporating magnetic caps, e.g. from FeCo, on their tips. Another strategy that we will explore is to use focused-electron-beam-induced or focused-ion-beam-induced deposition (FEBID or FIBID) of Co to grow magnetic tips at the NW ends. A system for FEBID and FIBID deposition will be installed at the Nano-imaging Lab here in Basel in January of 2021.

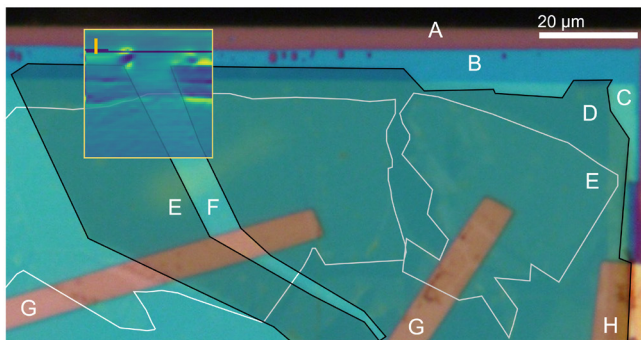


Fig. 2 MoS_2 Sample. A: Edge of undoped Si chip. B: Bottom HBN. C: Top HBN. D: Graphene back gate on top of bottom HBN. E: Multi-layer MoS_2 between back gate and top HBN. F: Multi-layer MoS_2 between bottom and top HBN. G: Leads for grounding the MoS_2 flakes. H: Lead for setting back gate potential. I: Voltage signal of FIBID Co-NW piezo-driven in PLL.

Second, we have started experiments using NW MFM to study a potentially spin-polarized electron state in monolayer MoS_2 . This work is a collaboration with the Warburton Group here in Basel, who has found evidence of this state in optical measurements [7, 8]. Their measurements support a first-order magnetic phase transition in a gated sample of MoS_2 . The phase boundary separates a ferromagnetic phase at low electron density and a paramagnetic phase at high electron density. The magnetic order is thereby controlled via the voltage applied to the gate electrode of the device. We now seek to use our extremely sensitive scanning magnetic probe, to find direct evidence of this magnetic state.

In collaboration with the Warburton Group, we have produced a gated monolayer MoS_2 sample, which can be approached using our NW MFM probe. This involved a complicated process designed to place the sample within a few tens of μm from the chip edge (Fig. 2). The sample was then characterized optically and was confirmed to show the same optical signatures of spin polarization as the original samples in references [7] and [8]. Then, the sample was loaded into our custom-built scanning NW microscope, which is capable of running at temperatures down to 4.2 K and in magnetic fields up to 8 T. The sample was mounted together with already tested and calibrated NW MFM probes made by our collaborators at the University of Zaragoza. These fully magnetic NWs made from nearly pure Co are grown by FEBID and are sensitive to a few nT/Hz^{1/2} [9]. We have also demonstrated their use as imaging probes by using them to make MFM maps of permalloy disks in magnetic vortex states [9].

The experiments on MoS_2 are currently on-going and have the potential to provide direct evidence for the proposed spin-polarized electronic state. Although conventional MFM is already applied to a wide array of samples for its ability to work at various temperatures, some experiments – like this one – remain out of reach because of limitations in magnetic field sensitivity. The extreme sensitivity to subtle magnetic field patterns offered by NW MFM makes experiments like this one on MoS_2 possible. The NWs' small tip size should also allow these magnetic sensors to work both close to a sample, maximizing spatial resolution, and in a regime of weak interaction, remaining non-invasive. We hope that these measurements in MoS_2 will serve to open a door to a large number of 2D magnets and other 2D materials with unexplored nanometer-scale magnetic contrast.

References

- [1] N. Rossi, F. R. Braakman, D. Cadeddu, D. Vasyukov, G. Tütüncüoğlu, A. Fontcuberta i Morral, M. Poggio, *Vectorial scanning force microscopy using a nanowire sensor*, Nat. Nanotechnol. **12**, 150 (2017)
- [2] N. Rossi, B. Gross, F. Dirnberger, D. Bougeard, M. Poggio, *Magnetic Force Sensing Using a Self-Assembled Nanowire*, Nano Lett. **19**, 930 (2019)
- [3] M. Kisiel, E. Gnecco, U. Gysin, L. Marot, S. Rast, E. Meyer, *Suppression of electronic friction on Nb films in the superconducting state*, Nat. Mater. **10**, 119 (2011)
- [4] M. Kisiel, F. Pellegrini, G. E. Santoro, M. Samadashvili, R. Pawlak, A. Benassi, U. Gysin, R. Buzio, A. Gerbi, E. Meyer, E. Tosatti, *Noncontact Atomic Force Microscope Dissipation Reveals a Central Peak of SrTiO_3 Structural Phase Transition*, Phys. Rev. Lett. **115**, 046101 (2015)
- [5] P. Grütter, Y. Liu, P. LeBlanc, U. Dürrig, *Magnetic dissipation force microscopy*, Appl. Phys. Lett. **71**, 279 (1997)
- [6] L. M. De Lépinay, B. Pigeau, B. Besga, P. Vincent, P. Poncharal, O. Arcizet, *A universal and ultrasensitive vectorial nanomechanical sensor for imaging 2D force fields*, Nat. Nanotechnol. **12**, 156 (2017)
- [7] J. G. Roch, G. Fröhlicher, N. Leisgang, P. Makk, K. Watanabe, T. Taniguchi, R. J. Warburton, *Spin-polarized electrons in monolayer MoS_2* , Nat. Nanotechnol. **14**, 432 (2019)
- [8] J. G. Roch, D. Miserev, G. Fröhlicher, N. Leisgang, L. Sponfeldner, K. Watanabe, T. Taniguchi, J. Klinovaija, D. Loss, R. J. Warburton, *First-Order Magnetic Phase Transition of Mobile Electrons in Monolayer MoS_2* , Phys. Rev. Lett. **124**, 187602 (2020)
- [9] H. Mattiat, N. Rossi, B. Gross, J. Pablo-Navarro, C. Magén, R. Badea, J. Berezovsky, J. M. De Teresa, M. Poggio, *Nanowire Magnetic Force Sensors Fabricated by Focused-Electron-Beam-Induced Deposition*, Phys. Rev. Appl. **13**, 044043 (2020)

Screening for nm-sized self-assembled molecular containers

Project P1906: Machine learning assisted design of heteromeric self-assembled molecular capsules

Project Leader: K. Tiefenbacher and A. von Lilienfeld

Collaborator: I. Martyn (SNI PhD Student)

Introduction

Self-assembled supramolecular capsules have exhibited promising behavior as catalysts, as their rigid internal cavity mimics the binding site of an enzyme. These structures can encapsulate guests and stabilize reactive intermediates with non-covalent interactions, providing a lower energy pathway for reactions such as terpene cyclisation [1]. However, most known hydrogen-bonded capsules are homomeric (assembled from only one building block). Homomeric capsules are limited in their ability to impose specific conformations on the encapsulated substrate, due to the high symmetry of the internal cavity (depicted in Fig. 1a) [2]. The aim of this project is to discover novel heteromeric capsules with an asymmetric cavity, which will shed light on the design principles of heteromeric capsules to inform future synthetic strategies.

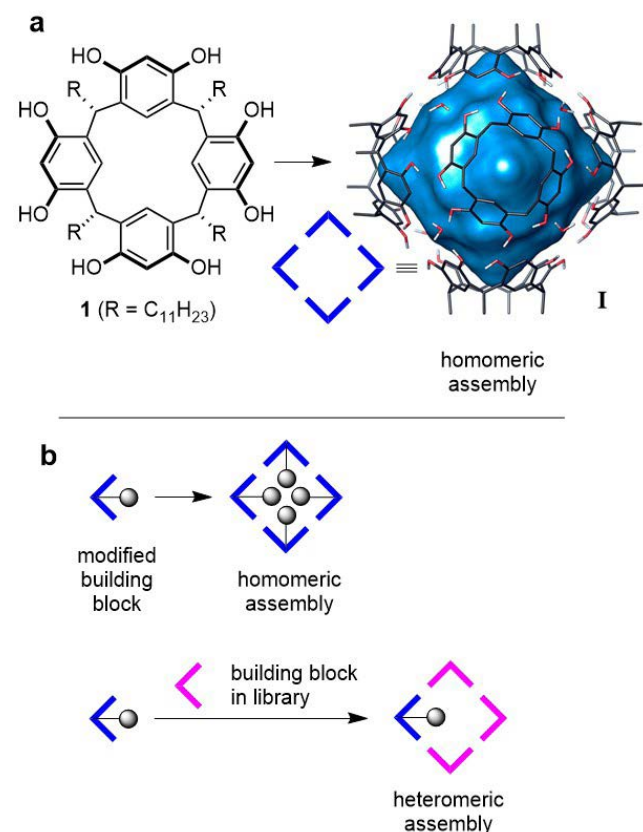


Fig. 1 a) Homomeric assembly of the resorcinarene capsule; b) Homomeric and heteromeric assembly of resorcinarene-based building blocks. The capsule remains symmetric even in the homomeric assembly of modified building blocks; symmetry is only reduced in the heteromeric assembly.

As no design principles for heteromeric hydrogen-bonded assemblies currently exist, the first stage of the project involves undirected manual screening of candidates. To achieve this, a library of over 50 suitable building blocks with hydrogen bonding motifs has been selected. The library consists of widely available compounds, that are available within the Tiefenbacher group, and others to be synthesized during the first stage of the project (Fig. 2). This library is screened for combinations of building blocks that can self-assemble into heteromeric structures, creating a combinatorial chemical space. Although some of these building blocks can form homomeric assemblies in solution, such as the hexameric resorcinarene capsule (Fig. 1a), the formation of energetically more favorable heteromeric assemblies (Fig. 1b) is also possible under certain conditions, provided that the correct mixture of building blocks is used [3]. Due to the large number of possible combinations, this space will be initially explored experimentally to provide training data, which will then be used to train QML (quantum machine learning) models that will screen the remaining combinations [4].

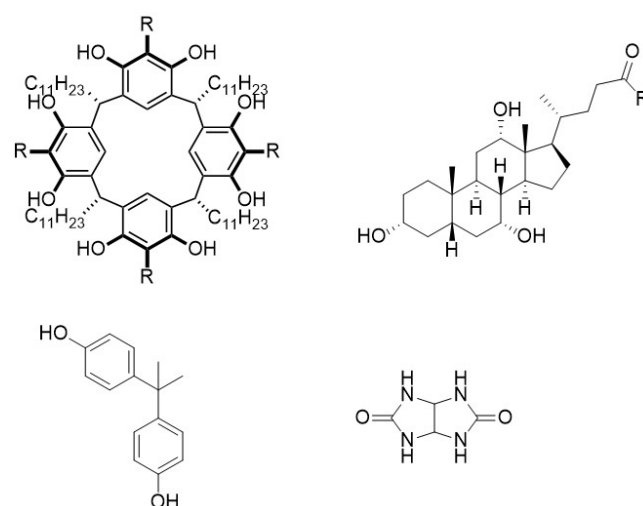


Fig. 2 Examples of building blocks in the library.

Screening

Screening of heteromeric assemblies is conducted by ¹H NMR. New, broadened, or missing peaks are all potentially indicative of heteromeric self-assembly. Further analysis of these assemblies is conducted by 2D NMR, DOSY, and other techniques as relevant. In order to quantify the experimental results, combinations of building blocks are graded from

0-4, with 0 being a solubility issue of one or more components and 4 being strong evidence of a heteromeric assembly.

Results

In the first four months of this project, seven building blocks have been synthesized. 17 building blocks were available either commercially or from within the Tiefenbacher group. Approximately 26 building blocks remain to be synthesized to complete the library.

166 unique binary and 176 unique ternary combinations have been screened, for a total of 342 binary and ternary combinations. Significant progress has been made towards the first milestone of 1'000 binary and ternary combinations in the first 12 months (Fig. 3).

	a	b	c	d	e	f	g	h	i	j	k	l	m	n	o	p	q	r	s	
a	1	1	1	1	1	1	1	1	1	1	1	1	1	1	1	1	1	1	1	1
b	1	1	1	1	1	1	1	1	1	1	1	1	1	1	1	1	1	1	1	1
c	1	1	1	1	1	1	1	1	1	1	1	1	1	1	1	1	1	1	1	1
d	1	1	1	1	1	1	1	1	1	1	1	1	1	1	1	1	1	1	1	1
e	1	1	1	1	1	1	1	1	1	1	1	1	1	1	1	1	1	1	1	1
f	1	1	1	1	1	1	1	1	1	1	1	1	1	1	1	1	1	1	1	1
g	1	1	1	1	1	1	1	1	1	1	1	1	1	1	1	1	1	1	1	1
h	1	1	1	1	1	1	1	1	1	1	1	1	1	1	1	1	1	1	1	1
i	1	1	1	1	1	1	1	1	1	1	1	1	1	1	1	1	1	1	1	1
j	1	1	1	1	1	1	1	1	1	1	1	1	1	1	1	1	1	1	1	1
k	1	1	1	1	1	1	1	1	1	1	1	1	1	1	1	1	1	1	1	1
l	1	1	1	1	1	1	1	1	1	1	1	1	1	1	1	1	1	1	1	1
m	1	1	1	1	1	1	1	1	1	1	1	1	1	1	1	1	1	1	1	1
n	1	1	1	1	1	1	1	1	1	1	1	1	1	1	1	1	1	1	1	1
o	1	1	1	1	1	1	1	1	1	1	1	1	1	1	1	1	1	1	1	1
p	1	1	1	1	1	1	1	1	1	1	1	1	1	1	1	1	1	1	1	1
q	1	1	1	1	1	1	1	1	1	1	1	1	1	1	1	1	1	1	1	1
r	1	1	1	1	1	1	1	1	1	1	1	1	1	1	1	1	1	1	1	1
s	1	1	1	1	1	1	1	1	1	1	1	1	1	1	1	1	1	1	1	1

Fig. 3 Binary combinations screened so far.

Three heteromeric assemblies have been discovered so far—two binary assemblies and one ternary. By varying the concentration of the building blocks, the optimum ratios of the building blocks for the formation of the assemblies has been determined. These assemblies are under further investigation by means of DOSY, 2D NMR, and guest uptake experiments, with definitive structure elucidation to be confirmed by X-ray crystallography.

Conclusion

Progress has been made towards the first milestone of 1'000 screened binary and ternary combinations. The undirected screening approach has already yielded evidence of heteromeric assemblies.

References

- [1] Q. Zhang, L. Catti, K. Tiefenbacher, *Catalysis inside the Hexameric Resorcinarene Capsule*, *Acc. Chem. Res.*, **51**, 2107-2114 (2018)
- [2] Q. Zhang, J. Rinkel, B. Goldfuss, J. Dickschat, K. Tiefenbacher, *Sesquiterpene cyclizations catalysed inside the resorcinarene capsule and application in the short synthesis of isolongifolene and isolongifolenone*, *Nat. Catal.*, **1**, 609-615 (2018)
- [3] A. Wu, L. Isaacs, *Self-Sorting: The Exception or the Rule?*, *J. Am. Chem. Soc.*, **125**, 4831-4835 (2018)
- [4] O. A. von Lilienfeld, *Quantum Machine Learning in Chemical Compound Space*, *Angew. Chem. Int. Ed.*, **57**, 4164-4169 (2018)

Light-mediated strong coupling of a nano-mechanical membrane to atomic spins

Project P1907: Spin-opto-nanomechanics

Project Leader: P. Treutlein and P. Maletinsky

Collaborators: G.-L. Schmid (SNI PhD Student), T. Karg, B. Gouraud, C. T. Ngai, M. Ernzer, M. Bosch, and K. Hammerer

Hybrid mechanical systems in which a nanomechanical oscillator is coupled to a spin system currently receive great interest, as they offer a powerful approach to cooling, control and detection of mechanical vibrations with potential applications in quantum metrology. Demonstrating strong spin-mechanical coupling is an important achievement in this context. Normally, strong coupling relies on short-range interactions between two systems that are placed very close to each other. In contrast, in our experiment we show that strong and highly tunable interactions between the vibrations of a nanomechanical membrane oscillator and the collective spin of a cold atomic ensemble can be mediated by light over a distance of 1 meter through a room-temperature environment [1]. This is achieved by connecting the two systems with laser light in a loop geometry [2]. Through the loop, the membrane and the atomic spin can exchange excitations via photons in a bidirectional fashion. At the same time, quantum noise introduced by the light can be made to interfere destructively in the loop, suppressing decoherence and resulting in strong Hamiltonian interactions.

Spin-membrane coupling scheme

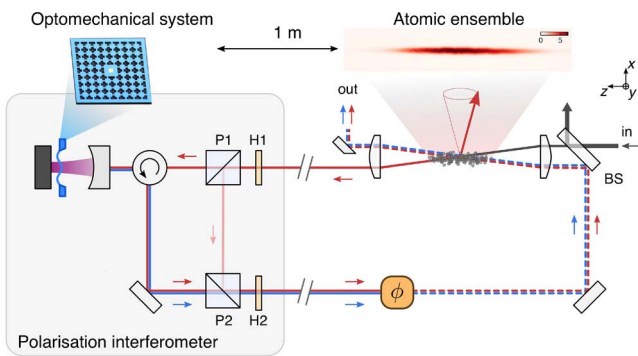


Fig. 1 Sketch of the experimental setup used to mediate the coupling between the collective spin state of a cold atomic ensemble and the membrane inside an optical cavity.

In our experiment, we couple the atomic spin two times to the optical mode, before and after the interaction with the membrane (Fig. 1). The spin-light-coupling is provided by the off-resonant Faraday interaction, with the spin polarized along a magnetic field perpendicular to the propagation direction of the light. Precession of the spin around the magnetic field rotates the linear polarization of the light by the Faraday interaction. This polarization modulation is converted to an amplitude modulation by polarization optics, resulting in a modulated radiation pressure force on the membrane inside the optomechanical cavity. A displacement of the membrane on the other hand leads to a phase

shift of the light exiting the cavity, which is converted with a polarization interferometer to a modulation of the circular polarization component of the light. By passing the atoms a second time, the circular polarization acts as an artificial magnetic field that drives the collective spin state. By changing the phase ϕ of this modulation, different interactions can be implemented.

For a loop phase of $\phi=\pi$, the effective interaction between the two systems is Hamiltonian [2]. With the spin and the membrane frequencies tuned into resonance, the coupling realizes a beam-splitter interaction between the two systems. Strong coupling is achieved if the spin-membrane coupling rate is larger than the local damping rates of the individual systems, resulting in a spin-membrane normal mode splitting. Figure 2 shows measured spectra of the membrane and the atoms which both show this normal mode splitting when the systems are coupled. In our paper [1], we also report further experiments with the coupled system, such coherent energy exchange oscillations, two-mode thermal noise squeezing, and strong dissipative coupling.

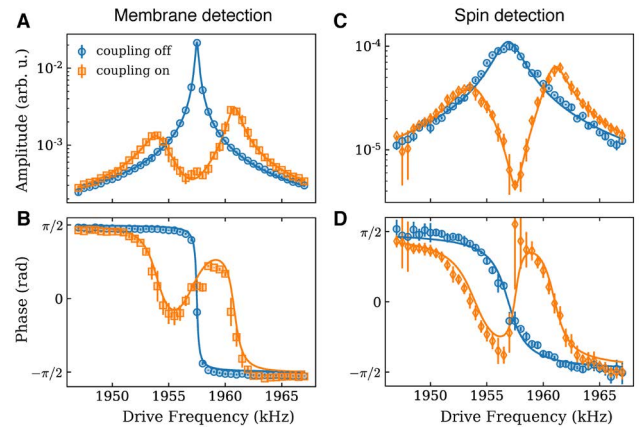


Fig. 2 Normal mode splitting of the membrane (A and B) and the spin (C and D). Here, the spectroscopy of each individual system is shown with (orange) and without (blue) coupling beam.

In the future it will be important to achieve quantum coherent coupling, for which the coupling rate has to be larger than the quantum decoherence rates of the individual systems, which are larger than the decay rates, in particular for the membrane due to its coupling to a thermal environment. In order to reach this regime, we are placing the membrane in a cryostat. On the spin side, we reduce noise in the spin-light interface and increase the coherence time with an improved active magnetic field stabilization.

Magnetic field stabilization

In our experiment, the spin is oriented perpendicular to the propagation axis of the light along a magnetic field of around $B_x = 2.8$ G. A small tilt of the spin leads to Larmor precession around this magnetic field. The Larmor precession frequency depends linearly on the magnetic field component B_x but only quadratically on the field components B_y and B_z . Thus, to stabilize the Larmor precession frequency we focus on stabilizing B_x . Limited by photon scattering from the coupling beam, a typical measurement takes between 0.5 ms to 10 ms. Thus, any magnetic field fluctuation which is faster than around 100 Hz will lead to spectral broadening of in a single measurement. Slower fluctuations of the magnetic field are not visible in a single experimental shot but are relevant if we average over many repetitions or do spectroscopic measurements. Thus, we are interested in stabilizing both, the slow and the fast fluctuations of the magnetic field.

In order to actively stabilize B_x , we installed a flux-gate sensor (bandwidth $f_{\text{sensor}} = 3$ kHz) 9 cm above the atoms (x-axis, see Fig. 3). Placing the sensor in proximity of the atoms is important because of the inhomogeneity of the magnetic field applied by the compensation coils (see insert in Fig. 3).

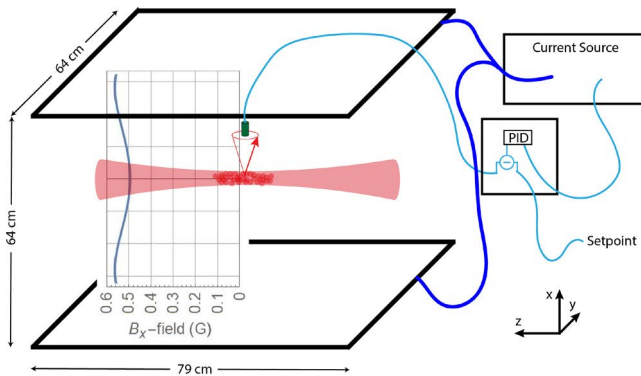


Fig. 3 Magnetic field stabilization. The inserted plot shows the effective magnetic field applied by the compensation coils along the x-axis in the central axis between the coils.

The sensor output is compared to a calibrated set-point defined by the control computer. The resulting error signal is fed back to the current source driving the compensation coils. The inductance of the coil pair is $L = 8.37$ mH. With our self-built low-noise current sources, this allows for active compensation of the fields with a bandwidth of $f_{\text{coils}} \cong 800$ Hz. Thus, we can compensate the strong magnetic field noise at 50 Hz, 150 Hz, and 450 Hz.

To characterize the performance, we used the collective atomic spin itself as magnetic field sensor. For that, we tilted the collective spin of a polarized atomic cloud by applying a small rf-field. This tilt is chosen to be small enough such that we do not significantly populate more than two Zeeman levels and thus avoid any effects due to quadratic Zeeman splitting. The spin is probed with linearly polarized light which propagates along the z-axis. Due to the Faraday interaction, the projection of the collective spin state along the propagation axis of the light is imprinted on the polarization state of the light which is then read out by homodyne detection.

A single experimental sequence takes around 2 s including MOT loading and saving the data. We repeated this magnetic field measurement for around 40 minutes. To the spectrum of each spin precession measurement, we fit a Lorentzian function (Fig. 4). The width of the Lorentzian provides a measure for the fast fluctuations of the magnetic field while

the shot-to-shot fluctuations of the center frequency provide information about the long-term stability.

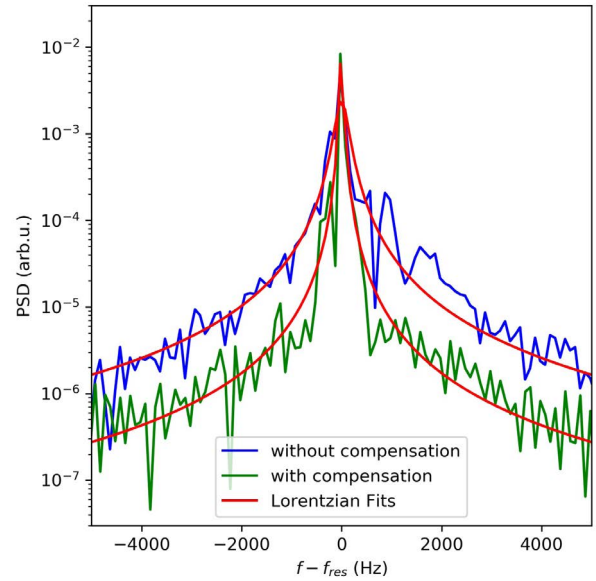


Fig. 4 Power spectral density of the spin signal with and without magnetic field stabilization. The data is normalized such that the area below both curves (and thus the spin response) is the same.

Without stabilization we observe shot-to-shot noise of 780 Hz RMS, the active stabilization lowers this to 40 Hz RMS. This fluctuation is much smaller than the typical features we are interested in. The mean line-width of the spin could be reduced from a FWHM of $340 \text{ Hz} \pm 90 \text{ Hz}$ to a FWHM of $60 \text{ Hz} \pm 30 \text{ Hz}$.

With the improved magnetic field stability we can perform measurements at low power or large atom-light detuning and still be limited by photon scattering rather than magnetic field fluctuations. This allows us to characterize the spin system much more precisely than without stabilization.

References

- [1] T. M. Karg, B. Gouraud, C. T. Ngai, G.-L. Schmid, K. Hammerer, P. Treutlein, *Light-mediated strong coupling between a mechanical oscillator and atomic spins 1 meter apart*, Science **369**, 174 (2020)
- [2] T. M. Karg, B. Gouraud, P. Treutlein, K. Hammerer, *Remote Hamiltonian interactions mediated by light*, Phys. Rev. A **99**, 063829 (2019)

Towards molecular VOC sensors – nanowires from chiral Pt(II) isocyanide complexes

Project P1908: Chiral Recognition in Molecular Nanowires from Square-Planar Platinum(II) Complexes

Project Leader: O. Wenger and C. Sparr

Collaborator: A. Huber (SNI PhD Student)

Motivation for artificial chiral VOCs sensors

Volatile organic compounds (VOCs) such as atmospheric terpenes are globally relevant not only due to their impact on climate change but also because of their diverse biological functions [1 - 3]. Notably, stereoisomers have specific roles in biology (e.g. plant communication, medicine). Detecting stereoisomers of VOCs in our environment can thus help gaining a better understanding of environmental relationships and reveal specific health risks and toxicity issues. Chiral recognition on artificial sensors is therefore highly desirable. For instance, the human nose can distinguish (R)-limonene (orange odor) from (S)-limonene (turpentine or lemon odor)[4].

To date, the fundamental aspects of chiral recognition of VOCs with nanostructured materials and their applications are underexplored [5, 6]. In this context, we designed new nanostructured “chiral nose”-type materials to selectively sense chiral VOCs. Controlled helical superstructures composed of stacked square planar platinum complexes are our key interest (Fig. 1). Interactions of small chiral molecules with the crystal lattice ideally provoke amplified changes in photoluminescence, vapochromism [7], or electrical conductance, thus exhibiting sensing behavior (Fig. 1).

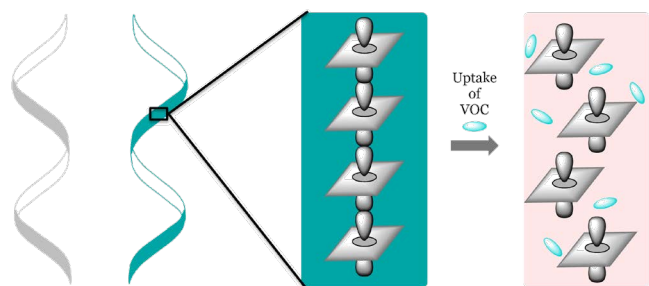


Fig. 1 Helical superstructure from stacked Pt-complexes showing VOC sensing behavior.

Stereogenic Pt(II) isocyanide complexes

In this project, we anticipate the preparation of new chiral Pt(II) complexes by introducing an atropisomeric moiety at the periphery of bi- or tri-dentate isocyanide ligands.

Thus, we take advantage of the Sparr group's expertise on atroposelective oligo-naphthylene synthesis [8, 9]. Selective formation of (R_a)- or (S_a)- atropisomeric oligonaphthylens is achieved by the iterative strategy of building block addition

to aromatic aldehydes and a subsequent arene-forming enantioselective aldol-condensation (Fig. 2a)[9]. The atropisomeric multiaxis scaffold will then be coupled to isocyanide chelate ligands, which were developed in the Wenger group (Fig. 2b)[10].

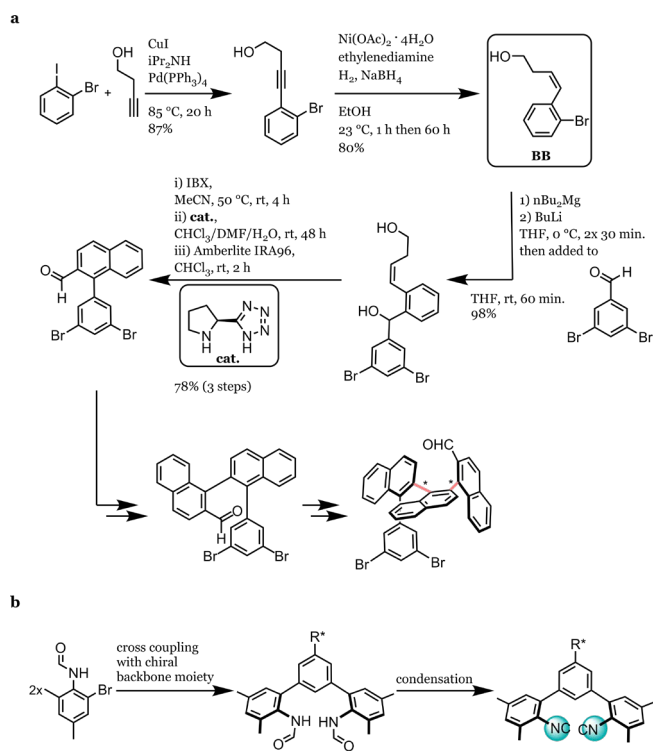


Fig. 2 a) Iterative formation of atropisomeric multi-axis scaffold. b) Schematic synthesis of bidentate isocyanide ligands coupled to the chiral moiety.

Towards controlled nanowire formation

The atropisomeric, sterically demanding ligand backbone was introduced for perturbation within the stacking orientations towards helical arrangement (Fig. 3). On the other hand, short metal-metal distances that stabilize the oligomer nanostructures can still form.

The preference of square planar Pt(II) complexes to form stacked aggregates arises from weak metal-metal interactions between the 5d_{z²} orbitals upon close contact (2-4 Å)[11]. Additionally, we increase the scope of our envisaged materials with the formation of double-salt structures. Electrostatic interactions between cationic and anionic Pt(II) complexes stabilize stacked arrangements incorporating the key atropisomeric elements.

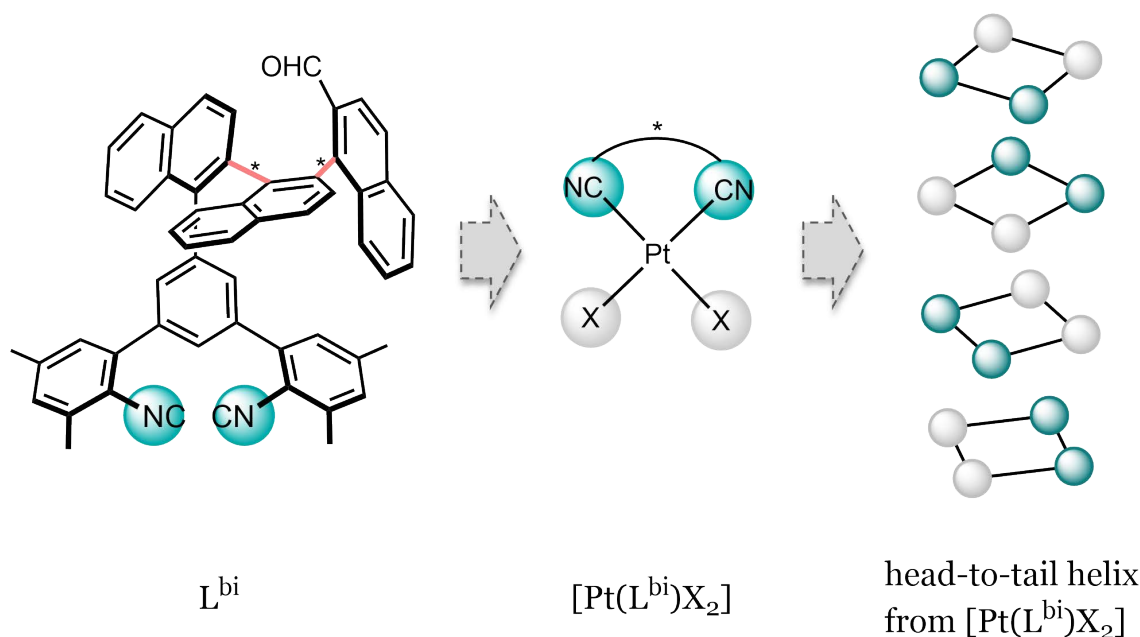


Fig. 3 Bidentate isocyanide ligand with atropisomeric moiety – corresponding Pt(II) complex – schematic helical stacking motif.

Stereoisomers of specific VOC analytes could interact with the nanowire crystal lattice by intercalation or through π - π interactions directly at the atropisomeric moieties. These subtle perturbations, can lead to measurable amplified changes in material properties.

To sum up, the naphthylene backbone synthesis proceeds towards forming the second chiral axis. Also, the parent bidentate isocyanide ligand was synthesized from 3,5-dimethylaniline and 1,3-dibromobenzene following reported methods [10]. First Pt(II) complexes are currently being investigated in terms of crystallizations, physical, and photophysical properties.

Next, the naphthylene backbone will be coupled to the isocyanide ligand. Physical characterization will focus on UV-Vis absorbance, photoluminescence, circular dichroism, and circularly polarized luminescence. The complexes and final nanostructures will be studied by X-Ray diffraction. Finally, we envisage sensing changes of the aforementioned properties upon exposure to chiral VOC analytes. Further investigations and optimization of synthesis, complexations, and crystallizations are ongoing.

References

- [1] G. Popkin, *The Forest Question*, Nature **565**, 7–9 (2019)
- [2] I. Paciência, J. Madureira, J. Rufo, A. Moreira, E. Fernandes, *A systematic review of evidence and implications of spatial and seasonal variations of volatile organic compounds (VOC) in indoor human environments*, J. Toxicol. Environ. Heal. - Part B Crit. Rev. **19(2)**, 47–64 (2016)
- [3] G. A. Sanadze, *Biogenic Isoprene (A Review)*, Russ. J. Plant Physiol., **51(6)**, 729–741 (2004)
- [4] R. Bentley, *The Nose as a Stereochemist. Enantiomers and Odor*, Chem. Rev. **106**, 4099–4112 (2006).
- [5] A. Prabodh, D. Bauer, S. Kubik, P. Rebmann, F. G. Klärner, T. Schrader, L. Delarue Bizzini, M. Mayor, F. Biedermann, *Chirality Sensing of Terpenes, Steroids, Amino Acids, Peptides and Drugs with Acyclic Cucurbit[n]urils and Molecular Tweezers*, Chem. Commun. **56**, 4652–4655 (2020)
- [6] Z. A. De los Santos, C. Wolf, *Optical Terpene and Terpenoid Sensing: Chiral Recognition, Determination of Enantiomeric Composition and Total Concentration Analysis with Late Transition Metal Complexes*, J. Am. Chem. Soc. **142**, 4121–4125 (2020)
- [7] O. Wenger, *Vapochromism in Organometallic and Coordination Complexes: Chemical Sensors for Volatile Organic Compounds*, Chem. Rev. **113**, 3686–3733 (2013)
- [8] D. Lotter, M. Neuburger, M. Rickhaus, D. Häussinger, C. Sparr, *Stereoselective Arene-Forming Aldol Condensation: Synthesis of Configurationally Stable Oligo-1,2-naphthylenes*, Angew. Chem. Int. Ed. **55**, 2920–2923 (2016)
- [9] D. Lotter, A. Castrogiovanni, M. Neuburger, C. Sparr, *Catalyst-Controlled Stereodivergent Synthesis of Atropisomeric Multiaxis Systems*, ACS Cent. Sci. **4**, 656–660 (2018)
- [10] L. Büldt, X. Guo, A. Prescimone, O. Wenger, *A Molybdenum(o) Isocyanide Analogue of Ru(2,2'-Bipyridine)₃2+: A Strong Reductant for Photoredox Catalysis*, Angew. Chem. Int. Ed. **55**, 11247–11250 (2016)
- [11] W. B. Connick, R. E. Marsh, W. P. Schaefer, H. B. Gray, *Linear-Chain Structures of Platinum(II) Diimine Complexes*, Inorg. Chem. **36**, 913–922 (1997)

Disruptive power storage technology applying electrolyte nano dispersions

Project A13.08: MEGAnanoPower (FHNW Muttentz, CSEM Muttentz, Aigys AG Rheinfelden)

Project Leader: U. Pieleš

Collaborators: S. Fricke, J. Schleuniger, M. Zinggeler, M. Waser, and A. Schimanksi

Background

The Aigys power storage technology is based on so-called redox-flow principle. The patented Aigys Power-Cell® technology uses solid dispersions instead of dissolved chemical compounds as charge carriers. This project aims to develop stable nano-dispersions as high capacity energy storage media and to apply surface enlarged nano/micro structured electrodes as efficient current collectors.

Introduction

In a first phase of the project electrolyte dispersion made of well-known lithium-based compounds were used to test the working principle of a solid dispersion redox-flow battery and to understand the basic behavior of particle based electrolyte dispersions. In the second stage of the project, the focus was on developing a water-based battery, which consists of environmentally friendly non-toxic and non-hazardous active components. A screening of potential materials, which have been already used for active components for batteries, led to iron oxides, which fulfill a large number of criteria, e.g. several oxidation stages, poor solubility, enormous abundance and complete harmlessness.

Iron oxide dispersion battery based on nano-particulate iron oxides

In a dispersion flow battery the dispersion consists ideally of stabilized nanoparticles with a small particle size, high concentration and low viscosity and thus enables a free flow of the dispersion, high contact surface area of particle to electrode and high energy density. $\gamma\text{-Fe}_2\text{O}_3$ and Fe_3O_4 in sizes from 2 - 20 nm were synthesized by basic precipitation of Fe^{2+} and Fe^{3+} in water.

While stabilizers investigated included compounds such as silanes and modified nitrodopamine which are covalently bound to the iron oxides, best stabilization was obtained with non-covalently bound compounds. For acidic dispersions nitric acid was used, ammonium citrate for neutral dispersions and tetraethylammonium hydroxide (TEAOH) for alkaline dispersions. These iron oxide dispersions are easily synthesized, can sustain high solid contents of up to 40% while keeping a fluid consistency and remained stable for months while the project was running. Moreover, when the oxidation state of the iron is changed the dispersion remains stable. A disadvantage however is that these dispersions are only stable within a certain concentration range of the dispersant and that high concentrations of dispersant lead to flocculation. For some experiments, a 5 molar potassium hydroxide or lithium hydroxide solution was used as supporting electrolyte which inhibited stabilization.

Electrochemical characterization

Within the project the focus lay on a half-cell setup in order to characterize the redox process of iron oxide. Half-cell systems with concentrated supporting electrolyte, 5 molar LiOH or KOH, with the disadvantage of sedimentation were characterized and systems which formed a supporting electrolyte but maintained stable dispersions.

For all systems with concentrated supporting electrolyte, chronoamperometric analysis showed currents that were orders of magnitude lower than what comparable redox-flow batteries deliver as current, independent of $\alpha\text{-Fe}_2\text{O}_3$ or $\gamma\text{-Fe}_2\text{O}_3$ and with either nanoparticles or microparticles as primary particles. Thus stable dispersions seemed to be more promising and were investigated for the continuation of the project.

Cyclic voltammetry (CV) of stable dispersion showed the influence of the solvent on the redox behavior of the dispersions (Fig. 1).

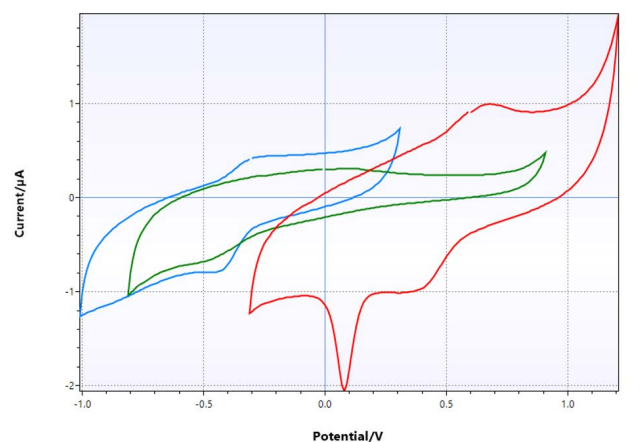


Fig. 1 Measured CV curves for dispersions of $\gamma\text{-Fe}_2\text{O}_3$ 1 mM in TEAOH 0.1 M (blue), ammonium citrate 0.1 M pH 7 (green) and HNO_3 0.1 M (red). Glassy carbon working electrode 3 mm, Pt counter electrode, Ag/AgCl reference electrode, scan rate: 10 mV/s

For dispersions in HNO_3 and TEAOH small reduction and oxidation waves can be observed. For ammonium citrate no wave is observed. This might be due to the insolubility around pH 7. For ammonium citrate with lower pH reduction and oxidation can be observed but it is almost at background level for $\text{pH} > 4$ [1]. The second reduction wave in HNO_3 at 0.1 V originates from nanoparticles already adsorbed to the surface of the electrode and corresponds to dissolution of nanoparticles [2]. Apart from different currents, also

different reduction potentials are observed between acidic and basic conditions.

Comparing the dispersion of $\gamma\text{-Fe}_2\text{O}_3$ to dissolved Fe^{3+} in HNO_3 shows similar reduction and oxidation waves (Fig. 2). The open circuit potential is different with 0.40 V and 0.56 V for $\gamma\text{-Fe}_2\text{O}_3$ and Fe^{3+} , respectively. The current for $\gamma\text{-Fe}_2\text{O}_3$ is controlled by rate of nanoparticle diffusion [1].

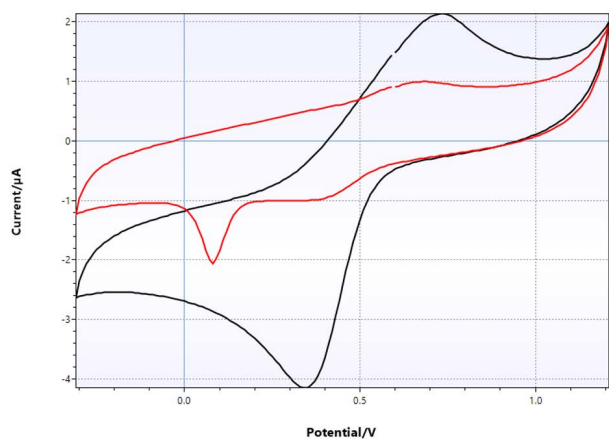


Fig. 2 CV of dispersion of $\gamma\text{-Fe}_2\text{O}_3$ 1 mM (red) vs FeCl_3 0.1 mM (black) both in HNO_3 0.1 M.

The solvent not only has an influence on the reduction potential of iron oxide nanoparticles but also on the potential window for electrochemical processes. Table 1 shows the limits at which water oxidation or reduction start to be the limiting factor.

Table 1 Potential window of used solvents

HNO_3	$(\text{NH}_4)_3\text{Cit}$	TEAOH
-0.8 V – 1.2 V	-1.2 V – 1.1 V	-1.8 V – 0.8 V

Further investigations of the electrochemical behavior were conducted with dispersions in HNO_3 . Acidic dispersions showed highest current response and can be easily compared with dissolved iron, as it is only soluble in acidic conditions. Chronoamperometry (CA) of stirred dispersions was performed to measure the possible charging/discharging currents of the studied systems. For CA a carbon felt working electrode was employed to increase the reactive surface area and therefore the currents to be measured. Figure 3 shows CA of a dispersion of iron (III) oxide vs a solution of Fe^{3+} .

As expected from the CV experiment, dissolved iron shows higher current than an iron oxide dispersion. Integration of the signals shows that figure 2C of charge for dissolved iron flowed both for reduction and oxidation. This is equal to complete reduction of Fe^{3+} to Fe^{2+} . About half of that charge flowed for iron oxide nanoparticles.

CA was also performed with the highest concentration of $\gamma\text{-Fe}_2\text{O}_3$ in nitric acid that showed no apparent increase in viscosity. At about 400 g/l $\gamma\text{-Fe}_2\text{O}_3$, which is 2.7 M, CA however showed oxygen formation at the counter electrode.

To test the applicability of nanoparticle dispersions as redox-flow battery system, two half cells were separated by an anion exchange membrane and carbon felts were used as electrodes. One half cell consisted of a $\gamma\text{-Fe}_2\text{O}_3$ nanoparticle dispersion and the other half cell of dissolved Fe^{2+} , both at a

concentration of 50 mM. The first step was a charging step to reduce Fe^{2+} . Then the cell was cycled at very low current densities of $5 \mu\text{A}/\text{cm}^2$ (Fig. 4). The cycling shows a strong voltage drop over time.

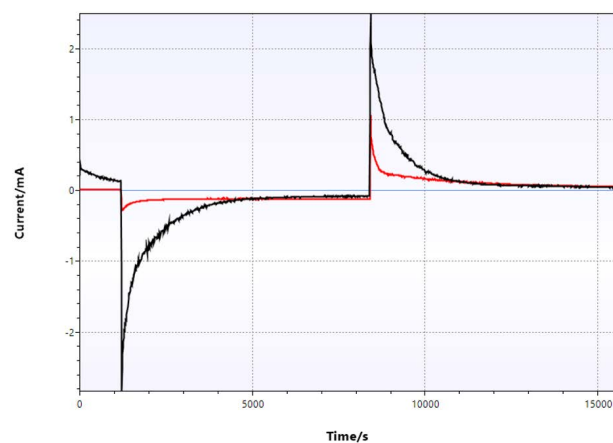


Fig. 3 CA of $\gamma\text{-Fe}_2\text{O}_3$ 5 mM (red) and FeCl_3 5 mM (black) in HNO_3 0.1 M. 20 min. at 1.0 V, then 2 h at 0.1 V and 2 h at 1.0 V. Carbon felt working electrode with an approximate surface area of 68 cm^2 for 4 ml of volume.

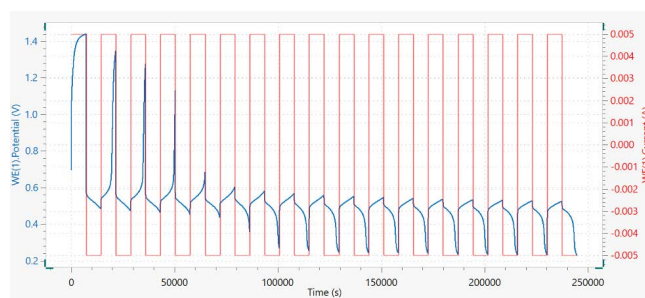


Fig. 4 Chrono charge-discharge galvanostatic for the full cell $\gamma\text{-Fe}_2\text{O}_3/\text{Fe}_3\text{O}_4//\text{Fe}^{2+}/\text{Fe}(0)$. Carbon felt WE and CE with surface area of approx. 1000 cm^2 .

Conclusion

Stable nano-dispersions have been formulated and in chrono-charge-discharge cycles the feasibility to use such nano-dispersions in redox flow cells has been demonstrated. Further investigations and developments of the nano-dispersions as well as the flow cell are needed to increase the capacity and the stability of such redox-flow cells.

References

- [1] J. J. P. Roberts, J. A. Westgard, L. M. Cooper, R. W. Murray, *Solution Voltammetry of 4 nm Magnetite Iron Oxide Nanoparticles*, *J. Am. Chem. Soc.* **136**, 10783–10789 (2014)
- [2] I. T. Lucas, E. Dubois, J. Chevalet, S. Durand-Vidal, *Reactivity of nanocolloidal particles $\gamma\text{-Fe}_2\text{O}_3$ at the charged interfaces : Part 1. The approach of particles to an electrode*, *Phys. Chem. Chem. Phys.* **10**, 3263–3273 (2008)

A detector for pesticides in drinking water

Project A14.04: DeePest (FHNW MuttENZ, FHNW Windisch, Mems AG Birmenstorf)

Project Leader: J. Pascal

Collaborators: D.-V. Nguyen, M. Olesinska, P. Shahgaldian, N. Karlen, E. Weingartner, and D. Matter

Introduction

The goal of the DeePest project (A Detector for Pesticides in Drinking Water) is to develop a novel pesticide monitoring system based on the remarkable molecular recognition capabilities of engineered nanostructured polymers associated to a bimodal electronic detector. The system shall first concentrate the pesticide by flowing water through the polymer and then detect it with a bimodal detector.

Nanostructured polymers: glyphosate-binding gels

DeePest detector relies on the high adsorption properties of a polymeric based pesticide concentrator cartridge. Here, we have developed a hydrogel-based system capable of molecular recognition [1] of glyphosate (Fig. 1). The project explored the effect of the size and porous structure of a gel as well as functionalization of the gel's polymeric backbone on the glyphosate binding.

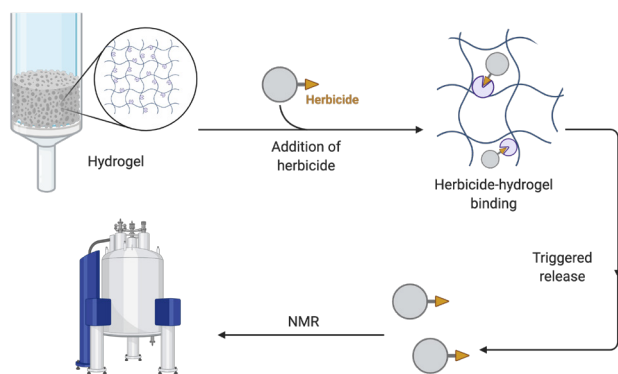


Fig. 1 Schematic representation of the herbicide recognition-storage-triggered release hydrogel-based system.

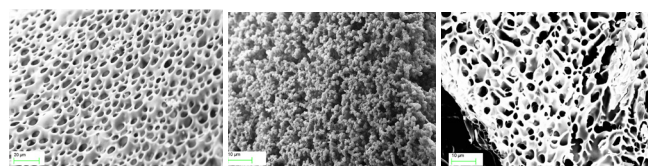


Fig. 2 SEM images of freeze-dried unfunctionalized H1, H2 and functionalized H3 hydrogels.

Several types of hydrogels have been synthesized in order to optimize their structural and mechanical properties such as porosity, swelling, durability, strength as well as the pesticide-unique recognition, adsorption and triggered release capabilities. Hydrogels with diverse monomer composition and different density of cross-links were formulated through a free radical polymerization with azobisisobutyronitrile

as a radical initiator. We used four types of monomers, i.e. maleic anhydride, N-isopropylacrylamide, acrylamide, 1-(2-Aminoethyl)maleimide and the cross-linker N,N'-methylene-bis-acrylamide to form an unfunctionalized and functionalized generation of hydrogels. Based on rheological and morphological characterization, unfunctionalized H1 and H2, as well as functionalized H3 hydrogels, were selected for further tests with glyphosate binding (Fig. 2). The glyphosate binding test with hydrogels was done using a concentrated aqueous solution of glyphosate in pH 2 and 11. Hydrogels were soaked in glyphosate solution and incubated in room temperature, with a mild shaking motion for over 24 h. Small samples of the soaking solution were taken out after 30 min, 1 h, 2 h, 5 h and 24 h; then tested via NMR using an internal standard. Comparison of the binding result for H1, H2 and H3 hydrogels is summarized in figure 3. The unfunctionalized hydrogels showed no effective recognition properties either based on their porosity or in different experimental conditions. The functionalized hydrogel H3 showed 77% binding efficiency of glyphosate from the solution in pH 2 after 24 soaking, and only 10% in pH 11.

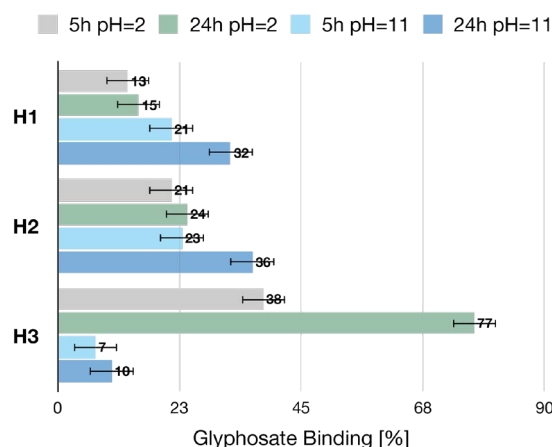


Fig. 3 Comparison of the glyphosate binding efficiency of H1, H2 and H3 type of hydrogel. Experiment done in MQ water in pH=2 and pH=11 over 5 h and 24 h.

Miniaturized NMR-detector

The first detection modality consists in an NMR measurement. The in-house NMR probe (Fig. 4) can work within a low magnetic field generated by palm-size permanent magnets (typically 0.5 to 1.5 T). We developed the circuitry connected to the probe which reads out the resonance signal picked up by the coil whereas the proton excitation is currently generated by a commercial NMR transmitter.

The experimental tests of the DeePest NMR probe have been carried out using the permanent magnet of a Magritek Spin-

solve 60 benchtop NMR. The DeePest probe, containing first water then ethanol, has been inserted inside the 1.5 T bore of the Spinsolve 60. Finally, the detection of Glyphosate and Atrazine has been tested. Ethanol was used to validate the capability of our setup to discriminate NMR peaks which are separated by less than 0.05 ppm as illustrated in figure 5. Figure 6 shows the results obtained with atrazine in acetonitrile at high concentration corresponding to the solubility (1 mg/mL). The present configuration of the electronics allows performing 16 scans, which leads to the limit of detection for atrazine. However, for Glyphosate the NMR signal is around ten times stronger than for atrazine and leads to NMR peaks that are clearly above the noise level. Further development of the DeePest NMR probe will allow us to improve the limit of detection. First a number of scans larger than 16 will be implemented. Second a new coil design which improves the minimum NMR pickup voltage that can be detected (presently 219 pV) will be investigated. This new design will allow us to detect atrazine also in lower concentration.



Fig. 4 DeePest NMR probe featuring the inserted coil and the matching/tuning circuit. The DeePest electronics is connected to this probe.

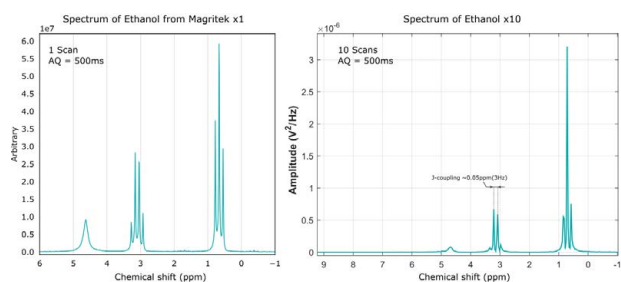


Fig. 5 NMR spectrum of ethanol obtained with the Magritek Spinsolve 60 (left) and with the DeePest NMR probe (right). The DeePest probe is capable of discriminating peaks down to 0.05 ppm.

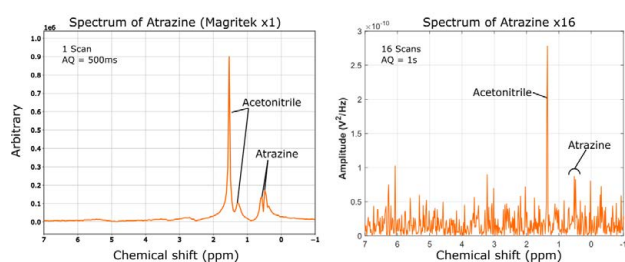


Fig. 6 NMR spectrum of atrazine in acetonitrile obtained with the Magritek Spinsolve 60 (left) and with the DeePest NMR probe (right). Only 16 scans lead to the limit of detection for the DeePest probe.

Fluorescence Detection of PAHs and Pesticides

The third module of the continuous monitoring system is a development to detect PAHs and pesticides by fluorescence. To allow a low detection limit despite a small detection volume, a spiral setup was designed. Its advantage is the high fluorescence light output combined with a low background

due to total reflection of the excitation light which stays inside the spiral (Fig. 7). Due to isotropic fluorescence radiation, the emission light can leave the spiral and be detected by a photomultiplier or photodiode. The final setup is cost-effective because only an LED and no optical filters are needed. To show the proof of concept, fluorescein was dissolved in distilled water and measured with a laser diode of 405 nm and 20 mW optical power (Fig. 8, left). In a next step, measurements can be transferred into the UV-wavelength range to measure pesticides using a customized low-cost LED.

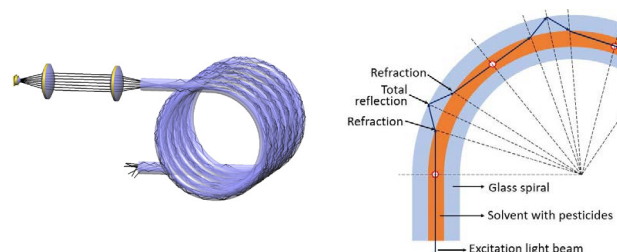


Fig. 7 Simulation of the excitation light (left) that stays inside the spiral by total reflection (right).

Measurements showed a linear correlation between the light detector signal and the fluorescein concentration (Fig. 8, right). The current setup allows a resolution of about 10 µg/l that corresponds to 0.5 ppb.

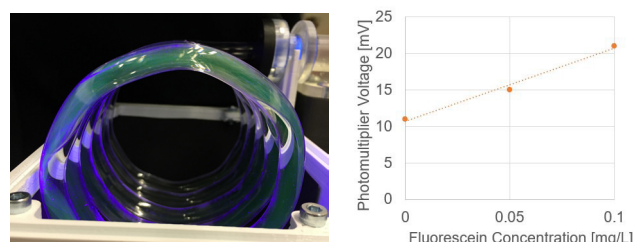


Fig. 8 Emitted fluorescence light in the spiral setup (left) and measurement results with a laser diode (right).

In a next optimization step, the signal offset should be minimized. Furthermore, a suitable low-cost LED light source has to be used with several milliwatt power and a light spectrum in the UV range. The signal slope can be increased by an optimized glass surface that prevents light losses over the spiral length.

In Switzerland a limit value of 0.1 µg/l in drinking water is defined for pesticides, e.g. Chlorothalonil. Assuming that the detected pesticides have a similar quantum yield as fluorescein, this technique has great potential to be further developed to a commercial measurement device especially because the pesticide concentration is enriched in the concentrator cartridge by several orders of magnitude.

Conclusion

The combination of pesticide concentrators based on nanostructured polymers with a bimodal sensing opens the way to the development of an inexpensive and lightweight device capable of detecting pesticides in drinking water.

References

- [1] M. Moradi, L.G. Tulli, J. Nowakowski, M. Baljovic, T. A. Jung, P. Shahgaldian, *Two-Dimensional Calix [4] arene-based Metal–Organic Coordination Networks of Tunable Crystallinity*, *Angew. Chem. Int. Ed.*, **56(46)**, 14395-14399 (2017)

Origami heart model based on nano-patterned paper scaffold for directed cardiac tissue engineering

Project A14.07: KOKORO (FHNW MuttENZ, University of Basel DBM, Omya International AG Oftringen)
Project Leader: M. R. Gullo
Collaborators: J. Köser, A. Banfi, A. Marsano, J. Schoelkopf, and G. Melo Rodriguez

Myocardial infarction is the leading cause of death (34% in 2015) and the third-leading cause of hospitalization (13% in 2015) in Switzerland. Current research efforts focus on in-vitro heart models for understanding the mechanistic function of healthy and diseased hearts, and test the efficacy of potential therapeutics. In particular, 3D contractile cardiac chambers are required to assess the effect on ventricle pressure, contractile forces, electro-physiological aspects and volume dynamics. Current efforts in 3D bioprinting such chambers resulted in fragile structures, rather suited for single proto-types [1 - 6]. However, for a representative assay a much higher number of models is necessary. The current project aims to address this challenge by developing nano-structured cellulose scaffolds for vascularized myocardial tissue growth. By origami methods, the planar tissue may then be folded into a 3D heart ventricle facsimile. A schematic representation of the method is shown in figure 1.

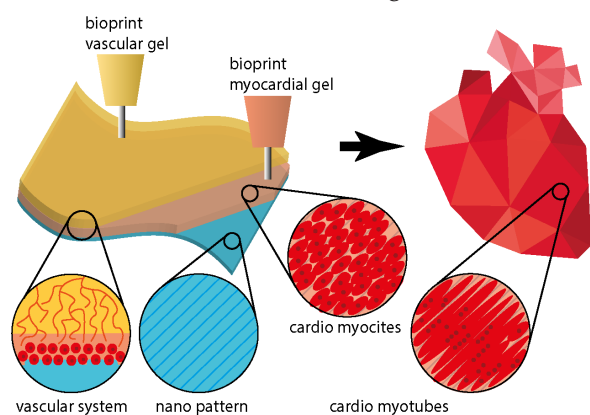


Fig. 1 Schematic representation of the project goals: A cellulose scaffold with the desired stiffness and nano-patterns. Hydrogels containing myocardial cells and vascularizing cells will be 3D bioprinted onto the scaffold. The scaffold sheets containing the differentiated/aligned myotubes will be folded into a heart shape by origami techniques.

Origami paper folding – prototype and upscale

Based on our previous origami patterns evaluation, a slightly modified Miura pattern was selected due to its unilateral deformability. A semi-automated folding method was developed to enable and speed up the manufacturing of miniaturized origami scaffolds. Two complementing stamps containing the Miura pattern were 3D printed and used to deform thin plastic foils (Fig. 2a). The paper scaffolds were then sandwiched between two unfolded foils. By folding the assembled layers, the pattern was dynamically embossed into the paper scaffolds (Fig. 2b). Similarly, the origami stamps were used to shape wire meshes from the paper-sheet former draining section. This alternative automated approach

will enable the upscaling of origami scaffolds (Fig. 2c). Therefore, different micro cellulose slurries were prepared in order to obtain scaffolds with the desired elasticity and fiber orientation promoting myocardial cell differentiation and alignment (Fig. 2d).

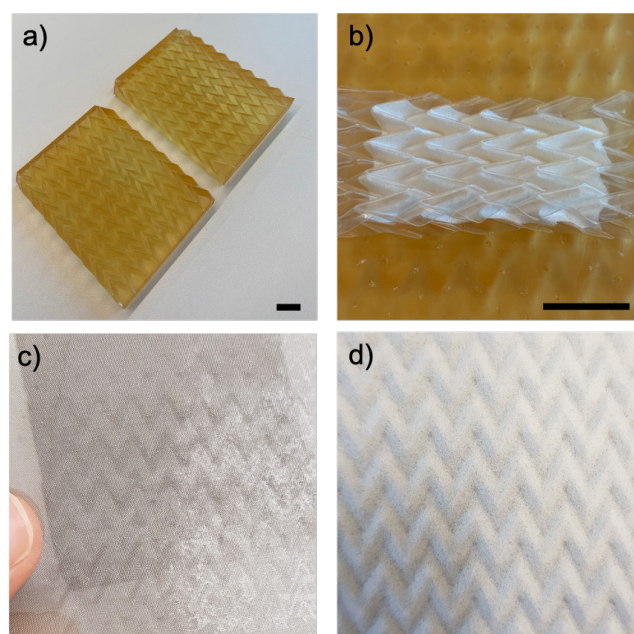


Fig. 2 a) 3D printed Origami stamps; b) Pattern transfer by deforming a pair of origami foils enclosing the paper scaffold; c) Formed metallic origami paper wire mesh; d) Sieved paper with 3D origami shape. (All scale bars 1 cm).

3D bioprinting and hydrogel development

Different blends of cell-laden hydrogels have been assessed for patterning cells onto the cellulose scaffolds. Compared to the previous blends, the structural stability has been improved by the addition of a sacrificial and supporting hydrogel (Fig. 3a).

Mixing the cell carrying and sacrificial hydrogel will form two distinct phases. This results in a porous construct after the dissolution of the sacrificial ink (Fig. 3b), which can promote nutrient diffusion and cell migration. The cell laden hydrogel showed high biocompatibility, printability and stability during cell culture. The printed structures kept stable for over 6 days in cell culture and the cardiomyocytes successfully developed into pacing cells. Printed cells showed excellent long-term viability, comparable to the control cell cultures in dishes and cells embedded in casted hydrogels.

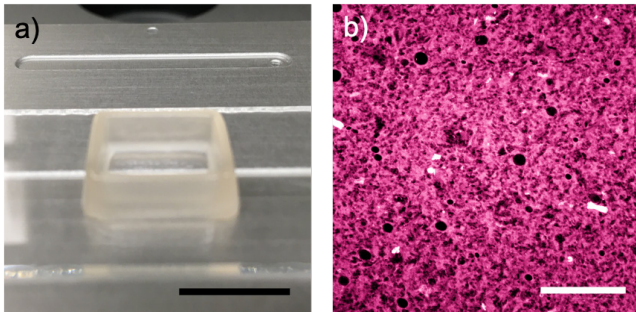


Fig. 3 a) Five consecutive layers printed on top of each other, demonstrating structural stability (scale bar 1 cm).; b) Confocal microscopy image showing the porosity of the bio ink. Cell carrying hydrogel was stained with Nile red (scale bar 500 μm).

Cardiomyocyte culture on patterned scaffolds

The influence of the paper scaffold and alignment structures on the cardiomyocyte culture, orientation and maturation was assessed. For this purpose, line patterns with various line widths and spacings were transferred onto gelatin beds on top of cellulose scaffolds by molding techniques. Similar to our previous results, line widths and spacings in the range of 25 μm were chosen as optimal starting point. Neonatal rat cardiac cells were then seeded either on the patterned or smooth gelatin surface. As we previously reported for model cell lines, immunofluorescence images of the cardiomyocytes and their analysis demonstrated a homogeneous directionality only in presence of alignment patterns (Fig. 4a-d).

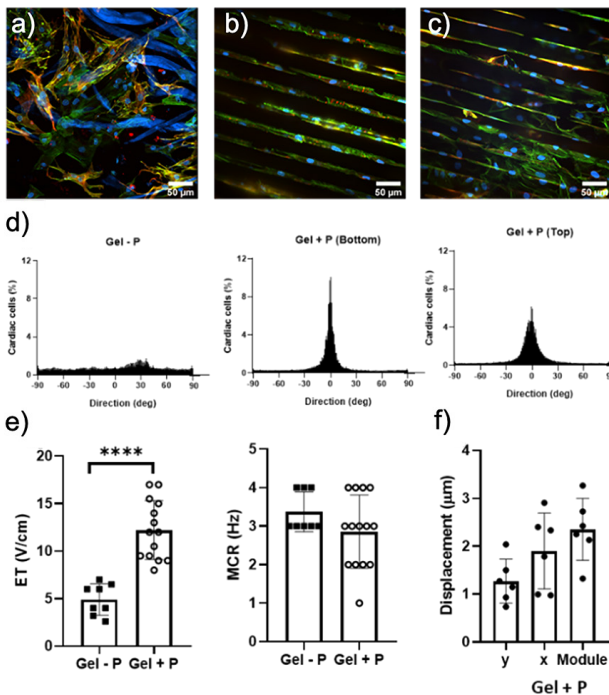


Fig. 4 Representative immunofluorescence images of cells cultured on paper supports in presence of gelatin without a) or with pattern (b-c). The top b) and bottom c) are stained for Troponin-T (red) and F-actin (green), while the nuclei were stained in blue (DAPI). d) Respective directionality histograms. e) Functional properties of the cells cultured on gelatin coated paper with and without pattern. Statistical analysis showed a significant difference ($****p < 0.0001$). f) Displacement of the paper along the x-axis, y-axis and the module of the displacement for gelatin with pattern.

The excitation threshold (ET) significantly increased in samples with pattern, while the Maximum Capture Rate (MCR)

was similar in both conditions (Fig. 4e). A lower ET corresponds to a superior functionality, possibly due to a more uniform distribution of cardiomyocytes on the top of the gelatin, making it easier to pull the paper during their contraction. The displacement analysis of the tissues showed a large displacement, preferentially along the alignment structures of the patterned papers (x-axis Fig. 4f). Hence, the presence of the pattern promoted a uniaxial direction of contraction.

Coculture method for combined tissues

To achieve a 3D co-culture of vascular and cardiac layers, it is first necessary to develop a culture medium that is suitable for the growth of both layers. Since endothelial structure formation requires a specific influence of the medium composition, this was first tested and specifically identified for a vascular layer on top of a static NRCMs monolayer culture. Cardiac cells were cultured either in the standard cardiac growth medium (lgDMEM) or in endothelial growth medium (EGM2) on a tissue culture plate for 7 days. The cardiomyocytes cultivated with the endothelial layer medium composition showed similar results compared to those cultured with the standard cardiac medium in terms of cardiac maturation and contraction capacity. In particular, in both conditions spontaneous beating of the cardiomyocytes were observed. Thus, the EGM2 proved to be suitable for the co-culture of cardiac and vascular tissue layers.

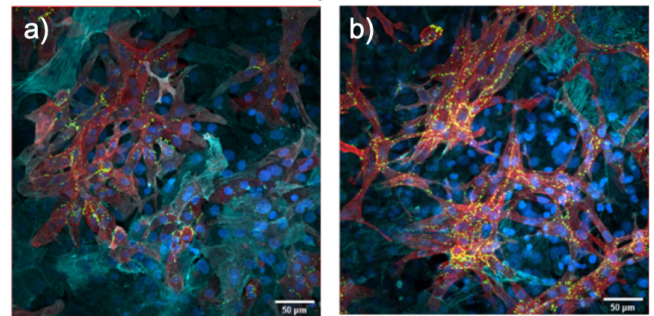


Fig. 5 Immunofluorescence images of the cells for the two culture conditions; a) low glucose DMEM and b) EGM2 culture medium. The red color represents the presence of Sarcomeric α -actinin, the green color of Connexin-43, the cyan color of α -SMA, while the nuclei are stained in blue (DAPI) (scale bars 50 μm).

References

- [1] K. H. Benam et al., *Engineered in vitro disease models*. Annu Rev. Pathol. **10**, 195 (2015)
- [2] E. Tzatzalos, O. J. Abilez, P. Shukla, J. C. Wu, *Engineered heart tissues and induced pluripotent stem cells*. Adv. Drug Deliv. Rev. **96**, 234 (2016)
- [3] L. A. MacQueen et al. *A tissue-engineered scale model of the heart ventricle*. Nat. Biomed. Eng. **2**, 930 (2018)
- [4] N. Ng et al. *Paper-based cell culture platform and its emerging biomedical applications*. Mater. **20**, 32 (2016)
- [5] S.-H. Kim et al. *Hydrogel based paper scaffold system for origami based tissue engineering*. PNAS **112**, 15426 (2015)
- [6] H.-J. Park, S. J. Yu, K. Yang, Y. Jin, A.-N. Cho, J. Kim, B. Lee, H. S. Yang, S. G. Im, S.-W. Cho, *Paper-based bioactive scaffolds for stem cell-mediated bone tissue engineering*. Biomaterials **35**, 9811 (2014)

Novel cancer-targeted nanoparticles

Project A14.13: NCTNano (University of Basel, Dept. of Chemistry, D-BSSE ETH Basel, TargImmune Therapeutics, Basel)

Project Leader: M. Zigler

Collaborators: M. Saxena, D. Bajic, B. Schade and A. Jarzebinska, M. J. Skowicki, V. Mihali, J. Schreiber, Y. Benenson, and C. G. Palivan

Physicochemical characterization: nanoparticle morphology

The efficacy safety of nucleic acid delivery by nanocarriers is strongly affected by their physicochemical properties such as size, shape and surface charge [1]. Cancer-Targeted Nanoparticles developed by TargImmune were characterized by dynamic light scattering (DLS) in order to determine the size distribution, nanoparticle tracking analysis (NTA) to establish their concentration and transmission electron microscopy (TEM) for their architecture. In addition, the stability of the samples was assessed by investigating changes of the z-average diameter obtained from DLS measurements in backscattering mode over time. We systematically studied the influence of various molecular parameters (e.g. the active pharmaceutical ingredient (API) molecular weight, the vector composition and the formulation) on the nanoparticles properties. The characterization methods served to identify key quality attributes of the nanoparticles (e.g. size, shape, charge, stability and aggregation in different conditions). We found that the high aspect ratio seen in TEM correlates with the increase in z-average diameter over time and multiple particle populations in NTA. Cross-correlation of the physical-chemistry properties of different nanoparticles and formulations of thereof with their biological activity in vitro enabled us to propose optimization of the API, gain better understanding of TAR001 structure-activity relationships and advance the formulation development.

Next, components of TAR001 were fluorescently labeled by random alkylation of RNA (Cy5 label) and covalent binding of Alexa Fluor 488 to the vector. The labeling density of RNA was optimized by measuring size distribution (DLS) and brightness of 3 differently labeled molecules. Fluorescence correlation spectroscopy (FCS) measurements confirmed sufficient brightness of the lowest dye concentration labeling. Fluorescently labeled nanoparticles allow the quantification of the free components, evaluation of the stability in biofluids and support understanding the uptake mechanism and their intracellular fate (see below).

Mode of Action: uptake mechanism

In order to obtain a better understanding of the MoA of cancer targeted nanoparticles extensive research has been conducted to identify the particle uptake mechanism. One of the main goals is to distinguish between receptor-mediated and unspecific uptake, which will ensure the selectivity of TAR001. For this purpose, TAR001 internalization experiments have been carried out utilizing different cell lines with both high and low receptor expression level. To study TAR001 internalization process and the fate of its compounds we utilized Alexa Fluor 488 and Cy5 labeling on two different components of the TAR001 nanoparticles. The use of fluorescently labeled TAR001 enabled a detailed internal-

ization study distinguishing the fate of both compounds (Fig. 1). Using laser scanning confocal microscope we successfully performed live cell imaging tracking of the fluorescently labeled particles. The internalization process and the fate of each of labeled TAR001 have been investigated in four cell lines during 8 hours. As expected, a higher TAR001 uptake has been obtained for cells with higher receptor expression levels [2].

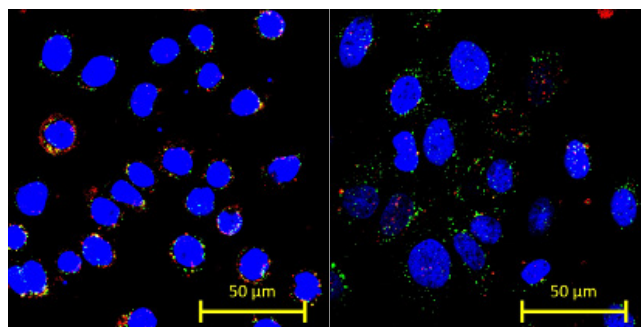


Fig. 1 Representative CLSM micrographs demonstrating targeted uptake of TAR001 in cancer cells (left: MDA-MB-468, right: BT-20). CLSM images were taken after 1h incubation with TAR001 using fluorescently labeled components of the nanoparticles: Cy5 (red) and Alexa Fluor 488 (green) dyes. Nuclei are counterstained with Hoechst 33342 (blue).

In order to investigate the uptake mechanism BacMam endosome-labeling reagents were used. The BacMam system uses a modified insect cell virus (baculovirus) as a vehicle to efficiently deliver and express genes in mammalian cells. By using BacMam reagents we were able to successfully label early and late endosomes with GFP and RFP, respectively. Experiments performed on endosome-stained BT-20 and MDA-MB468 cells showed colocalization of TAR001 with endosomes. In order to reveal more detailed uptake mechanism of TAR001, ongoing experiments with specific inhibitors (i.e. Chlorpromazine hydrochloride, Cytochalasin D, nystatin) serve to distinguish between clathrin-mediated endocytosis and clathrin-independent pathway. Together these results are contributing not only to understand the biological process and specificity of nanoparticles uptake.

Mode of Action: pathway activation and downstream effects

To elucidate the molecular MoA of TAR001, a comprehensive next generation sequencing study was performed based on the successful pilot study. To dissect a TAR001-specific signature, several conditions were analyzed: cancer cell lines responsive and non-responsive to TAR001, due to high or low target expression; non-cancer cells; treatment with TAR001, untargeted delivery of the functional, API, non-functional

API-mimics, and without payload. Key findings include: (i) identification of a common API-signature in target-overexpressing cancer cells; (ii) enrichment in pathways related to immune response; (iii) TAR001-regulated genes encoding for distinct transcription factors.

Altogether more than 60'000 different transcripts were recorded and about 6'000 exhibited a significant TAR001-dependent expression change. The common API-signature consisted of 347 TAR001-specifically regulated genes whose expression was unaltered in the relevant controls. This gene-set contained cytokines with abundant expression upon TAR001-treatment, which was confirmed on the protein level by ELISAs. There were also several regulated transcription factors implicated in the regulation of cancer cell survival. All of these transcription factors were downregulated and, hence, not suitable for reporter gene assays where an increased activity is preferred. Similarly, expression of a transcription factor inhibitor was downregulated following TAR001 treatment. A lower expression of an inhibitor should concomitantly increase the overall transcription factor activity. Thus, different reporters were designed and successfully tested in a proof-of-principle study utilizing HEK cells and TNF- α for induction of the transcription factor activity. However, low transfection efficiencies in the target-overexpressing cancer cells did not allow the establishment of a functional reporter assay despite employing several different protocols for cell lines refractory to transfection. Consequently, a set of five diverse genes was chosen based on expression levels and TAR001-specificity in target-overexpressing cancer cells and qRT-PCR assays were applied. All five genes displayed increased transcript levels upon TAR001 treatment in target-overexpressing cancer cells compared to target-low expressing cells. Collectively, these data facilitate biomarker choice for clinical studies and may form the basis for medium-throughput screening of the formulations.

Summary and conclusion

During this project, we established a combination of physical-chemistry methods for characterization of nanoparticles entrapping DNA such to support the understanding of the structure-bioactivity relationships. In addition, we advanced the in vitro evaluation of the nanoparticles by various combined assays in order to understand their MoA.

Together, the data resulting from this project supported by SNI significantly contribute to the development of TAR001 and advance the program towards IND.

References

- [1] S. Tarvidipour, X. Huang, V. Mihali, C.-A. Schoenenberger, C. G. Palivan, *Peptide-based nanoassemblies in gene therapy and diagnostics: Paving the way for clinical application*, *Molecules* **25**, 3482, 1-37, (2020)
- [2] A. Levitzki, *Targeting the Immune System to Fight Cancer Using Chemical Receptor Homing Vectors Carrying Polyinosine/Cytosine (PolyIC)*, *Front Oncol* **2**, 4 (2012)

Nano-in-nano platform system for local drug delivery

Project A14.15: PERIONANO (FHNW Muttenz, University of Basel HFZ, Credentis AG Windisch)

Project Leader: F. Koch

Collaborators: O. Germershaus, U. Pieleles, S. Stübinger, and M. Hug

Introduction

Peri-implant inflammations represent serious diseases affecting the surrounding hard and soft tissue. Due to prevalence of up to 56%, peri-implantitis may lead to the loss of the implant without prevention and appropriate therapeutic treatment. Since peri-implantitis is a relatively novel and poorly understood disease, several concepts such as air scaling, local or systemic application of antibiotics are common but not yet established.

Within this project an easily applicable construct that possess antimicrobial as well as regenerative potential will be developed. To this end, a variety of nano- and microparticles, containing different therapeutic compounds, will be embedded within a nanofibrillar hydrogel matrix, consisting of self-assembling peptides. This composite material is intended to support the physiological wound healing process and result in local suppression of microbial growth.

Evaluation of regenerative and antimicrobial compounds

Prior to the development of compound-loaded particles, a detailed evaluation of suitable regenerative and antimicrobial compounds was performed. This evaluation on the one hand included selection of compounds based on review of the scientific literature and on the other hand the comprehensive in vitro analysis using relevant cell culture and bacterial models.

Human periodontal ligament fibroblasts (HPDLF) were used as an in vitro model for dental tissue regeneration regarding cell proliferation, ECM protein expression and inflammatory reaction. The exposure of HPDLF with three selected phytochemicals showed a significant increase in cell proliferation after 72 h (Fig. 1).

Moreover, ECM protein expression, measured by collagen type I secretion, was significantly enhanced after incubation with 0.01 $\mu\text{g}/\text{ml}$ of two phytochemicals. For determination of the anti-inflammatory potential of the selected phytochemicals, HPDLF were exposed to 5 $\mu\text{g}/\text{ml}$ lipopolysaccharide (LPS) from *Porphyromonas gingivalis* strain and incubated simultaneously with 0.01 – 1 $\mu\text{g}/\text{ml}$ phytochemicals. The anti-inflammatory reaction was quantified by the measurement of interleukin-8 after 24 h exposure. IL-8 levels were significantly reduced after the exposure with the three phytochemicals, however at different concentrations. Overall, a beneficial effect of the selected phytochemicals in regard to necessary parameters for dental tissue regeneration such as cell proliferation, ECM protein expression and anti-inflammatory activity, was observed. This comprehensive in vitro analysis allowed the selection and determination of phytochemicals and their concentration.

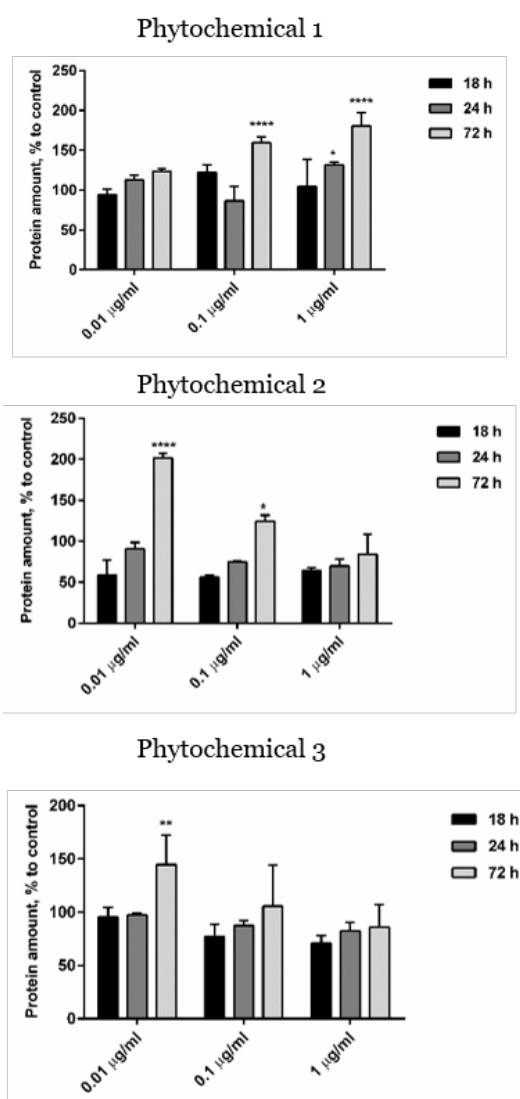


Fig. 1 Evaluation of proliferative potential of three phytochemicals at concentrations of 0.01, 0.1 and 1 $\mu\text{g}/\text{ml}$. Cell proliferation was determined by measuring the total protein amount after 18, 24 and 72 h incubation. As control, HPDLF were grown in cell culture medium. Data are shown in % to control, which was set to 100%.

To determine the effective concentrations of selected antimicrobial agents, the minimal inhibitory concentration (MIC) was assessed. For this purpose, an oral strain (*Streptococcus mutans*) was exposed for 24 h with three antimicrobial agents from variable therapeutic classes. Among the three tested substances, MIC values in the range of 4 to 100 $\mu\text{g}/\text{ml}$ have been detected.

Preparation of compound-loaded particles

As a next step of the project, the focus was put on the efficient generation of variable particle types, efficient compound encapsulation within these particles and suitable release characteristics. A biodegradable and regulatory acceptable polyester matrix was used for the preparation of micro- as well as nanoparticles. Furthermore, several different natural polymer matrices were investigated. All selected compounds, described in vitro tests (three phytochemicals and three antimicrobial substances), were successfully encapsulated using a suspension-based technique (Fig. 2). After particle generation, compound release was investigated using compound-specific analytical methods such as RP-HPLC.

The developed encapsulation method resulted in nano- to microparticles of appropriate size and morphology with suitable encapsulation efficiencies for most compounds. Drug release characteristics varied significantly, probably due to different physico-chemical interactions of the compounds.

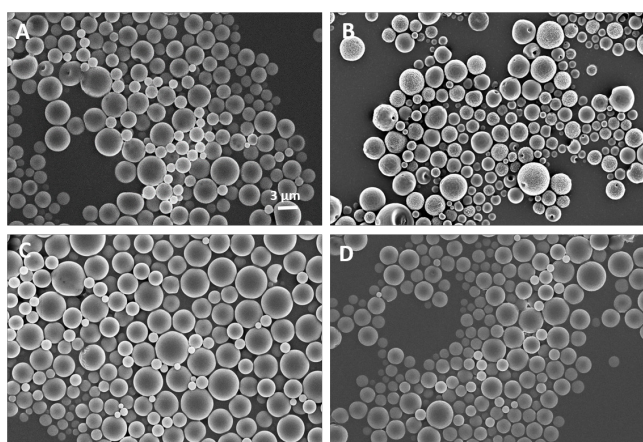


Fig. 2 Evaluation of particle size and morphology of compound-loaded particles by scanning electron microscopy. (A) + (B) Particles loaded with antimicrobial agents, (C) + (D) particles loaded with phytochemicals. Scale bar represents 3 μm .

Effectiveness of compound-loaded particles

After 1 h incubation of *S. mutans* in direct contact to antimicrobial loaded nano- and microparticles, the majority of live/dead stained bacteria were found to be non-viable (Fig. 3). Moreover, the effectiveness of the antimicrobial loaded particles was proven using an agar diffusion test. To this end, round filter discs were soaked with particle suspension at 2 and 5 mg/ml and transferred to a bacterial lawn. After 24 h of incubation, inhibition zones were formed at varying sizes, depending on the antimicrobial substance and concentration of the particle suspension.

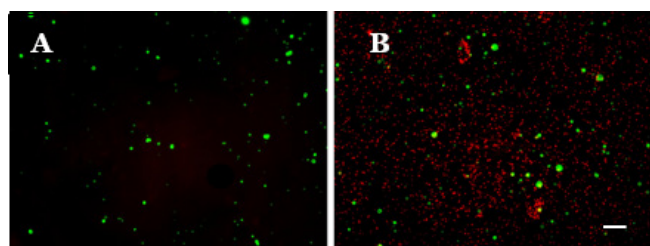


Fig. 3 Effect of antimicrobial loaded particles on *S. mutans*. (A) Particle control stained with Syto 9 without bacteria, (B) Particles and bacteria stained with Syto 9 and propidium iodide. Particles are shown in green, dead bacteria are visualized in red. Scale bar represents 10 μm .

Particle embedment into nanofibrillar hydrogels

As a final step, the ability of nanofibrillar peptide hydrogels to assemble in the presence of admixed particles was tested. The self-assembling process and thus hydrogelation was not influenced by the addition of nano- and microparticles (5% v/v) (Fig. 4A). Moreover, the formation of fibers, necessary for hydrogelation, was visualized by light microscopy (Fig. 4B). Release experiments of particle loaded nanofibrillar peptide hydrogels, proved compound concentrations within the therapeutic range. Moreover, by the combination of phytochemical and antimicrobial loaded particles in the peptide hydrogel a beneficial regenerative as well as antibacterial effect had been achieved.

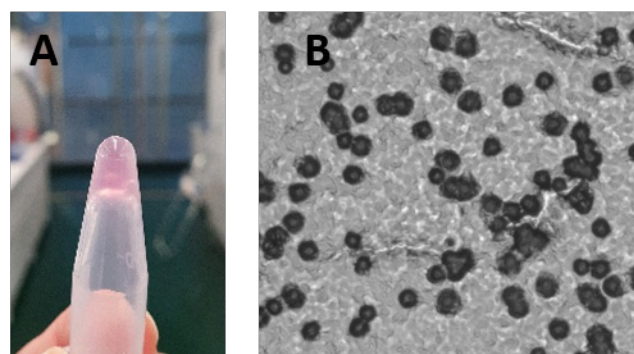


Fig. 4 Particle loaded nanofibrillar peptide hydrogel at 5% (v/v). (A) Tubing test, immediately upon mixing the peptide solutions, containing diverse particle types, a hydrogel was formed. (B) Microscopy study of a particle loaded nanofibrillar peptide hydrogel sample. Particles (black) were homogeneously distributed within the hydrogel, no accumulation was detected. Magnification of 20x was used.

Summary and outlook

Several compounds were evaluated with regards to their suitability for the intended delivery system and indication. Subsequently, different methods for the preparation of micro- and nanoparticles were evaluated. It was found that both, micro- and nanoparticles could be successfully prepared with variable compounds. The release of compounds from particles and from particle loaded nanofibrillar peptide hydrogels were found to be in the expected therapeutic ranges. Particle incorporation did not disturb the process of hydrogelation. Future studies will focus on optimization of further compound encapsulation and release to broaden the drug delivery platform capability.

Customized, nanostructured grating compressors for high repetition rate ultrafast laser

Project A14.19: UltraNanoGRACO (CSEM Muttenz, FHNW Windisch, Menhir Photonics AG Basel)

Project Leader: F. Lütolf

Collaborators: B. B. Resan, F. Emaury, F. Herzog, I. Kuznetsov, F. Friebe, T. Aderneuer, I. Zhurminsky, J. Schleuniger, J. Disser, G. Basset, B. Rudin, and R. Ferrini

Introduction

Grating compressors are key components in a technique called “chirped pulse amplification” (CPA). The development of CPA allowed lasers to generate shorter and more intense pulses. Such ultrafast lasers are nowadays used in applications ranging from medical surgery over industrial cutting to telecommunication.

To fulfill the needs of the laser manufacturing company Menhir Photonics AG, a cost efficient, but robust and high-efficiency compressor with a small footprint is developed in the project UltraNanoGRACO. Besides finding low-cost processes for fabricating the main component, a nanostructured diffractive grating, the project further seeks to scale down the size of the compressor and finally find an innovative solution for recompressing higher order phase components that are present in such pulses. To reach this ambitious goal, different nanostructuring processes were tested and successfully implemented.

The grating compressor

A final grating compressor design was established and the prototype with the according beam path is shown in figure 1. It is based on a so called 4-f layout, but the beam-path has been folded by utilizing well-aligned mirrors to avoid the use of an additional grating and to achieve a compact footprint. In short, a grating separates the wavelengths spatially, which allows for the introduction of a precise non-linear phase delay in a Fourier plane. Finally, the spread-out beam is reflected back towards the grating, which recombines all the wavelengths with optimized phases, to a single, ultrashort pulse. Sophisticated optical design eventually allowed reduction of the UltraNanoGRACO compressor footprint from 100 cm x 50 cm to (proof-of-concept compressor from 2019) 30 cm x 30 cm in its final configuration. Further packaging could enable reduction of the footprint to ~10 cm x 10 cm.

The components

The centerpiece of the compressor is the diffraction grating that separates the wavelengths with the highest possible efficiency. It is the most specialized component of a grating compressor, and accordingly costs ~10 times more than the other optical components. UltraNanoGRACO hence sought for a cost-efficient process to produce high-efficiency gratings on wafer-scale and found it in double-sided UV replication. The final device is shown in figure 2. Besides the diffractive grating (red), a much shorter period grating was used (blue) to act as the antireflective (AR) structure on the backside of the device. This AR grating allows for an efficiency increase of almost 6% in the chosen geometry (Fig. 3) and is hence critical for reaching efficiencies >90% as targeted in this project.

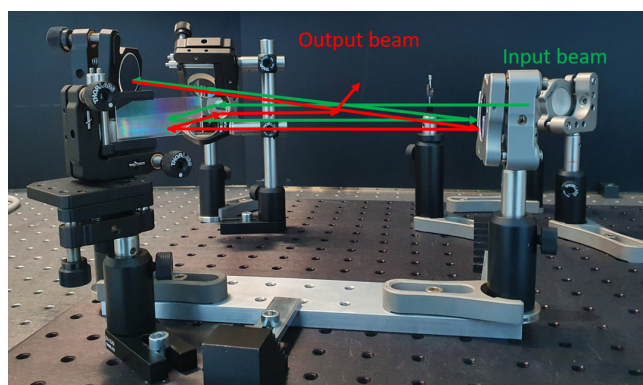
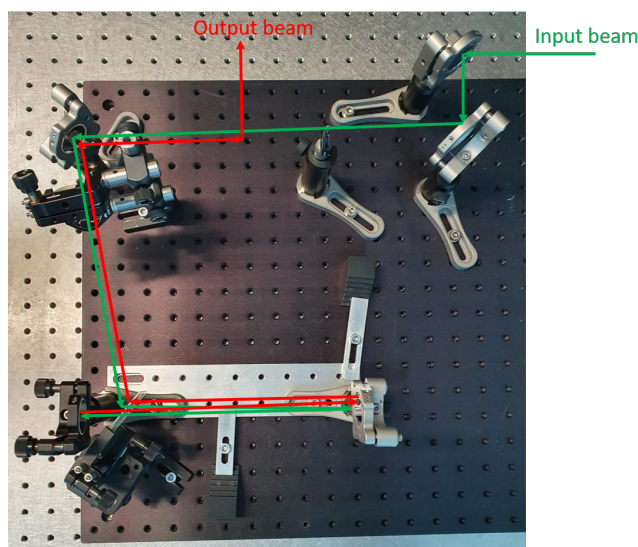


Fig. 1 The assembled, folded compressor with sketched beam-path in top-view (top) and side-view (bottom).

In contrast to the relatively standard AR grating, the Diffraction grating (red) has a high aspect ratio and is hence difficult to replicate. The developed process relies on a semi-soft mold with an anti-adhesive coating. It was found that replication of a lower depth grating followed by a short etch is much easier for manufacturing while still enabling very reproducible results. The final performance of this process is shown in figure 4. A peak efficiency of 92 % was achieved at 1550 nm wavelength in Littrow configuration, which nicely fulfills the goals set for the grating performance.

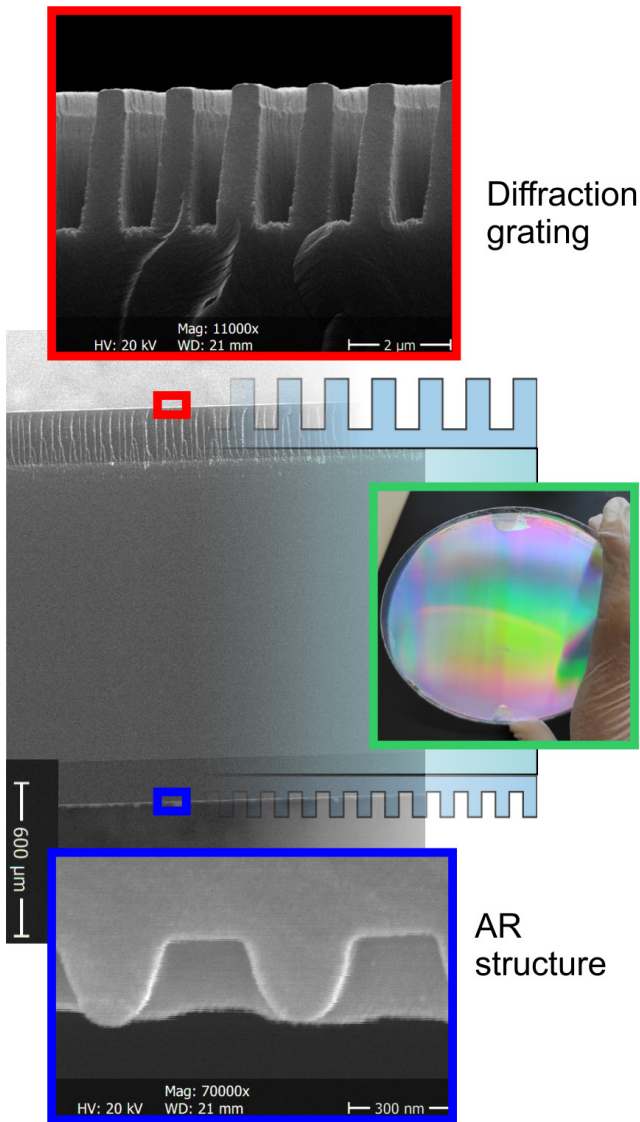


Fig. 2 Final full-wafer UltraNanoGRACO grating based on double-sided replication.

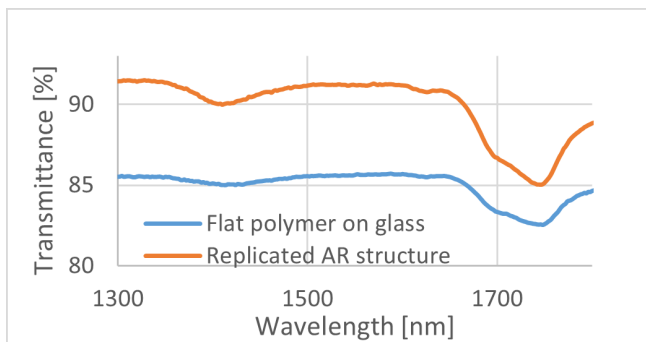


Fig. 3 Transmittance increase by applying a nanostructured polymer to a glass surface (AR structure).

The final challenge resides in compensating residual non-linear phase components to allow for even shorter pulses. The best place to do compensation is the Fourier plane of the compressor, where the spectral components are well-defined in space. While this principle is well-known, a novel approach for introducing the necessary phase shift is developed here: By inkjet printing high refractive index nanoparticles, refractive index variations and hence phase delays can be controlled with a lateral resolution of tens of micrometers (inset Fig. 5).

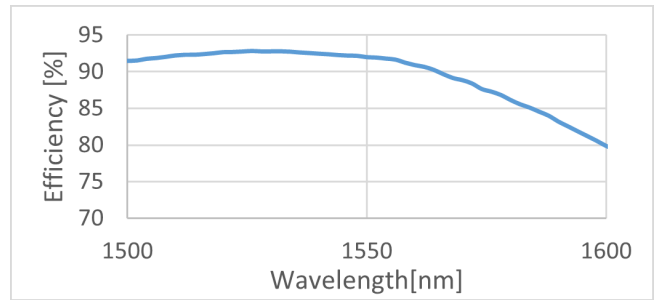


Fig. 4 Efficiency of the final UltraNanoGRACO grating

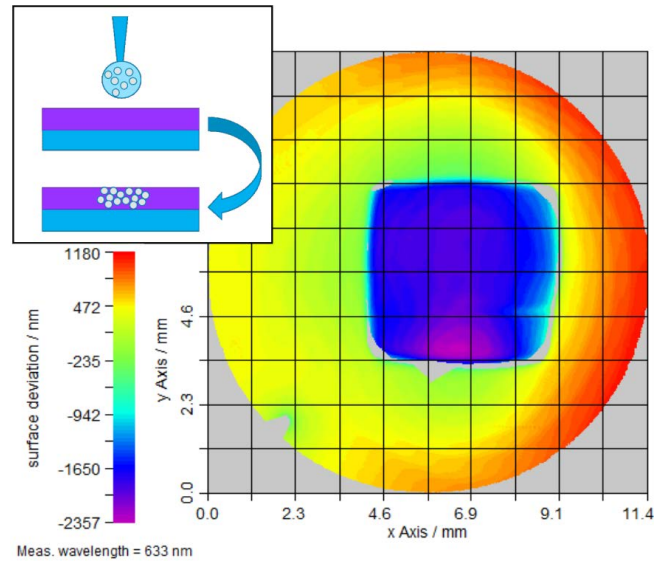


Fig. 5 First results of inkjet printed phase plates produced by the process sketched in the inset.

A first result of such a phase shifting print is shown in figure 5, measured by interferometry. $>2 \mu\text{m}$ phase delay could be generated with a single print, which is very promising. Utilizing very small nanoparticles ensures low scattering and hence losses, while inkjet printing allows for very flexible designs and cost-efficiency. This approach has the potential to individually tailor phase plates for each new laser produced by simply adapting the digital design sent to the printer. Even more, the approach is promising for various other phase manipulation applications.

Mechanoresponsive liposomes – formulation and process development

Project A15.01: ForMeL (FHNW Muttentz, ANAXAM, Acthera Therapeutics AG Basel)

Project Leader: O. Germershaus

Collaborators: A. Zumbühl, C. Grünzweig, and M. Kuentz

Introduction

Mechanoresponsive liposomes respond to variations of the shear force by release of their payload. This principle may be used to allow localized, shear force-dependent drug release, e.g. at the site of atherosclerotic lesions.

Within this project, different manufacturing methods and technologies are screened with regards to suitability for pilot- and large-scale manufacturing of mechanoresponsive liposomes. Promising manufacturing strategies are further optimized at lab scale and scaled-up to pilot scale.

Besides developing a manufacturing process suitable for large-scale manufacturing, the Nano-Argovia Project ForMeL also focuses on developing a stable pharmaceutical formulation of mechanoresponsive liposomes, which may be used for preclinical studies.

Finally, a range of analytical methods, potentially suitable for characterization of the drug product during manufacturing, at release and during stability studies are investigated, established, and optimized. These analytical methods focus on potential product quality characteristics such as morphology (e.g. TEM, SAXS), particle size distribution (e.g. DLS), composition (e.g. DSC), and drug load as well as mechanoresponsivity.

Manufacturing of SUV

With the aim to identify suitable manufacturing methods for the preparation of small unilamellar mechanoresponsive liposomes, different manufacturing methods and liposome formulations were screened. Besides thin-layer hydration, the most common liposome preparation process at lab scale, extrusion, microfluidics and ethanol injection and combinations of these methods were investigated.

Using an initial liposome formulation, all these methods resulted in formation of multilamellar vesicles with large mean particle size and broad, multimodal particle size distributions. Therefore, the liposome composition was optimized, ultimately resulting in substantially reduced mean particle size, narrow, monomodal size distribution and superior colloidal stability. Figure 1 shows the particle size distribution before and after optimization of the liposomal formulation determined by DLS. After optimization, liposomes show a mean diameter of 177 nm and a narrow particle size distribution (polydispersity index < 0.2).

Based on the current analysis, ethanol injection appears to be the most promising preparation method, due to the simple set-up and the short process duration [1, 2]. However, residual ethanol content, low encapsulation efficiency and relatively high temperatures during preparation are challenges that still need to be addressed.

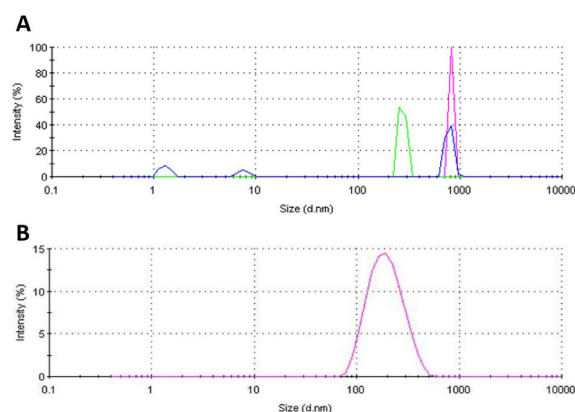


Fig. 1 Particle size distribution of liposomes prepared by ethanol injection method before (A) and after (B) optimization of the liposome composition. Particle size distributions were determined by dynamic light scattering.

Morphology by electron microscopy

ANAXAM and the team at Nano Imaging Lab have adapted a pre-developed and established method for sample preparation for electron microscopy of liposomal samples for this project. The Ultra Rapid Freezing and Drying (URFD) method is based on ultra-rapid freezing at -100°C and high vacuum. URFD is suitable for subsequent imaging using SEM, TEM, AFM and confocal laser microscopy. The advantage of the URFD method is the protection of structures, which are challenging to fixate chemically. Additionally, structures can be resolved with high quality and at high resolution. The method is especially suitable for processing samples at increased throughput because the preparation is independent from the imaging process and the preparations can be stored at room temperature until analysis. The method accompanied the development of the manufacturing procedures throughout the project and helped to evaluate differences between liposome preparations. Figure 2 shows micrographs of liposomes prepared by the thin-layer hydration method, processed by URFD and imaged with TEM.

Morphology by Small Angle X-Ray Scattering

Small angle X-ray scattering was performed at cSAXS beam line at Swiss Light Source (SLS). Different liposomal preparations were measured in a q -range of 1.4×10^{-2} to 1.7 nm^{-1} . Scattering data obtained with a liposomal formulation before extrusion and after extrusion using different pore diameters are shown in figure 3.

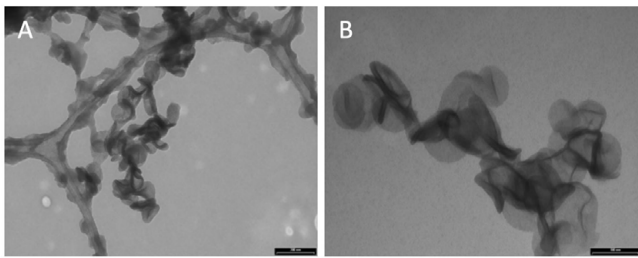


Fig. 2 Electron micrograph of mechanoresponsive liposomes manufactured with the thin-layer hydration method followed by an extrusion step before (A) and after (B) optimization of the liposome composition. The samples were prepared using URFD and imaged by TEM. The structure of the liposomes remained intact and differences in quality between the liposome preparations could be assessed.

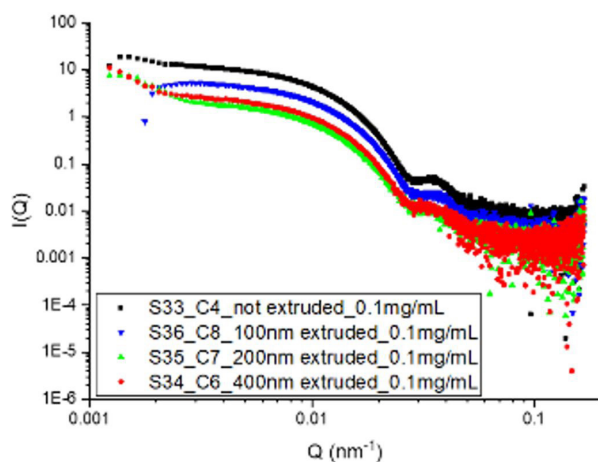


Fig. 3 Scattering data obtained from cSAXS measurement for samples with 0.1 mg/ml concentration extruded to different extend.

The scattering intensity decreased with the extend of the extrusion and the behavior was the same for all concentrations. Furthermore, for samples with the same extrusion condition, the scattering intensity increased with increasing concentration. The shape of the scattering curves for all conditions was similar, hence the scattering behavior of all samples was comparable. Analysis of the scattering data against a data set of lipid bilayers showed no fit. Analysis using an alternative model pointed to the presence of a secondary phase or structure. Further analysis will be performed to show if this hypothesis can be confirmed or if the shape of liposomes is responsible for the divergent scattering behavior.

SAXS experiments allowed to analyze different liposomal formulations, providing valuable information about liposome composition and potential challenges.

Conclusion and outlook

For the manufacturing of mechanoresponsive liposomes thin-lipid-layer hydration and ethanol injection methods were found to be especially suitable. However, the thin-lipid layer hydration and extrusion will likely result in challenging up-scaling to production scale. Therefore, a focus on ethanol injection or microfluidic procedures could be beneficial.

Storage stability of liposomal formulations depending on different manufacturing conditions is currently assessed for liquid dosage forms. In the next steps a pharmaceutical formulation allowing lyophilization of liposomes and a lyophilization process will be developed to further improve storage stability of liposomal preparations.

Further, the manufacturing and the lyophilization process will be up scaled to pilot scale to allow manufacturing of stable liposomal formulations for preclinical studies. Finally, the set of analytical methods used for in-process- and quality control is further developed and refined.

References

- [1] C. Jaafar-Maalej, R. Diab, V. Andrieu, A. Elaissari, H. Fessi, *Ethanol injection method for hydrophilic and lipophilic drug-loaded liposome preparation*. *J Liposome Res.* **20(3)** (2010)
- [2] O. R. Justo, A. M. Moraes, *Analysis of process parameters on the characteristics of liposomes prepared by ethanol injection with a view to process scale-up: Effect of temperature and batch volume*. *Chem Eng Res Des.* **89(6)** (2011)

Post-treatment of wear-resistant implant coatings

Project A15.08: Promucola (FHNW MuttENZ, ANAXAM, Orchid Orthopedics Switzerland GmbH, Baden-Dättwil)

Project Leader: M. de Wild

Collaborators: R. Burger, A. Carmona, N. P. M. Casati, C. S. T. Chang, M. de Wild, C. Grünzweig, M. Olbinado, A. Salito, and F. Schuler

Summary of the project progress

Due to the increasing number of patients with allergies to Co, Cr and Ni [1,2], attempts are being made to replace CoCr endo-prosthetic devices such as artificial knee, shoulder and elbow joints, with titanium implants. However, in order to avoid unacceptable wear [3], titanium surfaces must be coated with a wear-resistant layer. We propose a Protective multi-component layer on articulating implant surfaces made of titanium to ensure the longevity of the system. Advanced Plasma Spray is used as an industrially applicable method for the production of thick, ceramic, abrasion-resistant coatings [4]. Orchid Orthopaedics Switzerland GmbH wants to further develop the new Advanced Plasma Spray method and use a novel multi-component Al_2O_3/TiO_2 ceramic powder mixture as a biocompatible starting material that is injected in a plasma flame, where the particles melt. On the flight to the implant surface, the molten particle droplets start to cool down before impacting the substrate with high kinetic energy. Solidification under high cooling rates forms the multi-component surface coating.

Due to this thermal quenching a not fully ceramized coating is formed consisting of crystalline phases ($\alpha-Al_2O_3$, TiO_2 , aluminum titanate Al_2TiO_5 and $Al_6Ti_2O_{13}$) [5] as well as some pores and micro-cracks. These specific phases are expected to have a significant impact on the hardness and the wear properties of the surface. It is crucial to identify under what conditions these phases form and whether they can be subsequently transformed.

Based on previous work, the aim of this project is to investigate the influence of the following post-processes on the presence, property and stabilization of the metastable phase:

- Electrochemical treatment by anodizing and thereby oxidizing the phase.
- Heat-treatment within different oxygen containing atmospheres to oxidize the conductive phase.

These investigations need to be carried out in order to establish the post-treatment processes to understand and optimize the system.

Two types of titanium blanks were produced: $\phi 30$ mm samples for structural and $\phi 40$ mm samples for tribological experiments. Al_2O_3 -, TiO_2 - or multi-component mixture of Al_2O_3/TiO_2 -powder mixtures were used for Advanced Plasma coating (Fig. 1). The coated samples were subsequently polished to reach a specific surface roughness $Ra < 0.05 \mu m$.

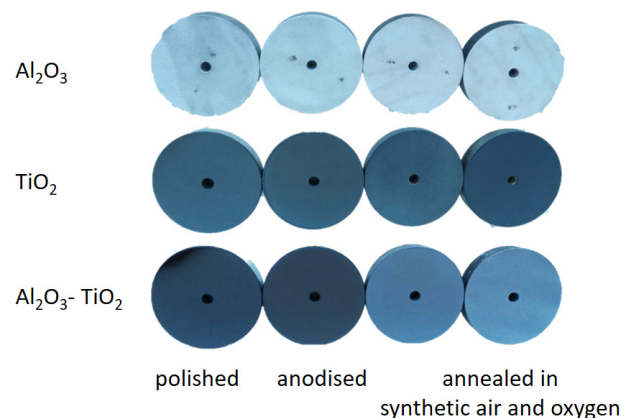


Fig. 1 Photographs of $\phi 40$ mm Ball-On-Disc samples Advanced Plasma-coated with Al_2O_3 (top row), TiO_2 (middle row) and ProMu-CoLa- Al_2O_3 - TiO_2 (bottom row) after post-treatment by polishing, anodizing and annealing in synthetic air or pure oxygen.

The following post-treatments have been established and performed: Heat-treatment and anodization (custom-built chamber, see Fig. 2). So far, no effects have been observed for anodized samples. A color-change was observed after the heat-treatments. The Vickers hardness (Fig. 3) as well as the wear rate of the coating is increased by oxidizing heat-treatments.

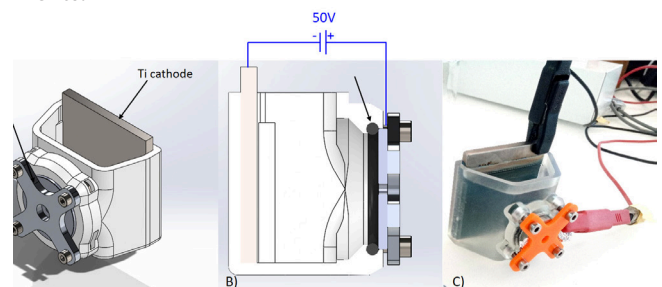


Fig. 2 A) and B) CAD model and C) photograph of the anodization chamber.

After all three coatings have been characterized by benchtop and high-resolution Synchrotron-XRD and the corresponding crystallographic phases have been identified, the post-treated coatings have further been investigated in a second beamtime (Fig. 4).

After anodizing, the diffraction patterns also do not show any change for all 3 types of coating, further supporting the observation that it does not alter the phases present in the coatings. For the Al_2O_3 -coatings, the diffraction patterns be-

fore and after heat-treatments are very similar (Fig. 4a). After heat-treating the TiO_2 -coatings, the phases transformed into rutile (Fig. 4b). The diffraction patterns do not differ when heat-treated in artificial air and O_2 . Phase transformation also happens after heat-treatments in the Al_2O_3 - TiO_2 -coatings (Fig. 4c). Rutile is still present but not as the major phase. Orthorhombic Al_2TiO_5 is not present anymore in the heat-treated coatings, and further analysis has to be done to clearly identify the now present phase.

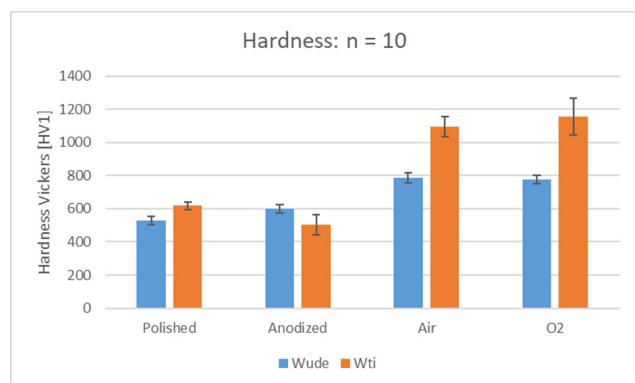


Fig. 3 Vickers hardness of an Al_2O_3 - TiO_2 - (blue) and TiO_2 -coatings (orange) before and after post-treatment.

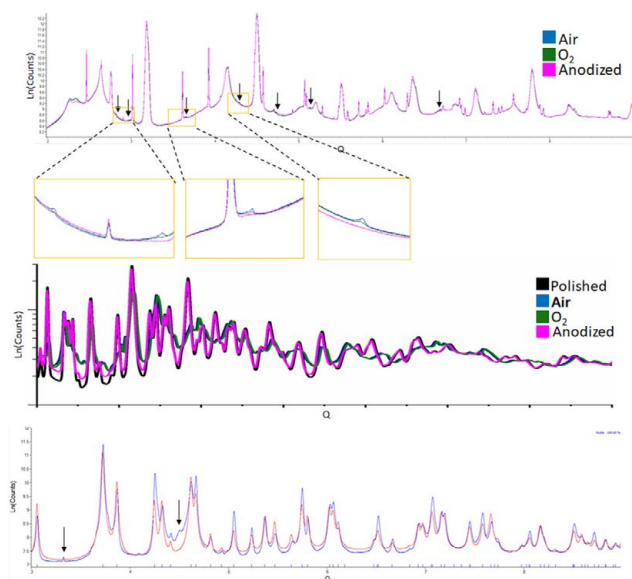


Fig. 4 High-resolution Synchrotron-XRD patterns of a) Al_2O_3 -coatings after anodizing (magenta), heat-treatment in artificial air (blue) and O_2 (green). Extra peaks are present after heat-treatments and are indicated in arrows and inserts. b) Experimental (blue) and calculated (red) diffraction patterns of TiO_2 -coatings after heat-treating in artificial air. Arrows indicating peaks not corresponding to the Rutile phase. c) Diffraction patterns of Al_2O_3 - TiO_2 -coatings with the following conditions: polished (black), heat-treated in artificial air (blue) and O_2 and anodized (magenta).

Coatings of Al_2O_3 , TiO_2 and Al_2O_3 - TiO_2 with and without the substrates were investigated by high-resolution Synchrotron X-ray micro-computed tomography (SXRµCT) at the TOMCAT beamline. In the reconstructed images, pores and cracks of the size of few microns can be observed (Fig. 5a). They could be segmented out from the matrix by setting a threshold intensity level (Fig. 5b and c). For investigating the interface between the coatings and the substrates, however, cutting the samples could not be avoided.

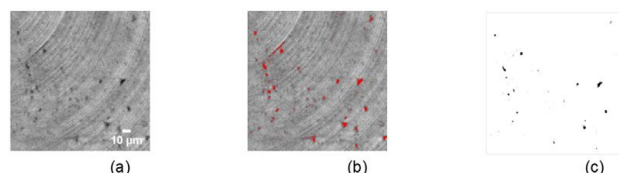


Fig. 5 a) High-resolution X-ray tomographs of the Al_2O_3 - TiO_2 coating without substrate. b) Segmentation was performed by applying an intensity threshold and the pores are identified as shown in c) with black color.

A zoom in into the volume at the interface is shown in figure 6. Several features can be found at the interface: 1) rippled interface, having a coating-substrate interlayer with thickness around $40\ \mu\text{m}$, 2) agglomeration of pores near the interface, 3) smaller pores in the coating, 4) various grey levels inside coatings due to different intensity measured. For further analysis, samples need to be cut into $1\ \text{mm}^3$ cubes to obtain a higher contrast. The features shown here will be further analyzed using 3D-volume rendering and fragmentation.

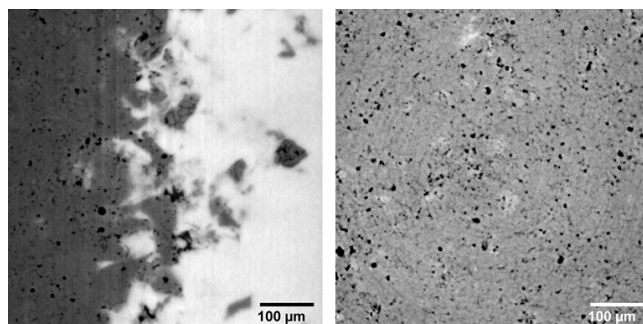


Fig. 6 Left: High resolution reconstructed SXRµCT images showing a substrate- Al_2O_3 -coating interface. The Ti-6%Al-4%V substrate shows the highest intensity (white), while the cracks and pores are shown as black in color.

On behalf of the entire Promucola project team, we would like to thank the Swiss Nanoscience Institute for supporting the project to investigate the influence of post-treatment on Plasma Sprayed coatings.

References

- [1] T. Schafer, E. Bohler, S. Ruhdorfer, L. Weigl, D. Wessner, B. Filipiak, H. E. Wichmann, J. Ring, *Epidemiology of contact allergy in adults*, *Allergy* **56**, 1192–6 (2001)
- [2] D. Guenther, P. Thomas, D. Kendoff, M. Omar, T. Gehrke, C. Haasper, *Allergic reactions in arthroplasty: myth or serious problem?*, *Int Orthop.* **40**, 239–44 (2016)
- [3] K.G. Budinski, *Tribological properties of titanium alloys*, *Wear* **151**, 203–17 (1991)
- [4] N. Vogt, K. Wozniak, A. Salito, M. de Wild, *Biocompatible wear-resistant VPS coatings*, *Curr. Dir. Biomed. Eng.* **2(1)**, 31–34 (2016)
- [5] A. Richter, L.-M. Berger, S. Conze, Y. J. Sohn, R. Vassen, *Emergence and impact of Al_2TiO_5 in Al_2O_3 - TiO_2 APS coatings*, *IOP Conf. Ser. Mater. Sci. Eng.* **480** 012007 (2019)

Design of chemically patterned UV-curable coatings with anti-fingerprint properties

Project A15.09: ReLaFunAF (FHNW Windisch, Paul Scherrer Institut, RadLab AG Killwangen)

Project Leader: S. Neuhaus

Collaborators: M. Wüthrich, A. Karpik, C. Padeste, V. Petry, A. Möck, and A. di Gianni

Introduction

UV curable coatings are adding value to products in a wide variety of industries with great success. Fingerprint repellency is a surface property of high interest for automotive, decorative and electronic applications among many others, but is very difficult to achieve.

As the UV curing industry is facing a shift from using traditional mercury UV lamps to more efficient and greener UV LED lamps, we developed a process coined Reactive Layer Functionalization of UV Curable Coatings (ReLaFun) [1]. Using this innovative approach, the UV LED specific problem of incompletely cured surfaces can be turned into an asset to produce very versatile functional coatings with, for instance, hydrophilic or anti-scratch properties.

Here, we refine the ReLaFun process further towards even more demanding and complex functionalities such as anti-fingerprint. Firstly, formulations for hydrophilic, lipophilic and hydrophobic/oleophobic coatings are developed. Patterns of these formulations are then prepared by selective irradiation through masks followed by backfilling with the second component, allowing us to identify the most powerful combination of functionalities for anti-fingerprint properties in a systematic and efficient manner. Moreover, we will build different nanoscale architectures by selection of molecules with different numbers of reactive sites. Thereby, we expect to unlock the full potential of the ReLaFun process and to develop a truly novel methodology for creation of surfaces with very good anti-fingerprint performance.

Results and discussion

We aim to create surfaces with patterns of highly dissimilar chemical functionalities. The rationale behind this approach is to mimic the complex composition of fingerprints, thereby camouflaging the visibility of the prints on the surface. To this end, we first developed formulations for homogeneous hydrophilic, oleophobic/hydrophobic or lipophilic coatings. The respective surface energy (components) reflect the different properties as anticipated (Fig. 1), with total energies ranging from about 14 for oleophobic to 55 mJ/m² for hydrophilic coatings.

In order to achieve chemically patterned surfaces, our core process revolves around the patterning of the first and backfilling of the second component as described in figure 2. This involves the steps of illuminating the first component through a mask, removing the unexposed parts and backfilling followed by the final irradiation.

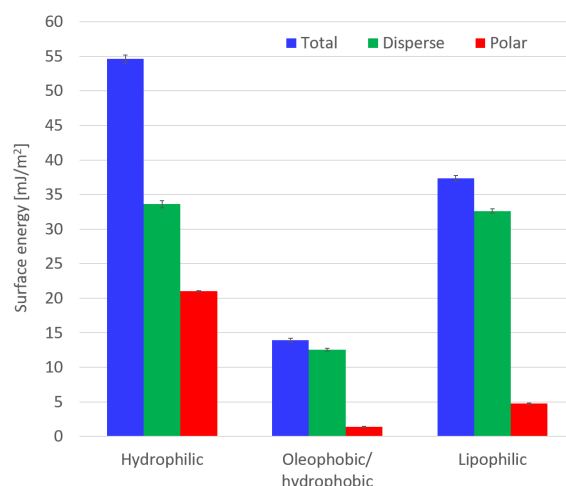


Fig. 1 Surface energy components of homogeneous samples coated with hydrophilic, oleophobic/hydrophobic or lipophilic formulations, respectively.

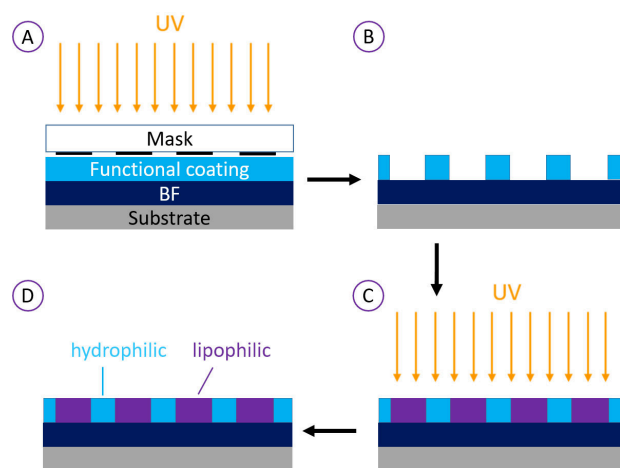


Fig. 2 After partial cure of the base formulation (BF) with UV LED, the first functional component is applied and irradiated through a patterned chromium quartz mask (A, «ReLaFun patterning»). After removal of unexposed parts, the structured functional coating is obtained (B). The second functional component is then used to backfill the patterned structure (C), and, after UV-curing, a chemical pattern with highly dissimilar components is obtained (D).

The distance to the lamp and the exposure conditions had to be optimized to obtain optimum cure and structure definition in step B. To complicate matters, different formulations also tend to have different sets of optimum curing conditions.

More challenges in the creation of binary chemical patterns involve the proper removal of unexposed parts in step B without damaging cured structures. Additionally, under- or overfilling needs to be avoided in step C.

An essential question we aspire to answer is what structure size and ratio of components is required for the best anti-fingerprint properties. In order to screen these parameters, a quartz masks with chromium structures arranged in nine different fields, showing feature sizes from 50 μm to 200 μm and fill factors (= exposed parts) from 30% to 70% was used (Fig. 3).

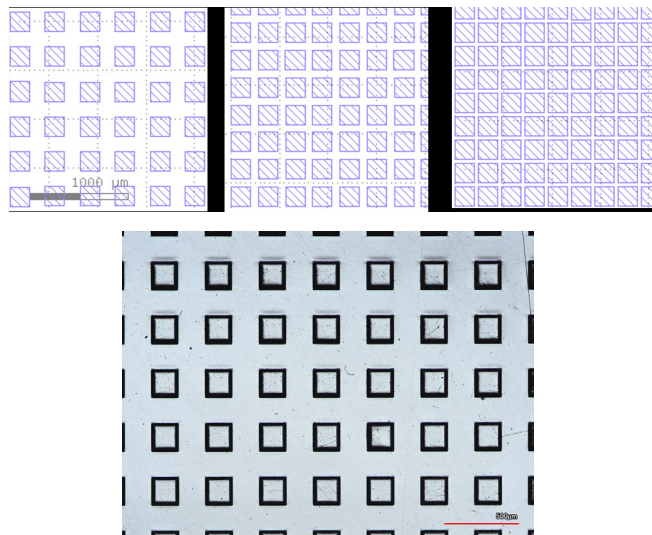


Fig. 3 Top: Three exemplary sections from the mask layout with 200 μm structure size and different fill factors (70%, 50% and 30% from left to right). Sections shown have a size of 2 mm x 2 mm each. Bottom: UV cured structured coating after removal of uncured parts (cf. step B in Fig. 1).

Structure quality is routinely assessed using confocal laser scanning microscopy and profilometry. The surface free energy of all backfilled structures is determined by contact angle measurements of different liquids, followed by calculation of the individual components. Comparison of the surface energy components of chemically patterned surfaces to homogeneous surfaces revealed that we were indeed successful in producing hybrid UV cured coatings with a completely new set of surface energy components.

The effect on anti-fingerprint properties is judged visually on coated glass samples. As an example, the results for hydrophilic patterns backfilled with an oleophobic/hydrophobic formulation are shown (Fig. 4). Noticeably, standardized fingerprints were less or much less visible on structures of all feature sizes for hydrophilic to oleophobic ratios of 50:50 or 30:70. Tests on other chemically structured surfaces will reveal whether these initial findings can be confirmed – namely that feature size is much less important than the ratio of the different components.

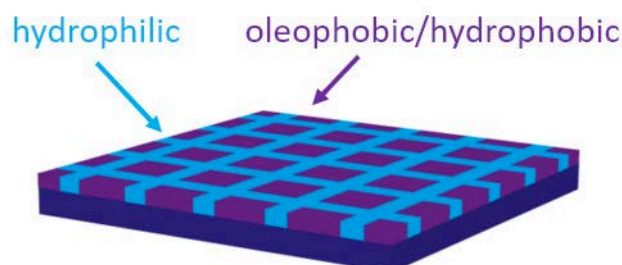
Outlook

We will prepare chemically patterned surfaces with all possible combinations of hydrophilic, oleophobic and lipophilic components and assess their anti-fingerprint properties. Raman mapping will be applied to obtain maps of functionality patterns and assess their quality.

Additionally, we will adapt formulations using multifunctional monomers such as polyhedral oligomeric silsesquioxanes (POSS) for select combinations. We hypothesize that a

denser network will limit the visibility of fingerprints even further due to limited penetration of fingerprint components.

Considering both obtainable quality on a microscopic and macroscopic scale and anti-fingerprint performance, we will define the best candidate for implementation in consumer products.



	Feature Size		
	50 μm	100 μm	200 μm
70:30	0	+	0
50:50	0	-	--
30:70	-	-	--

Fig. 4 Anti-fingerprint performance assessed visually on coated glass samples. Hydrophilic structures of different sizes were backfilled with oleophobic/hydrophobic formulation and cured. The ratio of hydrophilic to oleophobic areas was varied from 70:30 to 30:70. Fingerprints were rated to be equally visible (0), more visible (+), less visible (-) or much less visible (--) than on an uncoated piece of float glass.

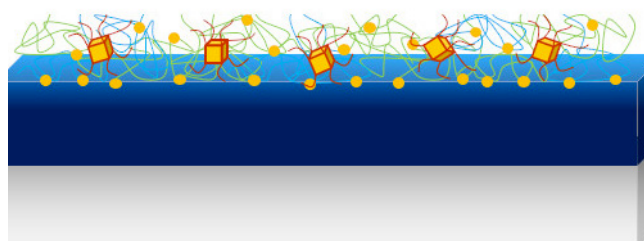


Fig. 5 Nanoscale architecture of a UV cured coating containing POSS.

References

- [1] M. Wink, V. Petry, A. Moeck, S. Neuhaus, *Reactive layer functionalization of UV curable coatings*, RadTech Conference Proceedings, October (2019)

“Less is more” – High-throughput nanoparticle detection for quality control of complex food matrices

Project A15.10: SiNPFood (FHNW Muttentz, University of Basel, Dept. of Chemistry, DSM Nutritional Products AG Kaiseraugst)

Project Leader: S. Saxer

Collaborators: V. Maffei, A. Dusterloh, A. Otter, and C. G. Palivan

Introduction

Nanoparticles (<100 nm) are wide-spread additives in various industrial products such as pharmaceuticals, cosmetics, food products etc. as thickeners, taste enhancer, dye, appearance, thickeners, gelling and anticaking agents [1, 2]. However, recent studies concerning nanoparticles as trigger for diseases [3, 4], e.g. including pulmonary inflammation, immune adjuvant effects and systemic effects including blood coagulation and cardiovascular effects [5, 6, 7], and the nanosize, indeed enables to crossing natural body barriers such as the mucosa of the gastrointestinal tract or the blood brain barrier [8]. Nanoparticles are engineered in various sizes and shape and readily commercial available, thus the characterization of nanoparticles is a standard procedure and various methods such as DLS, UV/Vis, TEM, SEM give reasonable specifications of the pure particles. These methods are well established for high purity and particle concentrations, however, recent interests in nanoparticle-free or -low products demand for methods that enable the detection of few nanoparticles and often in complex matrices, such as cremes, emulsions, suspensions etc. The matrices can contain additional particles, vesicles oils that can form micelles etc, which rises the level of difficulty for the distinct nanoparticle characterization tremendously. Therefore, standard protocols for the specification of nanoparticle-free formulations is of high demand for the industry. In the future, we expect such methods to be implemented in standard quality control of chemical processes, which demands for high throughput analysis and automated evaluation.

In this project, we use silica nanoparticles (SiNPs), a common anticaking agent (AA) in processed food, as model system to establish characterization methods with different levels of accuracy and limits of detection versus speed, sample handling, and automatization. Sample preparation methods that enable to isolate SiNPs for a quantitative analysis will be developed. Among the standard particle characterization techniques, we are also applying dynamic light scattering (DLS), energy-dispersive X-ray spectroscopy with a scanning transmission electron microscope (EDX-STEM), inductively coupled plasma mass spectrometry (ICP-MS) etc in order to gain specificity and sampling speed.

Results

Premix samples with and without silica AA added to it and also with different compositions were provided by DSM Nutritional Products AG (Switzerland) as a first test system. Standard SiNPs with defined sizes at 20, 40 and 120 nm were bought from general engineering & research LCC (USA) to test the different methods under reduced complexity and for validation.

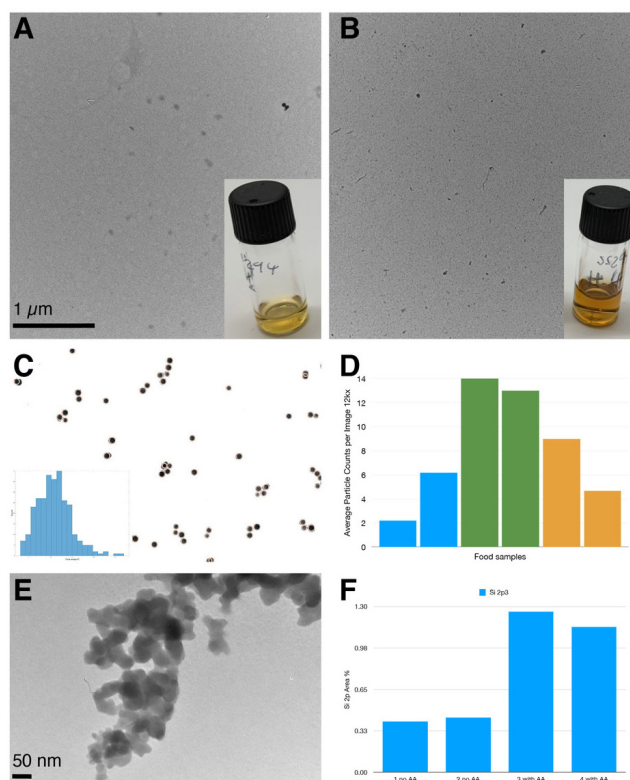


Fig. 1 SiNP evaluation A&B) Transmission electron microscope (TEM) micrographs of digested food samples (inset picture) without (A) and with anticaking agent (AA) (B). Samples were dried on carbon coated Formvar Copper grids and pictures were taken with a Zeiss EM900. C) automated MatLab counting of SiNPs (displayed on 40 nm standard SiNPs) and histogram of diameter distribution lower left. D) MatLab evaluation of food samples with no AA (blue), with AA (green) and with few AA (yellow). Two micrographs at 12kx were evaluated of each food sample. E) TEM micrographs of the pure anticaking agent. F) Silicon 1s atomic area percent measured by X-ray photoelectron spectrometry on 2x 2 food sample without and with AA each. Digested samples were dried on Ti-foil and measured with a PHI 5800, Mg/Al Twin Anode at 10 kV/10 mA, PE 23.5eV.

Sample preparation was difficult as the provided premix samples contain various natural polymers, such as starches, sugars etc, which are not soluble in aqueous solutions. Despite ethyl acetate enabled to obtain turbid solutions and the addition of surfactant such as span85 enhanced the solubility, when imaged by transmission electron microscope (TEM) the surfactants formed vesicles and the remaining organic part lead to a thick opaque coating. Samples were thus in a first step digested by Fenton's reagent, commonly used for

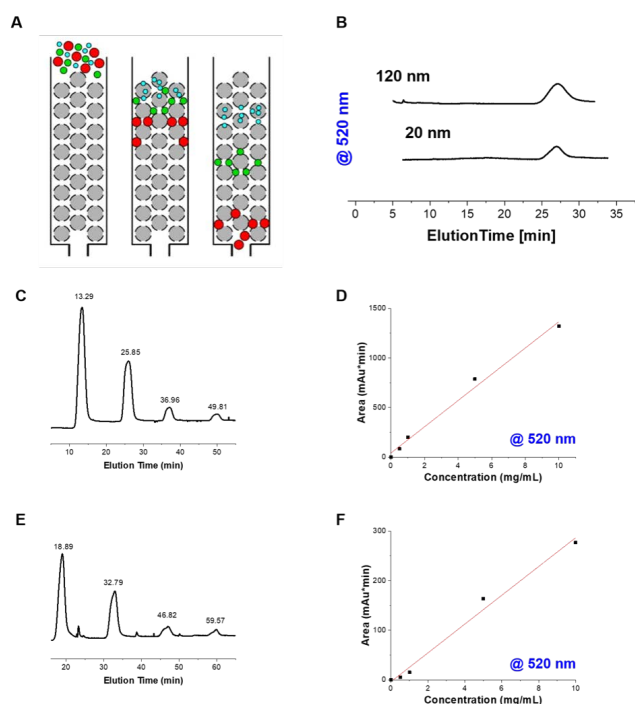


Fig. 2 SEC chromatograms of SiNPs. A) Schematic representation of the size-exclusion chromatography (gel filtration). B) Elution time of 20 and 120 nm SiNPs. C&D) Quantification at 10, 5, 1, 0.5 mg/mL of 120 nm SiNPs. E&F) Quantification at 10, 5, 1, 0.5 mg/mL of 20 nm SiNPs.

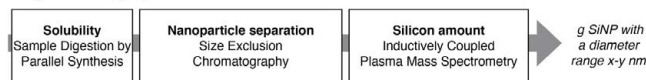
waste water treatment or milk digestion [9]. The digested residue allowed then imaging by TEM and remaining particles were counted with MatLab image processing script (Fig. 1C-D). Multiple particles were found, but when compared to the pure SiNP AA, we found that the SiNP are rather agglomerates of 20 nm amorphous SiNP than round shaped particles (Fig. 1E). The diameter of the agglomerates found in food samples (Fig. 1B) was in range of approx. 20-100 nm. Samples were then measured by STEM and EDX in order to proof the Si character of the particles, however the silicon-type STEM detector, the small particles and low concentration prevented a distinct determination. X-ray photoelectron spectrometry (XPS) performed on a drop of digested solution however showed a significant increase of Si in the sample with AA (Fig. 1F) but does not provide absolute values. ICP-MS enables the quantitative measurement of total Si in a sample, unfortunately food samples often also contain natural silicates in a non-particulate form. Although ICP-MS single particle method would enable to differentiate between silicates and SiNPs, it applies solely upon a NP diameter of >50 nm. Size exclusion chromatography (SEC) was found to separate the standard nanoparticles (20-120 nm SiNP) (Fig. 2) from the residual matrix and the Si content of the fractions was measured by ICP-MS and enables the distinction between silicates and SiNPs. Nevertheless, the combination needs to be further evaluated with the DSM premix samples.

Conclusion

Based on current state of the project we suggest following two SiNP verification methods (Fig. 3) for the quality control of food products: a) The high throughput method for a fast evaluation of large amount of production samples. It will start with the Fenton digestion, then the separation via SEC followed by the analysis by ICP-MS. It will deliver the amount of a range of SiNPs e.g 30 µg of SiNP with diameter range of 20-100 nm in 1L sample. If values are not within specifications, the sample will be further investigated by the

second qualitative but more elaborative method (b) that includes first the Fenton digestion followed by TEM imaging and automated image processing in order to clearly evaluate and characterize nanoparticles in terms of size, distribution, shape, agglomeration etc. Both methods should not only help to estimate a SiNP contamination but also enable to quantify and define lower limits and diameter range for so-called SiNP-free products. Yet for the ultimate proof of the concept more work has to be done during the prolonged project.

High throughput method



Qualitative method

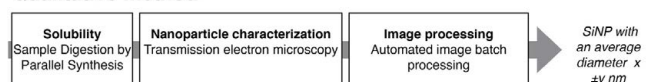


Fig. 3 Scheme of the two suggested SiNPs methods.

References

- [1] Commission recommendation on the definition of nanomaterial, O JEU, L 275/38 (2011)
- [2] M. Younes et al. *Scientific Opinion on the re-evaluation of silicon dioxide (E 551) as a food additive*. EFSA Journal **16**, 5088, 70 (2018)
- [3] N. Prajitha, S. S. Athira, P. V. Mohanan, *Bio-interactions and risks of engineered nanoparticles*, Environ. Res, **172**, 98-108, (2019)
- [4] K. Donaldson, L. Tran, L. A. Jimenez, R. Duffin, D. E. Newby, N. Mills, W. MacNee, V. Stone, *Combustion-derived nanoparticles: a review of their toxicology following inhalation exposure*. Part Fibre Toxicol. **2**, 10 (2005)
- [5] B. Granum, M. Løvik, *The Effect of Particles on Allergic Immune Response*, Toxicological Sciences **65**, 7-17, (2002)
- [6] P. J. A. Borm, W. Kreyling, *Toxicological hazards of inhaled nanoparticles-potential implications for drug delivery*, J. Nanosci. Nanotechnol. **4**, 521-31, (2004)
- [7] G. Oberdörster, E. Oberdörster, J. Oberdörster, *Nanotoxicology: an emerging discipline evolving from studies of ultrafine particles*, Environ Health Perspect. **113**, 823-839 (2005)
- [8] W. H. De Jong, P. J. A Borm, *Drug delivery and nanoparticles: applications and hazards*, Int. J. Nanomedicine. **3**, 133-149 (2008)
- [9] C. P. Shelor, C. A. Campbell, M. Kroll, P. K. Dasgupta, T. L. Smith, A. Abdalla, M. Hamilton, T. W. Muhammad, *Fenton Digestion of Milk for Iodinalysis*, Anal.Chem. **83**, 8300 (2011)

Antibacterial titanium nanostructures by helium plasma irradiation

Project A15.11: TiSpikes (University of Basel, Dept. of Physics and Klinik für Oral Health & Medicine, FHNW Muttentz, Institut Straumann AG Basel)

Project Leader: L. Marot

Collaborators: F. Sanchez, R. Steiner, R. Antunes, M. Kisiel, E. Meyer, K. Mukaddam, S. Köhl, M. Astasov-Frauenhoffer, I. Hauser-Gerspach, J. Köser, R. Wagner, and J. Hofstetter

Introduction

The development of biomaterials that hinder or prevent bacterial colonization and growth is an important challenge in biomaterial research. The inhibition of initial bacterial colonization avoids most implant-related infections and reduces the chance of biofilm formation. Therefore, the observation that nano-pillar surfaces on gecko skin exerted bactericidal effects on certain adherent bacteria by an assumed physico-mechanical mechanism drew much attention. In contrast to the majority of studies conducted on antibacterial materials, the proposed project aims at directly nanostructuring a material that is widely used in medical applications such as orthopedic and dental implants, namely titanium and titanium alloys.

Within this project, a unique nanostructuring method developed at the University of Basel will allow geometrical parameters of the nanostructures to be tuned in order to obtain surfaces exhibiting optimum bactericidal effects (low bacteria attachment and/or survival). Such a physical bactericidal method may become an attractive approach to tackle multi-antibiotic resistant bacteria and could solve an escalating medical issue that poses a threat to global public health. Nanostructuring of the implant surface will also be optimized towards improved soft tissue cell adhesion which is expected to reduce bacterial invasion in the space between implant and tissue leading to periimplantitis. Considering the objective of industrialization, dental implants and abutments will be tested in vivo for pre-clinical evaluation by our industrial partner.

Nanostructuring of the titanium surface

Ti and Ti alloy surfaces were nanostructured at the University of Basel by He ions exposure. A parametric study of the He source was conducted to understand and control the nanostructuring on Ti samples using a small electrode. Results are presented in table 1. Bias and discharge voltage have a strong influence on the mean ion energy. For selected parameters, the dependency of the temperature and ion energy was investigated, showing different growth rates. SEM images of Ti sample nanostructured under other conditions show spikes formation for various temperature and bias (Fig. 1). Ti-spikes with defined heights could be generated by varying the reaction temperature. For high bias (Fig. 1 bottom right), the peaks within one sample exhibit different heights and are promising candidate antibacterial structures.

Table 1 Parametric study of the He source.

Parameters	Ion current	Mean energy
BIAS	-	+++
Discharge voltage	++	++
Flow	-	-
Working pressure	++	+
Emission Amps	-	++
Discharge Amps	++	-

Low influence - High influence +++
 Best: High Bias / High discharge Voltage / Low Pressure / High discharge current / Shorter distance

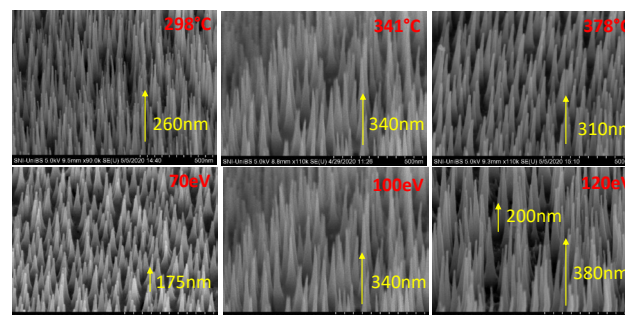
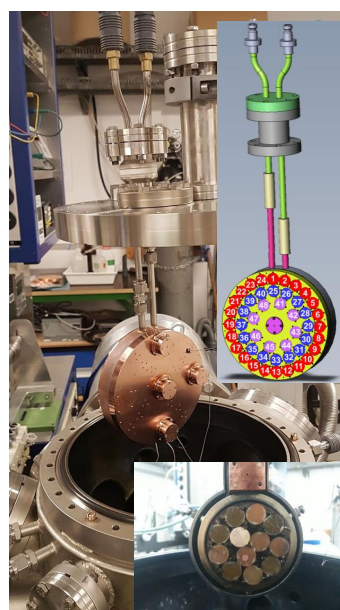


Fig. 1 Spikes formation for different temperatures and helium ion energies on Ti surface.



As the analysis of the antibacterial efficacy and the testing of soft tissue cells-titanium interaction require many samples, a new electrode for the parallel treatment of increased sample numbers (48 samples) was designed, manufactured, and tested (Fig. 2). However, nanostructured homogeneity was not achievable over the whole area for all samples and a smaller electrode was constructed which could deliver 12 homogeneous structured samples (Fig. 2 bottom).

Fig. 2 48 and 12 samples electrodes.

Topography of the nanostructured titanium surface

Atomic Force Microscopy (AFM) measurements were carried out. The left-hand side of figure 3 shows AFM topography image of plasma exposed titanium surface took under ambient conditions and in intermittent contact AFM mode (Fig. 2). The sample roughness is characterized by a long-wavelength “lunar” landscape and homogeneously distributed and densely packed pillars structure. The middle image is the zoom into the pillar structure, with an apparent height of the pillars equal to 400 nm. The image on the right-hand side was taken in water after transferring *E. coli* bacteria onto the plasma structured titanium surface (Fig. 3). The apparent height of the bacteria is equal to about 0.85 μm , and the *E. coli* bacteria membrane is broken by the titanium pillar spiky structure at two spots (one clearly visible on the left side of the bacteria membrane).

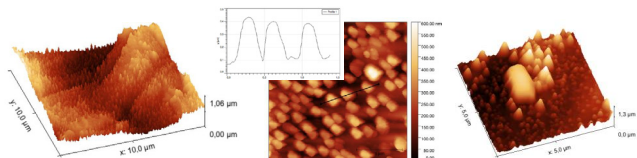


Fig. 3 Left, AFM images in air of nanostructured surface scanned with PPP-EFM cantilever (Topography scan). Middle, Spike's height was 400nm for this sample. Right, AFM images in filtered water of Ti surface with *E. coli* bacteria.

Analysis of antibacterial efficacy and effects on soft tissue cells (human gingival fibroblasts)

Analysis of antibacterial efficacy and effects on soft tissue cells were carried out on Ti nanostructured samples to investigate the effect of air or high purity water storage (Fig. 4). Interestingly the storage conditions had a large influence on the antibacterial efficacy which gives us a further parameter for the optimization of the antibacterial efficacy of the nanostructured titanium samples. The soft tissue cell tests were showing no differences for the samples stored under different conditions, while a higher antibacterial effect was detected by samples stored under air conditions. Thus, it was decided to conserve the samples for all the following experiments in air.

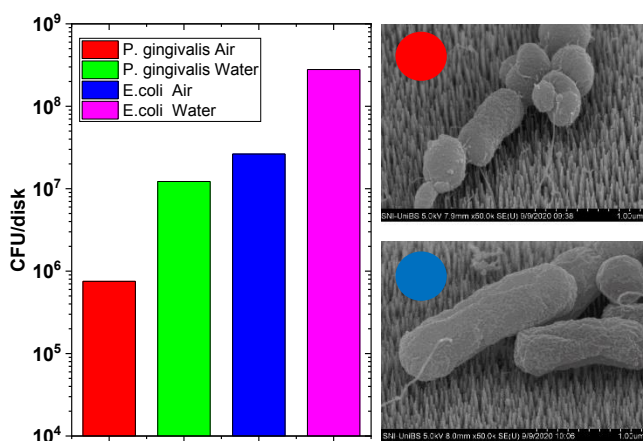


Fig. 4 Colony forming units (=living bacteria) of *P. gingivalis* and *E. coli* following incubation on nanostructured titanium samples stored in air or water. Corresponding SEM observations.

In detail, the influence of the different conservation methods on cultured HGF-1 cell viability and proliferation after 72 h was analyzed. Thirty thousand HGF cells were cultivated on the nanostructured titanium discs, which were conserved in air or purified water after production and tested against ma-

chined titanium discs (control) in 24 well plates. 72 h later, MTT (0.1 mg/ml) was added and HGF cells were incubated for further 4 h. The reaction was stopped by adding 125 μl of DMSO. The supernatants were harvested and the optical density was measured at 590 nm. Conservation of the nanostructured titanium surface in air or purified water does not influence the human gingival fibroblast viability or proliferation capacity (Fig. 5). A slightly reduced viability/proliferation on the sample tested was observed as compared to machined titanium but is in an acceptable range according to ISO 10993-5, however we will further assess soft tissue cell proliferation on samples with varying titanium nanostructure.

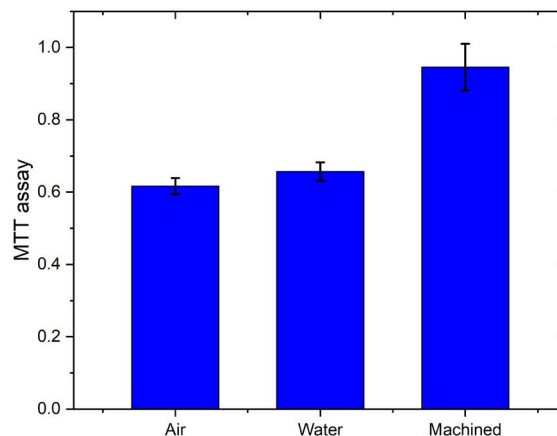


Fig. 5 Comparison of gingival fibroblast cell survival and proliferation on nanostructured titanium discs stored in air and purified water against a machined surface (control) in MTT assay. Values represent mean \pm SD. Three independent experiments were performed in triplicates.

Summary and outlook

Ti and Ti alloy surfaces were nanostructured at the University of Basel by He ion exposure. A parametric study of the He source was conducted to understand and control the nanostructuring on Ti samples using a small electrode. Analysis of antibacterial efficacy and effects on soft tissue cells were carried out on Ti nanostructured samples to investigate the effect of air or high purity water storage. The soft tissue cell tests were showing no differences for the samples stored under air or liquid, while a higher antibacterial effect was detected by samples stored under air conditions.

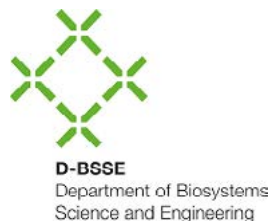
Further characterizations of antibacterial efficacy and effects on soft tissue cells are ongoing. Considering the objective of industrialization, more complex surfaces of commercially available dental implants and abutments will be nanostructured in a next step. If successful, these experimental samples will undergo mechanical and potential pre-clinical testing.

Publications

- Avsar SY, Kapinos LE, Schoenenberger CA, Schertler GFX, Muhle J, Meger B, et al. Immobilization of arrestin-3 on different biosensor platforms for evaluating GPCR binding. *Phys Chem Chem Phys* 2020, 22(41): 24086-24096. <https://doi.org/10.1039/DOCP01464H>
- Barbato S, Kapinos LE, Rencurel C, Lim RYH. Karyopherin enrichment at the nuclear pore complex attenuates Ran permeability. *J Cell Sci* 2020, 133(3). <https://doi.org/10.1242/jcs.238121>
- Batzer M, Shields B, Neu E, Widmann C, Giese C, Nebel C, et al. Single crystal diamond pyramids for applications in nanoscale quantum sensing. *Opt Mater Express* 2020, 10(2): 492-500. <https://doi.org/10.1364/OME.380362>
- Bayogan JR, Park K, Siu ZB, An SJ, Tang CC, Zhang XX, et al. Controllable p-n junctions in three-dimensional Dirac semimetal Cd₃As₂ nanowires. *Nanotechnology* 2020, 31(20). <https://doi.org/10.1088/1361-6528/ab6dfe>
- Ben Yaala M, Scherrer DF, Saeedi A, Moser L, Soni K, Steiner R, et al. Plasma-activated catalytic formation of ammonia from N₂-H₂: influence of temperature and noble gas addition. *Nucl Fusion* 2020, 60(1). <https://doi.org/10.1088/1741-4326/ab519c>
- Bordoloi A, Zannier V, Sorba L, Schonenberger C, Baumgartner A. A double quantum dot spin valve. *Commun Phys-Uk* 2020, 3(1). <https://doi.org/10.1038/s42005-020-00405-2>
- Di Leone S, Avsar SY, Belluati A, Wehr R, Palivan CG, Meier W. Polymer-Lipid Hybrid Membranes as a Model Platform to Drive Membrane-Cytochrome c Interaction and Peroxidase-like Activity. *J Phys Chem B* 2020, 124(22): 4454-4465. <https://doi.org/10.1021/acs.jpcc.0c02727>
- dos Santos EC, Belluati A, Necula D, Scherrer D, Meyer CE, Wehr RP, et al. Combinatorial Strategy for Studying Biochemical Pathways in Double Emulsion Templated Cell-Sized Compartments. *Adv Mater* 2020, 32(48). <https://doi.org/10.1002/adma.202004804>
- Einfalt T, Garni M, Witzigmann D, Sieber S, Baltisberger N, Huwyler J, et al. Bioinspired Molecular Factories with Architecture and In Vivo Functionalities as Cell Mimics. *Adv Sci* 2020, 7(4). <https://doi.org/10.1002/advs.201901923>
- Geirhos K, Gross B, Szigeti BG, Mehlin A, Philipp S, White JS, et al. Macroscopic manifestation of domain-wall magnetism and magnetoelectric effect in a Néel-type skyrmion host. *Npj Quantum Mater* 2020, 5(1): 44. <https://doi.org/10.1038/s41535-020-0247-z>
- Gross B, Philipp S, Geirhos K, Mehlin A, Bordacs S, Tsurkan V, et al. Stability of Neel-type skyrmion lattice against oblique magnetic fields in GaV₄S₈ and GaV₄Se₈. *Phys Rev B* 2020, 102(10). <https://doi.org/10.1103/PhysRevB.102.104407>
- Hedrich N, Rohner D, Batzer M, Maletinsky P, Shields BJ. Parabolic Diamond Scanning Probes for Single-Spin Magnetic Field Imaging. *Phys Rev Appl* 2020, 14(6). <https://doi.org/10.1103/PhysRevApplied.14.064007>
- Huber F, Lang HP, Lang D, Wuthrich D, Hinic V, Gerber C, et al. Rapid and Ultrasensitive Detection of Mutations and Genes Relevant to Antimicrobial Resistance in Bacteria. *Glob Chall* 2020. <https://doi.org/10.1002/gch2.202000066>
- Indolese DI, Karnatak P, Kononov A, Delagrangé R, Haller R, Wang LJ, et al. Compact SQUID Realized in a Double-Layer Graphene Heterostructure. *Nano Lett* 2020, 20(10): 7129-7135. <https://doi.org/10.1021/acs.nanolett.0c02412>
- Junger C, Delagrangé R, Chevallier D, Lehmann S, Dick KA, Thelander C, et al. Magnetic-Field-Independent Subgap States in Hybrid Rashba Nanowires. *Phys Rev Lett* 2020, 125(1). <https://doi.org/10.1103/PhysRevLett.125.017701>
- Karg TM, Gouraud B, Ngai CT, Schmid GL, Hammerer K, Treutlein P. Light-mediated strong coupling between a mechanical oscillator and atomic spins 1 meter apart. *Science* 2020, 369(6500): 174-+. <http://doi.org/10.1126/SCIENCE.ABB0328>
- Khattab IM, Sahi VP, Baltenweck R, Maia-Grondard A, Hugueney P, Bieler E, et al. Ancestral chemotypes of cultivated grapevine with resistance to Botryosphaeriaceae-related dieback allocate metabolism towards bioactive stilbenes. *New Phytol* 2020. <https://doi.org/10.1111/nph.16919>
- Kononov A, Abulizi G, Qu KJ, Yan JQ, Mandrus D, Watanabe K, et al. One-Dimensional Edge Transport in Few-Layer WTe₂. *Nano Lett* 2020, 20(6): 4228-4233. <https://doi.org/10.1021/acs.nanolett.0c00658>
- Krywko-Cendrowska A, di Leone S, Bina M, Yorulmaz-Avsar S, Palivan CG, Meier W. Recent Advances in Hybrid Biomimetic Polymer-Based Films: from Assembly to Applications. *Polymers (Basel)* 2020, 12(5). <https://doi.org/10.3390/polym12051003>
- Leisgang N, Shree S, Paradisanos I, Sponfeldner L, Robert C, Lagarde D, et al. Giant Stark splitting of an exciton in bilayer MoS₂. *Nat Nanotechnol* 2020, 15(11): 901-+. <https://doi.org/10.1038/s41565-020-0750-1>
- Li RY, Wang YF, Zhang JY, Meyer E. Tribochemistry of ultra-low friction fullerene-like carbon films in humid air. *Appl Surf Sci* 2020, 507. <https://doi.org/10.1016/j.apsusc.2019.145040>
- Liu Z, Wang YF, Glatzel T, Hinaut A, Zhang JY, Meyer E. Low Friction at the Nanoscale of Hydrogenated Fullerene-Like Carbon Films. *Coatings* 2020, 10(7). <https://doi.org/10.3390/coatings10070643>

- Martiel I, Mozzanica A, Opara NL, Panepucci E, Leonarski F, Redford S, et al. X-ray fluorescence detection for serial macromolecular crystallography using a JUNGFRU pixel detector. *J Synchrotron Radiat* 2020, 27: 329-339. <https://doi.org/10.1107/S1600577519016758>
- Mattiati H, Rossi N, Gross B, Pablo-Navarro J, Magen C, Badaea R, et al. Nanowire Magnetic Force Sensors Fabricated by Focused-Electron-Beam-Induced Deposition. *Phys Rev Appl* 2020, 13(4). <https://doi.org/10.1103/PhysRevApplied.13.044043>
- Mortelmans T, Kazazis D, Guzenko VA, Padeste C, Braun T, Stahlberg H, et al. Grayscale e-beam lithography: Effects of a delayed development for well-controlled 3D patterning. *Microelectron Eng* 2020, 225. <https://doi.org/10.1016/j.mee.2020.111272>
- Pawlak R, Drechsel C, D'Astolfo P, Kisiel M, Meyer E, Cerda JI. Quantitative determination of atomic buckling of silicene by atomic force microscopy. *P Natl Acad Sci USA* 2020, 117(1): 228-237. <https://doi.org/10.1073/pnas.1913489117>
- Pawlak R, Liu XS, Ninova S, D'Astolfo P, Drechsel C, Sangtarash S, et al. Bottom-up Synthesis of Nitrogen-Doped Porous Graphene Nanoribbons. *J Am Chem Soc* 2020, 142(29): 12568-12573. <https://doi.org/10.1021/jacs.0c03946>
- Pawlak R, Vilhena JG, D'Astolfo P, Liu X, Prampolini G, Meier T, et al. Sequential Bending and Twisting around C-C Single Bonds by Mechanical Lifting of a Pre-Adsorbed Polymer. *Nano Lett* 2020, 20(1): 652-657. <https://doi.org/10.1021/acs.nanolett.9b04418>
- Poggio M, Rossi N. Currents cool and drive. *Nature Physics* 2020, 16(1)10-11. <https://doi.org/10.1038/s41567-019-0723-1>
- Poggio M. 17 - Determining magnetization configurations and reversal of individual magnetic nanotubes. In: Vázquez M (ed). *Magnetic Nano- and Microwires (Second Edition)*. Woodhead Publishing, 2020, pp 491-517
- Riedel D, Flagan S, Maletinsky P, Warburton RJ. Cavity-Enhanced Raman Scattering for in situ Alignment and Characterization of Solid-State Microcavities. *Phys Rev Appl* 2020, 13(1). <http://dx.doi.org/10.1103/PhysRevApplied.13.014036>
- Roch JG, Miserev D, Froehlicher G, Leisgang N, Sponfeldner L, Watanabe K, et al. First-Order Magnetic Phase Transition of Mobile Electrons in Monolayer MoS₂. *Phys Rev Lett* 2020, 124(18). <http://dx.doi.org/10.1103/PhysRevLett.124.187602>
- Rösner B, Finizio S, Koch F, Döring F, Guzenko VA, Langer M, et al. Soft x-ray microscopy with 7 nm resolution. *Optica* 2020, 7(11): 1602-1608. <https://doi.org/10.1364/OP-TICA.399885>
- Rousounelou E, Schmitt S, Pestalozzi L, Held M, Roberts TM, Panke S. Ultra-high throughput screening for novel protease specificities. *Methods Enzymol* 2020, 644: 169-189. <https://doi.org/10.1016/bs.mie.2020.06.005>
- Santos JC, Boucher D, Schneider LK, Demarco B, Dilucca M, Shkarina K, et al. Human GBP1 binds LPS to initiate assembly of a caspase-4 activating platform on cytosolic bacteria. *Nat Commun* 2020, 11(1): 3276. <https://doi.org/10.1038/s41467-020-16889-z>
- Savchenko TM, Buzzi M, Howald L, Ruta S, Vijayakumar J, Timm M, et al. Single femtosecond laser pulse excitation of individual cobalt nanoparticles. *Phys Rev B* 2020, 102(20). <https://doi.org/10.1103/PhysRevB.102.205418>
- Scherb S, Hinaut A, Pawlak R, Vilhena JG, Liu Y, Freund S, et al. Giant thermal expansion of a two-dimensional supramolecular network triggered by alkyl chain motion. *Commun Mater* 2020, 1(1): 8. <https://doi.org/10.1038/s43246-020-0009-2>
- Scherubl Z, Fulop G, Moca CP, Gramich J, Baumgartner A, Makk P, et al. Large spatial extension of the zero-energy Yu-Shiba-Rusinov state in a magnetic field. *Nat Commun* 2020, 11(1): 1834. <https://doi.org/10.1038/s41467-020-15322-9>
- Tarvirdipour S, Huang X, Mihali V, Schoenenberger CA, Palivan CG. Peptide-Based Nanoassemblies in Gene Therapy and Diagnosis: Paving the Way for Clinical Application. *Molecules* 2020, 25(15). <https://doi.org/10.3390/molecules25153482>
- Tarvirdipour S, Schoenenberger CA, Benenson Y, Palivan CG. A self-assembling amphiphilic peptide nanoparticle for the efficient entrapment of DNA cargoes up to 100 nucleotides in length. *Soft Matter* 2020, 16(6): 1678-1691. <https://doi.org/10.1039/C9SM01990A>
- Thakkar P, Guzenko VA, Lu PH, Dunin-Borkowski RE, Abrahams JP, Tsujino S. Fabrication of low aspect ratio three-element phase shifters for voltage-controlled three electron beam interference. *J Appl Phys* 2020, 128(13). <https://doi.org/10.1063/5.0020383>
- Thomas FS, Baumgartner A, Gubser L, Jünger C, Fülöp G, Nilsson M, et al. Highly symmetric and tunable tunnel couplings in InAs/InP nanowire heterostructure quantum dots. *Nanotechnology* 2020, 31(13): 135003. <https://doi.org/10.1088/1361-6528/ab5ce6>
- Urosev I, Morales JL, Nash MA. Phase Separation of Intrinsically Disordered Protein Polymers Mechanically Stiffens Fibrin Clots. *Adv Funct Mater* 2020, 30(51). <https://doi.org/10.1002/adfm.202005245>
- Wang LJ, Makk P, Zihlmann S, Baumgartner A, Indolese DI, Watanabe K, et al. Mobility Enhancement in Graphene by in situ Reduction of Random Strain Fluctuations. *Phys Rev Lett* 2020, 124(15). <https://doi.org/10.1103/PhysRevLett.124.157701>
- Wu D, Rigo S, Di Leone S, Belluati A, Constable EC, Housecroft CE, et al. Brushing the surface: cascade reactions between immobilized nanoreactors. *Nanoscale* 2020, 12(3): 1551-1562. <https://doi.org/10.1039/C9NR08502E>
- Zelmer C, Zweifel LP, Kapinos LE, Craciun I, Guven ZP, Palivan CG, et al. Organelle-specific targeting of polymersomes into the cell nucleus. *P Natl Acad Sci USA* 2020, 117(6): 2770-2778. <https://doi.org/10.1073/pnas.1916395117>
- Zihlmann S, Makk P, Rehmann MK, Wang LJ, Kedves M, Indolese DI, et al. Out-of-plane corrugations in graphene based van der Waals heterostructures. *Phys Rev B* 2020, 102(19). <https://doi.org/10.1103/PhysRevB.102.195404>

Swiss Nanoscience Institute – A research initiative of the University of Basel and the Canton of Aargau





**Educating
Talents**
since 1460.

University of Basel
Petersplatz 1
P.O. Box 2148
4001 Basel
Switzerland
www.unibas.ch

Swiss Nanoscience Institute
University of Basel
Klingelbergstrasse 82
4056 Basel
Switzerland
www.nanoscience.ch